An Accurate and Efficient Varying Order NURBS Discretization Method for Isogeometric Analysis of Contact Problems

A Thesis Submitted

in the Partial Fulfilment of the Requirements

for the Degree of

Doctor of Philosophy

by

Vishal Agrawal

to the

Department of Mechanical Engineering

Indian Institute of Technology Guwahati

Guwahati 781039, Assam, India

November 2020

Declaration

I hereby declare that the information presented in the thesis titled **"An Accurate and Efficient Varying Order NURBS Discretization Method for Isogeometric Analysis of Contact Problems"** is entirely my account of the research under the supervision of Dr. Sachin Singh Gautam. No part of this work has been submitted for the award of any degree, diploma, associate-ship, fellowship, or its equivalent to any University or Institution. I have not violated any copyright and plagiarism law. In keeping with the general practice of reporting scientific observations, due acknowledgments have been made wherever the work described is based on the findings of other researchers.

November 2020 **Vishal Agrawal**

Certificate

This is to certify that the thesis entitled **"An Accurate and Efficient Varying Order NURBS Discretization Method for Isogeometric Analysis of Contact Problems"** submitted by **Vishal Agrawal**, Roll No. 146103021, to the Indian Institute of Technology Guwahati, for the award of the degree of Doctor of Philosophy in Mechanical Engineering, has been carried out by him under my supervision. The results contained in this thesis have not been submitted in part or full to any other University or Institute for the award of any degree.

November 2020

(Dr. Sachin Singh Gautam)
Assistant Professor
Department of Mechanical Engineering
Indian Institute of Technology Guwahati
Guwahati - 781039, India.

Acknowledgements

I want to express my sincere gratitude towards many people who have helped me during various phases of my PhD work. First and foremost, I wish to express my special thanks to my supervisor Dr. Sachin Singh Gautam, for his advice, patience, support, and comments on this thesis. I feel very privileged to have a supervisor who gave me the freedom to explore many things on my own and being encouraging and patient even when my steps faltered. His faith in me have helped me to keep motivated and moving forward in my PhD work. His valuable advice will help me in a long way in shaping my future career. I also wish to express my sincere gratitude to my Doctoral Committee members Professor Uday Shanker Dixit, Professor Arbind Kumar Singh (Civil Engineering), Dr. Arup Kumar Nandy, and Late Dr. Annem Narayana Reddy. Their valuable suggestions and encouragement have been beneficial in improving my research work.

I am further grateful to Prof. Roger A. Sauer (RWTH Aachen, Germany) for hosting me for three months and providing me an opportunity to work in a new research direction. His integral view on research has helped me in looking at the research from a different perspective. I am grateful to my supervisor for planning this research visit and for extending his support financially. I also would like to thank Dr. Thang X. Duong (RWTH, Aachen, Germany) for his time for many valuable discussions during my visit.

I am also grateful to my friends Saipraneeth, Kaushik, Ashish, and Sunil for their encouragement, support, and helping me in the various aspects of my PhD work. I am also thankful to my lab mates Utpal, Shashi, Subhajit, and Raktim. Without them, my stay in the lab would have been boring and monotonous. I also thank my friends outside IITG Ashish, Nikhil, Mayank, Avinash, Himanshu, and Narayan for their support and encouragement.

Most importantly, I owe my deepest gratitude to my parents and two brothers for their immeasurable love, patience, and continuous encouragement all the time. I also would like to express my appreciation to my wife for her love, care, and being a constant source of strength during my PhD work. The last words go to my little daughter for her unconditional love. She has given me the extra strength to get things done.

Abstract

In this work, a new method, denoted as varying order based NURBS discretization, is proposed to enhance the performance of isogeometric analysis (IGA) technique within the framework of computational contact mechanics. The method makes use of higher-order NURBS for the evaluation of contact integrals. The minimum orders of NURBS capable of representing the complex shape geometries exactly are employed for the bulk computations. With such a discretization procedure, the proposed methodology enables the order elevation based refinement of a NURBS discretized geometry in a controlled manner. To achieve this, a higher-order NURBS layer is used as the contact boundary layer of an initially lower-order of NURBS discretized geometry. The NURBS layer is constructed using different surface refinement strategies such that it is accompanied by a large number of additional degrees of freedom and matches with the bulk parameterization.

Further, a Gauss-point-to-surface contact algorithm with the penalty method is combined with the presented methodology towards developing a simple yet computationally efficient technique for isogeometric contact analysis. In order to demonstrate the efficacy and capabilities of the proposed method, various numerical examples involving small and large deformation contact between deformable bodies in two- as well as three-dimensional settings with or without accounting friction are considered. In addition, an adhesive peeling problem is analyzed to demonstrate its performance for the peeling computations. The results with the existing standard NURBS-based discretizations are used for the comparative assessment.

The obtained results show that with the proposed method, a much higher accuracy can be achieved even with a coarse mesh as compared to the existing NURBS discretization approach. It exhibits a major gain in the numerical efficiency without the loss of stability, robustness, and the intrinsic features of NURBS-based IGA technique for a similar accuracy level. The simplicity of the proposed method allows itself to be conveniently embedded into the standard NURBS-based IGA framework after only a few minor modifications.

Contents

List of Figures

List of Tables

Nomenclature

Latin symbols

A_H	Hamaker's constant
$\bar{\boldsymbol{b}}$	Body force per unit volume
$\boldsymbol{B}$	Left Cauchy-Green deformation tensor
C^{p-1}	Inter-element continuity of a p^{th} order of basis function
$\boldsymbol{C}$	Right Cauchy-Green deformation tensor
d	Dimension of the physical space
E	Young's modulus
$\boldsymbol{E}$	Green-Lagrangian strain tensor
$\mathbf{f}$	System force vector
$\mathbf{f}_{\text{c}}$	Contact force vector
$\mathbf{f}_{\text{ext}}$	External force vector
$\mathbf{f}_{\text{int}}$	Internal force vector
$\mathbf{f}^e$	Elemental force vector
$\boldsymbol{F}$	Deformation gradient tensor
g_{N}	Normal gap function
g_{T}	Tangential gap function
$\boldsymbol{I}$	Identity tensor
$\mathbf{I}_d$	Identity matrix of dimension d
j^e	Transformation gradient from parametric element to current configuration
J^e	Transformation gradient from parametric element to reference configuration
J_c^e	Stretch of contact surface element

$\mathbf{k}$	System tangent matrix
$\mathbf{k}_{\mathrm{c}}$	Contact tangent matrix
$\mathbf{k}_{\mathrm{int}}$	Internal tangent matrix
$\mathbf{k}^e$	Elemental tangent matrix
$\boldsymbol{n}$	Normal vector
n^e_{cp}	Number of control points in a bulk element
n^e_{cps}	Number of control points on the contact surface of an element
n_{el}	Number of bulk elements in a body
n_{elc}	Number of contact elements in a body
n_i	Number of control points in i^{th} parametric direction
N_{l,p_i}	p^{th} order of l^{th} B-spline function
p_i	Interpolation order along i^{th} parametric direction
p_c	Interpolation order of NURBS on contact surface
r	Distance between two interacting points
r_0	Equilibrium distance of Lennard-Jones potential
r_{eq}	Equilibrium distance between two interacting points
R^p	Univariate NURBS function
R^{p_1,p_2}	Bivariate NURBS function
R^{p_1,p_2,p_3}	Trivariate NURBS function
R_A	Multi-variate A^{th} NURBS function
$\mathbf{R}$	NURBS function matrix
$\boldsymbol{S}$	Second Piola-Kirchoff stress tensor
$\boldsymbol{t}$	Traction vector
$\bar{\boldsymbol{t}}$	Prescribed traction vector
$\boldsymbol{t}_{\mathrm{N}}$, t_{N}	Normal traction vector, magnitude
$\boldsymbol{t}_{\mathrm{T}}$, t_{T}	Tangential traction vector, magnitude
$\boldsymbol{T}_c$, T_c	Adhesive traction vector, magnitude
$\bar{\boldsymbol{u}}$	Prescribed displacement vector
$\boldsymbol{u}^e$	Control point displacement vector of element e
$\boldsymbol{U}$	Right stretch tensor
$\boldsymbol{V}$	Left stretch tensor
W	Normalizing weight function
$\bar{W}$	Strain energy density function per unit volume

$\boldsymbol{x}$	Position vector of a point in current configuration
$\mathbf{x}^e$	Control point position vector of element e in the current configuration
$\bar{\boldsymbol{x}}^{\mathrm{m}}$	Physical coordinate of closest projection point on master contact surface
$\boldsymbol{X}$	Position vector of a point in reference configuration
$\mathbf{X}^e$	Control point position vector of element e in the reference configuration
$\boldsymbol{X}^w$	Projective control point vector

Greek symbols

γ	Slip parameter
δ_{ij}	Kronecker's delta
ϵ_{N}	Normal penalty parameter
ϵ_{T}	Tangential penalty parameter
λ	Bulk modulus
μ	Shear modulus
μ_f	Friction coefficient
ν	Poisson's ration
$\hat{\lambda}, \hat{\mu}$	Effective Lamé moduli
ξ^i	i^{th} parametric space
$\boldsymbol{\xi}$	Position vector of a point in parametric space
ξ_l^i	Coordinate of a l^{th} knot point in i^{th} parametric direction
ξ_{m}^i	i^{th} convective coordinate at master contact surface
$\boldsymbol{\xi}_{\mathrm{m}}$	Convective coordinate vector at master contact surface
ρ_0	Mass-density of a body in the reference configuration
ρ	Mass-density of a body in the current configuration
$\boldsymbol{\sigma}$	Cauchy stress tensor
$\boldsymbol{\tau_\alpha}$	Co-variant tangent vector
$\boldsymbol{\tau^\alpha}$	Contra-variant tangent vector

Φ	Slip function
$\boldsymbol{\varphi}$	Deformation mapping
∇_0	Gradient operator with respect to reference configuration
∇	Gradient operator with respect to current configuration
Ξ^i	Knot vector along ξ^i parametric space
Γ^e_{0c}	Contact surface of an element in reference configuration
Γ^e_c	Contact surface of an element in current configuration
Ω^e_0	Bulk element of a body in reference configuration
Ω^e	Bulk element of a body in the current configuration

Special symbols

$\mathcal{A}_c$	Active-set of contact points
$\mathcal{B}_0$	Contacting body in reference configuration
$\mathcal{B}$	Contacting body in current configuration
$\mathbb{c}$	Fourth-order spatial elasticity tensor
$\partial\mathcal{B}_0$	Boundary of a body in reference configuration
$\partial\mathcal{B}$	Boundary of a body in current configuration
$\partial_c\mathcal{B}$	Contact boundary of a body in current configuration
$\partial_t\mathcal{B}$	Traction boundary of a body in current configuration
$\partial_u\mathcal{B}$	Displacement boundary of a body in current configuration
$\mathcal{D}$	Dissipation due to frictional slip
$\mathcal{I}$	Fourth-order identity tensor
$\mathbb{R}$	Coordinate space of real numbers
$\mathcal{W}$	Total virtual work
$\mathcal{W}_{\text{c}}$	Contact virtual work
$\mathcal{W}_{\text{ext}}$	External virtual work
$\mathcal{W}_{\text{int}}$	Internal virtual work

Mathematical symbols

$[\,\cdot\,]$	Matrix representation of a tensor
$[\,\cdot\,]^e$, $(\,\cdot\,)^e$	Matrix, column vector containing control point values of an element e

$(\cdot)^{\mathrm{T}}$	Transpose of a quantity
$\lvert\cdot\rvert$	Absolute value of a quantity
$\lvert\lvert\cdot\rvert\rvert$	Norm of a matrix or vector
$\dot{(\,)}$	First-order time derivative of a quantity
$\ddot{(\,)}$	Second-order time derivative of a quantity
$\bar{(\cdot)}$	Quantity computed at the projection point
$\delta(\cdot)$	Variation of a quantity
$\Delta(\cdot)$	Increment of a quantity
$(\cdot)_n$	Quantity evaluated at time t_n
$(\cdot)_{n+1}$	Quantity evaluated at time t_{n+1}
$(\cdot)^{\mathrm{s}}$	Quantity associated to slave contact body
$(\cdot)^{\mathrm{m}}$	Quantity associated to master contact body
$(\cdot)^{\mathrm{k}}$	Quantity associated to a body $k = \{s, m\}$
$(\,)_{st}$	Quantity evaluated at the stick state
$(\,)_{sl}$	Quantity evaluated at the slip state
$\mathrm{d}(\cdot)$	Differentiation of a quantity
$\partial(\cdot)$	Partial derivative of a quantity
,	Partial differentiation if the following subscript is a letter; for example $\mathbf{R}^e_{,x} = \frac{\partial \mathbf{R}^e}{\partial x}$

Chapter 1

Introduction and Literature Review

1.1 Contact mechanics

Contact problems, which are studied in contact mechanics, exist virtually in all the structural, mechanical as well as in the biological systems. In a car, for instance, the contact appears in the bearings between ball and rings, in the gear systems where contact forces transmit from one to another gear, within combustion engine where contact takes places between piston and cylinder, etc. In the sheet metal forming process, one can find the contact between a deformable or rigid punch and a metal sheet and a die. In the animal or human body, the contact interactions can be found between the mating bones of the skeleton joints, and between the blood cells and blood vessels.

From an engineering point of view, gaining a fine understanding of contact interactions between the bodies and determining the distributions of the contact responses at the interface are of great importance since it provides the necessary information to design a better, safe, and optimum physical system. For example, at the macro-scale level, contact mechanics is used to assess the load-capabilities and service life of the mechanical systems whose underlying multi-components slide or interact with each other, e.g. in the bearings and gear-box systems. Moreover, in the automobile industry, crashworthiness analysis of cars is of great importance as it significantly reduces the excessive cost and time associated with the prototyping process, as can be seen in Fig. 1.1a. Beyond that, modelling and development of complex engineering processes such as deep-drawing, sheet metal-forming, and many more largely exploit the prin-

(a)

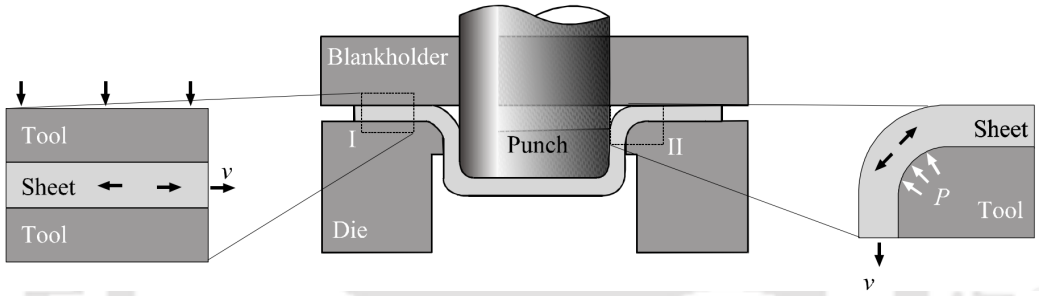

(b)

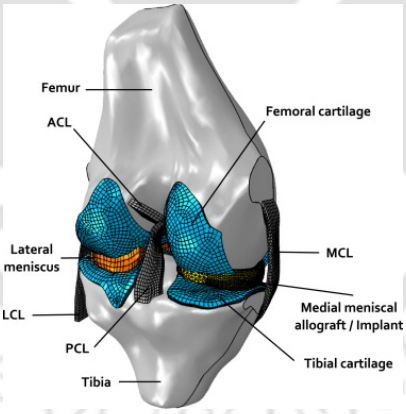

(c)

Figure 1.1: Examples of contact: (a) Crashworthiness analysis of a car against a deformable barrier using the experimental (top) and numerical simulation (bottom) (Reprinted with permission from [1]); (b) Schematic of the deep drawing process where the contact is present between a rigid blank holder and a deformable sheet and a rigid die (Reprinted with permission from [2]); (c) A model of the knee joint where the contact is present between the femoral and tibial cartilage surfaces of the lateral and medial meniscal compartments (Reprinted with permission from [3]).

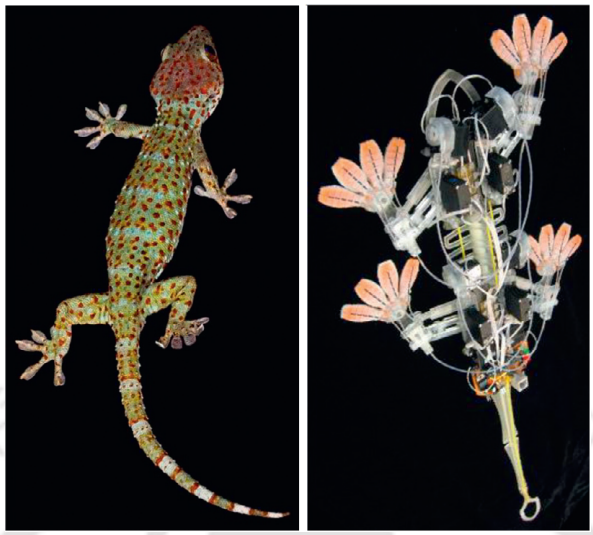

Figure 1.2: Studying the adhesion mechanism of hairy toes of Tokay Gecko (right) and biologically inspired stickybot that can climb on smooth surfaces (left) (Reprinted with permission from [4]).

cipal of contact mechanics, see Fig. 1.1b. Furthermore, contact mechanics of human skeleton joints, e.g. knee joint as shown in Fig. 1.1c, allows the injury predictions and vulnerability assessment under the weight of the body in different circumstances.

At the micro- and nano-scale levels, contact mechanics is helpful to understand the interaction characteristics of various adhesive systems. An example is the adhesion mechanism of geckos and insects, which is useful to design the biologically inspired systems such as adhesive tapes and stickybots (climbing-robots), as shown in Fig. 1.2.

Despite their fundamental role in the solids and structural mechanics, contact effects are not often taken into account in conventional engineering analysis [5]. This is since the mechanical problems involving contact are inherently non-linear even if the problem setup is quite simple (linear elastic deformation and simple loading conditions). This non-linearity stems from the fact that actual contact surface on which bodies comes into contact and the stresses developed on it are not known *a prior* to the application of the load to a body. Thus, the mathematical description of the contact problem naturally involves the unknown boundary conditions, possibly changing over time [6]. In addition to this, the overall contact phenomena involve the influence of one or more closely related effects such as sticking and sliding states during frictional contact, adhesion interactions, lubrication, and wear on the interaction surface, which envisages the extreme complexities in describing the mathematical model

of contact interactions. Besides, the typical non-linearities inherent in solids mechanics such as large deformations and non-linear material behaviour additionally makes a contact problem strongly non-linear. Therefore, rigorous mathematical modelling and analysis of a mechanical problem involving contact that altogether takes the contact phenomena, and the additional non-linearities into account is extremely complex and challenging.

1.1.1 Historical background

The numerical study of contact began in the 1880s with the classical analytical work by German physicist Heinrich Rudolf Hertz [7], which is considered to have laid the foundation of the field of contact mechanics [8]. While attempting to understand the optical interference patterns of the stacked glass lenses, Hertz developed the theory that gives the distribution of stresses and indentation for the frictionless elastic contact between elliptical bodies that were subjected to compressive load. After that, the new developments in the study of contact problems, having a common feature to overcome the restrictions of Hertz's theory, such as pure elasticity, frictionless, and small deformations, did not appear until the beginning of 20^{th} century. A comprehensive overview of the most important analytical solutions and approaches for contact problems can be found in the textbooks by Johnson [8], and Kikuchi and Oden [9], and references therein.

Since the analytical solution approaches are very restrictive and can only be used to obtain the closed-form solution of a few simple geometries, boundary conditions, and mainly for linear materials. Thus, they are inconceivable for real-world or industrial contact problems, which usually include geometrical and material non-linearities and effects of closely related interactions at the contact surface of arbitrary geometries.

With the advent of the finite element method (FEM) and simultaneous rapid growth of the computational technology, numerical simulations have become a commonplace among the engineering and scientific communities [10]. The first attempts to solve the structural mechanic's problems using FEM were published in 1960s [11]. Thereafter, the literature on the application of FEM to various classes of problems that could not be solved using analytical methods grew exponentially. The first procedures for the treatment of contact problems using the finite element method appeared in the 1970s. In this direction, the early works by Wilson and Parsons [12], and Chan and Tube [13]

are identified as the first contributions towards solving the elastic contact problems using the FEM. Later, the continuum-based formulation and numerical implementations of the FEM for frictionless contact problems between the linearly elastic bodies was presented by Hughes et al. [14]. Thereafter, the numerical analysis of contact problems with Coulomb's friction between an elastic body and a rigid foundation is described in work by Campos et al. [15]. The extension of the existing mathematical framework to large deformation frictional contact between an elastic body and different shapes of rigid foundations was presented by Wriggers et al. [16]. The general continuum-based finite element formulation for large deformation frictional contact problems between two deformable bodies is introduced by Laursen and Simo [17]. A comprehensive overview of the treatment of different contact problems using the FEM can be found in the textbook by Laursen [18] and Wriggers [6], and the references therein.

1.2 Finite element analysis of contact problems and smoothing procedures

The huge importance of contact problems in many engineering fields has motivated the development of robust and efficient algorithms to improve the accuracy of the numerical simulations [19, 20]. As is widely recognized, the robustness and accuracy of the numerical simulation of contact problems are determined by two main aspects [6, 20, 21]. The first aspect is the type of method employed for the enforcement of contact constraints into the variational formulations of the problem. The most popular choices are the penalty method [16, 22], Lagrange multiplier method [23], and a combination of both these methods, known as augmented Lagrange multiplier method [24–26]. The second aspect is the type of scheme employed for expressing the contact contributions to the discretized weak form in a specific manner. The widely adopted options are: Node-to-Segment (NTS) [16, 22, 27], Gauss-Point-to-Surface (GPTS) [28–31], and mortar contact formulation [32–37]. The relative merits and demerits of the above-mentioned methods and schemes can be found in the above-cited references and the textbooks of Laursen [18] and Wriggers [6].

Another factor that adversely influences the performance of the contact algorithms mainly in terms of the robustness and accuracy is, namely, the geometrical discontinuity in the contact surface induced by the spatial discretization [6, 20, 21]. It is widely

known that the C^0-continuous Lagrange polynomial based FE discretization leads to the non-smooth or faceted representation of the smooth contact boundaries originally defined in a CAD system. As a result, it causes the non-smooth variation of the contact kinematics and kinetic variables, i.e. non-uniquely defined normal (and tangential) vector field across the contact surface. However, such a faceted representation of the contact surface works well if the geometries retain the low surface curvature throughout the simulation and for small deformation problems. But, serious computational issues occur for the applications involving arbitrary large curvature geometries and in the simulation of large relative sliding contact problems, even in a two-dimensional setting. In such cases, during sliding the sudden change of the direction of normal (and tangential) vector across the faceted boundaries of contact elements strongly affects the numerical stability of the nonlinear solution algorithm and generates the spurious oscillations or jumps in the contact response even when the convergence is achieved. These issues become even more prominent on increasing the interpolation order of the underlying Lagrange shape functions due to the Gibbs effect [10]. It should be emphasized that these issues exist regardless of the method adopted for the enforcement of contact constraints and are of primary concern within the pointwise contact algorithms where contact constraints are enforced directly at the interacting points, i.e. either at the nodes or quadrature points [6, 21].

Thus, considerable research progress has been made in the context of computational contact mechanics to alleviate the issues emanating from the geometrical discontinuity in the contact surface. In the following, first, an overview of the various contact surface smoothing procedures introduced in the framework of FEM are briefly presented. In the next section, the isogeometric analysis technique, which is a more general approach as compared to surface smoothing procedures, is described in a detailed manner.

1.2.1 Contact surface smoothing procedures

In order to circumvent the issues stemming from the faceted representation of the contact surface, various smoothing strategies have been introduced. They utilize the CAD interpolation functions for the smooth description of the contact surface of the bodies discretized with the C^0-continuous finite elements. In particular, for two-dimensional contact problems, these strategies include: cubic Hermite polynomials (Pietrzak and Curnier [26], and Padmanabhan et al. [38]), cubic Bernstein polynomial (Wriggers

et al. [39]), and cubic splines polynomials (El-Abbasi et al. [40], and Al-Dojayli and Meguid [41]) as shape functions that provide the C^1-continuous representation of the contact surface. The non-uniform rational B-spline (NURBS) based technique introduced by Stadler et al. [42] allows an arbitrary level of C^n-continuous contact surfaces for two-dimensional contact problems.

Moreover, a number of smoothing strategies have also been presented for three-dimensional contact problems. In case of regular quadrilateral mesh, Bézier interpolation-based strategies (Pietrzak and Curnier [26], and Landon et al. [43]) provide the C^1-continuous description of the contact surface. For unstructured mesh, the smoothing method introduced by Puso and Laursen [44] uses Gregory patches to attain C^1- and G^1-continuity at the boundaries of quadrilateral elements and between two patches, respectively. The approach presented by Krstulovic-Opara et al. [45] utilizes triangular Bézier patches to attain the quasi C^1-continuous representation of the contact surface. The subdivision surface scheme introduced by Stadler and Holzapfel [46] provides C^2-continuity everywhere in the regular mesh domain except at the irregular vertices, where the inter-element continuity is C^1.

Since the above-described strategies ensure the smooth (C^1- or C^2-continuous) representation of the discretized contact surface by using high-order CAD interpolation functions. Thus, they, in general, enhances the robustness and accuracy of the contact algorithms. The unique definition of the normal and tangential vector fields is obtained at the intersections of contact elements. Although C^2-continuity is not required for the continuous normal vector field, it is essential in case of dynamic analysis, where the acceleration field is otherwise discontinuous at the intersection of the contact elements [6].

However, the design of these smoothing procedures introduces an additional layer, i.e. smoothed contact surface on top of the existing finite element mesh, which has to be inevitably constructed in each iteration of the solution algorithm. This not only introduces the complications in implementation but also in the data management. As pointed out by [38], some implementation can even lead to the loss of spare structure of the system stiffness matrix. Moreover, designing a smooth contact surface for the three-dimensional bodies is even a more complex task than that for the two-dimensional case since they demand the additional treatment of FE nodes, especially for the unstructured finite element mesh [1, 21].

Another limitation is that these strategies do not increase the order of spatial

convergence since they leave the bulk behaviour of the interacting solids unchanged. Furthermore, in case of large deformations and large sliding contact problems where the strong interactions between the surface and bulk discretizations take places, irregular and large amplitude oscillations of contact forces can still be present due to fact that the higher-order interpolations are not considered for the bulk behaviour of the interacting bodies [21, 30, 47]. In problems that are governed by the strong interactions between the bulk and contact discretizations, higher than C^1-continuity in the description of the contact surface is needed to enable the deformable bodies to conform better according to each other's geometry [30, 47].

The layer-wise enrichment of shape functions approach for two-dimensional contact computations by Konyukhov and Schweizerhof [48, 49] can also be viewed as a surface smoothing technique. Therein, the contact layer of each finite element is represented with the higher-order shape functions, while the interior domain of the contact body is discretized with the linear order shape functions. In this, a covariant contact description in combination with the higher-order shape functions are utilized for the contact layer, which provides the exact geometric representation of the contact boundary with the blended function method. It is shown that for the classical Hertz contact problem, although a good correlation with the analytical solution can be attained even with a very coarse mesh. But, oscillation occurs if the contact and non-contact zones appear within an element laying at the boundary of the contact surface. It has been shown that for such instances, decreasing the interpolation order of the contact layer shape functions in combination with the under-integration of the contact quantities of these boundary elements improves the quality of the result. However, from a general point of view, such an approach has limitations since the oscillations can not be eliminated completely. This is due to the inability of the underlying shape functions in capturing the non-smooth variation of the local contact response within the boundary contact element.

In the enriched contact finite element strategy introduced by Sauer [50, 51], the contact finite elements are locally enriched either with the cubic-order Hermite or higher-order Lagrange interpolations. The remaining bulk domain of the body remains unchanged, i.e. with the linear finite elements. Unlike the above-described approaches, it considers the smoothing of the slave contact surface in order to increase the evaluation accuracy of the contact integrals even at the coarse finite element mesh. It is shown that the proposed enrichment strategy considerably improves the accuracy

and robustness for the peeling and sliding computations as compared to standard liner Lagrange polynomial based FE at a fixed mesh resolution. Due to the C^1- inter-element continuity, cubic-order Hermite enriched elements are found to be more useful than the high-order Lagrange interpolations. Compared to the C^0-continuous higher-order of Lagrange interpolations, which suffers from large amplitude oscillations with increasing the interpolation order, Hermite enriched elements yields more accurate results which are free from the non-physical oscillation of contact responses. However, the development of a Hermite enriched contact finite element for the three-dimensional body is far from trivial. Moreover, the proposed strategy also limits the higher-order spatial convergence rate since the linear Lagrange interpolation are used for the bulk description.

1.3 Isogeometric analysis of contact problems

As an alternative to FE discretization, Hughes et al. [52] (2005) introduced NURBS-based isogeometric analysis (IGA) technique with the purpose of integrating the computer-aided design (CAD) modelling and the finite element analysis (FEA) processes into one unified framework. With this, IGA circumvents the computationally overwhelming FE suitable mesh generation process that is additionally associated with the traditional FEA approach and directly enables the analysis on the NURBS constructed exact geometric models [53]. Within the IGA framework, the NURBS functions that are used to construct the given CAD geometry exactly are used as a basis for the approximation of the unknown solution fields [52, 53].

The intrinsic key features of the NURBS function that makes it distinct from the Lagrange polynomial are: the ability to represent complex geometry exactly even with a coarse mesh, variational diminishing and convex-hull properties, tailorable inter-element continuity, and the non-negativeness. Within the last two decades, due to the aforementioned distinguished intrinsic feature of its underlying basis function, IGA has received great attention and has been established as an advantageous computational technology for various classes of problems, especially to those where the exact and smooth representation of the geometry is highly desirable. For example, in the thin shell analysis, the smoothness of the NURBS functions allows the straightforward construction of thin-shell elements without the rotational degrees of freedom [54, 55]; in the field of structural shape optimization, IGA provides a tight coupling of the CAD, FEA,

and the shape optimization which facilitates the direct return of the design model to the CAD system [56, 57]; in the structural vibration analysis, the higher-order of NURBS discretizations yield much more robust and accurate frequency spectra than with the higher-order Lagrange discretizations [58, 59]; in cohesive zone modelling, the NURBS discretizations are found to be efficient in terms of degrees of freedom (DOFs) and computational efforts due to their tailorable inter-element continuity feature [60–62]; in the analysis of interfacial cracks and functionally graded material plates, NURBS discretizations provide much more accurate results than its FEM counterpart [63–65], etc.

Contact modeling belongs to one of these classes that have significantly been benefited from the aforementioned intrinsic features of the IGA technology. In contrast to C^0-continuous Lagrange polynomial, the NURBS based description naturally provides the smooth representation of the contact interface. With this, a continuous normal (and tangential) vector field at the intersections of contact elements can be directly obtained even with a very coarse mesh, even for the geometries having large curvature [52, 53]. Thus, the NURBS based discretization inherently eliminates the issues stemming from C^0-continuous FE discretization of the contact surface without the need of any intermediate surface smoothing techniques mentioned in Section 1.2.1. Moreover, by retaining the advantages of higher-order approximations not only for the contact description but also to the bulk behavior of the contacting bodies, isogeometric NURBS discretizations intrinsically avoid the drawbacks associated with the contact surface smoothing procedures and offer a huge potential for the analysis of large deformation and large relative sliding contact problems. In the following, the literature review on the treatment of contact problems with NURBS-based isogeometric analysis technique is presented.

The first investigations on the isogeometric analysis of contact problems with NURBS are conducted by Temizer et al. [30, 47], De Lorenzis et al. [29, 66], and Lu [67].

Temizer et al. [30] initiated a systematic study of NURBS-based IGA technique to frictionless thermo-mechanical contact problems using the mortar and non-mortar contact formulations. De Lorenzis et al. [29] investigated the performance of NURBS-based IGA technique to two-dimensional large deformation frictional contact problems between deformable bodies using the mortar and non-mortar contact formulations. In these works [29, 30], the penalty method is adopted for the enforcement of contact con-

straints. Later, De Lorenzis et al. [66] extended the application of IGA technique to three-dimensional finite strain frictionless contact problems between deformable bodies using the mortar and non-mortar contact formulations. Herein, the contact constraints are enforced using the augmented-Lagrange multiplier method. Thereafter, Temizer et al. [47] presented the isogeometric analysis based treatment of three-dimensional frictional contact of two deformable bodies in finite deformation regime using mortar-based contact formulation as an extension of works on frictionless thermo-mechanical contact in [30] and two-dimensional large deformation friction contact in [29]. In these works [29, 30, 47, 66], C^0-continuous Lagrange-polynomial based discretizations are used to perform the comparative assessment of NURBS discretizations. It is demonstrated that although non-mortar contact formulation provides sufficient quality results for different two- and three-dimensional finite deformation contact problems, the quantitative investigation on the quality of normal and tangential contact pressure distribution revealed that it is over-constrained in nature and leads to poor quality and highly oscillatory results, especially with the large value of penalty parameter. It is demonstrated that with the mortar based formulation, the quality of the contact pressures distribution improves significantly with NURBS over the Lagrange discretizations for both the small and finite deformation contact problems. With the NURBS based discretization, the quality of the distribution of the contact pressure remains practically insensitive with increasing the order at a fixed mesh resolution. Conversely, Lagrange discretization displays the non-physical oscillation behaviour whose amplitude increases with increasing interpolation order, especially at the coarse mesh resolution. For a fixed interpolation order of NURBS functions, the quality of the pressure distribution improves monotonically on increasing the mesh resolution, whereas a non-monotonic improvement is attained in case of Lagrange discretization. Furthermore, it is observed that regardless of the interpolation order, contact pressure distribution stemming from NURBS is always point-wise positive as compared to Lagrange discretization which may produce a non-physical negative result, in particular with increasing the interpolation order. Moreover, in large deformation frictionless and frictional sliding contact problems, the convergence issues associated with the local contact search procedure are intrinsically eliminated due to the smooth description of the contact surface with C^1-continuous NURBS discretizations. In addition to this, the global higher inter-element continuity of NURBS discretization also allows the direct integration of the frictional evolution equations, which consequently eliminates the need of complex book-

keeping task required to continuously track the position of the sliding point across the contact elements boundary in the context of Lagrange discretizations. Furthermore, the evolution of global responses such as the vertical and horizontal contact forces and twisting moment computed with NURBS are remarkably smoother than with those obtained with Lagrange functions. The accuracy or smoothness of these responses further improves in quality with increasing the interpolation order of the NURBS discretizations. Conversely, the global responses computed with Lagrange discretization display spurious oscillations of contact forces whose amplitude and irregularity further increases with increasing the interpolation order, which may even lead to the failure of the simulation in some cases [29, 30, 47, 66].

Lu [67] introduced the application of the isogeometric framework for the analysis of two- and three-dimensional large deformation frictionless contact problems between deformable bodies, using segment-to-segment based different contact formulations originally presented by Papadopoulos and Taylor [27] in the context of FE framework. A strategy based on the minor perturbation of the repeated knot values is also presented for the smoothing of sharp corner geometries. He showed that the intrinsically smooth NURBS based discretization alleviates the non-physical oscillations of the contact force that otherwise seen with the Lagrange based discretizations. Further, he showed that NURBS constructed geometries are capable of capturing the intricate mechanics of the soft fabric such as their smooth motion including the large wrinkles with a very coarse mesh or small number of DOFs.

Later, Dittman et al. [68] investigated the application of NURBS-based isogeometric analysis technique to three-dimensional transient thermo-mechanical contact and impact problems in the context of nonlinear elasticity using a variationally consistent thermo-mechanical mortar contact formulation. A new segmentation procedure of surface interactions is developed to compute the mortar integrals in an efficient manner. It is demonstrated that the proposed isogeometric thermo-mechanical mortar contact formulation permits the modelling of energy transfer between the interacting surfaces and enables capturing the effects of frictional dissipation of energy into the thermal field. Consequently, it leads to a fully coupled thermo-mechanically consistent frictional mortar contact formulation for an arbitrary order of NURBS based discretization. It is also shown that due to the simplified mortar segmentation procedure, IGA framework leads to the significantly higher computational efficiency while retaining the practically sufficient accuracy for the modelling of contact problems.

Seitz et al. [69] developed a dual mortar method for isogeometric analysis of mechanical and tied contact problems and carried out the first systematic investigation on the spatial converge rate of different interpolation order of the NURBS based discretizations. As compared to the standard mortar contact formulation, the dual mortar method enables easy elimination of the additional Lagrange multiplier DOFs from the global system of equations, and leads to a smaller size and positive definite global system. Consequently, it significantly enhances the computational efficiency of mortar contact algorithms for NURBS-based isogeometric analysis of contact problems. It is demonstrated that isogeometric dual mortar formulation delivers sufficiently smooth results in comparison to the standard mortar method where oscillations are observed in the contact pressure distribution for an arbitrary order of NURBS based discretization. It is also shown that as compared to NURBS, the Lagrange discretization yields non-physical oscillations and locally negative contact pressure distribution on increasing the interpolation order, particularly at the boundary of the contact interface. Moreover, investigation on the spatial convergence in unilateral contact application shows that the optimal convergence rates are met for the different order of NURBS based discretizations.

As an isogeometric counterpart of the NTS approach, Matzen et al. [70] introduced a point to segment (PTS) contact formulation for isogeometric analysis of geometrically non-linear problems in the two-dimensional frictionless setting. In this, the physical points, namely Greville and Botella points computed at the contact surface of NURBS discretized body, are used to collocate the contact integrals instead of geometrical control points. Convergence investigation of the Hertzian contact problem showed that for a contact area adjacent to the patch boundary Greville points provides slightly more accurate results. Moreover, it was shown that for the large sliding problem, the PTS approach with NURBS based discretization is able to deliver a nearly equivalent result in terms of the amplitude of oscillations in the reaction forces to significantly more sophisticated isogeometric mortar method with linear Lagrange polynomials. Furthermore, the numerical simulation of the same problem using PTS (in case of IGA) and NTS (in case of FEA) approaches show that with the Lagrange discretizations no convergence is achieved, which in other words, demonstrate the much more robust feature of the higher-continuous NURBS over the C^0-continuous Lagrange discretizations. Two different methods for the recovery of contact stresses from the discreet value of Lagrange multiplier at the physical points are also examined. Later, a weighted

point-based method which easily permits the transmission of contact stresses along the contact surface is introduced by Matzen and Bischoff [71] as an extension of their previous PTS approach for isogeometric contact analysis.

Much research efforts have also been devoted to develop the isogeometric collocation methods for contact applications since they provide an excellent computationally efficient alternative to conventional Galerkin approaches, especially for higher-order NURBS discretizations [72–75]. As compared to the standard Galerkin approaches, where computations are performed at a set of quadrature points in each element, the collocation method can be interpreted as one-point quadrature rule in the context of IGA. In this direction, De Lorenzis et al. [72] introduced hybrid collocation-Galerkin and enhanced collocation approaches to circumvent the issues emanating from the strong imposition of Neumann boundary conditions, and the enforcement of contact constraints in the isogeometric collocation framework. Later, Kruse et al. [73] extended the application of isogeometric collocation approach for large deformation and frictional contact problems using two-half pass contact algorithm [76, 77], which seems to be the most favourable algorithms for isogeometric collocation approach. Later, Weeger et al. [74] presented an isogeometric collocation method for non-linear dynamic analysis of three-dimensional spatial rods, involving frictional contact. Recently, Nguyen-Thanh et al. [75] introduced an adaptive isogeometric collocation method which enables the adaptive isogeometric analysis of two-dimensional frictional contact problems. Numerical results showed that it offers stable and accurate results, and yields nearly the same spatial convergence as that with the Galerkin approach.

Moreover, different approaches to accurately capture the active contact zone within the two-dimensional curved surface contact bodies have also been introduced under the isogeometric analysis setting. An exact extraction of the contact zone in boundary element leads to the smooth distribution of the local contact response in the vicinity of the contact region. It, otherwise, is a difficult and computationally expensive task with the conventional procedures [78]. In the approach by Kim and Youn [79], the active and inactive contact segments in an element that lies across the boundary of the contact region are divided using the knot insertion scheme. An iterative procedure based on the bisection method is adopted to precisely identify the boundary of the active contact zone. During the iterative process, the newly inserted knots are utilized only temporarily for the purpose of contact integration and are eliminated thereafter to prevent the increase of DOFs. In the approach by Bidkhori and Hassani [80], an

adaptive refinement is carried out near the boundary of the contact region. The new knots are inserted in the parametric domain of each contacting body in a geometrical progression fashion. It is demonstrated that with the proposed approach, the contact zone can be determined more accurately than with the uniform refinement approach.

Further, NURBS-based isogeometric analysis technique has also attracted interests in the field of computational homogenization [81, 82]. It is shown that the numerical models developed in the framework of isogeometric analysis provides improved descriptions of both the contact surface and bulk domain in the determination of macroscopic effective coefficient of friction for rubber as a function of sliding velocity and applied external pressure [81], and also to accurately capture the temperature jump across the macroscopic contact interface in the finite deformation regime [82].

Besides, due to its advantageous features, NURBS-based IGA technique has been adopted in many investigations focusing on various contact applications such as in the modelling of constrained solid and liquid membranes [83], dynamic cloth simulation [84, 85], sheet metal forming analyses [86, 87], patient-specific structural analysis of aortic valve closure [88], numerical plate testing of dry woven fabrics [89], and modelling of revolute clearance joint with friction [90]. A comprehensive overview on the growth of various isogeometric based treatment procedures and their advantages for contact mechanics as compared to traditional Lagrange based finite element analysis can be found in the paper by De Lorenzis et al. [21].

1.4 Local mesh refinement strategies for isogeometric contact analysis

As the multivariate NURBS functions are defined by the tensor product, the standard NURBS based discretization suffers from the lack of local mesh refinement. As such, the addition of a new control point to a two-dimensional NURBS entity requires the insertion of an entire row or column of control points to maintain its rigid tensor product structure [31, 53, 91, 92]. Since the contact is mainly a surface dominated phenomena, employment of the globally refined mesh to accurately resolve the variation of contact responses at the interface is not desirable from the analysis point of view. To this date, various strategies that enable the local mesh refinement within the context of isogeometric contact analysis, i.e. T-splines [31, 61, 62, 92, 93], NURBS-based hierar-

chical refinement [94, 95], and locally refined (LR) NURBS [96], have been devised. In the following, the literature review on the application and performance aspects of the various local mesh refinement strategies is provided.

T-splines based IGA technique was first applied by Dimitri et al. [31] to model the large deformation frictionless contact problems between deformable bodies. Within the presented formulation, a classical Gauss-point-to-surface contact algorithm combined with the penalty method has been used for the treatment of contact constraints within the context of IGA. For the discretizations of the contact bodies, the cubic T-splines and cubic NURBS have been considered. It is shown that the T-splines coupled with the local mesh refinement accurately captures the distribution of the contact pressure across the contact interface with a far fewer number of DOF than with standard NURBS discretization. Further, the convergence study showed that the error curve obtained with the T-spline lies below the error curves with the standard NURBS discretizations even after relocating the NURBS mesh to the contact zone for the same global number of DOFs. Later, Dimitri et al. [61] employed the T-spline based IGA for the modelling of cohesive interface debonding problems using the GPTS based isogeometric contact formulation. It is demonstrated that in comparison to NURBS, the T-spline based discretization leads to macroscopically smooth results in the computation of the cohesive forces with the same number of DOFs. After that, Dimitri and Zavarise [62] extended the application of T-spline based isogeometric discretizations to the modelling of frictional contact and mixed-mode cohesive debonding problems. It was shown that for a given number of DOFs, T-spline based discretization, due to its local refinement capability, yields more accurate global time-histories responses, as well as the normal and tangential contact pressure distributions across the contact interface, and also the better resolution of the debonding zones as compared to uniform NURBS based discretizations. A detailed summary of the advantages of the T-splines based isogeometric discretizations in terms of computational accuracy and efficiency in comparison to NURBS as well as standard Lagrange polynomial based discretizations for the frictionless contact and debonding problems can be found in the review paper by Dimitri [97].

As an alternative to the T-splines, the NURBS-based hierarchical refinement scheme has been presented by Temizer and Hesch [94] for the IGA of frictionless contact problems. It has been shown that the proposed scheme combined with the mortar based contact algorithm yields smoother results for the contact forces as well as for the contact

pressure distributions even with the coarse meshes. Later, Hesch et al. [95] extended the application of the NURBS-based hierarchical refinement scheme to simulate fracture problems arising from the finite deformation frictional contact situations. It has been shown that the NURBS-based hierarchical refinement reduces the computational efforts considerably as compared to standard NURBS based discretization.

Apart from the local mesh refinement approach, an adaptive local surface refinement technique based on the Locally Refined (LR) NURBS has been presented by Zimmerman and Sauer [96] in the context of computational contact. To perform the adaptive local refinement and coarsening of LR NURBS discretizations, a local error measurement technique that indicates the domain for appropriate refinement is presented. It has been demonstrated that with the LR NURBS, a considerable gain in the accuracy is achieved at much lower computational efforts in terms of DOFs as compared to standard NURBS based discretizations.

1.5 Combined FE-IGA discretization strategies for contact analysis

As an alternative to the employment of standard NURBS based discretizations for a contacting body, various FE-IGA methods that integrate an arbitrary order of NURBS discretization of the contact surface into the standard lower-order of Lagrange based FE discretizations have been introduced. The central feature of these methods is to combine the geometric smoothness and high approximation advantages of the NURBS for the smooth contact formulation with a simple description of the bulk domain using the standard Lagrange based finite elements to improve the accuracy, reliability, and robustness of the contact algorithm. In the following, a literature review on the various FE-IGA discretization methodologies and their performance aspects is presented.

In the NURBS-enriched contact finite element approach by Corbett and Sauer [98], the contact surface of each element is locally enriched with the NURBS, whereas the bulk part of the body is discretized with the standard linear finite elements. To integrate the NURBS functions into the FE structure, the Bézier extraction operator that was introduced by Borden et al. [99] is utilized. The operator allows the numerical integration of the C^n-continuous basis function to be performed within a FE compatible C^0-continuous Bézier element. For modelling the contact between the deformable

bodies, a two-half pass contact algorithm introduced by Sauer and De Lorenzis [76] is utilized. As compared to the surface smoothing procedures described in Section 1.2.1, the proposed approach uses the NURBS as a basis for the smooth representation of the contact surface as well as for the evaluation of the contact integrals. It provides considerable improvement in the accuracy of contact forces for the sliding contact and the bending moments for adhesive strip peeling problem at a fixed mesh as compared to the linear, higher-order Lagrange enriched, and cubic-order Hermite enriched elements of Sauer [50]. Moreover, for the twisting contact, the proposed approach gives more accurate results while reducing the overall analysis time by approximately 35% in comparison to linear Lagrange elements due to the considerable reduction in the number of the Newton iteration steps required for the convergence. Furthermore, as compared to the full NURBS based discretization, the proposed approach has the benefit of lower computational cost since the bulk domain of the body is discretized with the standard finite elements. However, the linear order approximation of the bulk domain limits the higher-order spatial convergence rate, which was also the case with surface smoothing strategies [21].

Later, Corbett and Sauer [100] proposed an isogeometric enrichment technique for three-dimensional linear- and quadratic-order Lagrange finite elements as an extension of their previous work on NURBS-enriched contact finite elements [98]. The technique is applied to mixed-mode cohesive debonding and frictional contact between the deformable bodies using the two-half pass contact algorithm [77]. As in their previous work, the Bézier extraction operator [99] is utilized to incorporate the C^n-continuous bi-variate NURBS functions into the standard C^0-continuous tri-linear finite element. It is shown that the NURBS enrichment improves the robustness of the contact computations and provides more accurate results at a fixed mesh as compared to tri-linear finite elements for both the mixed-mode debonding and frictional contact problems. Compared to the full quadratic "NURBS-based finite elements (IGA2)", the corresponding "NURBS-enriched Lagrange finite element (Q2N2)" delivers very similar accuracy for the problem that does not require surface continuity. Besides, usage of quadratic-order Lagrange polynomial for the bulk description also overcomes the shear locking behaviour observed with the linear elements for the large bending problem. However, "Q2N2" element takes much higher computational efforts since it requires approximately 5 times more DOFs than the "IGA2" element. Furthermore, the higher-order NURBS enriched finite element provides much higher accuracy at a fixed mesh

for frictional contact problem as compared to linear and quadratic NURBS based finite elements.

After that, Maleki-Jebeli et al. [101] proposed a hybrid NURBS based isogeometric-finite element discretization technique for two-dimensional cohesive interface contact/debonding problems. In this, the geometric smoothness and higher-accuracy features of NURBS are used for the description of contact/cohesive interfaces regions with high-stress gradient, while the rest of the domain is discretized with either the linear- or quadratic-order Lagrange finite elements. The transition from NURBS to standard FE discretization is carried out using the NURBS-enriched contact finite elements initially introduced by Corbett and Sauer [98]. For the incorporation of the NURBS into the FE structure, the Bézier extraction operator [99] is utilized. A mortar-based formulation is presented to model the cohesive behaviour and impenetrability constraint at the contact interface. Numerical examples show that the proposed hybrid discretization technique leads to improved performance in terms of robustness even with the considerably lower number of DOFs as compared to the standard Lagrange based finite elements. Moreover, the smooth contact pressure distribution is obtained across the interface due to higher inter-element continuity with the NURBS based discretization.

Otto et al. [102] introduced a coupled FE-NURBS discretization approach to model the contact problems between the arbitrary order of finite element discretized bodies. In this, an auxiliary NURBS layer is added between the higher-order FE discretized contacting bodies. It enables the smooth contact formulation within the FEM setting and avoids the need for full NURBS based discretizations. In order to tie the NURBS layer with the FE discretization, the point-wise GPTS and mortar based mesh tying conditions are used. It is shown that mortar based mesh tying procedure delivers robust and accurate results for the different order of NURBS and FE discretizations. The point-wise mesh tying yields large amplitude oscillations in the contact stresses. On increasing the continuity of the NURBS layer, the error in the contact computations and tying discretizations is reduced. Recently, this approach has been used to solve the two- and three-dimensional impact and wave propagation problems between finite element discretized elastic bodies [103].

In work by Dias et al. [104], the geometric mapping of the curved surfaces of the contact element is performed with NURBS in the two- and three-dimensional domains. High-order mortar contact element with arbitrary interpolation order, which has been proposed by Dias et al. [105, 106] for two-dimensional contact problems, is extended

to three-dimensional setting using the Augmented Lagrange Multiplier method. In contrast to the isogeometric analysis technique [52] and the NURBS-enriched contact finite element approach [98, 100], which use NURBS as a basis for the smooth description of the contact surface and evaluation of the contact integrals, they utilized the NURBS only to perform the mapping of the geometric position of high-order FE nodes on the curved contact surfaces. After that, the contacting geometry and the solution fields in the bulk domain and contact surface are interpolated with the higher-order Lagrange functions. It is shown that the application of the NURBS mapping yields smooth variation of the contact stress field and improves the robustness and reliability of the contact algorithm.

1.6 Motivation and objectives of the thesis

Based on the above-presented literature review, the following observations are made:

- Due to their distinguished intrinsic features, the NURBS based discretizations deliver significantly superior performance in terms of accuracy, stability, and robustness for the analysis of contact problems as compared to their Lagrange polynomial based counterparts. But, due to the rigid tensor product nature of the NURBS, the underlying mesh can be refined only globally. Moreover, the interpolation order of the underlying NURBS basis functions that are used for the discretization of the contact boundary layer, and the remaining bulk domain of the contact body can be elevated only uniformly. It is known that the accuracy of the contact responses is primarily governed by the coarse or fine mesh and lower or higher-order NURBS based description of the contact surface. Thus, from the analysis viewpoint, utilization of the fine mesh and/or higher-order NURBS in the region away from the contact surface is not desirable [1, 21, 47]. It should also be emphasized that usage of higher-order NURBS discretization diminishes one of the key advantages of IGA, which is its ability to represent the geometry with high-accuracy even using a coarse description. It, therefore, becomes desirable to develop an improved method that circumvents the above-described limitations and accordingly enhances the performance of the IGA technique within the framework of computational contact mechanics.

- As of now, in order to enhance the computational efficiency of the IGA technique

for contact modelling, various approaches that enable the local mesh refinement, i.e. T-splines [31, 61, 62], Hierarchical NURBS [94, 95], and LR NURBS [96], have been devised. However, the idea to refine a NURBS discretized geometry through a controllable order elevation based strategy remains unexplored as initially noted by Temizer et al. [47].

- As an alternative to standard NURBS based discretizations, a number of FE-IGA discretization strategies, which integrate the higher-order NURBS based description of the contact surface into the standard lower-order of Lagrange based FE mesh, have been introduced in the context of FE analysis of contact problems. Within these strategies, additional tools such as Bézier extraction operator as in [98, 100, 101] and mesh tying conditions as in [102, 103] are required for the incorporation of NURBS functions into the standard Lagrange based FE framework. On the other hand, no such effort, which fully retains the intrinsic key features of IGA and directly enables the higher order NURBS based description of the contact surface into a lower-order of NURBS discretized geometry, has been devoted for the isogeometric analysis of contact problems.

In view of the above observations, the objective of this work is to develop *a new method that enables the order elevation based refinement of a fully NURBS discretized geometry in a controlled manner* such that the arbitrary higher-order of NURBS functions are employed only for the discretization of the contact boundary layer and for the evaluation of the contact integrals. Simultaneously, it allows the utilization of the minimum order NURBS that are capable of representing the complex shaped CAD geometry exactly for the computations in the bulk domain that does not come into the contact.

In order to demonstrate the capabilities and efficacy of the developed method for the isogeometric analysis of contact problems following procedure is adopted.

- The developed method is applied to various two-dimensional small and large deformations contact problems, with or without considering friction between the two deformable bodies.

- The developed method is also applied to analyze a class of two-dimensional contact problem where the contact forces arise due to the van der Waals interactions.

- Then, the developed method is applied to three-dimensional large deformation frictionless contact problem between two deformable bodies.

In each of the cases above, to carry out the systematic assessment of the performance of the developed method, the results obtained with the standard NURBS based discretizations are used for comparisons. The performance of the method is analyzed mainly in terms of accuracy, robustness, and computational efficiency as compared to standard NURBS based discretizations.

1.7 Structure of the thesis

The rest of the thesis is organized into 7 chapters, which are followed by the appendices and references:

In **Chapter 2**, an overview of the standard geometric modelling procedure within the context of isogeometric analysis is provided. Since NURBS are built from B-spline, first, a brief overview of the B-spline is given. This includes the discussion on the knot vectors, B-spline functions, and the construction of the B-spline geometries. Thereafter, an extension to NURBS is summarized. An overview of the different existing strategies that are used for the refinement of a NURBS discretized geometry is given.

In **Chapter 3**, first, the theoretical background in the continuum solid mechanics that is necessary to derive the governing equations for a general boundary value problem is summarized. Next, the basic equations that are used to describe the normal and tangential contact between two-deformable bodies undergoing large deformations from the continuum mechanics point of view are thoroughly discussed. Thereafter, the governing equations for the adhesive contact problem in the continuum setting are outlined.

In **Chapter 4**, the NURBS based discretization of the weak form of the governing equations summarized in Chapter 3 is presented. The description of the isogeometric contact algorithm employed in the present work for the treatment of contact with the NURBS based discretization is provided. The force equilibrium equations for a two-body contact system undergoing large deformations are derived. Moreover, the linearization of the resulting system of nonlinear equations and the solution algorithm, which gives an overall picture of solving the contact problem, are summarized.

In **Chapter 5**, the new method that is developed to enable the order elevation based

refinement of a fully NURBS discretized geometry in a controlled manner in the two- and three-dimensional settings is introduced. It includes the description of two different types of procedures that are used for the higher-order NURBS based construction of the contact boundary layer in a lower-order of NURBS discretized geometry. Moreover, some remarks on the integration of the proposed method into the standard NURBS-based isogeometric framework are given to complete its implementation aspect.

In **Chapter 6**, the validation of the isogeometric contact formulation developed in Chapter 4 is presented by solving a number of two- and three-dimensional examples taken from the literature. In particular, the validity of the formulation is verified for the NURBS based isogeometric analysis of the two-dimensional: small and large deformations frictionless and frictional contact between deformable bodies, and three-dimensional: small and large deformations frictionless contact between deformable bodies.

In **Chapter 7**, the capabilities and performance of the varying order based NURBS discretization method proposed in Chapter 5 are demonstrated using various numerical examples involving small and large deformations contact between deformable bodies in the two- and three-dimensional settings with or without considering friction. The performance of the proposed method is analyzed mainly in terms of accuracy, robustness, and computational efficiency. The results with the existing NURBS based discretizations are used for comparisons.

In **Chapter 8**, first, a summary of the work carried out in this thesis is presented, followed by the conclusions drawn from the results presented in Chapter 7. Finally, the scope for future work is provided.

Chapter 2

Overview of Isogeometric Analysis

The isogeometric analysis has emerged as successful integration of computer-aided-design (CAD) and finite element analysis technique. It utilizes the CAD polynomials as a basis for the modeling of complex-shaped geometries in an exact manner and approximation of unknown solution fields using the isoparametric concept. In this work, NURBS functions, which are the most popular in the CAD domain, are utilized for the description of the continuum as well as the contact surface.

In this chapter, the existing geometric modelling procedure within the context of isogeometric analysis is summarized. Since the NURBS are built from B-splines, in the first Section 2.1, a brief overview of B-splines is presented. After that, in Section 2.2, the extension to NURBS is discussed. Later, in Section 2.3, different strategies that are used for the refinement of a NURBS constructed geometry are summarized. The issues associated with the existing discretization approach are also highlighted. For the detailed description, the monographs by Pigel and Tiller [91] and Cottrell et al. [53] are refereed. It is noted that in the following, the linear, quadratic, cubic, etc. interpolation order of spline functions is denoted by $p = 1,\ 2,\ 3,$ etc., respectively. This is as per the notation introduced by Hughes et al. [52].

2.1 B-splines

In this section, the essential ingredients to construct B-splines are summarized. This includes the definition of the knot vectors, B-spline functions, and the construction of the B-spline geometries. Moreover, the important properties of B-spline functions are discussed.

2.1.1 Knot vectors

A *knot vector* in one-dimension is a set of non-decreasing values of coordinates in the parametric space ξ^i ($i = 1,\ 2\,,$ and 3), given by

$$\Xi^i = \left[\xi^i_1,\ \xi^i_2,\ \ldots\ ,\ \xi^i_l,\ \ldots\ ,\ \xi^i_{n_i+p_i+1}\right]\ , \tag{2.1}$$

where $\xi^i_l \in \mathbb{R}\ \ \forall\, i$ is the l^{th} knot, $l = 1, 2, \ldots, n_i + p_i + 1$, p_i is the interpolation order, and n_i denotes the total number of basis functions defined by the knot vector in the ξ^i parametric direction. The non-zero interval between by any two consecutive knot values $[\xi^i_l,\ \xi^i_{l+1}] > 0$ is called as the *knot span*. Each non-zero knot span partitions the parametric space ξ^i into elements, which using the B-spline functions are mapped to the physical space.

Based on the difference between any two consecutive knots values, a knot vector can be categorized either as *uniform* or *non-uniform*. If the difference between any two consecutive knots remains fixed throughout, it is said to be a uniform knot vector, which implies that the knots are placed equally in the parametric space ξ^i. Otherwise, if the knot values are spaced unequally, it is said to be a non-uniform knot vector. A knot vector is called *open*, if its first, ξ^i_1, and last knot entries, $\xi^i_{n_i+p_i+1}$, appear $p_i + 1$ times. An open knot vector is a standard in the IGA literature since with this the resultant basis functions are interpolatory at the ends of the parametric space $[\xi^i_1,\ \xi^i_{n_i+p_i+1}]$, which is illustrated in the following.

2.1.2 B-spline function

For a given knot vector Ξ^i specified along the ξ^i parametric direction, a univariate B-spline function is defined using the following Cox-de Boor recursive relation [91]:

$$\begin{aligned}
&\text{for } p_i = 0, \quad N_{l,0}(\xi^i) = \begin{cases} 1, & \text{if } \ \xi^i_l \le \xi^i < \xi^i_{l+1}\,, \\ 0, & \text{otherwise}\,. \end{cases} \\
&\text{for } p_i > 0, \quad N_{l,p_i}(\xi^i) = \frac{\xi^i - \xi^i_l}{\xi^i_{l+p_i} - \xi^i_l} N_{l,p_i-1} \ + \ \frac{\xi^i_{l+p_i+1} - \xi^i}{\xi^i_{l+p_i+1} - \xi^i_{l+1}} N_{l+1,p_i-1}\,,
\end{aligned} \tag{2.2}$$

where the subscripts of N_{l,p_i} denote the function number l and its interpolation order p_i, respectively. In the above equation, it can be seen that each set of B-spline function of order p_i is dependent on the previous set of B-spline functions of order $p_i - 1$. Moreover,

during the recursive relation, if any of the denominator of the fraction gets zero, such rational fraction is defined zero.

B-spline basis functions have many advantageous properties. The most beneficial feature is that a p_i^{th} order of basis function offers C^{p_i-m} continuous derivatives across each knot value ξ_l^i, where m is the knot multiplicity. It means that a p^{th} order of B-spline function at a unique knot value ($m = 1$) at ξ_l^i, provides the C^{p_i-1} inter-element continuity, while for a knot value that is repeated by p_i times it has C^0-continuity. This tailorable inter-element continuity feature has many extremely beneficial implications that has led to the extensive use of splines as a basis for isogeometric analysis. Another important property is that each function is point-wise positive at any given parametric knot value ξ^i, i.e.

$$N_{l,p_i}(\xi^i) \geq 0 \quad \forall\, \xi^i \tag{2.3}$$

Moreover, these basis functions also constitute the partition of unity over the entire knot span, i.e.

$$\sum_{l=1}^{n_i} N_{l,p_i}(\xi^i) = 1 \quad \forall\, \xi^i \tag{2.4}$$

It is also worth noting that each basis function has the local support, i.e. $N_{l,p_i} > 0$, in a knot span interval $[\xi_l^i\,, \xi_{l+p_i+1}^i]$. Moreover, in each knot span $[\xi_l^i\,, \xi_{l+1}^i]$, at most $p_i + 1$ number of basis functions are non-zero. It is also noted that the B-spline basis functions of order $p_i = 0$ and $p_i = 1$ are equivalent to standard piecewise constant and linear Lagrange shape functions, respectively, see e.g. Fig. 5 of [53].

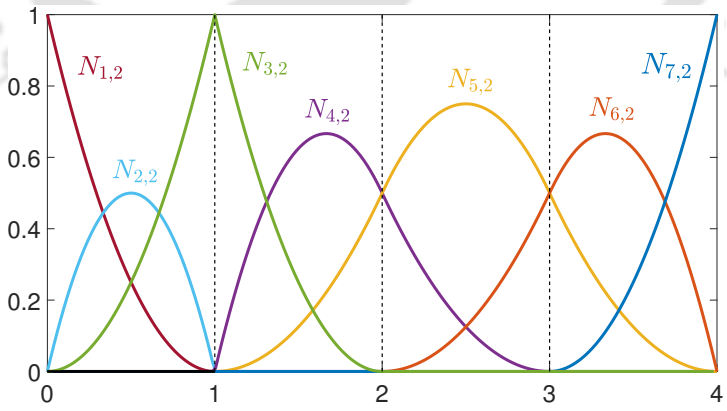

Figure 2.1: The quadratic order of B-spline functions corresponding to an open knot vector $\Xi = [0, 0, 0, 1, 1, 2, 3, 4, 4, 4]$ with a knot value $\xi = 1$ repeated two times.

Figure 2.1 shows the quadratic order of B-spline functions for an open knot vector

$\Xi^1 = [0, 0, 0, 1, 1, 2, 3, 4, 4, 4]$. For the considered knot vector, the basis functions are C^1-continuous at the each unique interior knot value, except at the domain boundary where it is C^0-continuous. Moreover, the multiplicity of the knot value $\xi = 1$ is varied to show the change in the inter-element continuity with knot repetition. In the plot, each B-spline function is shown with a specific color and is labeled according to Eq. (2.2). The dotted vertical lines at $\xi = 1$, 2, and 3, splits the entire parametric domain $[0, 4]$ into four sub-domains or elements.

2.1.3 B-spline geometries

B-spline curves

For a given knot vector Ξ^i and a set of *control points* $\boldsymbol{X}_l \in \mathbb{R}^d$, where $l = 1, 2, \ldots, n_i$ and d denotes the dimension of the physical space[1], a p^{th} order of B-spline curve is constructed using the following linear combination:

$$\boldsymbol{C}(\xi^i) = \sum_{l=1}^{n} N_{l,p_i}(\xi^i)\, \boldsymbol{X}_l = \mathbf{N}_p(\xi^i)\, \mathbf{X}\,, \tag{2.5}$$

where $\mathbf{N}_p(\xi^i)$ is the $[1 \times n_i]$ size of vector constituting the N_{l,p_i} basis functions that are computed using the relation in Eq. (2.2) and $\mathbf{X} \in \mathbb{R}^{n_i \times d}$ denote the control point matrix, where the vector valued coefficient of basis functions, $\boldsymbol{X}_l$, is referred as the *control point*. Moreover, the piecewise linear interpolation of the control points is called as the control polygon. The B-spline curve with $p_i = 1$ coincides with the control polygon. A composition of knot vector with associated control points constitutes a patch, which is a standard terminology in IGA.

Figure 2.2 shows a quadratic B-spline curve that is built from the basis functions shown in Fig. 2.1. The control points are marked by the red circles, and the control polygon is shown by the dashed line. Since the curve is constructed using an open knot vector, it is interpolatory at the first and last control points. Moreover, due to the C^0-continuity of the basis function at the repeated knot value $\xi = 1$, a control point lies on the curve. The knots which define the mesh by partitioning the curve into four elements are shown by black squares. It is noted that the properties of the B-spline curves are directly transferred from their underlying basis functions.

[1] which is 3 for a control point $\boldsymbol{X} = [X_1, X_2, X_3]$ defined in the three-dimensional physical space

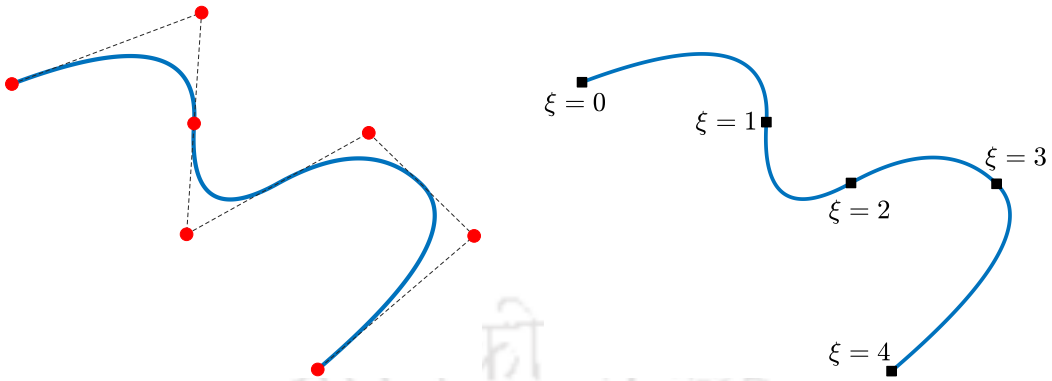

(a) Curve and control points

(b) Curve and elements denoted by knot locations

Figure 2.2: The quadratic B-spline curve in $\mathbb{R}^2$ (in a blue line) corresponding to knot vector $\Xi = [0, 0, 0, 1, 1, 2, 3, 4, 4, 4]$. (a) The control points are denoted by the red circle and the control polygon with a dashed line. (b) The boundaries of the four elements corresponding to knot vector Ξ are denoted by black squares.

B-spline surfaces

B-spline surfaces are constructed by using the concept of tensor product. For a given *control point net* $\boldsymbol{X}_{lm} \in \mathbb{R}^d$, $l = 1, 2, \ldots, n_1$, $m = 1, 2, \ldots, n_2$, polynomial orders p_i and knot vectors $\Xi^i = \left[\xi^i_1, \xi^i_2, \ldots, \xi^i_l, \ldots, \xi^i_{n_i+p_i+1}\right]$, along the $i = 1, 2$ parametric directions, a tensor product B-spline surface is defined by

$$\mathbf{S}(\xi^1, \xi^2) = \sum_{l=1}^{n_1} \sum_{m=1}^{n_2} N_{l,p_1}(\xi^1)\, N_{m,p_2}(\xi^2)\, \boldsymbol{X}_{lm}\,, \tag{2.6}$$

Since the bivariate function $N_{l,p_1}(\xi^1)\, N_{m,p_2}(\xi^2)$ are the tensor product of their univariate parts, the local support of these functions is given by

$$N_{l,p_1}(\xi^1)\, N_{m,p_2}(\xi^2) = [\xi^1_l\,, \xi^1_{l+p_1+1}] \times [\xi^2_m\,, \xi^2_{m+p_2+1}]\,, \tag{2.7}$$

which implies that the bivariate functions are non-zero over the area defined by the knot spans $[\xi^1_l\,, \xi^1_{l+p_1+1}] \times [\xi^2_m\,, \xi^2_{m+p_2+1}]$, where p_1 and p_2 are the interpolation order of basis functions along the ξ^1 and ξ^2 parametric directions, respectively. Moreover, the partition of unity for these functions reads

$$\sum_{l=1}^{n_1} \sum_{m=1}^{n_2} N_{l,p_1}(\xi^1)\, N_{m,p_2}(\xi^2) = \left(\sum_{l=1}^{n_1} N_{l,p_1}(\xi^1)\right) \left(\sum_{m=1}^{n_2} N_{m,p_2}(\xi^2)\right) = 1\,. \tag{2.8}$$

It can also be shown that in analogous to their univariate parts Eq. (2.3), the bivariate functions are pointwise non-negative for any knot value in the entire $\Xi^1 \times \Xi^2$ domain.

B-spline solids

Tensor product B-spline solids are constructed in a similar manner to B-spline surface. For a given *control point lattice* $\boldsymbol{X}_{lmn} \in \mathbb{R}^d$, $l = 1, 2, \ldots, n_1$, $m = 1, 2, \ldots, n_2$, $n = 1, 2, \ldots, n_3$, polynomial orders p_i, and knot vectors $\Xi^i = \left[\xi^i_1, \xi^i_2, \ldots, \xi^i_l, \ldots, \xi^i_{n_i+p_i+1}\right]$, along the $i = 1, 2, 3$ parametric directions, a B-spline solid is defined by

$$\mathbf{V}(\xi^1, \xi^2, \xi^3) = \sum_{l=1}^{n_1} \sum_{m=1}^{n_2} \sum_{n=1}^{n_3} N_{l,p_1}(\xi^1)\, N_{m,p_2}(\xi^2)\, N_{n,p_3}(\xi^3)\, \boldsymbol{X}_{lmn}\,. \tag{2.9}$$

The trivariate B-spline basis function $N_{l,p_1}(\xi^1)\, N_{m,p_2}(\xi^2)\, N_{n,p_3}(\xi^2)$ has the local support over the volume restricted by the knot spans $[\xi^1_l\,, \xi^1_{l+p_1+1}] \times [\xi^2_m\,, \xi^2_{m+p_2+1}] \times [\xi^3_n\,, \xi^3_{n+p_3+1}]$. In a similar fashion to Eqs. (2.8) and (2.3), it can be shown that the trivariate B-spline functions also constitute the partition of unity and are pointwise non-negative for any knot value in the $\Xi^1 \times \Xi^2 \times \Xi^3$ domain.

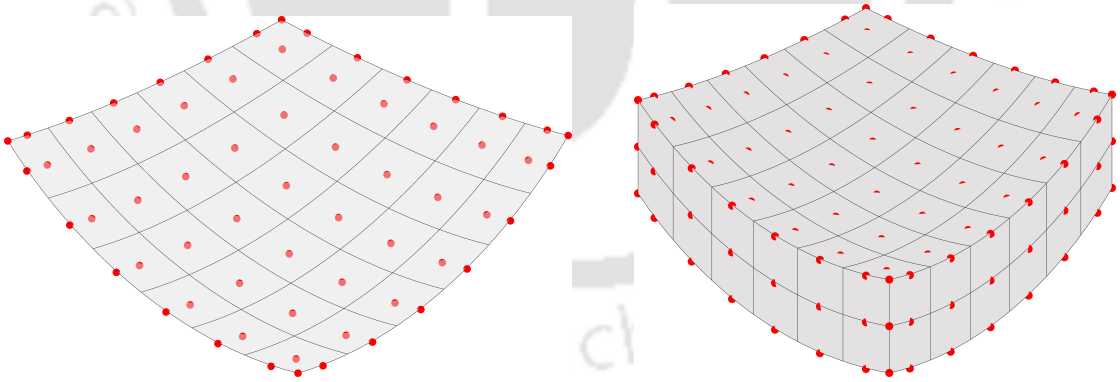

(a) Surface and control points **(b)** Solid and control points

Figure 2.3: (a) The quadratic order of B-spline surface, where the knot vectors in each parametric directions are: $\Xi^1 = \Xi^2 = [0, 0, 0, 0.6, 1.3, 2, 2.6, 3.3, 4, 4, 4]$. (b) The B-spline solid, where the knot vectors in each parametric directions are: $\Xi^1 = \Xi^2 = [0, 0, 0, 0.6, 1.3, 2, 2.6, 3.3, 4, 4, 4]$ and $\Xi^3 = [0, 0, 0.5, 1, 1]$. The associated control points with the surface and solid geometry are denoted by red dots.

2.2 Non-Uniform Rational B-splines

Non-uniform rational B-splines, as the name implies, are rational of B-spline. However, NURBS can represent the conical sections such as circles, ellipsoids, paraboloids, and hyperboloids in an exact manner in contrast to B-splines that fail to create them exactly. In their description, NURBS incorporates an additional coordinate of control point called as *weight*, while the definitions of the knot vector, interpolation order, and the tensor product nature remain unchanged.

2.2.1 The geometric point of view

A NURBS geometry in $\mathbb{R}^d$ is obtained through the projective transformation of a B-splines geometry in $\mathbb{R}^{d+1}$. An example is shown in Fig. 2.4, where a NURBS described circle in $\mathbb{R}^2$ is constructed by the projective transformation of a piecewise quadratic B-spline curve in $\mathbb{R}^3$. The additional coordinate of a control point $\boldsymbol{X}_l^w$ for a B-spline curve in $\mathbb{R}^{d+1}$ space is the weight w_l. Here, the superscript 'w' in $\boldsymbol{X}_l^w$ indicates that they are "projective control point" in the $\mathbb{R}^{d+1}$ space. The control points for the desired NURBS curve in $\mathbb{R}^d$ are obtained using the following relation

$$\begin{aligned} (\boldsymbol{X}_l)_j &= (\boldsymbol{X}_l^w)_j \,/\, w_l \,, \qquad \text{for } j = 1, \ldots, d \\ w_l &= (\boldsymbol{X}_l^w)_{d+1} \,. \end{aligned} \tag{2.10}$$

where $(\boldsymbol{X}_l^w)_j$ denotes the j^{th} component of the projective control point vector $\boldsymbol{X}_l$. In Fig. 2.4a, the z-components of the control points $\boldsymbol{X}_l^w$ in $\mathbb{R}^3$ corresponds to the weights w_l and the dashed line shows the projection ray through the origin. The control points $\boldsymbol{X}_l$ for the NURBS curve, which are computed using the Eq. (2.10), are marked by blue dots. Such a transformation is carried out by projecting each control point of the B-spline curve onto a plane at $z = 1$.

2.2.2 The algebraic point of view

A p_i^{th} order of a rational basis function for a NURBS curve is defined as

$$R_l^{p_i}(\xi^i) = \frac{w_l}{W(\xi^i)} N_{l,p_i}(\xi^i) \,, \tag{2.11}$$

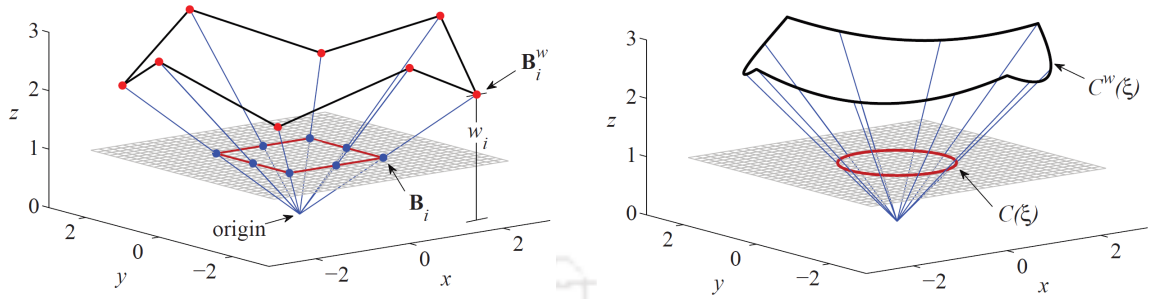

(a) NURBS control points $\boldsymbol{X}_l$ on the projective plane $z = 1$ corresponding to B-spline control points in projective space $\boldsymbol{X}_l^w$

(b) NURBS circle corresponding to B-spline curve

Figure 2.4: Construction of a NURBS circle in $\mathbb{R}^2$ through the projective transformation of a quadratic piecewise B-spline in $\mathbb{R}^3$. This figure has been reprinted with permission from Cottrell et al. [53].

where the normalizing weighting function is given as

$$W(\xi^i) = \sum_{l=1}^{n_i} w_l^i N_{l,p_i}(\xi^i)\,. \tag{2.12}$$

The rational basis functions for the NURBS surface and solids are defined analogously as

$$R_{lm}^{p_1,p_2}(\xi^1,\xi^2) = \frac{w_{lm}}{W(\xi^1,\xi^2)}\, N_{l,p_1}(\xi^1)\, N_{m,p_2}(\xi^2)\,, \tag{2.13}$$

$$R_{lmn}^{p_1,p_2,p_3}(\xi^1,\xi^2,\xi^3) = \frac{w_{lmn}}{W(\xi^1,\xi^2,\xi^3)}\, N_{l,p_1}(\xi^1)\, N_{m,p_2}(\xi^2)\, N_{n,p_3}(\xi^3)\,. \tag{2.14}$$

In the above equations, the weighting functions are defined in terms of the weight points and the B-spline functions as

$$W(\xi^1,\xi^2) = \sum_{l=1}^{n_1}\sum_{m=1}^{n_2} w_{lm}\, N_{l,p_1}(\xi^1)\, N_{m,p_2}(\xi^2)\,. \tag{2.15}$$

$$W(\xi^1,\xi^2,\xi^3) = \sum_{l=1}^{n_1}\sum_{m=1}^{n_2}\sum_{n=1}^{n_3} w_{lmn}\, N_{l,p_1}(\xi^1)\, N_{m,p_2}(\xi^2)\, N_{n,p_3}(\xi^3)\,. \tag{2.16}$$

It is noted that the advantageous properties of B-splines functions discussed earlier are also demonstrated by the rational spline functions. In particular, the inter-element continuity and local support of NURBS are the equivalent as for B-splines. The NURBS

functions are also pointwise non-negative for any value of knot coordinates and constitute the partition of unity. It is also useful to point out that if the value of all the weights are equal to unity, NURBS become B-splines, i.e. $R_l^{p_i}(\xi^i) = N_{l,p_i}(\xi^i)$. It shows that B-spline is a special case of NURBS.

2.2.3 NURBS geometries

The NURBS curves, surfaces, and solids are constructed in manner similar to its B-spline counterpart, except that the basis functions are different. Using Eq. (2.11) together with the control points of Eq. (2.10), a NURBS curve of order p_i is constructed using

$$\mathbf{C}(\xi^i) = \sum_{l=1}^{n_i} R_l^{p_i}(\xi^i)\, \boldsymbol{X}_l \,. \tag{2.17}$$

Similarly, the NURBS surface and solids are defined by

$$\mathbf{S}(\xi^1, \xi^2) = \sum_{l=1}^{n_1}\sum_{m=1}^{n_2} R_{lm}^{p_1,p_2}(\xi^1, \xi^2)\, \boldsymbol{X}_{lm} = \sum_{A=1}^{n_{\text{cp}}} R_A(\boldsymbol{\xi})\, \boldsymbol{X}_A \tag{2.18}$$

$$\mathbf{V}(\xi^1, \xi^2, \xi^3) = \sum_{l=1}^{n_1}\sum_{m=1}^{n_2}\sum_{n=1}^{n_3} R_{lmn}^{p_1,p_2,p_3}(\xi^1, \xi^2, \xi^3)\, \boldsymbol{X}_{lmn} = \sum_{A=1}^{n_{\text{cp}}} R_A(\boldsymbol{\xi})\, \boldsymbol{X}_A \,. \tag{2.19}$$

In the above Eq. (2.18), $n_{\text{cp}} = n_1 \times n_2$ denotes the total number of control points associated with the NURBS surface and $R_A(\boldsymbol{\xi})$ is the bivariate NURBS function that is defined in Eq. (2.13). Similarly, in Eq. (2.19), $n_{\text{cp}} = n_1 \times n_2 \times n_3$ represents the total number of control points associated with the NURBS solid and $R_A(\boldsymbol{\xi})$ is trivariate NURBS function that is defined in Eq. (2.14).

It is highlighted that within the existing NURBS discretization approach for isogeometric analysis of contact problems, the NURBS description of the contact surface is inherited directly from the bulk discretization, see e.g., [29, 30, 47, 66]. For example, let us assume that the boundary curve of a NURBS constructed surface, which is defined along the ξ^1 parametric direction, is taken as the contact layer. For the NURBS contact boundary layer, the knot vector Ξ^1, interpolation order p_1, and the control points at $\xi_l^2 = \xi_1^2$, i.e. $\boldsymbol{X}_l = \boldsymbol{X}_{l1}$ are inherited directly from the NURBS surface discretization. Similarly, in case of a NURBS discretized solid, the NURBS discretization of the contact boundary surface that is defined along the ξ^1 and ξ^2 parametric

directions at $\xi_l^3 = \xi_1^3$, is taken from the NURBS volume discretization.

2.3 Refinement strategies

One of the key advantages of adopting CAD polynomials for isogeometric analysis is that the constructed geometries can be refined in a straightforward fashion. The refinement strategies enrich the underlying basis functions, which consequently allows the accurate capture of the sharp variations in the solution field [52, 58]. The two basic methods that are used to refine the geometry are the *knot insertion*, which introduces additional knots or elements in a given knot vector, and *order elevation*, which as the name implies, elevates the interpolation order of the basis functions. A specific application of order elevation before the knot insertion leads to another strategy, namely *k−refinement*. These strategies provide control over the existing knot span or mesh size, inter-element continuity, and interpolation order of the underlying basis functions, while with their applications, the geometry and its parameterization remain intact. Since NURBS entities in $\mathbb{R}^d$ are the projective transformation of the B-spline entity in $\mathbb{R}^{d+1}$, all the refinement strategies for NURBS basis functions are analogous to B-splines except the modification that they are directly applied to higher $\mathbb{R}^{d+1}$ space.

2.3.1 Knot insertion

In the knot insertion strategy, a new knot is inserted into a given knot vector. Insertion of a unique knot into an existing knot span splits it into two and creates an additional span or element without changing the inter-element continuity of the underlying basis functions. If the existing knot value is repeated through the knot insertion, it without changing the total number of elements results in the reduction of the continuity of the basis functions according to the knot multiplicity, as detailed in Section 2.1.3.

With the knot insertion strategy, the geometry or the parametrization of the curve does not change. However, it leads to an additional basis function and consequently an additional control point. Let $\Xi^i = \left[\xi_1^i, \xi_2^i, \ldots, \xi_k^i, \xi_{k+1}^i, \ldots, \xi_{n_i+p_i+1}^i\right]$ be a given knot vector defined along the ξ^i parametric direction. Insertion of a new, unique knot $\bar{\xi}^i \in \left[\xi_k^i, \xi_{k+1}^i\right)$ into the original knot vector results in a new knot vector $\bar{\Xi}^i = \left[\xi_1^i, \xi_2^i, \ldots, \xi_k^i, \bar{\xi}^i, \xi_{k+1}^i, \ldots, \xi_{\bar{n}_i+p_i+1}^i\right]$, where $\bar{n}_i = n_i + 1$. Thus, insertion of a new knot leads to an additional basis function and an additional control point. The existing

basis functions for the new knot vector are redefined according to Eq. (2.2) and the new control points, denoted by $\{\bar{\boldsymbol{X}}_l\}_{l=1}^{\bar{n}_i}$, are computed from the linear combination of original control points $\{\boldsymbol{X}_l\}_{l=1}^{n_i}$, by

$$\bar{\boldsymbol{X}}_l = \begin{cases} \boldsymbol{X}_1, & l = 1 \\ \alpha_l \boldsymbol{X}_l + (1-\alpha_l)\boldsymbol{X}_{l-1}, & 1 < l < \bar{n}_i \\ \boldsymbol{X}_{n_i}. & l = \bar{n}_i \end{cases} \tag{2.20}$$

In the above equation, the value of α_l is computed using the following relation

$$\alpha_l = \begin{cases} 1, & 1 \leq l \leq k - p_i \\ \dfrac{\bar{\xi}^i - \xi^i_l}{\xi^i_{l+p} - \xi^i_l}, & k - p_i + 1 \leq l \leq k \\ 0. & k < l \leq \bar{n}_i \end{cases} \tag{2.21}$$

An example of knot insertion starting with a knot vector $\Xi^1 = [0, 0, 0, 4, 4, 4]$ is shown in Fig. 2.5. In this, the number of elements are increased from one to four by inserting three unique knot values $\bar{\xi}^i = 1$, 2, and 3.

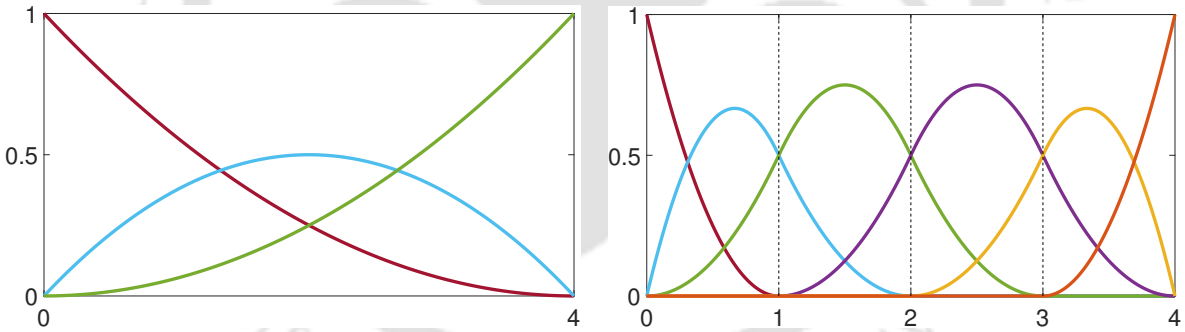

(a) Original basis function **(b)** New basis functions

Figure 2.5: Knot insertion: (a) The original basis functions corresponding to an initial knot vector $\Xi^i = [0, 0, 0, 4, 4, 4]$. (b) The new basis functions corresponding to the knot vector $\Xi^i = [0, 0, 0, 1, 2, 3, 4, 4, 4]$ after the insertion of three new and unique knot values $\bar{\xi}^i = 1$, 2, and 3.

2.3.2 Order elevation

The second method to enrich the basis function is the order elevation strategy. This, as the name implies, elevates the interpolation order of the underlying basis functions

used to represent the geometry and solution field. As discussed in Section 2.1.2, a p_i^{th} order of basis function has $p_i - m$ continuous derivatives across the element boundaries or each knot value. Thus, it is clear that, for each step of order elevation, which raises p_i, the knot multiplicity m must also be increased in an analogous manner to retain the original continuity of the basis functions across element boundary. It means that the first step of order elevation, which increases the interpolation order from p_i to p_i+1, the multiplicity of each knot value ξ_l^i of the existing knot vector Ξ^i must also be increased by one. With the order elevation, neither the geometry nor its parametrization is changed. However, the total number of basis functions and associated control points are increased. It is also noted that since no new unique knot is added to the knot vector, the total number of elements remains the same.

The concept of order elevation of underlying basis functions is illustrated in Fig. 2.6. The quadratic functions that are defined over two different knot vectors, i.e. $\Xi^i = [0, 0, 0, 4, 4, 4]$ and $\Xi^i = [0, 0, 0, 1, 1, 2, 3, 4, 4, 4]$, are considered as a starting point, see Figs. 2.6a and 2.6b, respectively. In the first case, the basis functions are C^1-continuous everywhere except at the end knot values, where they are interpolatory. For the second knot vector, this behaviour is same, with an exception that the functions are C^0-continuous at knot value $\xi^i = 1$ due to knot repetition. Figures 2.6c and 2.6d, and 2.6e and 2.6f illustrate that with each step of order elevation, the knot multiplicity in each knot vector is increased by one time. It can also be seen that as compared to original basis functions, their total number increases after performing order elevation, however no new element is created, and their inter-element continuity also remains preserved.

2.3.3 k-refinement

The $k-$refinement strategy, which was originally introduced in [52], is been predominantly utilized in various applications of isogeometric analysis as compared to order elevation. This is due to its advantageous feature, which increases the inter-element continuity and the interpolation order of the basis functions in a simultaneous manner. As discussed in Section 2.1.2, the highest level of continuity that can be attained at a unique knot value for a p^{th} order basis function is C^{p_i-1}. To perform $k-$refinement, first, the interpolation order of the original p order of functions, which are C^{p_i-1} continuous, is elevated to a desired value. Each step of order elevation leads to an increment

in the continuity of the basis functions simultaneously for the coarsest possible form of the knot vector of a given geometry. After that, the given knot values are inserted, which thereby creates new elements.

An example is shown in Fig. 2.7, where the quadratic order of basis functions with $\Xi^i = [0, 0, 0, 4, 4, 4]$ knot vector is considered to start with. As can be seen, the new knot values $\bar{\xi}^i = 1$, 2, and 3 are inserted after elevating the order of the basis functions

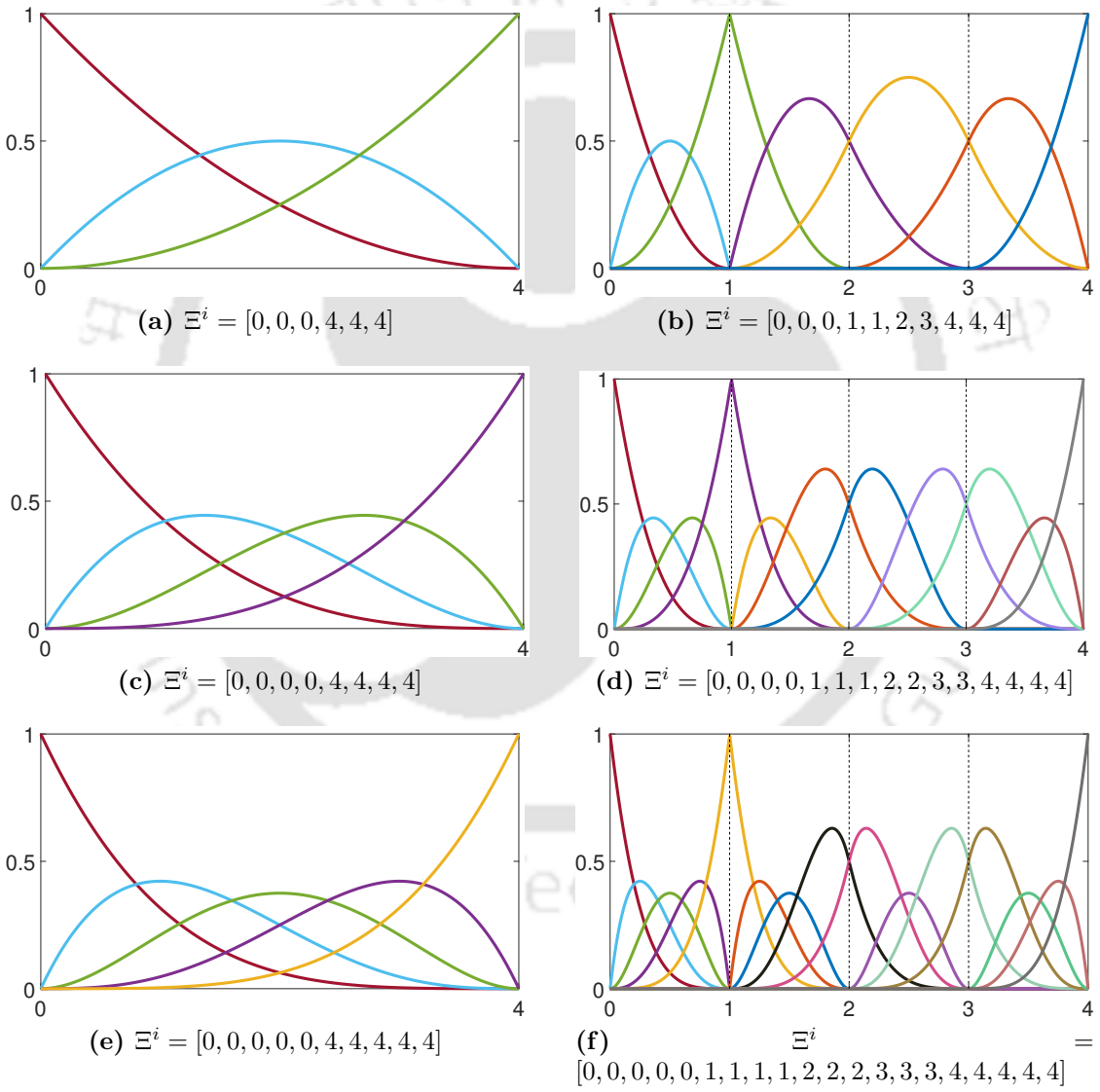

(a) $\Xi^i = [0, 0, 0, 4, 4, 4]$ **(b)** $\Xi^i = [0, 0, 0, 1, 1, 2, 3, 4, 4, 4]$

(c) $\Xi^i = [0, 0, 0, 0, 4, 4, 4, 4]$ **(d)** $\Xi^i = [0, 0, 0, 0, 1, 1, 1, 2, 2, 3, 3, 4, 4, 4, 4]$

(e) $\Xi^i = [0, 0, 0, 0, 0, 4, 4, 4, 4, 4]$ **(f)** $\Xi^i = [0, 0, 0, 0, 0, 1, 1, 1, 1, 2, 2, 2, 3, 3, 3, 4, 4, 4, 4, 4]$

Figure 2.6: Order elevation of original quadratic basis functions (top row) defined over two different knot vectors (column-wise). New basis functions after the order elevation to polynomial order $p_i = 3$ (middle row) and $p_i = 4$ (bottom row) basis functions.

by two. The resulting knot vector is $[0,0,0,0,0,1,2,3,4,4,4,4,4]$ and the new basis functions are of order $\bar{p}_i = 4$ and have C^3-continuity across the element boundaries.

Within the existing order elevation based refinement of the NURBS discretized geometry, the interpolation order of the NURBS constructed geometry including its boundary layer is elevated uniformly. However, for the problems that are dominated by the surface effects, e.g. contact problems, such a uniform order elevation of a NURBS discretized geometry has the negative impact on the performance of IGA technique since the higher-order of NURBS functions that are set on the surface additionally have to be utilized in the large majority of the domain that is away from the surface. It, therefore, becomes desirable to develop an improved NURBS-based discretization method that provides a possibility to perform controllable order-elevation for a NURBS described geometry, as initially suggested by Temizer et al. [47]. Such a method is proposed in this work and is described in detail in Chapter 5.

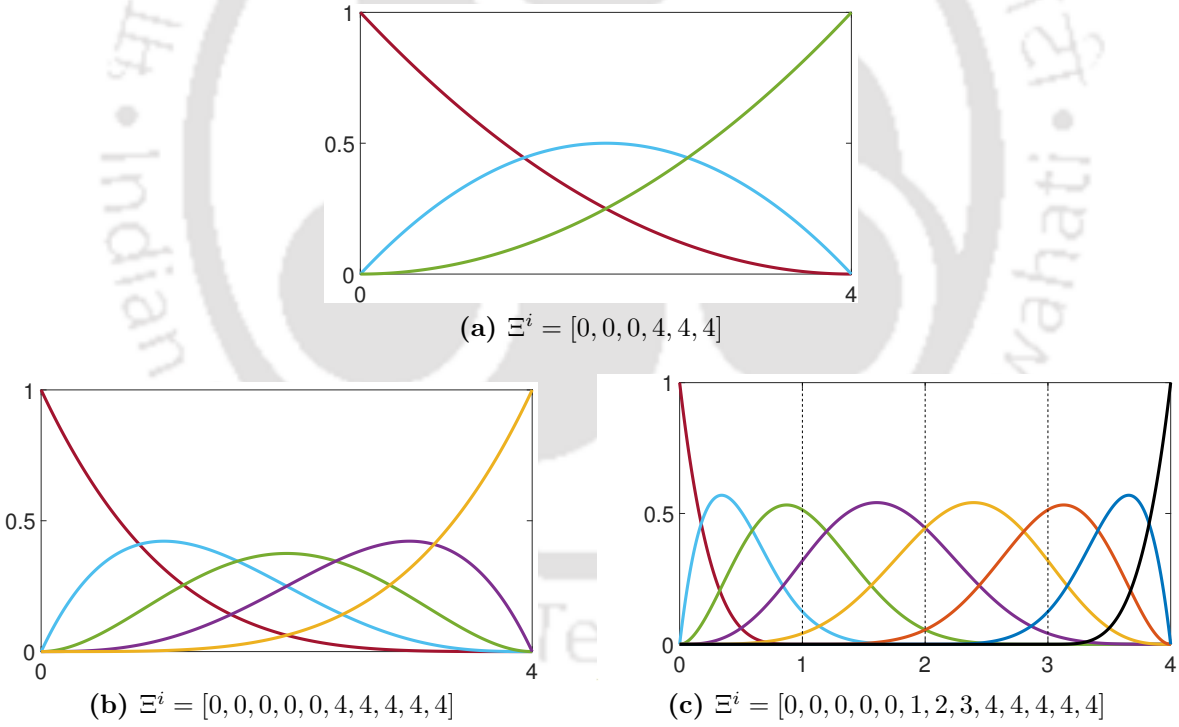

(a) $\Xi^i = [0,0,0,4,4,4]$

(b) $\Xi^i = [0,0,0,0,0,4,4,4,4,4]$

(c) $\Xi^i = [0,0,0,0,0,1,2,3,4,4,4,4,4]$

Figure 2.7: $k-$refinement of basis functions. The knot insertion (from (a) to (b)) after the order elevation (from (b) to (c)) leads to increment in the polynomial order and inter-element continuity of basis functions (from (a) to (c)).

Chapter 3

Mathematical Formulation

In this chapter, first, the theoretical background of the continuum mechanics that is used to numerically analyze the nonlinear physical behavior of solids undergoing finite deformation is summarized in Section 3.1. It is neither intended to be exhaustive nor complete but is rather the necessary basis for the computational contact mechanics. After that, in Section 3.2, the basic equations that are used to describe the normal and frictional contact between two deformable bodies are summarized. Thereafter, in Section 3.3, the continuum formulation for adhesive contact that is used to analyze the adhesive peeling problem is briefly outlined.

In the following discussion, to make the distinction between the scalar and tensor quantities, the former is denoted by italicized letters, while the latter by bold italicized symbols, e.g. a_i is i^{th} component of a tensor $\boldsymbol{a}$.

3.1 Continuum mechanics

The continuum theory provides a convenient mathematical framework that allows to model the physical phenomenons. The fundamental (simplifying) assumption made in the continuum mechanics theory is that the entire physical space of an object is continuously filled with the material without the presence of any empty space. With this definition, *continuum* can be considered as an idealization of an actual physical material model, where the discreet behavior of the material particles is characterized by its underlying molecular or grain structures. Therefore, all the physical properties such as density, displacement, velocities, stresses, etc., are continuously differentiable within

a *continuum* material. In addition to the continuum theory, continuum-mechanical based description as in [107–109] can also be used to model the phenomena at the nano-scale or atomic level.

In the following subsections, the most important basic equations for the continuum mechanics are summarized. The kinematics of a deformable-material body is presented in subsection 3.1.1, followed by the balance laws for the quasi-static case in subsection 3.1.2. The constitutive relations for the hyper-elastic material model is introduced in subsection 3.1.3. Finally, the strong and weak formulations for the boundary value problem is presented in subsection 3.1.4.

For the detailed discussion on the topic of continuum mechanics, the textbooks by Malvern [110], Bonet and Wood [111], Holzapfel [112], Reddy [113], Wriggers [114], and Belytschko et al. [115] can be referred.

3.1.1 Kinematics

In this subsection, the fundamental kinematic relationships that are used to mathematically describe the arbitrary large deformation of a homogeneous body are discussed. These relations are required within the constitutive expressions and weak formulation of the mechanical boundary value problem. In this work, the inertial effects are neglected.

Description of deformation

Consider a deformable material body occupying a domain $\mathcal{B}_0$ with boundary $\partial\mathcal{B}_0$ at pseudo-time t_0. According to the continuum approach, the domain $\mathcal{B}_0$ is composed of continuously distributed material points $P \in \mathcal{B}_0$. Each point P occupies a unique position $\boldsymbol{X}$ in the three-dimensional space $\mathbb{R}^3$, as shown in Fig. 3.1. The configuration $\mathcal{B}_0$ is referred as the initial or reference configuration and the components X_i as the material coordinates. After the application of prescribed external loads at pseudo-time $t \in [0, T]$, the geometric shape of the continuum changes and acquires a new configuration, denoted by $\mathcal{B}$, which is referred as the current or deformed configuration. The configuration $\mathcal{B}$ is obtained through one-to-one mapping $\boldsymbol{\varphi} : \mathcal{B}_0 \to \mathcal{B}$. The deformation mapping $\boldsymbol{\varphi}$ takes a material point P having position $\boldsymbol{X}$ (from the initial configuration)

and maps it to a new unique position $\boldsymbol{x} \in \mathbb{R}^3$ in the deformed configuration $\mathcal{B}$ as

$$\boldsymbol{x} = \boldsymbol{\varphi}(\boldsymbol{X}, t)\,, \qquad \forall\ \boldsymbol{X} \in \mathcal{B}_0 \ \text{ and } t > 0\,. \tag{3.1}$$

This implies that for the fixed initial position $\boldsymbol{X} \in \mathcal{B}_0$ of a material point P, the function $\boldsymbol{\varphi}$ returns the new position $\boldsymbol{x} \in \mathcal{B}$ of the same material point P at a given pseudo-time t. With the assumption that $\boldsymbol{\varphi}$ is uniquely invertible, the inverse form of Eq. (3.1) can be obtained with

$$\boldsymbol{X} = \boldsymbol{\varphi}^{-1}(\boldsymbol{x}, t)\,. \tag{3.2}$$

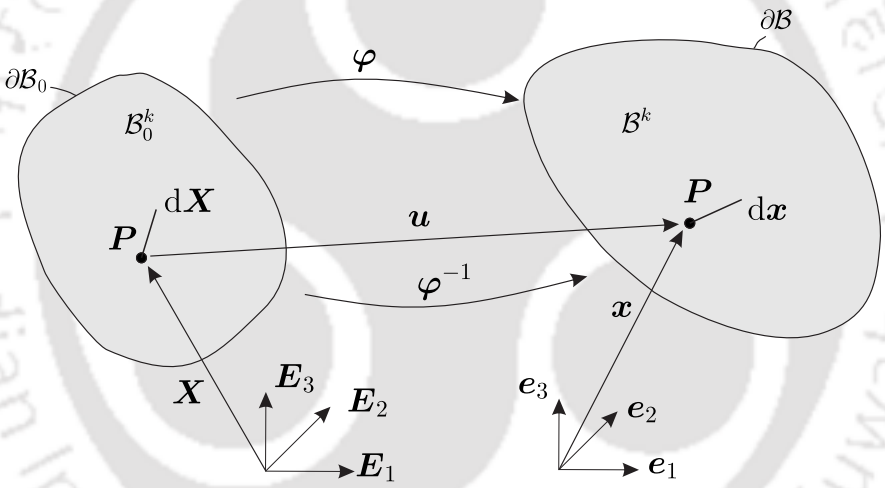

Figure 3.1: Configurations of the body. $\{\boldsymbol{E}_1, \boldsymbol{E}_2, \boldsymbol{E}_3\}$ and and $\{\boldsymbol{e}_1, \boldsymbol{e}_2, \boldsymbol{e}_3\}$ are the basis systems in $\mathbb{R}^3$ for the reference $\mathcal{B}_0$ and current $\mathcal{B}$ configurations, respectively.

Since the motion described by Eq. (3.1) is characterized with respect to the material point coordinates $\boldsymbol{X}$, it is referred as the *material* or *Lagrangian description*. In the Lagrangian description, an observer follows an individual material point as it moves through space and time. On the other hand, the motion given by Eq. (3.2) is referred as the *spatial* or *Eulerian* description as it is characterized with respect to the spatial coordinates $\boldsymbol{x}$. In the Eulerian description, the attention is paid to a specific point in space, and the change of motion is observed as time changes. In this thesis, the Lagrangian description is used to describe the deformation.

Displacement field

The displacement field $\boldsymbol{u}$ of a material point P is given by the difference between its corresponding position vectors $\boldsymbol{x}$ and $\boldsymbol{X}$ that are defined in the current and initial configurations, respectively. Therefore, the displacement is given by

$$\boldsymbol{u}(\boldsymbol{X}, t) = \boldsymbol{x} - \boldsymbol{X} \,. \tag{3.3}$$

Deformation gradient

The motion of the material points $\boldsymbol{X}$ can be described by utilizing their current position $\boldsymbol{x} \in \mathcal{B}$ and displacement field $\boldsymbol{u}$. However, the definition of these position vectors alone is not sufficient to determine whether the considered body is undergoing deformation or rigid-body translation. Therefore, the changes in the material elements' length, area, and volume are needed to be determined. For this, the deformation gradient tensor $\boldsymbol{F}$, which enables the transformation of the material line element from the reference configuration to the current configuration, is defined by

$$\mathrm{d}\boldsymbol{x} = \boldsymbol{F}\,\mathrm{d}\boldsymbol{X} \,, \tag{3.4}$$

$$\boldsymbol{F} = \frac{\partial \boldsymbol{\varphi}}{\partial \boldsymbol{X}} = \frac{\partial \boldsymbol{x}}{\partial \boldsymbol{X}} \equiv \boldsymbol{\nabla}_0 \boldsymbol{x} \,, \tag{3.5}$$

where $\mathrm{d}\boldsymbol{x}$ and $\mathrm{d}\boldsymbol{X}$ are the line elements consisting same material points in the current and reference configurations, respectively, as shown in Fig. 3.1. Also, $\boldsymbol{\nabla}_0$ is the gradient with respect to the reference configuration. On substituting the expression of $\boldsymbol{x}$ from Eq. (3.3) to above Eq. (3.5), $\boldsymbol{F}$ can also be defined in terms of $\boldsymbol{u}$ as

$$\boldsymbol{F} = \frac{\partial}{\partial \boldsymbol{X}}(\boldsymbol{u} + \boldsymbol{X}) = \boldsymbol{I} + \boldsymbol{\nabla}_0 \boldsymbol{u} \,. \tag{3.6}$$

For a physically realistic change in the shape of the material element, the deformation gradient tensor $\boldsymbol{F}$ must not be singular, which is equivalent to

$$J = \det \boldsymbol{F} \neq 0 \,, \tag{3.7}$$

where J is called the Jacobian of deformation. In addition, $J > 0$ is essential to exclude the self-penetration of the body during deformation. Using the definition of deformation gradient tensor $\boldsymbol{F}$, the change in the area and volume elements can also

be determined.

In analogous to Eq. (3.4), the transformation of the surface area element from the reference to the current configuration at pseudo-time t is given by Nanson's formula as

$$\mathrm{d}\boldsymbol{a} = J\,\boldsymbol{F}^{-\mathrm{T}}\,\mathrm{d}\boldsymbol{A}\,, \tag{3.8}$$

where $\mathrm{d}\boldsymbol{a}$ and $\mathrm{d}\boldsymbol{A}$ are the area elements in the current and the reference configurations, respectively.

Consequently, the transformation of the volume element from the reference to the current configuration is provided by the relation

$$\mathrm{d}v = J\mathrm{d}V\,, \tag{3.9}$$

where $\mathrm{d}v$ and $\mathrm{d}V$ are the infinitesimal volume elements in the current and reference configurations, respectively.

According to the polar decomposition theorem, the deformation gradient tensor can be decomposed into a symmetric tensor ($\boldsymbol{U}$ or $\boldsymbol{V}$) and a orthogonal tensor $\boldsymbol{R}$ as

$$\boldsymbol{F} = \boldsymbol{R}\boldsymbol{U} = \boldsymbol{V}\boldsymbol{R} \tag{3.10}$$

where $\boldsymbol{R}$ is also denoted as the *rotation tensor*, and $\boldsymbol{U}$ and $\boldsymbol{V}$ are referred as the *right* and *left stretch tensors*, respectively.

Strain measures

The deformation gradient tensor $\boldsymbol{F}$ defined in the preceding section is considered as a fundamental tensor that characterizes the changes of a material element at $\boldsymbol{X}$ during the deformation. These changes are measured in terms of Green-Lagrangian strain tensor. It is used to describe the arbitrary large deformation of a continuum body.

Using Eq. (3.4), the square lengths of a line element in the current and reference configurations are given by

$$||\mathrm{d}\boldsymbol{x}||^2 = \mathrm{d}\boldsymbol{x}\cdot\mathrm{d}\boldsymbol{x} = \mathrm{d}\boldsymbol{X}\cdot(\boldsymbol{F}^{\mathrm{T}}\,\boldsymbol{F})\,\mathrm{d}\boldsymbol{X} \equiv \mathrm{d}\boldsymbol{X}\cdot\boldsymbol{C}\,\mathrm{d}\boldsymbol{X}\,, \tag{3.11}$$

$$||\mathrm{d}\boldsymbol{X}||^2 = \mathrm{d}\boldsymbol{X}\cdot\mathrm{d}\boldsymbol{X} = \mathrm{d}\boldsymbol{x}\cdot(\boldsymbol{F}^{-\mathrm{T}}\,\boldsymbol{F}^{-1})\,\mathrm{d}\boldsymbol{x} \equiv \mathrm{d}\boldsymbol{x}\cdot\boldsymbol{B}^{-1}\,\mathrm{d}\boldsymbol{x}\,, \tag{3.12}$$

where

$$\boldsymbol{C} = \boldsymbol{F}^{\mathrm{T}}\boldsymbol{F} \qquad \text{and} \qquad \boldsymbol{B} = \boldsymbol{F}\boldsymbol{F}^{\mathrm{T}} \tag{3.13}$$

are called the *right* and *left Cauchy-Green deformation* tensors, respectively. For the measurement of strain during the deformation, the change in the square lengths of a line element is expressed as

$$||\mathrm{d}\boldsymbol{x}||^2 - ||\mathrm{d}\boldsymbol{X}||^2 = 2\mathrm{d}\boldsymbol{X} \cdot \boldsymbol{E}\,\mathrm{d}\boldsymbol{X} \tag{3.14}$$

where $\boldsymbol{E}$ is defined as the Green-Lagrangian strain tensor. In view of above Eqs. (3.11)-(3.13), $\boldsymbol{E}$ can be defined in terms of $\boldsymbol{C}$ as

$$\boldsymbol{E} := \frac{1}{2}(\boldsymbol{C} - \boldsymbol{I})\,, \tag{3.15}$$

where $\boldsymbol{I}$ is the second-order identity tensor. Also, it can be shown that $\boldsymbol{C}$, $\boldsymbol{B}$, and $\boldsymbol{E}$ are symmetric tensors.

3.1.2 Stress tensor and balance laws

In this section, the definition of the stress tensor, which is essential in continuum mechanics, is presented. The balance of linear momentum and balance of angular momentum, which are the fundamental principles in continuum mechanics, are also briefly described.

Stress tensor

Stress is the consequence of material point interactions that arise through the application of external loads and prescribed boundary conditions. By definition, stress can be considered as a measure of internal forces uniformly distributed to per unit material area of the deformed configuration.

Consider an arbitrary plane surface that imaginary cuts a continuum body at a point $\boldsymbol{x}$ in the current configuration. The direction of the orientation of the plane is specified by a unit normal vector $\boldsymbol{n}$. According to the Cauchy's stress theorem: there exists a second-order stress tensor $\boldsymbol{\sigma}$ such that the traction vector $\boldsymbol{t}$ at any point P on

the plane surface can be expressed as

$$\boldsymbol{t} = \boldsymbol{\sigma}\,\boldsymbol{n}\,. \tag{3.16}$$

Here, $\boldsymbol{\sigma}$ denotes the *Cauchy stress tensor* in the current configuration and is defined as

$$\boldsymbol{\sigma} = \begin{bmatrix} \sigma_{11} & \sigma_{12} & \sigma_{13} \\ \sigma_{21} & \sigma_{22} & \sigma_{23} \\ \sigma_{31} & \sigma_{32} & \sigma_{33} \end{bmatrix}. \tag{3.17}$$

Balance of linear momentum

The conservation of linear momentum states that the time rate of change of linear momentum is equal to the sum of body forces and external loads acting over the physical volume $\mathcal{B}$ and surface $\partial\mathcal{B}$. Mathematically,

$$\frac{\mathrm{d}}{\mathrm{d}t}\int_{\mathcal{B}} \rho\,\dot{\boldsymbol{x}}\,\mathrm{d}v = \int_{\mathcal{B}} \bar{\boldsymbol{b}}\,\mathrm{d}v + \int_{\partial\mathcal{B}} \boldsymbol{t}\,\mathrm{d}a\,, \tag{3.18}$$

where $\dot{\boldsymbol{x}}$ denotes the first-order time derivative of $\boldsymbol{x}$ and $\bar{\boldsymbol{b}}$ is the body forces per unit volume, e.g. gravitational forces. Inserting the expression of traction vector $\boldsymbol{t}$ from Eq. (3.16) in Eq. (3.18) and using the Gauss-divergence theorem [116], the above equation can be defined as

$$\int_{\mathcal{B}} (\mathrm{div}\,\boldsymbol{\sigma} + \bar{\boldsymbol{b}})\,\mathrm{d}v = \int_{\mathcal{B}} \rho\,\ddot{\boldsymbol{x}}\,\mathrm{d}v\,. \tag{3.19}$$

Since the above equation is valid for any volume size $\mathrm{d}v$. Hence, one can obtain the local form of the balance of linear momentum as

$$\mathrm{div}\,\boldsymbol{\sigma} + \bar{\boldsymbol{b}} = \rho\,\ddot{\boldsymbol{x}}\,, \tag{3.20}$$

which holds for all points $\boldsymbol{x}$ and for all times t.

Balance of angular momentum

The conservation of angular momentum states that the time rate of change of moment of momentum is equal to the vector sum of all moments stemming from body forces

and external loads. Mathematically,

$$\frac{\mathrm{d}}{\mathrm{d}t}\int_{\mathcal{B}} \boldsymbol{x}\times\rho\,\dot{\boldsymbol{x}}\,\mathrm{d}v = \int_{\mathcal{B}} \boldsymbol{x}\times\bar{\boldsymbol{b}}\,\mathrm{d}v + \int_{\partial\mathcal{B}} \boldsymbol{x}\times\boldsymbol{t}\,\mathrm{d}a \tag{3.21}$$

On inserting the expression for the traction $\boldsymbol{t}$ from Eq. (3.16) in Eq. (3.21) and using the Gauss-divergence theorem [116], it can be shown that in the absence of any body couples

$$\boldsymbol{\sigma} = \boldsymbol{\sigma}^{\mathrm{T}}, \qquad \forall\,\boldsymbol{x}\in\mathcal{B}, \tag{3.22}$$

which implies that if the conservation of angular momentum is satisfied, then the *Cauchy stress tensor* is *symmetric*.

Using the symmetry of Cauchy stress tensor in above expression, $\boldsymbol{\sigma}$ in Eq. (3.17) can be described as

$$\boldsymbol{\sigma} = \begin{bmatrix} \sigma_{11} & \sigma_{12} & \sigma_{13} \\ \vdots & \sigma_{22} & \sigma_{23} \\ sym & \dots & \sigma_{33} \end{bmatrix}. \tag{3.23}$$

Using the Voigt notation, Eq. (3.23) can be written as

$$\boldsymbol{\sigma} = [\sigma_{11},\ \sigma_{22}\,,\sigma_{33}\,,\sigma_{12}\,,\sigma_{23}\,,\sigma_{31}]^{\mathrm{T}} \tag{3.24}$$

3.1.3 Constitutive relations

In this work, a particular class of material known as *hyperelastic material* is considered. It accounts for both the nonlinear stress-strain behavior and geometrically nonlinear changes to the material subjected to large deformations. The constitutive relation for a compressible hyperelastic material is characterized by energy as heat during the deformation process. The corresponding relation between the stress and strain is derived from the strain energy density function $\bar{W}$ (per unit volume) as

$$\boldsymbol{S} = \frac{\partial\bar{W}}{\partial\boldsymbol{E}} = 2\frac{\partial\bar{W}}{\partial\boldsymbol{C}} \tag{3.25}$$

where $\boldsymbol{S}$ denotes the second Piola-Kirchhoff stress tensor.

In the present work, the *isotropic* class of compressible hyperelastic material is accounted. A material is said to be isotropic if the material properties or constitutive behavior is independent of the material directions. Thus, $\bar{W}$ can be defined in terms

of the principal invariants I_1, I_2, I_3 of the right Cauchy-Green deformation tensor $\boldsymbol{C}$ as

$$\bar{W}(\boldsymbol{C}) = \bar{W}(I_1, I_2, I_3)\,. \tag{3.26}$$

Using the above relation, the second Piola-Kirchhoff stress tensor $\boldsymbol{S}$ is defined as

$$\boldsymbol{S} = 2\left(\frac{\partial \bar{W}}{\partial I_1}\frac{\partial I_1}{\partial \boldsymbol{C}} + \frac{\partial \bar{W}}{\partial I_2}\frac{\partial I_2}{\partial \boldsymbol{C}} + \frac{\partial \bar{W}}{\partial I_3}\frac{\partial I_3}{\partial \boldsymbol{C}}\right) \tag{3.27}$$

where the invariants are given as: $I_1 = \boldsymbol{C}$, $I_2 = \frac{1}{2}[(\mathrm{tr}\,\boldsymbol{C})^2 - \mathrm{tr}\boldsymbol{C}^2]$, and $I_3 = \det(\boldsymbol{C})$.

The Cauchy stress tensor $\boldsymbol{\sigma}$ can be obtained as

$$\boldsymbol{\sigma} = J^{-1}\,\boldsymbol{F}\,\boldsymbol{S}\,\boldsymbol{F}^{\mathrm{T}} \tag{3.28}$$

In the present work, a *compressible isotropic Neo-Hookean material model* is employed for which the strain energy density function is defined as

$$\bar{W} = \frac{\lambda}{2}(\ln J)^2 + \frac{\mu}{2}(\mathrm{tr}(\boldsymbol{B}) - 3) - \mu(\ln J)\,, \tag{3.29}$$

where Lamé constants λ and μ, called as the bulk and shear moduli, respectively, are given in terms of Young's modulus E and Poisson's ratio ν as

$$\lambda = \frac{2\mu\nu}{(1-2\nu)}\,, \qquad \text{and} \qquad \mu = \frac{E}{2(1+\nu)}\,, \tag{3.30}$$

With the above-defined equations, the Cauchy stress tensor can be defined as

$$\boldsymbol{\sigma} = \frac{\lambda}{J}(\ln J)\boldsymbol{I} + \frac{\mu}{J}(\boldsymbol{B} - \boldsymbol{I})\,, \tag{3.31}$$

and the corresponding spatial elasticity tensor $\mathbb{c}$ is given by

$$\mathbb{c} = \hat{\lambda}\,(\boldsymbol{I} \otimes \boldsymbol{I}) + 2\hat{\mu}\,\mathcal{I}\,, \tag{3.32}$$

where $\hat{\lambda} = \lambda/J$ and $\hat{\mu} = (\mu - \lambda \ln J)/J$ are the effective Lamé moduli, and $\mathcal{I}$ is the fourth-order identity tensor and in component form is given as $\mathcal{I}_{ijkl} = \frac{1}{2}(\delta_{ik}\delta_{jl} + \delta_{il}\delta_{jk}) = \delta_{ij}\delta_{kl}$. The spatial elasticity tensor can be expressed in the component form as

$$\mathbb{c}_{ijkl} = \hat{\lambda}\,\delta_{ij}\,\delta_{kl} \;+\; 2\,\hat{\mu}\,\delta_{ik}\,\delta_{jl}\,. \tag{3.33}$$

Using the *Voigt notation*, $\mathbb{c}_{ijkl}$ can be expressed as 6×6 matrix form as

$$\mathbb{c} = \begin{bmatrix} \hat{\lambda}+2\hat{\mu} & \hat{\lambda} & \hat{\lambda} & 0 & 0 & 0 \\ & \hat{\lambda}+2\hat{\mu} & \hat{\lambda} & 0 & 0 & 0 \\ & & \hat{\lambda}+2\hat{\mu} & 0 & 0 & 0 \\ & \vdots & & \hat{\mu} & 0 & 0 \\ \dots & sym & \dots & & \hat{\mu} & 0 \\ & \vdots & & & & \hat{\mu} \end{bmatrix} . \tag{3.34}$$

In the case of plane strain condition, the above expression reduces to

$$\mathbb{c} = \begin{bmatrix} \hat{\lambda}+2\hat{\mu} & \hat{\lambda} & 0 \\ \vdots & \hat{\lambda}+2\hat{\mu} & 0 \\ sym & \dots & \hat{\mu} \end{bmatrix} . \tag{3.35}$$

3.1.4 Mechanical boundary value problem

In this subsection, the strong formulation, followed by the weak form of the mechanical boundary value problem (BVP) is summarized.

Strong form

In continuum mechanics, the system of partial differential equations (PDEs) that is obtained through the combinations of above-described ingredients, including kinematical relations, balance laws, and the constitutive relation, has to be solved using a numerical method like FEM. A system of governing PDEs, together with the prescribed boundary conditions, is referred to as the strong formulation of the BVP that can be summarized as follows.

Given the reference configuration $\mathcal{B}_0$, the prescribed displacement $\bar{\boldsymbol{u}}$ on the displacement boundary $\partial_u\mathcal{B} \subset \partial\mathcal{B}$, and traction $\bar{\boldsymbol{t}}$ on the traction boundary $\partial_t\mathcal{B} \subset \partial\mathcal{B}$ as well as body forces $\rho\,\bar{\boldsymbol{b}}$ in $\mathcal{B}$, the objective is to find the displacement field $\boldsymbol{u}(\boldsymbol{X}, t) \;\; \forall t \in [0, T]$ that satisfies the following equilibrium equation

$$\begin{aligned} \operatorname{div}\boldsymbol{\sigma} + \rho\,\bar{\boldsymbol{b}} &= \boldsymbol{0} \quad \text{in} \;\; \mathcal{B}\,, \\ \boldsymbol{u} &= \bar{\boldsymbol{u}} \quad \text{on} \;\; \partial_u\mathcal{B}\,, \end{aligned} \tag{3.36}$$

$$\boldsymbol{t} = \boldsymbol{\sigma}\,\boldsymbol{n} \;=\; \bar{\boldsymbol{t}} \qquad \text{on} \;\; \partial_t \mathcal{B}\,.$$

Here, the Cauchy-stress tensor $\boldsymbol{\sigma}$ is symmetric and computed using the constitutive relation for the isotropic Neo-Hookean material model from Eq. (3.31). The strong formulation states that the governing equations must be satisfied at every point of the domain.

The computation of the first term in Eq. (3.36), i.e. $\operatorname{div}\boldsymbol{\sigma}$, imposes the strong continuity requirement on the displacement field as it involves the second-order derivative of $\boldsymbol{u}$. This serves as a limitation to many problems. Thus, a closed-form expression or analytical solution of the governing PDEs is not always feasible, especially in the case of nonlinear BVP.

An alternative is to use a numerical method, e.g. FEM or IGA, to find an approximate solution of the governing PDEs that do not admit the analytical solution. To solve the given BVP using FEA or IGA, the *strong formulation* is converted to a *variational* or *weak formulation*.

Weak form

To derive the *weak formulation*, first a test function or virtual deformation, i.e. $\delta\boldsymbol{\varphi}$, satisfying the condition $\delta\boldsymbol{\varphi} \equiv \boldsymbol{0}$ on $\partial_u \mathcal{B}$ is multiplied to Eq. (3.36). After that the corresponding system of equations is integrated over the volume of the body $\mathcal{B}$ leading to

$$\int_{\mathcal{B}} \operatorname{div}\boldsymbol{\sigma} \cdot \delta\boldsymbol{\varphi}\,\mathrm{d}v + \int_{\mathcal{B}} \rho\,\bar{\boldsymbol{b}} \cdot \delta\boldsymbol{\varphi}\,\mathrm{d}v = 0\,. \qquad \forall \delta\boldsymbol{\varphi} \in \mathcal{V} \tag{3.37}$$

where $\mathcal{V}$ denotes the space of *kinematically admissible variations* $\delta\boldsymbol{\varphi}$. The application of the Gauss-divergence theorem to the first term of above equation together with the boundary conditions, Eq. (3.37) becomes

$$\delta\mathcal{W} := \underbrace{\int_{\mathcal{B}} \boldsymbol{\sigma} : \operatorname{grad}(\delta\boldsymbol{\varphi})\,\mathrm{d}v}_{\delta\mathcal{W}_{\text{int}}} \underbrace{- \int_{\mathcal{B}} \rho\,\bar{\boldsymbol{b}} \cdot \delta\boldsymbol{\varphi}\,\mathrm{d}v \;-\; \int_{\partial_t\mathcal{B}} \bar{\boldsymbol{t}} \cdot \delta\boldsymbol{\varphi}\,\mathrm{d}a}_{-\delta\mathcal{W}_{\text{ext}}} = 0\,. \tag{3.38}$$

As can be seen in the weak formulation of a BVP, the governing PDEs are satisfied in an *average* or *integral sense* rather than in a *pointwise manner* as in strong formulation. It reduces the higher continuity requirement on the solution field as it involves only the first-order derivatives of $\boldsymbol{u}$. The first term, $\delta\mathcal{W}_{\text{int}}$, in above equations denotes the

virtual work arising from the internal stresses, and last term, i.e. $\delta\mathcal{W}_{\text{ext}}$, represents the virtual work due to external forces.

In order to solve the weak form of the boundary value problem given by Eq. (3.38) with iterative algorithms, e.g. Newton's method, it needs to be linearized. In Appendix A.1, the details of the linearization of the $\delta\mathcal{W}_{\text{int}}$ and $\delta\mathcal{W}_{\text{ext}}$ terms are presented.

3.2 Contact mechanics and weak form

In this section, the basic equations that are used to describe the contact between two deformable bodies are summarized. Specific attention is paid to the non-penetration and sticking conditions and frictional phenomena between the surfaces. Contact problems can be seen as adding the kinematic constraints to the mechanical boundary value problems described in the previous section. For an extensive discussion on computational contact mechanics, the textbooks by Laursen [18] and Wriggers [6] can be referred.

3.2.1 Contact kinematics

This subsection summarizes the kinematics of the normal and frictional contact between the two deformable bodies undergoing the large deformations. The extension to the multi-body contact can be achieved by considering each pair of bodies in an individual manner. The contact between a deformable and a rigid body combination, which is also known as *Signorini problem*, can be considered a special case of a two-body contact system summarized in the following.

Description of contact between two deformable bodies

It is assumed that two bodies come into contact and undergo large deformations, as shown in Fig. 3.2. The transformation of the bodies from the reference to the current configurations and their kinematical relations are the same as discussed in subsection 3.1.1. In this work, according to the convention used in [6], one of them is denoted as the slave body $\mathcal{B}^{\text{s}}$ and another as the master body $\mathcal{B}^{\text{m}}$. Thus, in the following, a superscript $k = \{\text{s}, \text{m}\}$ is used to specify the slave and master bodies, respectively. It is assumed that the bodies come into contact through the application of prescribed external surface traction and/or displacement. The boundary $\partial\mathcal{B}^k$ of a

body $\mathcal{B}^k$ consists of the following three distinct parts

$$\partial\mathcal{B}^k = \partial_t\mathcal{B}^k \cup \partial_u\mathcal{B}^k \cup \partial_c\mathcal{B}^k\,, \qquad \forall\, t \in T \tag{3.39}$$

where $\partial_t\mathcal{B}^k$ and $\partial_u\mathcal{B}^k$ are the boundaries where the traction and displacement are prescribed, and $\partial_c\mathcal{B}^k$ is the potential surface where the contact occurs. Further, it is assumed that these boundaries satisfy:

$$\partial_t\mathcal{B}^k \cap \partial_u\mathcal{B}^k \cap \partial_c\mathcal{B}^k = \emptyset\,, \qquad \forall\, t \in T \tag{3.40}$$

The counterparts in the reference configurations are denoted by $\partial\mathcal{B}_0^k\,, \partial_t\mathcal{B}_0^k\,, \partial_u\mathcal{B}_0^k$, and $\partial_c\mathcal{B}_0^k$, respectively.

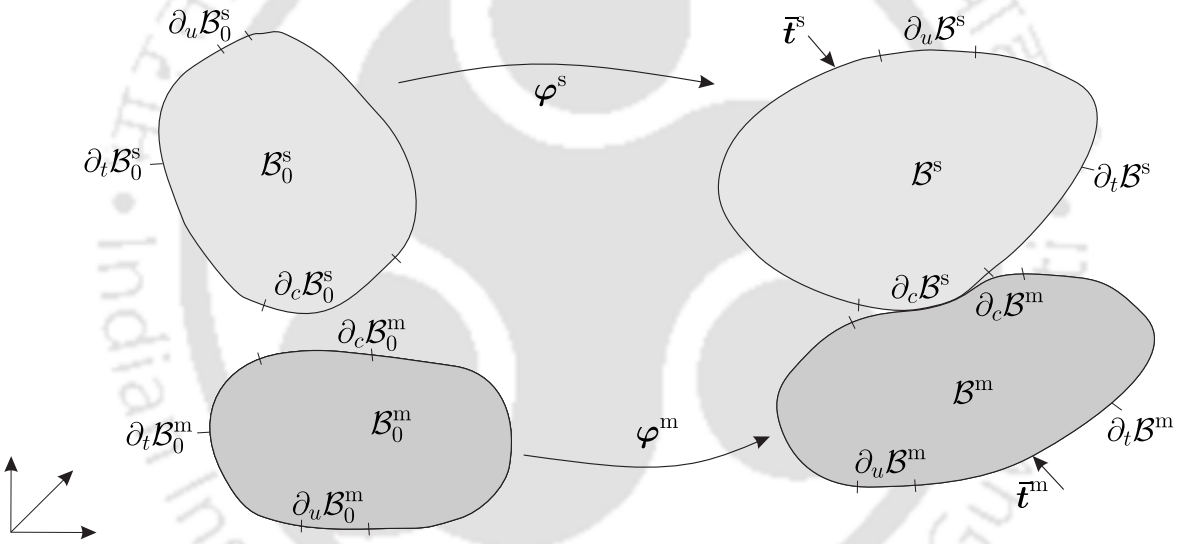

Figure 3.2: Kinematics and basic notations in the reference and current configuration of the two contacting bodies.

In order to identify the contact, the closest normal gap between the slave and the master contact surfaces is determined. For this, first, the master surface is parametrized using the convective coordinate vector $\boldsymbol{\xi}_{\mathrm{m}} = (\xi^1_{\mathrm{m}}, \xi^2_{\mathrm{m}})$, see Fig. 3.3, where ξ_m denotes the parametric point computed at the master contact surface. Also, $\Gamma^{\mathrm{m}}_{\mathrm{c}}$ represents the parametrized master contact surface. A contact point $\boldsymbol{x}^{\mathrm{m}} \in \Gamma^{\mathrm{m}}_{\mathrm{c}}$ on the master surface is defined by the parametric coordinates $\boldsymbol{\xi}_{\mathrm{m}}$ as $\boldsymbol{x}^{\mathrm{m}}(\boldsymbol{\xi}_{\mathrm{m}})$. The covariant tangent vectors at $\boldsymbol{\xi}_{\mathrm{m}}$ are defined by

$$\boldsymbol{\tau}_\alpha = \frac{\partial \boldsymbol{x}^{\mathrm{m}}}{\partial \xi^\alpha_{\mathrm{m}}} = \boldsymbol{x}^{\mathrm{m}}_{,\alpha}\,, \qquad \alpha = 1, 2\,. \tag{3.41}$$

The contravariant tangent vectors can be obtained directly using the following relation

$$\boldsymbol{\tau}^{\alpha} = m^{\alpha\beta}\,\boldsymbol{\tau}_{\alpha}\,, \tag{3.42}$$

where $m^{\alpha\beta} = [m_{\alpha\beta}]^{-1}$ is the component of the inverse of the metric tensor that is defined by $m_{\alpha\beta} = \boldsymbol{\tau}_{\alpha} \cdot \boldsymbol{\tau}_{\beta}$. The outward unit normal vector to the master surface at a parametric point $\boldsymbol{x}^{\mathrm{m}}(\boldsymbol{\xi}_{\mathrm{m}})$ is given by

$$\boldsymbol{n} = \frac{\boldsymbol{\tau}_1 \times \boldsymbol{\tau}_2}{||\boldsymbol{\tau}_1 \times \boldsymbol{\tau}_2||}\,. \tag{3.43}$$

The component of the curvature tensor is defined as $k_{\alpha\beta} = \boldsymbol{\tau}_{\alpha,\beta} \cdot \boldsymbol{n}$.

Next, the procedure to compute the closest projection point is summarized.

Closest projection point procedure

In order to distinguish whether the contact between the two bodies is active or not, the closest normal gap function between the points on the contact surfaces needs to be determined. However, the location of a point $\boldsymbol{x}^{\mathrm{m}}$ on the master contact surface $\Gamma_{\mathrm{c}}^{\mathrm{m}}$ corresponding to a given (fixed) point $\boldsymbol{x}^{\mathrm{s}} \in \Gamma_{\mathrm{c}}^{\mathrm{s}}$ is not known *a priori* in the current configuration. For the determination of $\boldsymbol{x}^{\mathrm{m}}$ on the master surface, a distance function

$$\hat{d}(\boldsymbol{\xi}_{\mathrm{m}}) := ||\boldsymbol{x}^{\mathrm{s}} - \boldsymbol{x}^{\mathrm{m}}(\boldsymbol{\xi}_{\mathrm{m}})|| \tag{3.44}$$

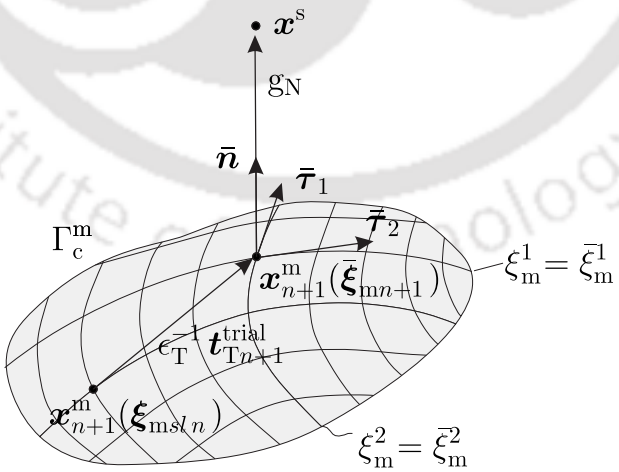

Figure 3.3: A schematic illustration of the three-dimensional frictional contact quantities for a given slave point $\boldsymbol{x}^{\mathrm{s}}$. The master contact surface Γ_{c}^{m} is parametrized by the coordinates ξ^i. The quantities computed at the projection point $\bar{\boldsymbol{\xi}}_{\mathrm{m}}$ are denoted with bar.

is introduced. With this, the gap between a slave point $\boldsymbol{x}^{\mathrm{s}} \in \Gamma_{\mathrm{c}}^{\mathrm{s}}$ and an arbitrary point $\boldsymbol{x}^{\mathrm{m}}(\boldsymbol{\xi}_{\mathrm{m}}) \in \Gamma_{\mathrm{c}}^{\mathrm{m}}$ can be computed. The necessary condition that yields the closest contact point onto the master surface corresponding to a slave point is obtained by the minimum of the distance function

$$\frac{d}{d\xi_{\mathrm{m}}^{\alpha}}\,\hat{d}(\boldsymbol{\xi}_{\mathrm{m}}) = [\boldsymbol{x}^{\mathrm{s}} - \boldsymbol{x}^{\mathrm{m}}(\boldsymbol{\xi}_{\mathrm{m}})] \cdot \boldsymbol{\tau}_{\alpha}(\boldsymbol{\xi}_{\mathrm{m}}) = 0\,. \tag{3.45}$$

The above derivative vanishes if the line describing the gap distance between the slave point $\boldsymbol{x}^{\mathrm{s}}$ and master point $\boldsymbol{x}^{\mathrm{m}}(\boldsymbol{\xi}_{\mathrm{m}})$ is orthogonal to the direction of the covariant tangent vector $\boldsymbol{\tau}_{\alpha}$ computed at $\boldsymbol{\xi}_{\mathrm{m}}$. The corresponding parametric point $\bar{\boldsymbol{\xi}}_{\mathrm{m}}$ at which $\frac{d}{d\xi_{\mathrm{m}}^{\alpha}}\,\hat{d}(\bar{\boldsymbol{\xi}}_{\mathrm{m}}) = 0$ is referred as *closest projection point*. Since Eq. (3.45) is nonlinear, an iterative solution method is required to compute the $\bar{\boldsymbol{\xi}}_{\mathrm{m}}$. In the present work, the Newton Raphson (NR) method is used. In the subsequent description, all the quantities computed at the projection point will be denoted with a bar, e.g. $\boldsymbol{x}^{\mathrm{m}}(\bar{\boldsymbol{\xi}}_{\mathrm{m}}) = \bar{\boldsymbol{x}}^{\mathrm{m}}$ and similarly unit normal vector $\boldsymbol{n}$ at $\bar{\boldsymbol{\xi}}_{\mathrm{m}}$ is denoted by $\bar{\boldsymbol{n}}$, as shown in Fig. 3.3.

Normal gap function

Once the projection point $\bar{\boldsymbol{x}}^{\mathrm{m}}$ corresponding to a slave point $\boldsymbol{x}^{\mathrm{s}}$ is defined, the normal gap $\mathrm{g_N}$ can be computed with

$$\mathrm{g_N} = (\boldsymbol{x}^{\mathrm{s}} - \bar{\boldsymbol{x}}^{\mathrm{m}}) \cdot \bar{\boldsymbol{n}}\,, \qquad \forall\, \boldsymbol{x}^{\mathrm{s}} \in \partial\mathcal{B}_{c}^{\mathrm{s}}\,. \tag{3.46}$$

The above expression can also be understood as a directional distance between the points $\boldsymbol{x}^{\mathrm{s}}$ and $\bar{\boldsymbol{x}}^{\mathrm{m}}$. From this expression, it can also be noticed that the deformed or current configuration of contacting bodies is sufficient to describe the gap function. According to the definition given by Eq. (3.46), the gap is regarded as *open*, i.e. $\mathrm{g_N} > 0$, i.e. bodies are not in contact. Conversely, the negative value of gap function specifies that bodies have penetrated each-other. Moreover, the zero value, i.e. $\mathrm{g_N} = 0$ indicates that the bodies are in perfect contact, which is not the case in general. However, for a physically meaningful contact, an essential non-penetration condition between the bodies needs to be incorporated. For this, the gap function defined in Eq. (3.46) is reformulated as

$$\mathrm{g_N} \geq 0\,, \qquad \forall\, \boldsymbol{x}^{\mathrm{s}} \in \partial\mathcal{B}_{c}^{\mathrm{s}}\,. \tag{3.47}$$

In the above expression, the inequality characteristics of the non-penetration condition describe a numerical challenge that has to be dealt with for the formulation of contact problems. In this work, for the regularization of inequality non-penetration constraint, the penalty method is used, which will be discussed in subsection 3.2.4.

Relative tangential velocity

In the tangential direction of the contact, the status between the bodies is characterized based on the two states, namely (*i*) *the stick state*, and (*ii*) *the slip state*. The first one occurs when a contact point on one body does not have any tangential movement with respect to the corresponding point of another body over time. Conversely, in the second, i.e. slip (or sliding) state, the point of interest moves in the tangential direction over the contact surface relative to another point.

To describe the change in the contact state of the slave point $\boldsymbol{x}^{\mathrm{s}} \in \Gamma_{\mathrm{c}}^{\mathrm{s}}$ relative to its closet projection point $\bar{\boldsymbol{x}}^{\mathrm{m}} \in \Gamma_{\mathrm{c}}^{\mathrm{m}}$ with time, another essential kinematic quantity, referred as relative tangential velocity function $\dot{\mathbf{g}}_{\mathrm{T}}$, is introduced. Considering the perfect contact, the relative tangential velocity is defined as

$$\dot{\mathbf{g}}_{\mathrm{T}} := (\dot{\boldsymbol{x}}^{\mathrm{s}} - \dot{\bar{\boldsymbol{x}}}^{\mathrm{m}}) = \dot{\bar{\xi}}_{\mathrm{m}}^{\alpha}\, \bar{\boldsymbol{\tau}}_{\alpha}\,. \tag{3.48}$$

The unknown time derivative of the convective parametric coordinates $\bar{\boldsymbol{\xi}}_{\mathrm{m}}$ can be computed by taking the time derivative of the relation given by Eq. (3.45), which leads to

$$\dot{\bar{\xi}}_{\mathrm{m}}^{\alpha} = (\bar{m}_{\alpha\beta} + \mathrm{g_N}\, \bar{k}_{\alpha\beta})^{-1} \left[(\boldsymbol{x}^{\mathrm{s}} - \bar{\boldsymbol{x}}^{\mathrm{m}}) \cdot \bar{\boldsymbol{\tau}}_{\beta} - \mathrm{g_N}\, \bar{\boldsymbol{n}} \cdot \dot{\bar{\boldsymbol{x}}}^{\mathrm{m}}_{,\beta}\right]. \tag{3.49}$$

Here, $\bar{m}_{\alpha\beta}$ and $\bar{k}_{\alpha\beta}$ are the components of metric tensor and curvature tensors, respectively, defined in the above discussion.

In case of stick state, no relative tangential motion between the slave and master contact points occurs with time. It means that the convective parametric coordinate values, obtained with the closest projection point, do not move during motion, i.e. $\dot{\bar{\boldsymbol{\xi}}}_{\mathrm{m}} = (\dot{\bar{\xi}}^{1}_{\mathrm{m}}, \dot{\bar{\xi}}^{2}_{\mathrm{m}}) = \mathbf{0}$. Thus, the stick state condition can be formulated as

$$\dot{\mathbf{g}}_{\mathrm{T}} = \mathbf{0} \;\Leftrightarrow\; \mathbf{g}_{\mathrm{T}} = \mathbf{0}\,, \tag{3.50}$$

Since the sticking condition described by Eq. (3.50) is obtained in the current configuration of contact bodies, it imposes a geometrical nonlinear constraint on the motion

along the contact interface in general. For its regularization, the penalty method is used, which will be discussed in subsection 3.2.4.

On the other hand, in case of a slip, the convective parametric coordinate $\bar{\boldsymbol{\xi}}_{\mathrm{m}}$ of the projection point changes its value over the master surface with time. The incremental expression of the infinitesimal tangential relative sliding is given as

$$\mathrm{d}\mathbf{g}_{\mathrm{T}} \;=\; \dot{\mathbf{g}}_{\mathrm{T}}\,\mathrm{d}t \;=\; \dot{\bar{\xi}}^{\alpha}_{\mathrm{m}}\,\bar{\boldsymbol{\tau}}_{\alpha}\,\mathrm{d}t\,. \tag{3.51}$$

The above equation describes that unlike the normal and tangential stick cases, the current geometry is not sufficient to determine the kinematics in the tangential direction. It additionally involves tracking the geometry with time. It is noted that the time can be regarded as the fictitious parameter in the case of (quasi-)static analysis.

3.2.2 Balance equations for contact

In case of active contact between the bodies, the resulting contact traction vector $\boldsymbol{t}_{\mathrm{c}}$ acting at a point $\boldsymbol{x}^{\mathrm{s}} \in \partial_c\mathcal{B}^{\mathrm{s}}$ can be decomposed along the normal and tangent vectors computed at the master projection point $\bar{\boldsymbol{\xi}}_{\mathrm{m}} \in \Gamma^{\mathrm{m}}_{\mathrm{c}}$ as

$$\boldsymbol{t}_{\mathrm{c}} = \boldsymbol{t}_{\mathrm{N}} - \boldsymbol{t}_{\mathrm{T}}\,. \tag{3.52}$$

In the above equation, the sign convention used by Laursen [18] is followed. The normal part of the contact traction vector is defined as

$$\boldsymbol{t}_{\mathrm{N}} = (\boldsymbol{t}_{\mathrm{c}}\cdot\bar{\boldsymbol{n}})\,\bar{\boldsymbol{n}} = (\bar{\boldsymbol{n}}\otimes\bar{\boldsymbol{n}})\,\boldsymbol{t}_{\mathrm{c}}\,, \tag{3.53}$$

and the magnitude is given by $t_{\mathrm{N}} = \boldsymbol{t}_{\mathrm{c}}\cdot\bar{\boldsymbol{n}}$. With this, $\boldsymbol{t}_{\mathrm{N}}$ can be expressed as

$$\boldsymbol{t}_{\mathrm{N}} = t_{\mathrm{N}}\,\bar{\boldsymbol{n}}\,. \tag{3.54}$$

Moreover, the tangential component of the contact traction vector can be given as

$$\boldsymbol{t}_{\mathrm{T}} = t^{\alpha}_{\mathrm{T}}\,\bar{\boldsymbol{\tau}}_{\alpha}\,, \tag{3.55}$$

where the contravariant component of tangential vector is defined as $t^{\alpha}_{\mathrm{T}} = \boldsymbol{t}_{\mathrm{c}}\cdot\bar{\boldsymbol{\tau}}^{\alpha}$. The contravariant tangent vector $\bar{\boldsymbol{\tau}}^{\alpha}$ can be computed using Eq. (3.42).

Using Eqs. (3.54) and (3.55), the contact traction vector defined in Eq. (3.52) can be expressed as

$$\boldsymbol{t}_{\mathrm{c}} = t_{\mathrm{N}}\,\bar{\boldsymbol{n}} - t_{\mathrm{T}}^{\alpha}\,\bar{\boldsymbol{\tau}}_{\alpha}\,, \tag{3.56}$$

In the above expression, the normal component of contact traction $t_{\mathrm{N}} < 0$ corresponds to the compression at $\boldsymbol{x}^{\mathrm{s}}$. However, the tangential component in its covariant bases can have arbitrary sign depending upon the sliding direction. But, it vanishes in case of frictionless contact, i.e. $t_{\mathrm{T}}^{\alpha} = 0$.

Furthermore, the contact traction vector $\boldsymbol{t}_{\mathrm{c}}$ acting at the contact interface (in deformed configuration) obeys the Newton's third law of motion, i.e.

$$\boldsymbol{t}_{\mathrm{c}}(\bar{\boldsymbol{\xi}}_{\mathrm{m}}) = -\boldsymbol{t}_{\mathrm{c}}\,. \tag{3.57}$$

Consequently, it follows that

$$t_{\mathrm{N}}(\bar{\boldsymbol{\xi}}_{\mathrm{m}}) = t_{\mathrm{N}}\,, \tag{3.58}$$

and

$$\boldsymbol{t}_{\mathrm{T}}(\bar{\boldsymbol{\xi}}_{\mathrm{m}}) = -\boldsymbol{t}_{\mathrm{T}}\,. \tag{3.59}$$

Equation (3.58) is referred to as the local contact equilibrium condition, which describes that the normal contact traction is exactly transferred from the slave to the master surface.

3.2.3 Contact constraint equations

Normal contact conditions

In the normal direction, the two sets of conditions, i.e. (i) if $\mathrm{g}_{\mathrm{N}} = 0$ then $t_{\mathrm{N}} < 0$, and (ii) if $\mathrm{g}_{\mathrm{N}} > 0$ then $t_{\mathrm{N}} = 0$, lead to the following constraint statement

$$\mathrm{g}_{\mathrm{N}} \geq 0\,, \quad t_{\mathrm{N}} \leq 0\,, \quad \mathrm{g}_{\mathrm{N}}\, t_{\mathrm{N}} = 0\,, \qquad \forall\, \boldsymbol{x}^{\mathrm{s}} \in \partial_c \mathcal{B}^{\mathrm{s}}\,. \tag{3.60}$$

These are known as Karush-–Kuhn-–Tucker (KKT) conditions in constrained optimization theory or as Hertz-Signorini-Moreau conditions in the context of contact mechanics [6]. A schematic illustration of these conditions is provided in Fig. 3.4. The first inequality constraint in Eq. $(3.60)_1$ describes the impenetrability contact condition. The second inequality constraint in Eq.$(3.60)_2$ indicates the normal contact traction

can only be compressive at the contact interfaces. The third inequality constraint in Eq.(3.60)$_3$, also known as complementary condition, implies that normal contact traction vanishes if the gap is open, and conversely, is compressive when the normal gap $\mathrm{g_N} = 0$.

From Fig. 3.4, it can be observed that KKT conditions for normal contact lead to the non-smooth relationship between the normal gap and the normal contact traction. Hence, appropriate numerical treatment is required for their regularization and is summarized in the next subsection 3.2.4.

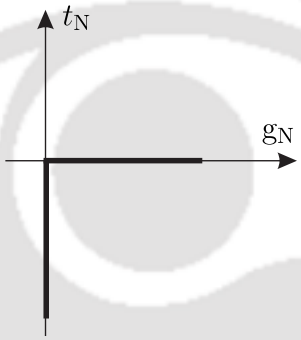

Figure 3.4: Contact conditions in the normal direction.

Tangential contact conditions

In the context of computational contact mechanics, the constitutive equations for Coulomb friction, which is considered in this work, are often formulated in the framework of elasto-plasticity [6]. According to this analogy, the total tangential slip $\mathbf{g}_{\mathrm{T}}$ can be decomposed into an elastic (or stick) part $\mathbf{g}_{\mathrm{T}st}$ and an inelastic (or slip) part $\mathbf{g}_{\mathrm{T}sl}$ as

$$\mathbf{g}_{\mathrm{T}} = \mathbf{g}_{\mathrm{T}st} + \mathbf{g}_{\mathrm{T}sl} \,. \tag{3.61}$$

The tangential stick $\mathbf{g}_{\mathrm{T}\,st}$ as given by Eq. (3.50) is characterized by no relative tangential motion between the surfaces during the frictional contact. With this, the elastic part of the total tangential slip is defined as

$$\mathbf{g}_{\mathrm{T}st} = \mathbf{0} \,. \tag{3.62}$$

The tangential slip $\mathbf{g}_{\mathrm{T}sl}$ is characterized by the sliding of a slave point $\boldsymbol{x}^{\mathrm{s}} \in \partial\mathcal{B}^{\mathrm{s}}_c$ relative to the master surface Γ^{m}_c, which is a dissipative process. The constitutive evo-

lution equation for the inelastic relative tangential slip $\mathbf{g}_{\mathrm{T}sl}$ (accounting the dissipation due to the frictional slip) is expressed as

$$\mathcal{D} = \boldsymbol{t}_{\mathrm{T}} \cdot \mathcal{L}\, \mathbf{g}_{\mathrm{T}sl} \geq 0\,. \tag{3.63}$$

where the Lie derivative of inelastic slip $\mathbf{g}_{\mathrm{T}sl}$ is given by

$$\mathcal{L}\, \mathbf{g}_{\mathrm{T}sl} = \dot{\xi}^{\alpha}_{sl}\, \boldsymbol{\tau}^{sl}_{\alpha}\,, \qquad \text{with} \quad \boldsymbol{\tau}_{\alpha} = \left.\frac{\partial \boldsymbol{x}^{\mathrm{m}}}{\partial \xi^{\alpha}_{\mathrm{m}}}\right|_{\xi_{sl}}\,, \tag{3.64}$$

In the above expression, $\boldsymbol{\tau}^{sl}_{\alpha}$ is the covariant tangent vector computed at the slip parametric point $\xi^{\alpha}_{sl} \in \Gamma^{\mathrm{m}}_{c}$.

Next, an elastic domain $\mathbb{E}$ in the space of tangential contact traction $\mathbf{t}_{\mathrm{T}}$ is considered and is given by

$$\mathbb{E} := \{\boldsymbol{t}_{\mathrm{T}} \in \mathbb{R}^2 \mid \Phi \leq 0\}\,. \tag{3.65}$$

Here, Φ is referred as slip function that accounts the admissible tangential traction (for Coulomb's friction law) $\boldsymbol{t}_{\mathrm{T}}$ satisfying

$$\Phi := ||\boldsymbol{t}_{\mathrm{T}}|| - \mu_f\, \mathrm{t_N} \;\leq 0\,, \tag{3.66}$$

where μ_f is the Coulomb's friction coefficient. The slip function and the contact conditions in the tangential direction for Coulomb's friction law is illustrated in Fig. 3.5. The value $\Phi = 0$ corresponds to a surface in the traction space $(t_{\mathrm{N}}, t_{\mathrm{T}})$.

The evolution of the constitutive equation for the tangential plastic slip can be derived by using the concept of maximum dissipation principle. With this, the constitutive evolution equation for the plastic slip is given by

$$\mathcal{L}\, \mathbf{g}_{\mathrm{T}sl} = \gamma\, \boldsymbol{n}_{\mathrm{T}}\,, \qquad \text{with } \boldsymbol{n}_{\mathrm{T}} := \frac{\partial \Phi}{\partial \boldsymbol{t}_{\mathrm{T}}} = \frac{\boldsymbol{t}_{\mathrm{T}}}{||\boldsymbol{t}_{\mathrm{T}}||}\,, \tag{3.67}$$

which is equivalent to

$$\dot{\mathbf{g}}_{\mathrm{T}sl} = \gamma\, \frac{\boldsymbol{t_T}}{||\mathrm{t}_{\boldsymbol{T}}||}\,. \tag{3.68}$$

Inserting Eq. (3.64), the above equation, as in [77], can be expressed in terms of

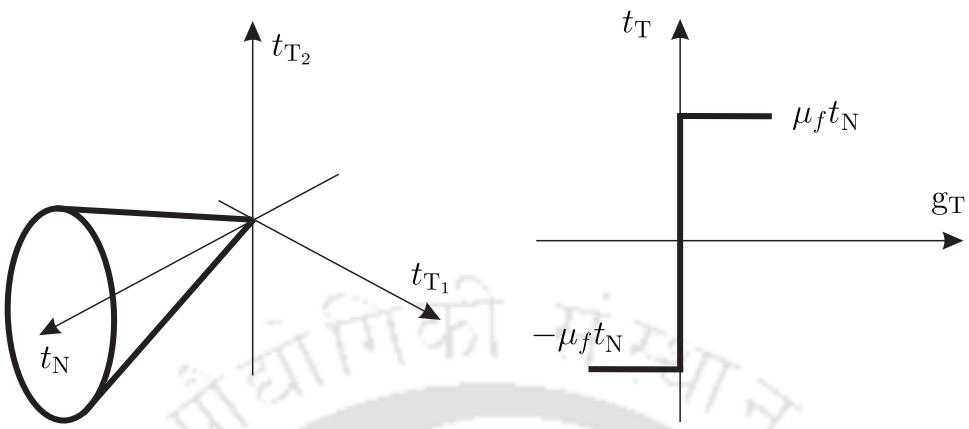

(a) The slip function **(b)** Coulomb's friction law

Figure 3.5: The slip function and KKT conditions in the tangential direction for frictional contact.

the parametric slip coordinates as

$$\dot{\xi}^{\alpha}_{sl} = \gamma \, \boldsymbol{n}_{\mathrm{T}} \cdot \boldsymbol{\tau}^{\alpha}_{sl} \,, \tag{3.69}$$

where $\boldsymbol{\tau}^{\alpha}_{sl}$ is a contravariant tangent vector computed at ξ^{α}_{sl} and γ is the slip parameter.

Using implicit Euler method, the parametric slip coordinate at time step $t = t_{n+1}$ is defined as

$$\xi^{\alpha}_{sl\,n+1} = \xi^{\alpha}_{sl\,n} + \Delta\xi^{\alpha}_{sl\,n+1} \,, \tag{3.70}$$

$$\text{with} \quad \Delta\xi^{\alpha}_{sl\,n+1} \approx \Delta\gamma_{n+1} \, \boldsymbol{n}_{\mathrm{T}\,n+1} \cdot \boldsymbol{\tau}^{\alpha}_{sl\,n+1} \,. \tag{3.71}$$

In the following, all the quantities defined in the current configuration at time step $t = t_{n+1}$ will be denoted with subscript $n+1$. Similarly, all the quantities at the previous time step $t = t_n$ with subscript n.

The slip parameter γ is determined using the following conditions

$$\gamma \geq 0 \,, \quad \Phi \leq 0 \,, \quad \text{and} \quad \gamma \, \Phi = 0 \,, \tag{3.72}$$

which are known as the loading-unloading conditions in KKT form and enables the determination of the plastic parameter γ.

3.2.4 Constraints enforcement method

In this subsection, the penalty method, which is employed in the present work to enforce the normal and tangential contact conditions, described by Eqs. (3.60) and (3.72), respectively, is summarized. For the other methods such as Lagrange multiplier method and Augmented Lagrange multiplier method, the textbook by Wriggers [6] can be referred.

Penalty method

The penalty parameter method is the widely used contact condition enforcement method in practice due to its simple implementation and physical interpretability. The penalty method can, in fact, be interpreted as the insertion of linear spring between the slave and master contact point pair in the normal and tangential directions. With this understanding, the penalty parameter can be seen as the spring stiffness. Thus, the larger value of the penalty parameter will lead to a smaller resultant penetration. The only drawback with the penalty method is that the contact conditions can be fulfilled only in an approximate manner, as it allows a small penetration for the moderate value of the penalty parameter.

The penalty regularized normal contact constraint is defined as

$$\boldsymbol{t}_{\mathrm{N}} = \begin{cases} -\epsilon_{\mathrm{N}}\, \mathrm{g}_{\mathrm{N}}\, \bar{\boldsymbol{n}}, & \text{if } \mathrm{g}_{\mathrm{N}} < 0 \\ \boldsymbol{0}, & \text{otherwise}\,, \end{cases} \tag{3.73}$$

where $\epsilon_{\mathrm{N}} > 0$ denotes the normal penalty parameter. The penalty regularized contact conditions in the normal direction are illustrated in Fig. 3.6a.

Further, during frictional contact, the advancement of the frictional states from the stick to slip is updated based on the predictor-corrector algorithm. With this algorithm, first, the penalty regularized elastic trial step is computed, followed by the trial slip function with [6, 77]

$$\boldsymbol{t}^{\mathrm{trial}}_{\mathrm{T}n+1} = \epsilon_{\mathrm{T}} \left(\boldsymbol{x}^{\mathrm{m}}_{n+1}(\bar{\boldsymbol{\xi}}_{\mathrm{m}\,n+1}) - \boldsymbol{x}^{\mathrm{m}}_{n+1}(\boldsymbol{\xi}_{\mathrm{m}\,sl\,n}) \right), \tag{3.74}$$

$$\Phi^{\mathrm{trial}}_{n+1} = ||\boldsymbol{t}^{\mathrm{trial}}_{\mathrm{T}n+1}|| - \mu_f\, t_{\mathrm{N}n+1}\,. \tag{3.75}$$

Here, $\epsilon_{\mathrm{T}} > 0$ denotes the tangential penalty parameter, $t_{\mathrm{N}} = -\epsilon_{\mathrm{N}}\, \mathrm{g}_{\mathrm{N}}$, and the penalty regularized tangential traction for Coulomb's friction law is shown in Fig. 3.6b. The

expression in the parenthesis is refereed as the elastic part of the slip function. Moreover, $\boldsymbol{x}^{\mathrm{m}}_{n+1}(\bar{\boldsymbol{\xi}}_{\mathrm{m}\,n+1})$ and $\boldsymbol{x}^{\mathrm{m}}_{n+1}(\boldsymbol{\xi}_{\mathrm{m}\,sl\,n})$ are the physical coordinates corresponding to the closest projection point $\bar{\boldsymbol{\xi}}_{\mathrm{m}\,n+1}$ computed at t_{n+1} and tangential slip point $\boldsymbol{\xi}_{\mathrm{m}\,sl\,n}$ computed at t_n, respectively, see Fig. 3.3 for their illustration. According to [6, 77], the tangential traction is determined based on the changes in stick-slip status with

$$\boldsymbol{t}_{\mathrm{T}} = \begin{cases} \boldsymbol{t}^{\mathrm{trial}}_{\mathrm{T}n+1}, & \text{if } \Phi^{\mathrm{trial}}_{n+1} \leq 0\,, \\ \mu_f\, t_{\mathrm{N}n+1}\, \boldsymbol{n}_{\mathrm{T}n+1}, & \text{otherwise}\,. \end{cases} \tag{3.76}$$

where $\boldsymbol{n}_{\mathrm{T}n+1} = \boldsymbol{t}^{\mathrm{trial}}_{\mathrm{T}n+1}/||\boldsymbol{t}^{\mathrm{trial}}_{\mathrm{T}n+1}||$. Finally, using the definition of normal contact traction given by Eq. (3.73) and tangential traction given by Eq. (3.76), the contact traction $\boldsymbol{t}_{\mathrm{c}}$ can be computed using the relation given by Eq. (3.52).

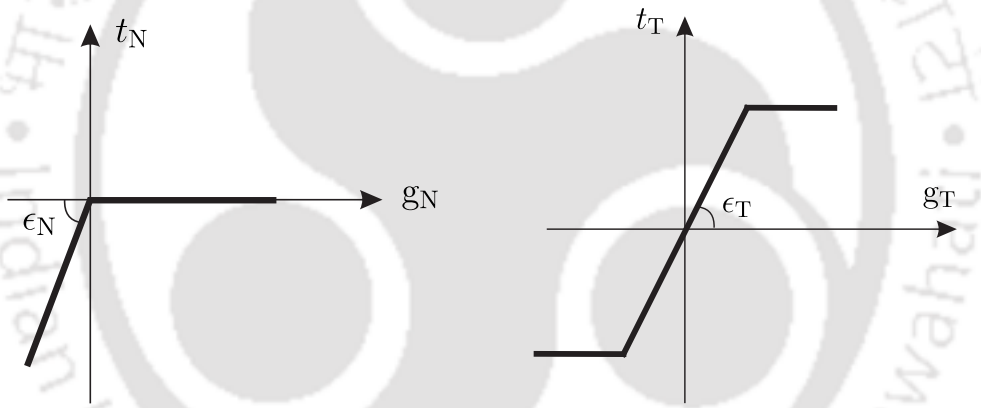

(a) Normal contact **(b)** Tangential contact

Figure 3.6: Penalty regularized (a) normal contact condition, and (b) Coulomb's friction law in the tangential direction.

3.2.5 Contact boundary value problem

This subsection presents the strong formulation, followed by the weak form of the contact boundary problem (CBVP). From the conceptual viewpoint, the CBVP can be seen as adding inequality constraints stemming from the contact conditions into the mechanical BVP.

Strong form of the CBVP

Given the two reference configurations $\mathcal{B}_0^k,\ k=\{s,m\}$, the prescribed displacement $\bar{\boldsymbol{u}}^k$ on $\partial_u\mathcal{B}^k$, traction $\bar{\boldsymbol{t}}^k$ on $\partial_t\mathcal{B}^k$, and body forces $\rho^k\,\bar{\boldsymbol{b}}^k$ in $\mathcal{B}^k$, the objective is to find the displacement field $\boldsymbol{u}^k \in \mathcal{B}^k$, such that at an instance it satisfies the two sets $k=\{s,m\}$ of the following equilibrium equations

$$\begin{aligned} \operatorname{div}\boldsymbol{\sigma}^k + \rho^k\,\bar{\boldsymbol{b}}^k &= \boldsymbol{0} \qquad \text{in} \quad \mathcal{B}^k\,, \\ \boldsymbol{u}^k &= \bar{\boldsymbol{u}}^k \qquad \text{on} \quad \partial_u\mathcal{B}^k\,, \\ \boldsymbol{t}^k = \boldsymbol{\sigma}^k\boldsymbol{n}^k &= \bar{\boldsymbol{t}}^k \qquad \text{on} \quad \partial_t\mathcal{B}^k\,. \end{aligned} \tag{3.77}$$

subjected to contact constraints given by Eqs. (3.60) and (3.72)

$$\mathrm{g_N} \geq 0\,, \quad t_\mathrm{N} \leq 0\,, \quad \mathrm{g_N}\,t_\mathrm{N} = 0\,, \tag{3.78}$$

$$\gamma \geq 0\,, \quad \Phi \leq 0\,, \quad \gamma\,\Phi = 0\,, \tag{3.79}$$

which must hold for all $\boldsymbol{x}_c^\mathrm{s} \in \partial\mathcal{B}^\mathrm{s}$. In the above set of equations, the solution, which is the displacement field $\boldsymbol{u}^k$, imposes the strong C^2-continuity or differentiability requirement at every point of $\mathcal{B}^k$. As is shown in the next section, this requirement can be reduced by taking the weak form of CVBP into account.

Weak form statement of CBVP

The weak form of CVBP can be obtained by multiplying Eq. (3.77), with the test function $\delta\boldsymbol{\varphi}^k$ and performing the integration over the volume of $\mathcal{B}^k$. This results in

$$\delta\mathcal{W} = \sum_k^{s,m}\left(\delta\mathcal{W}_\mathrm{int}^k - \delta\mathcal{W}_\mathrm{ext}^k\right) + \delta\mathcal{W}_\mathrm{c} = 0\,, \qquad \forall\ \delta\boldsymbol{\varphi}^k \in \mathcal{V}^k \tag{3.80}$$

where

$$\delta\mathcal{W}_\mathrm{int}^k = \int_{\mathcal{B}^k} \boldsymbol{\sigma}^k : \operatorname{grad}\left(\delta\boldsymbol{\varphi}^k\right) \mathrm{d}v\,, \tag{3.81}$$

$$\delta\mathcal{W}_\mathrm{ext}^k = \int_{\mathcal{B}^k} \rho^k\,\bar{\boldsymbol{b}}^k \cdot \delta\boldsymbol{\varphi}^k\,\mathrm{d}v + \int_{\partial_t\mathcal{B}^k} \bar{\boldsymbol{t}}^k \cdot \delta\boldsymbol{\varphi}^k\,\mathrm{d}a \tag{3.82}$$

and the virtual work due to contact traction is defined as

$$\delta \mathcal{W}_{\mathrm{c}} = -\int_{\partial_c \mathcal{B}^{\mathrm{s}}} \boldsymbol{t}_{\mathrm{c}} \cdot \delta \boldsymbol{\varphi}^{\mathrm{s}} \, \mathrm{d}a + \int_{\partial_c \mathcal{B}^{\mathrm{s}}} \boldsymbol{t}_{\mathrm{c}} \cdot \delta \boldsymbol{\varphi}^{\mathrm{m}} \, \mathrm{d}a \,, \tag{3.83}$$

where the contact traction $\boldsymbol{t}_{\mathrm{c}}$ is defined in Eq. (3.52) for the normal and tangential contact. As such in Eq. (3.83), the integration of the contact traction is carried over one specific surface, i.e. slave contact surface $\partial_c \mathcal{B}^{\mathrm{s}}$, and the action-reaction principle $\boldsymbol{t}_c^{\mathrm{m}} = -\boldsymbol{t}_c^{\mathrm{m}}$ (see Section 3.2.2) is taken into account. Thus, the contact algorithm based on contact virtual work given by Eq. (3.83) is referred to as "one-pass" [6, 20] or "full-pass" [76, 77], and will be discussed in detail in Section 4.3.

The discussion on the linearization of the internal virtual work $\delta \mathcal{W}_{\mathrm{int}}^k$ and external virtual work $\delta \mathcal{W}_{\mathrm{ext}}^k$ is followed directly from Appendix A.1, except the modification that the superscript k for each quantity associated with $\mathcal{B}^k$ is omitted. It is noted that the linearization of the contact virtual work, i.e. $\delta \mathcal{W}_{\mathrm{c}}$, is presented in Section 4.4.3 and Appendix A.3.

3.3 van der Waals adhesion

In this section, a brief overview of the adhesion formulation is presented in the framework of computation contact mechanics. This formulation is based on the coarse-grained contact model of Sauer and Li [109] and Sauer and Wriggers [117], which uses the Lennard-Jones potential to describe the van der Waals attraction and repulsion between the molecules of two interacting surfaces in the general continuum setting. In this work, it is used to analyze the adhesive contact under the influence of van der Waals interactions.

In order to compute the adhesive traction, the distance between the two interacting surface points is determined. Once the closest projection point $\bar{\boldsymbol{x}}^{\mathrm{m}}$ on the neighboring surface Γ_c^{m} corresponding to a given point $\boldsymbol{x}^{\mathrm{s}}$ is evaluated (using the closest projection procedure given in Section 3.2.1), the distance between the surfaces at $\boldsymbol{x}^{\mathrm{s}}$ can be computed from

$$r(\boldsymbol{x}^{\mathrm{s}}) = ||\boldsymbol{x}^{\mathrm{s}} - \bar{\boldsymbol{x}}^{\mathrm{m}}|| \,. \tag{3.84}$$

According to [50], van der Waals adhesive traction $\boldsymbol{T}_{\mathrm{c}}$ at $\boldsymbol{x}^{\mathrm{s}}$, which can be obtained

from integrating the Lennard-Jones potential four times, is described by the function

$$\boldsymbol{T}_{\mathrm{c}}(\boldsymbol{x}^{\mathrm{s}}) = T_{\mathrm{c}}(r)\,\bar{\boldsymbol{n}} = \frac{A_{\mathrm{H}}}{2\pi r_0^3}\left[\frac{1}{45}\left(\frac{r_0}{r}\right)^9 - \frac{1}{3}\left(\frac{r_0}{r}\right)^3\right], \tag{3.85}$$

where A_{H} denotes the Hamaker's constant, r_0 is the molecular equilibrium spacing for the Lennard-Jones potential, and $\bar{\boldsymbol{n}}$ is the unit normal vector computed at $\bar{\boldsymbol{x}}^{\mathrm{m}}$. Figure 3.7 shows the variation of the adhesive function T_{c} defined in Eq. (3.84) over the distance function r as a solid line. The distance is normalized by the equilibrium distance $r_{\mathrm{eq}} = \sqrt[6]{1/15}r_0$ and the traction is normalized by the minimum traction

$$T_{\mathrm{min}} = T(\tilde{r}) = -\sqrt{5}\frac{A_H}{9\pi r_0^3}, \quad \tilde{r} = \sqrt[6]{3}r_{\mathrm{eq}}\,. \tag{3.86}$$

From Fig. 3.7, it can be seen that the adhesive traction function goes to infinity as the minimum surface distance approaches zero. Thus, the van der Waals adhesive traction function is needs to be regularized for a value below the equilibrium distance, i.e. $r < r_{\mathrm{eq}}$. The expression for the regularized van der Waals traction function, which is shown in Fig. 3.7 as a dotted line, is given by [117]

$$T_{\mathrm{c}}(r) = \begin{cases} T_{\mathrm{c}}(r), & r \geq r_{\mathrm{eq}}\,, \\ T_{\mathrm{c}}(r_{\mathrm{eq}}) + T_{\mathrm{c}}'(r_{\mathrm{eq}})\,(r - r_{\mathrm{eq}}), & r < r_{\mathrm{eq}}\,, \end{cases} \tag{3.87}$$

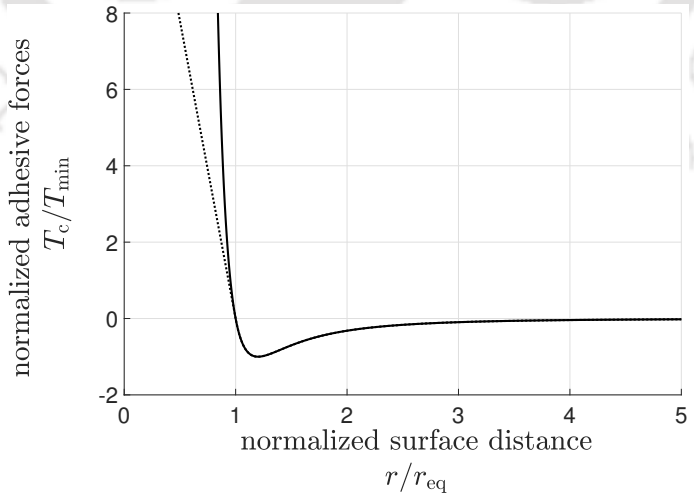

Figure 3.7: Contact forces due to van der Waals adhesion (solid line) and regularized van der Waals adhesion (dotted line).

where the derivative of T_c with respect to surface distance r is defined as

$$T_c'(r) = \frac{\partial T_{\mathrm{c}}(r)}{\partial r} = -\frac{A_{\mathrm{H}}}{2\pi r_0^4}\left[\frac{1}{5}\left(\frac{r_0}{r}\right)^{10} - \left(\frac{r_0}{r}\right)^{4}\right]. \tag{3.88}$$

Since in this work the master contact body is considered as a flat, rigid substrate for adhesive contact numerical examples, virtual work due to adhesive forces at slave point $\boldsymbol{x}^{\mathrm{s}}$ is given as [50]

$$\delta \mathcal{W}_{\mathrm{c}} = -\int_{\partial_c \mathcal{B}_0^{\mathrm{s}}} \boldsymbol{T}_{\mathrm{c}} \cdot \delta \boldsymbol{\varphi} \, \mathrm{d}A \,. \tag{3.89}$$

From the above expression, it can be noticed that the virtual work due to adhesive forces term is written as an integral over the reference configuration of the interacting surface $\partial_c \mathcal{B}_0^{\mathrm{s}}$. This is as per the adhesion formulation of Sauer [50], according to which performing the integration in the reference configuration is highly advantageous. It is noted that the remaining terms in the weak form of adhesive contact problem, i.e. internal and external virtual work, are written as the integrals over the current configuration of the bodies as for CBVP, see Eqs. (3.81) and (3.82).

Chapter 4

Discretization of the Weak Form

In this chapter, the NURBS based discretization of the weak form of the contact boundary value problem, summarized in the previous chapter, is discussed. First, in Section 4.1, the description of the NURBS elements that are used for the discretization of the domain and its corresponding boundary is given. It is followed by the description of the isoparametric concept within the context of IGA (Section 4.2). After that, in Section 4.3, a detailed description of the full-pass isogeometric contact algorithm that is employed in the present work for the incorporation of the contact constraints into the variational form is provided. Later, in Section 4.4, the force equilibrium equations for a two-body contact system are summarized. Finally, in Section 4.5, the linearized system of equilibrium equations is obtained. The isogeometric contact formulation presented herein is based on [6, 29, 53, 66, 76, 77].

It is noted that in the following, the vector and matrices that are associated with the control points of an element are denoted by bold symbols.

4.1 NURBS described elements

As discussed in Chapter 2, with NURBS, the domains $\mathcal{B}_0^k$ and $\mathcal{B}^k$, $k = \{s, m\}$, which are defined in the reference and current configurations, respectively, are discretized in an exact geometric manner with n_{el}^k number of finite size sub-domains: Ω_0^{ke} and Ω^{ke}, as

$$\mathcal{B}_0^k = \bigcup_{e=1}^{n_{\text{el}}^k} \Omega_0^{ke}\,, \qquad \text{and} \quad \mathcal{B}^k = \bigcup_{e=1}^{n_{\text{el}}^k} \Omega^{ke}\,, \tag{4.1}$$

which are referred as *NURBS described (bulk) elements*. In an analogous fashion, it can be shown that with the NURBS discretizations, the overall boundaries $\partial\mathcal{B}_0^k$ and $\partial\mathcal{B}^k$ are also divided into geometrically exact sub-boundaries, i.e. Γ_0^{ke} and Γ^{ke}, which in the following will be referred as the NURBS described *surface elements* or the *boundary face* of the bulk elements.

In each NURBS element, the position of a physical point belonging to the reference configuration $\boldsymbol{X}^{ke}$ is given as

$$\boldsymbol{X}^{ke} = \sum_{A=1}^{n_{\text{cp}}^{ke}} R_A^e(\boldsymbol{\xi}^k)\,\mathbf{X}_A^k = \mathbf{R}^{ke}(\boldsymbol{\xi}^k)\,\mathbf{X}^{ke}\,, \qquad \in\ \Omega_0^{ke}\,, \tag{4.2}$$

and in the current configuration as

$$\boldsymbol{x}^{ke} = \sum_{A=1}^{n_{\text{cp}}^{ke}} R_A^k(\boldsymbol{\xi}^k)\,\mathbf{x}_A^k = \mathbf{R}^{ke}(\boldsymbol{\xi}^k)\,\mathbf{x}^{ke}\,, \qquad \in\ \Omega^{ke}\,, \tag{4.3}$$

where $n_{\text{cp}}^{ke} = \prod_{i=1,2,3}(p_i+1)$ denotes the total number of control points whose corresponding NURBS basis functions $R^k(\boldsymbol{\xi}^k)$ have the local support in the element Ω_0^{ke} or Ω^{ke}. Moreover, in the above equation, $\mathbf{R}^{ke}$ represents the array of NURBS basis functions, and $\mathbf{X}^{ke}$ and $\mathbf{x}^{ke}$ are position vectors of the control points in the reference and current configurations, respectively. These arrays are defined as

$$\mathbf{R}^{ke} = \begin{bmatrix} R_1^k\,\mathbf{I}_d \\ \vdots \\ R_{n_{\text{cp}}^{ke}}^k\,\mathbf{I}_d \end{bmatrix}, \qquad \mathbf{X}^{ke} = \begin{bmatrix} \mathbf{X}_1^k \\ \vdots \\ \mathbf{X}_{n_{\text{cp}}^{ke}}^k \end{bmatrix}, \qquad \text{and} \quad \mathbf{x}^{ke} = \begin{bmatrix} \mathbf{x}_1^k \\ \vdots \\ \mathbf{x}_{n_{\text{cp}}^{ke}}^k \end{bmatrix}. \tag{4.4}$$

where $\mathbf{I}_d$ is the identity matrix of physical dimension d, and the NURBS basis functions for $d=2$ are defined in Eq. (2.13), and for $d=3$ in Eq. (2.14) for the standard NURBS-based discretizations.

4.2 Isoparametric concept

The key idea of the isogeometric analysis technique is that the CAD functions that are used to represent/discretize the given geometry exactly are also utilized as a basis for

the approximation of the solution variables. Thus, using the *isoparametric concept*, the NURBS based approximation of the displacement field $\boldsymbol{u}^{ke}$ in an element Ω^{ke} is given as

$$\boldsymbol{u}^{ke} = \sum_{A=1}^{n_{\rm cp}^{ke}} R_A^k(\boldsymbol{\xi}^k)\, \mathbf{u}_A^k = \mathbf{R}^{ke}(\boldsymbol{\xi}^k)\, \mathbf{u}^{ke}\,, \qquad \mathbf{u}^{ke} = \mathbf{x}^{ke} - \mathbf{X}^{ke}\,, \tag{4.5}$$

where $\mathbf{u}^{ke}$ denotes the displacement vector of control points and is defined as $\mathbf{u}^{ke} = [\boldsymbol{u}_1^k, \ldots, \boldsymbol{u}_{n_{\rm cp}^{ke}}^k]^{\rm T}$.

Using the standard Galerkin approach, the same NURBS functions that are used for the approximation of the displacement field are also utilized for the approximation of the test function, $\delta\boldsymbol{\varphi}^{ke}$, as

$$\delta\boldsymbol{\varphi}^{ke} = \delta\boldsymbol{u}^{ke} = \sum_{A=1}^{n_{\rm cp}^{ke}} R_A^k(\boldsymbol{\xi}^k)\, \delta\mathbf{u}_A^k = \mathbf{R}^{ke}(\boldsymbol{\xi}^k)\, \delta\mathbf{u}^{ke} \quad \in \Omega^{ke}\,. \tag{4.6}$$

The NURBS based approximation of the deformation gradient tensor $\boldsymbol{F}^{ke}$ and its determinant are given as

$$\boldsymbol{F}^{ke} = \boldsymbol{j}^{ke}\,(\boldsymbol{J}^{ke})^{-1}\,, \qquad \text{and} \quad J^{ke} = \det\boldsymbol{F}^{ke} = \frac{\det\boldsymbol{j}^{ke}}{\det\boldsymbol{J}^{ke}}\,, \tag{4.7}$$

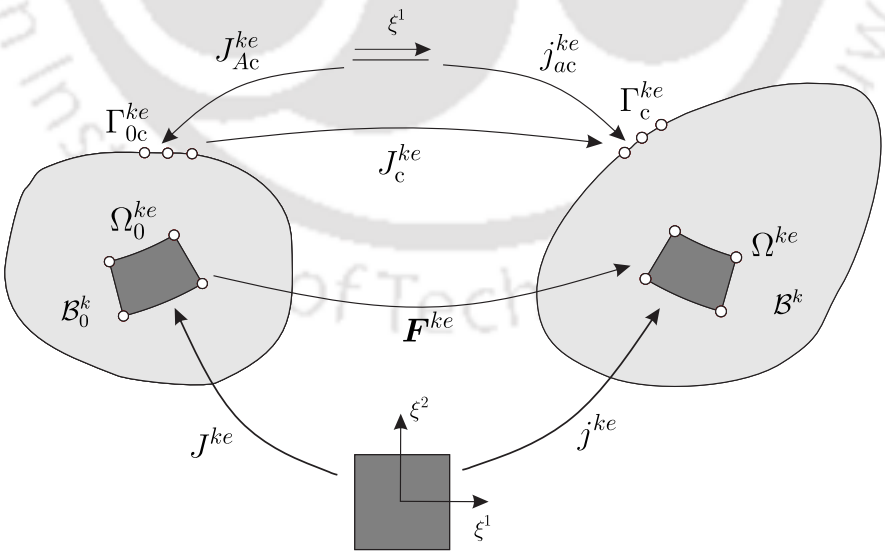

Figure 4.1: Mapping of the bulk and surface elements of the parametric space to the elements of either the reference or current configurations.

where $\boldsymbol{j}^{ke}$ and $\boldsymbol{J}^{ke}$ are denoted as the elemental Jacobians which enable the transformation of a bulk element from the parametric space to the physical space either in the current or the reference configuration, respectively, as shown in Fig. 4.1, and are defined as

$$\boldsymbol{j}^{ke} = \frac{\partial \boldsymbol{x}^{ke}}{\partial \boldsymbol{\xi}^{k}} = \sum_{A=1}^{n_{\text{cp}}^{ke}} \mathbf{x}^{ke} \otimes \frac{\partial R_A^k}{\partial \boldsymbol{\xi}^{k}} \,, \tag{4.8}$$

$$\boldsymbol{J}^{ke} = \frac{\partial \boldsymbol{X}^{ke}}{\partial \boldsymbol{\xi}^{k}} = \sum_{A=1}^{n_{\text{cp}}^{ke}} \mathbf{X}^{ke} \otimes \frac{\partial R_A^k}{\partial \boldsymbol{\xi}^{k}} \,. \tag{4.9}$$

Using the above definition of the elemental Jacobian $\boldsymbol{j}^{ke}$, the partial derivative (or spatial gradient) of the NURBS basis functions in the current configuration is determined with

$$\frac{\partial R_A^k}{\partial \boldsymbol{x}^{k}} = (\boldsymbol{j}^{ke})^{-1} \frac{\partial R_A^k}{\partial \boldsymbol{\xi}^{k}} \,. \tag{4.10}$$

For the brevity, the above equation can be rewritten into the following form

$$\nabla R_A^k = (\boldsymbol{j}^{ke})^{-1} \nabla_\xi R_A^k \,. \tag{4.11}$$

In a similar fashion to the bulk elements, the contact surface of the bulk elements defined in the parametric space are also mapped to the physical space either to the current or reference configuration (see Fig. 4.1), using the contact element Jacobians j_{ac}^{ke} or J_{ac}^{ke} that are defined as (see Sauer and De Lorenzis [77], Eq. (46))

$$j_{ac}^{ke} = \sqrt{\det \bar{m}_{\alpha\beta}} \,, \qquad J_{\text{Ac}}^{ke} = \sqrt{\det \bar{M}_{\alpha\beta}} \,, \qquad J_{\text{c}}^{ke} = \frac{j_{ac}^{ke}}{J_{\text{Ac}}^{ke}} \,, \tag{4.12}$$

where J_{c}^{ke} denotes the stretch of a surface element, which can be visualized from Fig. 4.1.

Furthermore, from Eq. (4.6), the gradient of the test function is given by

$$(\text{grad}\, \delta\boldsymbol{\varphi}^{ke})^{\text{s}} = \nabla^s(\delta\boldsymbol{\varphi}^{ke}) = \frac{1}{2} \sum_{A=1}^{n_{\text{cp}}^{ke}} [\delta \mathbf{u}_A^{ke} \otimes \nabla R_A^k + \nabla R_A^k \otimes \delta \mathbf{u}_A^{ke}] \,. \tag{4.13}$$

Since $\nabla^s(\delta\boldsymbol{\varphi}^{ke})$ is a symmetric second-order tensor, it has six independent components

which can be written using Voigt notation as

$$\nabla^s(\delta\boldsymbol{\varphi}^{ke}) := [\delta\boldsymbol{\varphi}^{ke}_{1,1},\ \delta\boldsymbol{\varphi}^{ke}_{2,2},\ \delta\boldsymbol{\varphi}^{ke}_{3,3},\ 2\delta\boldsymbol{\varphi}^{ke}_{1,2},\ 2\delta\boldsymbol{\varphi}^{ke}_{2,3},\ 2\delta\boldsymbol{\varphi}^{ke}_{3,1}]^{\mathrm{T}}\,. \tag{4.14}$$

With the above definition, Eq. (4.13) can be cast into the following matrix form

$$\nabla^s(\delta\boldsymbol{\varphi}^{ke}) = \mathbf{B}^{ke}\,\delta\mathbf{u}^{ke} \tag{4.15}$$

where

$$\mathbf{B}^{ke} = [\mathbf{B}^k_1, \mathbf{B}^k_2, \ldots, \mathbf{B}^k_{n^{ke}_{\mathrm{cp}}}]\,, \qquad \text{with} \quad \mathbf{B}^k_A = \begin{bmatrix} \frac{\partial R^k_A}{\partial x_1} & 0 & 0 \\ 0 & \frac{\partial R^k_A}{\partial x_2} & 0 \\ 0 & 0 & \frac{\partial R^k_A}{\partial x_3} \\ \frac{\partial R^k_A}{\partial x_2} & \frac{\partial R^k_A}{\partial x_1} & 0 \\ 0 & \frac{\partial R^k_A}{\partial x_3} & \frac{\partial R^k_A}{\partial x_2} \\ \frac{\partial R^k_A}{\partial x_3} & 0 & \frac{\partial R^k_A}{\partial x_1} \end{bmatrix} \tag{4.16}$$

Furthermore, since the Cauchy stress tensor $\boldsymbol{\sigma}^{ke}$ is symmetric, its six independent components can be written using Voigt notation as

$$\boldsymbol{\sigma}^{ke} = [\sigma^k_{11},\ \sigma^k_{22},\ \sigma^k_{33},\ \sigma^k_{12}\,,\sigma^k_{23}\,,\sigma^k_{13}]^{\mathrm{T}}\,. \tag{4.17}$$

4.3 Contact algorithm

In the present work, the classical full-pass version of the two-half pass contact algorithm originally introduced by Sauer and De Lorenzis [77] is utilized for the isogeometric analysis of the contact problems, owing to its simplicity and efficiency features over the existing approaches [6, 20].

The full-pass contact algorithm was first introduced by Fischer and Wriggers [28] for the Lagrange-polynomial based FE analysis of the contact problem. It was later extended by Temizer et al. [30], De Lorenzis et al. [29, 66] and Dimitri et al. [31, 61, 62] for the NURBS based isogeometric analysis of contact problems. Recently, Dimitri et al. [31, 61, 62] further extended this algorithm for T-spline based isogeometric analysis of contact, cohesive zone modeling, and mixed-mode debonding problems. In these works, a number of terminologies have been adopted to denote the classical full-pass approach such as "mortar" in [28], "Knot-to-Surface" in [30], "non-mortar" in [29, 66],

and "Gauss-point-to-surface (GPTS)" in [31, 61, 62]. In the present work, as in [31, 61, 62], this approach is also denoted as GPTS, since within this the contact constraints, i.e. impenetrability in Eq. (3.60) and sticking in Eq. (3.72), are enforced independently at each quadrature point that enables the evaluation of the contact integrals. The GPTS based contact formulation passes the contact patch test within the quadrature error, which ensures the convergence of the solution upon mesh refinement [28, 118]. The only drawback is that the GPTS based contact treatment leads to the over-constrained formulation, as demonstrated in [29, 30, 66]. The over-constraining stems from directly enforcing the contact constraints at too many numbers locations that, as a result, leads to numerical instability, see [9] for the contact cases. Further, with the GPTS approach, oscillatory responses of contact forces are obtained if a large value of the penalty parameter is employed. However, for the examples considered in this work, the value of the penalty parameter, for which the loss of the numerical stability issues becomes significant with the GPTS approach, lay beyond those required to obtain a satisfactory quality solution from the engineering perspective. The values lie within a range where ill-conditioning of the global system matrix related issues still arises. The post-processing smoothing scheme of Sauer [51] can also be used in case of a large value of penalty parameter, as in [31, 61], to alleviate the oscillatory responses of contact forces effectively.

It is noted that the mathematically more sophisticated mortar contact algorithms, e.g. by Temizer et al. [30, 47], De Lorenzis et al. [29, 66], Seitz et al. [69], and Duong et al. [119], that have been introduced for the treatment of contact within the framework of IGA can also be employed. However, the employment of such contact algorithms lay beyond the scope of the present work. Within the mortar contact algorithms, the contact constraints are enforced in a weak sense. As compared to GPTS, these algorithms pass the contact patch test within machine precision and are numerically stable due to their rigorous mathematical background. For an extensive reviews and recent developments on the treatment of contact problems using different mortar methods, the contributions by Popp and Wall [120] and Popp [121] can be referred.

4.4 NURBS based approximation

In this section, the NURBS based approximation/discretization of the weak form of the contact boundary value problem summarized in the previous chapter is presented.

4.4.1 Internal virtual work

Having discretized the domain with n_{el}^k number of NURBS elements, the internal virtual work, defined in Eq. (3.81), can be expressed in terms of its element contributions as

$$\delta \mathcal{W}_{\text{int}}^k = \bigcup_{e=1}^{n_{\text{el}}^k} \int_{\Omega^{ke}} \boldsymbol{\sigma}^{ke} : \text{grad}\,(\delta \boldsymbol{\varphi}^{ke})\, \mathrm{d}\Omega\,. \tag{4.18}$$

Using Eqs. (4.15) and (4.17) in Eq. (4.18) leads to

$$\delta \mathcal{W}_{\text{int}}^{ke} = \bigcup_{e=1}^{n_{\text{el}}^k} (\delta \mathbf{u}^{ke})^{\mathrm{T}} \int_{\Omega^{ke}} (\mathbf{B}^{ke})^{\mathrm{T}} \boldsymbol{\sigma}^{ke}\, \mathrm{d}\Omega\,. \tag{4.19}$$

The elemental internal force vector corresponding to an element, Ω^{ke}, is defined as

$$\mathbf{f}_{\text{int}}^{ke}(\mathbf{u}^{ke}) = \int_{\Omega^{ke}} (\mathbf{B}^{ke})^{\mathrm{T}} \boldsymbol{\sigma}^{ke}\, \mathrm{d}\Omega\,, \tag{4.20}$$

Using Eq. (4.20), the internal virtual work for $\mathcal{B}^k$ can be expressed as

$$\delta \mathcal{W}_{\text{int}}^k = \bigcup_{e=1}^{n_{\text{el}}^k} (\delta \mathbf{u}^{ke})^{\mathrm{T}}\, \mathbf{f}_{\text{int}}^{ke}(\mathbf{u}^{ke}) \;=\; (\delta \mathbf{u}^k)^{\mathrm{T}}\, \mathbf{f}_{\text{int}}^k(\mathbf{u}^k)\,, \tag{4.21}$$

where $\mathbf{f}_{\text{int}}^k$ denotes the global internal force vector of control points for $\mathcal{B}^k$.

4.4.2 External virtual work

By inserting Eq. (4.6) into Eq. (3.82), the external virtual work can be written as

$$\delta \mathcal{W}_{\text{ext}}^k = \bigcup_{e=1}^{n_{\text{el}}^k} (\delta \mathbf{u}^{ke})^{\mathrm{T}} \int_{\Omega^{ke}} \rho^k\, (\mathbf{R}^{ke})^{\mathrm{T}}\, \bar{\boldsymbol{b}}^k\, \mathrm{d}\Omega + \bigcup_{e=1}^{\tilde{n}_{\text{el}}^k} (\delta \mathbf{u}^{ke})^{\mathrm{T}} \int_{\Gamma_t^{ke}} (\mathbf{R}^{ke})^{\mathrm{T}}\, \bar{\boldsymbol{t}}^k\, \mathrm{d}\Gamma \tag{4.22}$$

where $\tilde{n}_{\text{el}}^k$ denote the total number of elements where prescribed traction is applied to the boundary Γ_t^k. The elemental external force vector corresponding to an element Ω^{ke} is given by

$$\mathbf{f}_{\text{ext}}^{ke} = \int_{\Omega^{ke}} \rho^k\, (\mathbf{R}^{ke})^{\mathrm{T}}\, \bar{\boldsymbol{b}}^k\, \mathrm{d}\Omega + \int_{\Gamma_t^{ke}} (\mathbf{R}^{ke})^{\mathrm{T}}\, \bar{\boldsymbol{t}}^k\, \mathrm{d}\Gamma \tag{4.23}$$

In analogous to Eq. (4.21), the external virtual work for $\mathcal{B}^k$ is given by

$$\delta\mathcal{W}^k_{\text{ext}} = \bigcup_{e=1}^{n^k_{\text{el}}+\tilde{n}^k_{\text{el}}} (\delta\mathbf{u}^{ke})^{\mathrm{T}}\,\mathbf{f}^{ke}_{\text{ext}} \;=\; (\delta\mathbf{u}^{k})^{\mathrm{T}}\,\mathbf{f}^{k}_{\text{ext}}\,. \tag{4.24}$$

where $\mathbf{f}^k_{\text{ext}}$ is the global external force vector of control points for $\mathcal{B}^k$.

4.4.3 Contact virtual work

By substituting Eq. (4.6) into Eq. (3.83), the contact virtual work can be defined in terms of its element contributions as

$$\delta\mathcal{W}_{\text{c}} = \bigcup_{e=1}^{n^{\text{s}}_{\text{elc}}} \left(-(\delta\mathbf{u}^{\text{s}e})^{\mathrm{T}} \int_{\Gamma^{se}_c} (\mathbf{R}^{\text{s}e})^{\mathrm{T}}\,\boldsymbol{t}_c\;\mathrm{d}\Gamma + (\delta\mathbf{u}^{\text{m}e})^{\mathrm{T}} \int_{\Gamma^{se}_c} (\mathbf{R}^{\text{m}e})^{\mathrm{T}}\,\boldsymbol{t}_c\;\mathrm{d}\Gamma \right), \tag{4.25}$$

where $n^{\text{s}}_{\text{elc}}$ denotes the total number of the element on the slave contact surface and contact traction vector $\boldsymbol{t}_c$ is given by Eq. (3.56). The elemental contact force vector $\mathbf{f}^{ke}_{\text{c}}$ corresponding to the contact surface Γ^{s}_c are given as

$$\mathbf{f}^{se}_{\text{c}} = -\int_{\Gamma^{se}_c} (\mathbf{R}^{se})^{\mathrm{T}}\,\boldsymbol{t}_c\;\mathrm{d}\Gamma\,, \qquad \mathbf{f}^{\text{m}e}_{\text{c}} = \int_{\Gamma^{se}_c} (\mathbf{R}^{\text{m}e})^{\mathrm{T}}\,\boldsymbol{t}_c\;\mathrm{d}\Gamma\,. \tag{4.26}$$

It is noted that in the above equation the NURBS basis function arrays, i.e. $\mathbf{R}^{se}$ and $\mathbf{R}^{\text{m}e}$ are defined in an analogous manner as to array $\mathbf{R}^{ke}$ in Eq. (4.4) for $\mathcal{B}^k$, with the change that the dimension of the identity matrix reduces to $d-1$ and the NURBS basis functions R^{ke}_A, $A = 1, 2, \cdots, n^{ke}_{\text{cps}}$, are defined for the contact surface of the bulk element, where n^{ke}_{cps} denotes the total number of basis functions having local support in an element Γ^{ke}_c. Using Eq. (4.26), the contact virtual work for $\mathcal{B}^k$ can be written as

$$\delta\mathcal{W}_{\text{c}} = \bigcup_{e=1}^{n^{\text{s}}_{\text{elc}}} \left[(\delta\mathbf{u}^{se})^{\mathrm{T}}\,\mathbf{f}^{se}_{\text{c}} + (\delta\mathbf{u}^{\text{m}e})^{\mathrm{T}}\,\mathbf{f}^{\text{m}e}_{\text{c}} \right], \tag{4.27}$$

and analogous to Eqs.(4.21) and (4.24), Eq. (4.27) can be expressed into the following form

$$\delta\mathcal{W}_{\text{c}} = \bigcup_{e=1}^{n^{\text{s}}_{\text{elc}}} \sum_{k}^{s,m} (\delta\mathbf{u}^{ke})^{\mathrm{T}}\mathbf{f}^{ke}_{\text{c}} \;= \sum_{k}^{s,m} (\delta\mathbf{u}^{k})^{\mathrm{T}}\mathbf{f}^{k}_{\text{c}} \tag{4.28}$$

For adhesive contact problem, the discretized virtual work due to adhesive force can be defined in a similar fashion as discussed above for the contact virtual work. For this case, Eq. (4.6) is substituted into Eq. (3.89) and the elemental adhesive force vector $\mathbf{f}^{se}$ acting on the slave contact surface Γ_{c}^{se} is given as

$$\mathbf{f}_{\mathrm{c}}^{se} = \int_{\Gamma_0^{se}} (\mathbf{R}^{se})^{\mathrm{T}} \boldsymbol{T}_{\mathrm{c}} \, \mathrm{d}\Gamma \tag{4.29}$$

In this work, as such, the master body is considered as the rigid substrate for the adhesive contact problem. Thus, only the contributions with respect to the slave body are accounted.

4.4.4 NURBS discretized weak form of CBVP

Substitution of Eqs. (4.21), (4.24), and (4.28)/(4.29) into Eq. (3.80) yields

$$\sum_{k}^{s,m} (\delta \mathbf{u}^k)^{\mathrm{T}} \left[\mathbf{f}_{\mathrm{int}}^k - \mathbf{f}_{\mathrm{ext}}^k + \mathbf{f}_{\mathrm{c}} \right] = \mathbf{0} \,, \qquad \forall \delta \boldsymbol{u}^k \in \mathcal{V}^k \tag{4.30}$$

The NURBS discretized weak form of the contact boundary value problem can be obtained by summing up contributions from the control points of each $\mathcal{B}^k$ into a global system of *all* control points. This implies

$$(\delta \mathbf{u})^{\mathrm{T}} \left[\mathbf{f}_{\mathrm{int}} - \mathbf{f}_{\mathrm{ext}} + \mathbf{f}_{\mathrm{c}} \right] = \mathbf{0} \,, \tag{4.31}$$

where $\mathbf{f}_{\mathrm{int}}$, $\mathbf{f}_{\mathrm{ext}}$, and $\mathbf{f}_{\mathrm{c}}$ are identified as the global internal force vector, global force vector due to external loads, and global contact force vector, respectively, corresponding to the two-body system. The objective is to find the displacement $\boldsymbol{u}$ of those control points where the virtual displacement $\delta \boldsymbol{u} \in \mathcal{V}$ is arbitrary such that it satisfy the force equilibrium equation, i.e.

$$\mathbf{f}(\mathbf{u}) := \mathbf{f}_{\mathrm{int}}(\mathbf{u}) - \mathbf{f}_{\mathrm{ext}} + \mathbf{f}_{\mathrm{c}}(\mathbf{u}) = \mathbf{0} \,. \tag{4.32}$$

4.5 Solution procedures

In this section, the solution procedures that are used to solve the above-described NURBS discretized weak form of the contact boundary value problem are summarized.

4.5.1 Newton-Raphson method

Due to the non-linear effects such as finite deformations, non-linear constitutive law, and the contact non-linearity, the above derived internal and contact force vectors, which are the functions of displacement $\mathbf{u}$, results in a system of non-linear equations (4.32). Thus, the linearization of the system of non-linear equations is necessary to solve it using the Newton-Raphson method. The Taylor series expansion of Eq. (4.32) at a known value of displacement $\mathbf{u} = \mathbf{u}_j$ (after neglecting the higher-order terms) leads to a linear system of equations, i.e.

$$\mathbf{f}(\mathbf{u}_j + \Delta\mathbf{u}) \approx \mathbf{f}(\mathbf{u}_j) + \frac{\partial \mathbf{f}(\mathbf{u}_j)}{\partial \mathbf{u}_j}\Delta\mathbf{u} = 0 \tag{4.33}$$

It can be solved in an iterative manner for the displacement increment

$$\Delta\mathbf{u} = -[\mathbf{k}(\mathbf{u}_j)]^{-1}\,\mathbf{f}(\mathbf{u}_j) \tag{4.34}$$

with an update $\mathbf{u}_{j+1} = \mathbf{u}_j + \Delta\mathbf{u}$, until the out-of-balance loads on the displacement increment, i.e. $W_j = \mathbf{f}(\mathbf{u}_j) \cdot \Delta\mathbf{u}$, is within a predefined tolerance value, i.e. $W_j < \epsilon_{\text{Tol}}$.

In the present work, the external force vector is considered independent of the displacement $\mathbf{u}$. Therefore, the system tangent matrix is given as

$$\mathbf{k} = \frac{\partial \mathbf{f}}{\partial \mathbf{u}} = \frac{\partial \mathbf{f}_{\text{int}}}{\partial \mathbf{u}} + \frac{\partial \mathbf{f}_{\text{c}}}{\partial \mathbf{u}} = \mathbf{k}_{\text{int}} + \mathbf{k}_{\text{c}} \tag{4.35}$$

where $\mathbf{k}_{\text{int}}$ and $\mathbf{k}_{\text{c}}$ are the global tangent matrices corresponding to the internal and contact forces, respectively. In an analogous fashion to global force vectors appearing in Eq. (4.32), the global internal and contact tangent matrices are obtained from the assembly of their respective elemental contributions. The elemental contributions of the internal tangent matrix, contact tangent matrices, and adhesive contact tangent matrix are referred from Appendix A.2, Appendix A.3, and Appendix A.4, respectively.

4.5.2 Active set strategy

As discussed above, in order to solve the contact problem, the Newton-Raphson (NR) iterative method is utilized. For every NR iteration step, the normal gap between a slave point $\boldsymbol{x}^{\text{s}}(\boldsymbol{\xi}^{\text{s}}) \in \Gamma_c^{\text{s}}$ and its corresponding master contact point $\bar{\boldsymbol{x}}^{\text{m}}(\bar{\boldsymbol{\xi}}^{\text{m}}) \in \Gamma_c^{\text{m}}$ is determined using Eq. (3.46). A slave point $\boldsymbol{x}^{\text{s}}$ is said to be active if normal gap is:

$g_N < 0$. Otherwise, the point is considered as inactive for the normal gap: $g_N \geq 0$. Accordingly, at each contact point $\boldsymbol{x}^s(\boldsymbol{\xi}^s)$, the value of an active set, i.e. $\mathcal{A}_c$, is assigned as

$$\mathcal{A}_c = \begin{cases} 1 & \text{if } g_N < 0\,, \\ 0 & \text{if } g_N \geq 0\,. \end{cases} \tag{4.36}$$

With this, the contact forces and the associated gradients are computed only at the active contact points.

However, during the Newton-Raphson iterations, the consecutive changes in the status of contact points from active to non-active or vice-versa often lead to a phenomena referred to as zig-zagging (Wriggers [6]). It signifies that the solution jumps between two values in the consecutive NR iterations. One possibility to resolve this issue, which is employed in this work, is to temporary freezing the updation of the active-set for a few initial steps of NR iterations until the value of residual out-of-balance loads is smaller, then a certain user-specified tolerance (ϵ_{acts}), see e.g. Box 2 in Chapter 10 of Wriggers [6]. The other more advanced approaches, e.g. refined boundary quadrature by Duong and Sauer [122], which considers the adaptive refinement of the contact boundary during the Newton-Raphson iterations, where the zig-zagging issue is noteworthy, can also be adopted.

4.5.3 Solution algorithm for the contact problem

With the above discussed necessary ingredients, the solution algorithm 1, which gives an overall picture of solving the contact problem, is illustrated below.

Algorithm 1 Solution algorithm for the contact problem.

Define tolerances: ϵ_{TOL} and ϵ_{acts}.
for Loop over prescribed loading **do**
  Apply load: in an incremental form.
  Initial guess: take the active set from the previous load step.
  for Newton-Raphson iterations $j \to j+1$ until convergence **do**
    Start with: an initial guess $\mathbf{u}_j$, i.e. obtained at previous load-step.
    for Loop over n_{el} number of bulk elements Ω^e **do**
      Compute: $\mathbf{f}^e_{\text{int}}$ using (4.20) and $\mathbf{k}^e_{\text{int}} = \mathbf{k}^e_{\text{geo}} + \mathbf{k}^e_{\text{mat}}$ using (A.11, A.13).
      Assemble: $\mathbf{f}^e_{\text{int}} \to \mathbf{f}$ and $\mathbf{k}^e_{\text{int}} \to \mathbf{k}$ into global arrays.
      Compute: $\mathbf{f}^e_{\text{ext}}$ using (4.23).
      Assemble: $\mathbf{f}^e_{\text{ext}} \to \mathbf{f}$ into global force array.
    end for
    for Loop over n_{elc} number of contact surface elements Γ_c **do**
      for Loop over the contact points **do**
        if $W_j < \epsilon_{\text{acts}}$ **then**
          if $\text{g}_{\text{N}} < 0$ **then**
            $\mathcal{A}(\boldsymbol{\xi}) = 1$.
          else if $\text{g}_{\text{N}} \geq 0$ **then**
            $\mathcal{A}(\boldsymbol{\xi}) = 0$.
          end if
        end if
        if $\mathcal{A}(\boldsymbol{\xi}) == 1$ **then**
          Compute: $\mathbf{f}^e_{\text{c}}$ using (4.26) and $\mathbf{k}^e_{\text{c}}$ using (A.15).
          Assemble: $\mathbf{f}^e_{\text{c}} \to \mathbf{f}$ and $\mathbf{k}^e_{\text{c}} \to \mathbf{k}$.
        end if
      end for
    end for
    Apply: prescribed boundary conditions.
    Solve: $\mathbf{k}\,\Delta\mathbf{u} = -\mathbf{f}$.
    Update: $\mathbf{u}_{j+1} = \mathbf{u}_j + \Delta\mathbf{u}$.
    Compute: $W_j = \mathbf{f}(\mathbf{u}_j) \cdot \Delta\mathbf{u}$.
    Check convergence: $W_j < \epsilon_{\text{TOL}}$.
  end for
end for

Chapter 5

Varying Order based NURBS Discretization Method

For contact problems that are primarily dominated by the surface effects, it is highly desirable to increase the accuracy of the contact integrals evaluation. At a fixed mesh, this can be achieved by employing the higher-order functions as a basis for the approximation of the quantities on the contact surface. However, within the existing NURBS based discretization approach, the interpolation order of the NURBS functions used for the discretization of the contact boundary layer and the remaining bulk domain of a contact body can be elevated only in a uniform manner, owing to the rigid tensor product nature of the NURBS structures [21]. With this, the higher-order NURBS that are originally intended for the computations of the contact quantities additionally have to be utilized in the vast (bulk) region of a contact body that is away from the contact surface. From the analysis point of view, usage of such higher-order NURBS discretizations of the contact geometries uniformly is not desirable since a substantial amount of computational cost is associated. Moreover, it dismisses one of the key advantages of IGA, which is its ability to represent the geometry to high-accuracy even with a coarse description. It, thus, becomes desirable to develop an improved method that circumvents the above-described uniform order elevation limitation of a NURBS discretized geometry, and accordingly enhances the performance of the IGA technique within the framework of computational contact mechanics.

In view of the above, in this work, a varying order based NURBS discretization method is proposed. It enables the usage of user-defined higher-order NURBS basis

functions only for the evaluation of the contact integrals, while the minimum order NURBS capable of representing a given contact geometry exactly are employed for the bulk computations. This way, the proposed methodology enables the application of order elevation based refinement in a controlled manner for isogeometric analysis. In the following, first, the theory of the proposed method is detailed for the two-dimensional NURBS constructed geometry. This includes the discussion on the two different discretization procedures, which are used for the higher-continuous or higher-order based NURBS discretization of the contact boundary layer as compared to the lower order NURBS discretization of the bulk domain. Thereafter, in Section 5.2, the extension of the proposed method to three-dimensional NURBS discretized geometry is presented. Finally, in Section 5.4, some remarks on the integration of the proposed method into the standard NURBS-based IGA framework are given to complete its implementation aspect.

5.1 Two-dimensional VO NURBS discretization[1]

The basic concept of the proposed varying order (VO) based NURBS discretization for isogeometric contact analysis is illustrated in Fig. 5.1. Consider a body $\mathcal{B}^k$ having contact boundary layer Γ_c^k. Let p_1 and p_2 be the minimum orders of NURBS functions that are capable of representing the given geometry in an exact manner. The coarse mesh for the geometry is given by the tensor product of open knot vectors $\Xi^1 \times \Xi^2$ defined along the ξ^1 and ξ^2 parametric directions, as shown in Fig. 5.1a. Next, in order to make use of the higher-order NURBS functions for contact computations, the originally p_1 discretized NURBS contact boundary Γ_c^k is replaced with a higher-order $p_c > p_1$ of NURBS layer as shown in Fig. 5.1b. The resultant discretization is accordingly denoted by N_p–N_{p_c}, where N_p ($p = \max(p_1, p_2)$) is the order of NURBS used for the description of bulk domain and N_{p_c} ($p_c > p$) for the contact boundary layer.

5.1.1 Different discretization procedures for contact layer

The new NURBS layer is constructed either using the $k-$refinement or through a combination of $k-$refinement and order-elevation strategies in such a manner that it matches

[1]The presentation in this section is taken from Agrawal and Gautam [123] with slight modifications.

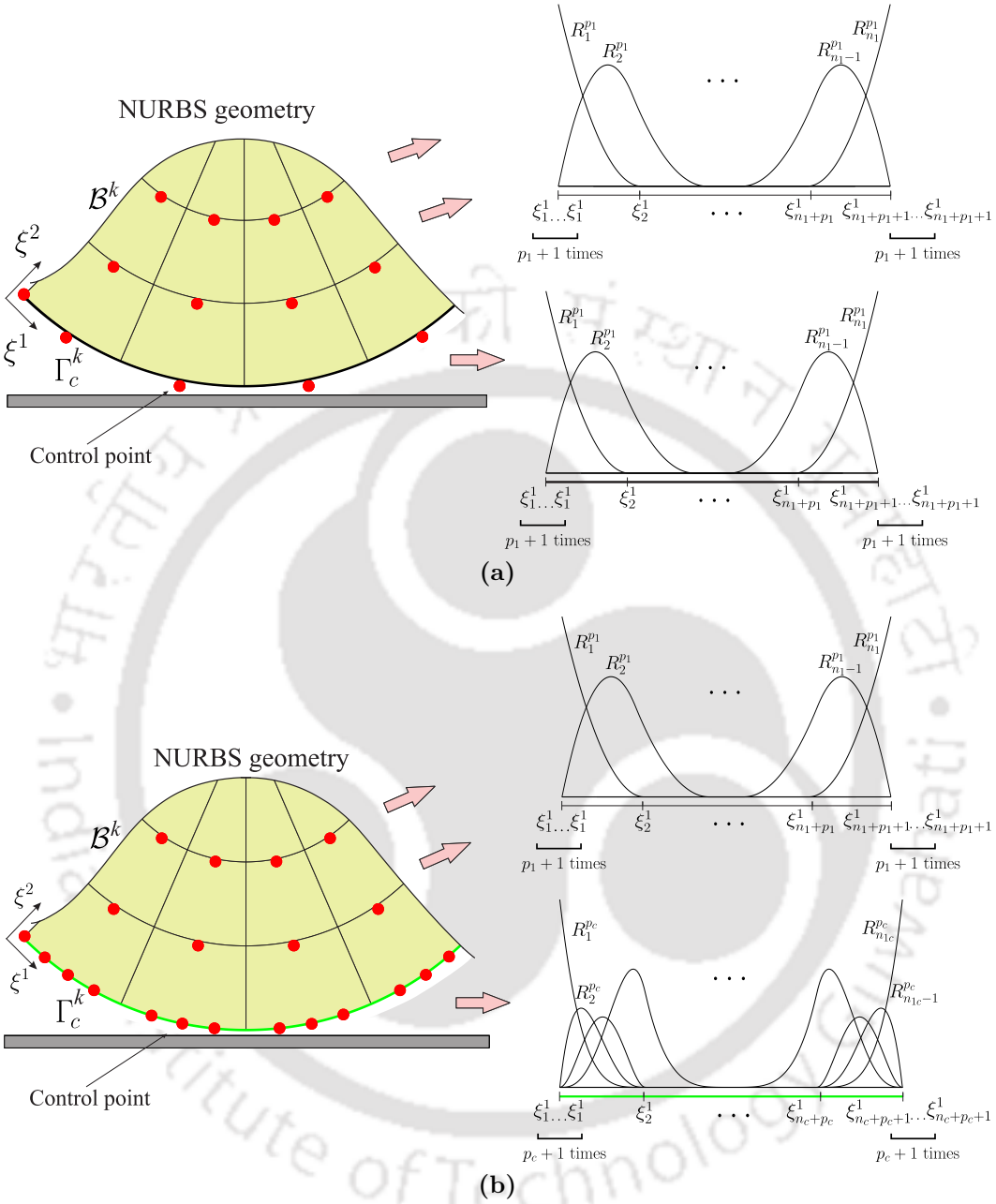

Figure 5.1: A schematic illustration of the VO based NURBS discretization method for a given two-dimensional geometry. (a) Exact representation of the geometry with minimum p_1 and p_2 order of NURBS along the ξ^1 and ξ^2 parametric directions with a very coarse mesh. (b) Representation of the VO NURBS discretized geometry where higher-order NURBS (i.e. $p_c > p_1$) are used for the contact boundary layer, and minimum order NURBS interpolations are used for the remaining bulk domain. The accompanying control points are shown with red dots and the new contact boundary layer with a bold green line. The corresponding basis functions for the contact surface and bulk domain are also shown.

the bulk parametrization, as shown in Fig. 5.1b. The application of the $k-$refinement strategy to the NURBS contact layer increases the inter-element continuity as well as interpolation order of the NURBS functions, see Fig. 5.2. On the other hand, application of one or two additional steps of order-elevation to a $k-$refined NURBS layer introduces a large number of additional control points along the contact boundary layer while the inter-element continuity, i.e. C^{p_c-1}, remains unchanged, see Fig. 5.3. Such resulting higher-continuous and higher-order based NURBS discretization of the contact boundary layer as compared to the lower-order NURBS discretized bulk domain, are denoted by $\mathrm{N}_p-\mathrm{N}_{p_c}$ and $\mathrm{N}_p-\mathrm{N}_{p_c \cdot p_s}$, respectively. Here, the new subscript p_s is the step number of order elevation strategy that is additionally applied to the N_{p_c} order of NURBS contact layer.

Next, to illustrate the difference between the above two strategies used for the discretization of the contact layer, one VO NURBS discretized contact element in Figs. 5.2 and 5.3 is highlighted. As shown in Fig. 5.2, for employing the higher-continuous NURBS for contact computations, the contact boundary layer of an original N_2 discretized example geometry is replaced with a user-defined C^{p_c-1} continuous N_{p_c} NURBS layer, where ($p_c = 3, \text{and } 4$). For a N_{p_c} discretization, $(p_c + 1)$ number of basis functions have local support in a contact element, see right column in Fig. 5.2. Later, in Chapter 7 it is shown that although sufficient continuous basis functions improves the accuracy of the global contact responses in the large deformation contact problems. But, very smooth basis functions are incapable of accurately capturing the sharp changes in the distribution of local contact responses. This is related to the multi knot-span support of the smooth functions, which widens by an additional knot-span on linearly increasing their smoothness, e.g. from C^2 to C^3 as shown in Fig. 5.2. Thus, the much higher-continuous NURBS does not considerably improve the accuracy of the contact responses.

On the contrary, as the basis functions plots show in Fig. 5.3, the application of additional one step of order elevation to the sufficiently C^1 smooth contact layer leads to the shrinking of the multi-knot span support of the basis functions. Further, the knot-span support of the basis functions remains unvaried on applying an additional or second step of order elevation to the contact layer. Such a sufficiently smooth and higher-order NURBS functions with a moderate knot-span support can adequately capture the sudden changes in the local contact responses as shown in Chapter 7. It is also highlighted that although each type of $\mathrm{N}_2-\mathrm{N}_{p_c}$ ($p_c = 3,$ and 4) discretization,

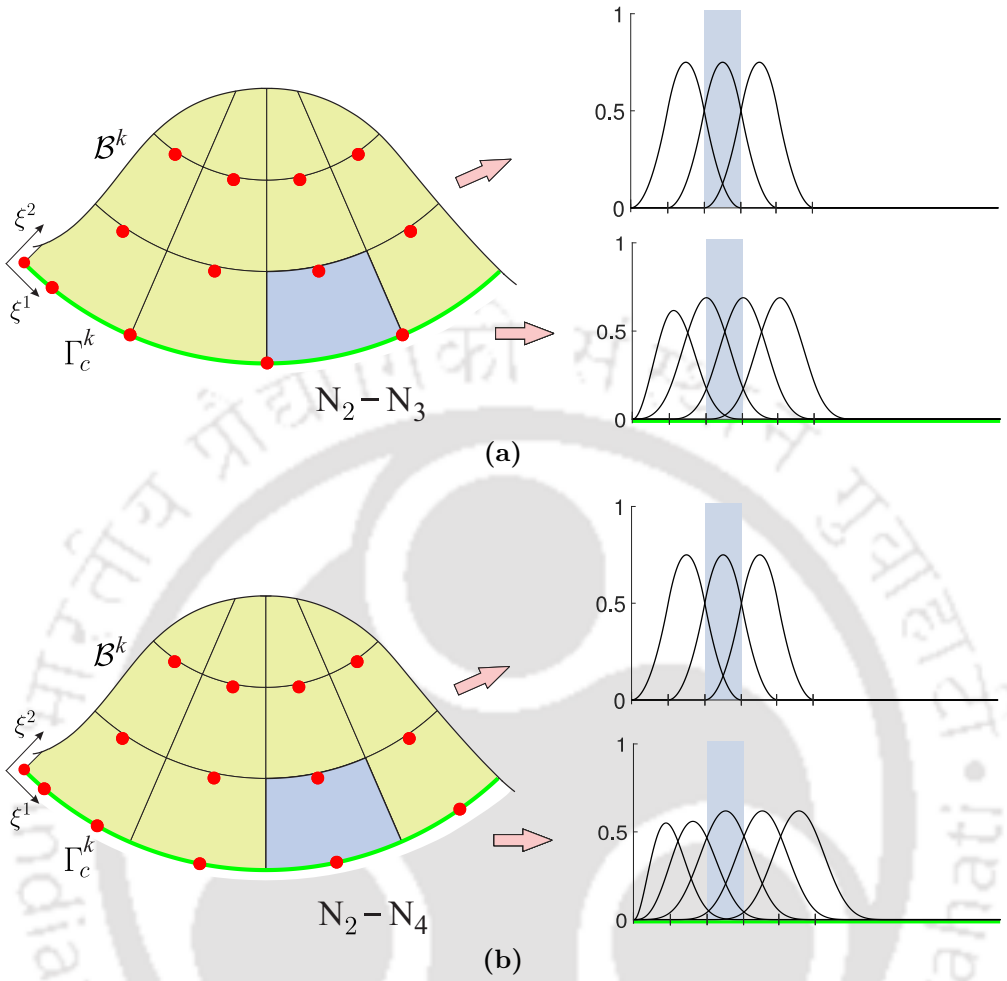

Figure 5.2: VO NURBS based $N_2{-}N_{p_c}$ ($p_c = 3,$ and 4) discretization of an original N_2 discretized geometry. In this arrangement, the $k-$refined contact boundary layer is constructed using the (a) C^2- (with N_3), and (b) C^3-continuous (with N_4) NURBS functions. The basis functions corresponding to the contact boundary and bulk part of a (highlighted) contact element for each $N_2{-}N_{p_c}$ arrangement are shown in the right column.

and its equivalent version $N_2{-}N_{p_c \cdot p_s}$, ($p_c \cdot p_s = 2 \cdot 1,$ and $2 \cdot 2$), respectively, has same (p_c+1) or (p_c+p_s+1) number of non-zero basis functions across the contact boundary of an element. But, the moderate knot-span support of a $N_2{-}N_{p_c \cdot p_s}$ is accompanied by additional large number of overall control points across the contact interface as compared to $N_2{-}N_{p_c}$ discretization, respectively, see Figs. 5.2 and 5.3.

In brief, with the VO based NURBS discretization: (i) the higher-order NURBS basis functions are utilized only for the evaluation of contact contributions or contact integrals in a fully NURBS discretized geometry, (ii) a large number of additional

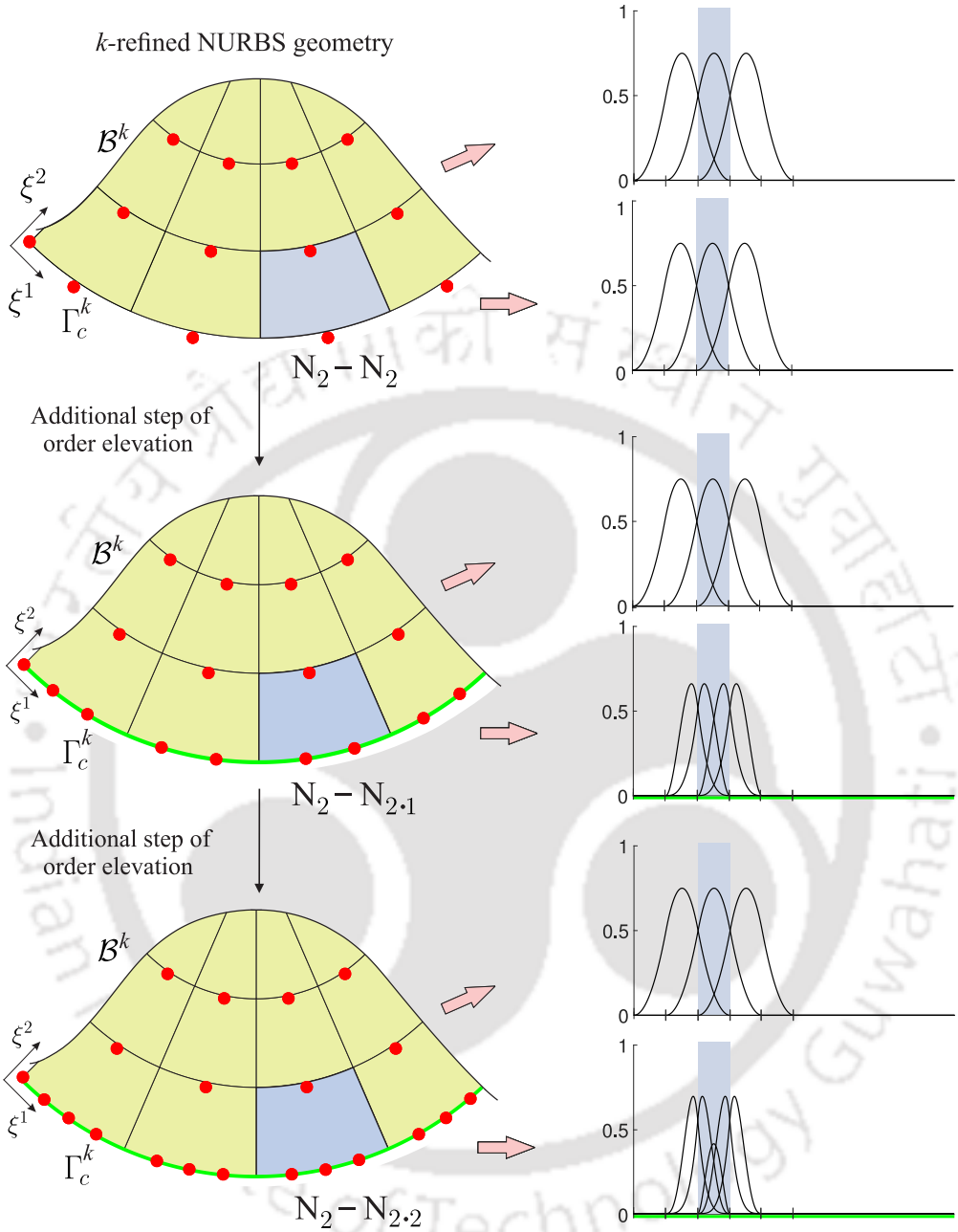

Figure 5.3: VO NURBS based $N_2{-}N_{p_c \cdot p_s}$ discretization of an original N_2 discretized geometry. The applications of the one and two additional steps of order elevation to the contact boundary layer of a $k-$refined $N_2{-}N_2$ NURBS discretized geometry (shown in the first row) are shown in the middle and bottom rows, respectively. The basis functions corresponding to a $N_2{-}N_{2\cdot p_s}$ ($p_s = 1,$ and 2) discretized contact element are shown in the right column.

degrees of freedom are introduced across the contact surface without changing the mesh size, and (*iii*) the minimum order of NURBS capable of representing the given

geometry exactly are employed for the description of the bulk domain that does not come into contact. The resulting VO based NURBS discretized contact element is characterized by $n^e_{cp} = (p_c + 1) + (p_1 + 1) \times p_2$ number of control points, where $p_c + 1$ are present on the contact layer and $(p_1 + 1) \times p_2$ in its remaining part.

5.1.2 Bivariate NURBS functions

The bivariate NURBS basis functions for a VO discretized two-dimensional contact element are defined as

$$\begin{aligned}
R^{p_c,p_2}_1(\xi^1,\xi^2) &:= \frac{w_{11}}{W(\xi^1,\xi^2)} N_{1,p_c}(\xi^1) N_{1,p_2}(\xi^2)\,, \\
&\vdots \qquad\qquad \vdots \\
R^{p_c,p_2}_{p_c+1}(\xi^1,\xi^2) &:= \frac{w_{(p_c+1)1}}{W(\xi^1,\xi^2)} N_{p_c+1,p_c}(\xi^1) N_{1,p_2}(\xi^2)\,, \\
R^{p_1,p_2}_{p_c+2}(\xi^1,\xi^2) &:= \frac{w_{12}}{W(\xi^1,\xi^2)} N_{1,p_1}(\xi^1) N_{2,p_2}(\xi^2)\,, \\
&\vdots \qquad\qquad \vdots \\
R^{p_1,p_2}_{n^e_{cp}}(\xi^1,\xi^2) &:= \frac{w_{(p_1+1)2}}{W(\xi^1,\xi^2)} N_{p_1+1,p_1}(\xi^1) N_{2,p_2}(\xi^2)\,,
\end{aligned} \tag{5.1}$$

where the normalizing weight function is given by

$$W(\xi^1,\xi^2) = \sum_{i=1}^{(p_c+1)} w_{i1} N_{i,p_c}(\xi^1) N_{1,p_2}(\xi^2) + \sum_{i=1}^{(p_1+1)} w_{i2} N_{i,p_1}(\xi^1) N_{2,p_2}(\xi^2)\,. \tag{5.2}$$

The basis functions defined in Eqs. (5.1) exhibit the non-negativity property, i.e.

$$R^{p_c,p_2}_a(\boldsymbol{\xi}) \geq 0 \quad \forall\, \boldsymbol{\xi} \in \Omega^e_c \qquad \text{where } a = 1, 2, \ldots, n^e_{cp}\,, \tag{5.3}$$

and they also satisfy the partition of unity property:

$$\sum_{a=1}^{n^e_{cp}} R^{p_c,p_2}_a(\boldsymbol{\xi}) = 1\,, \qquad \forall\, \boldsymbol{\xi} \in \Omega^e_c\,. \tag{5.4}$$

It is noted that the proposed VO based NURBS discretization approach bears some similarities with the NURBS-enriched contact finite element strategy by Corbett and

Sauer [98] and two-dimensional hybrid isogeometric-finite element based discretization technique by Maleki-Jebeli et al. [101]. The common focus of these strategies is to improve the performance of the Lagrange-polynomial based finite element method in the context of contact mechanics. For this, the intrinsic features of the NURBS polynomials are coupled with the FE based discretizations. The Bézier extraction operator [99] is required to enable the incorporation of NURBS into the FE structure. In contrast, the present work aims to improve the performance of the NURBS-based IGA technique in the context of contact mechanics while fully retaining its original key purpose, i.e. the unified treatment of design and analysis processes by employing the same functions for the analysis that are used for the construction of a geometry exactly. For this purpose, the VO based NURBS discretization method is introduced. This unexplored idea, as initially noted by Temizer et al. [47] presents a possibility to perform the controllable order-elevation based refinements of the NURBS discretized structures. It is highlighted that the proposed discretization method can also be converted to the enrichment strategy of Corbett and Sauer [98] if the linear order NURBS are chosen for the bulk description. This is since the linear order NURBS are equivalent to linear order Lagrange polynomials [53]. However, the proposed method, unlike the enrichment strategy of [98], does not require the Bézier extraction operator.

5.2 Three-dimensional VO NURBS discretization

Next, the extension of the varying order based NURBS discretization for three-dimensional contact geometries is illustrated in Fig. 5.4. Let p_1, p_2, and p_3 are the minimum interpolation order of the NURBS functions that are capable of accurately representing the given three-dimensional CAD geometry exactly. The coarsest mesh is given by the tensor product of the knot vectors defined along the ξ^1, ξ^2, and ξ^3 parametric directions, i.e. $\Xi^1 \times \Xi^2 \times \Xi^3$. As in the two-dimensional case, the original minimum-order of NURBS discretized contact boundary surface, which is defined along the ξ^1 and ξ^2 parametric directions, is replaced with a new higher-order $p_{1c} > p_1$ and $p_{2c} > p_2$ NURBS surface such that it matches the volume parametrization as shown in Fig. 5.4.

In an analogous manner to two-dimensional setup, the new contact boundary surface of three-dimensional geometry can be constructed either using the $k-$refinement or with a combination of $k-$refinement and order elevation based approaches, which as

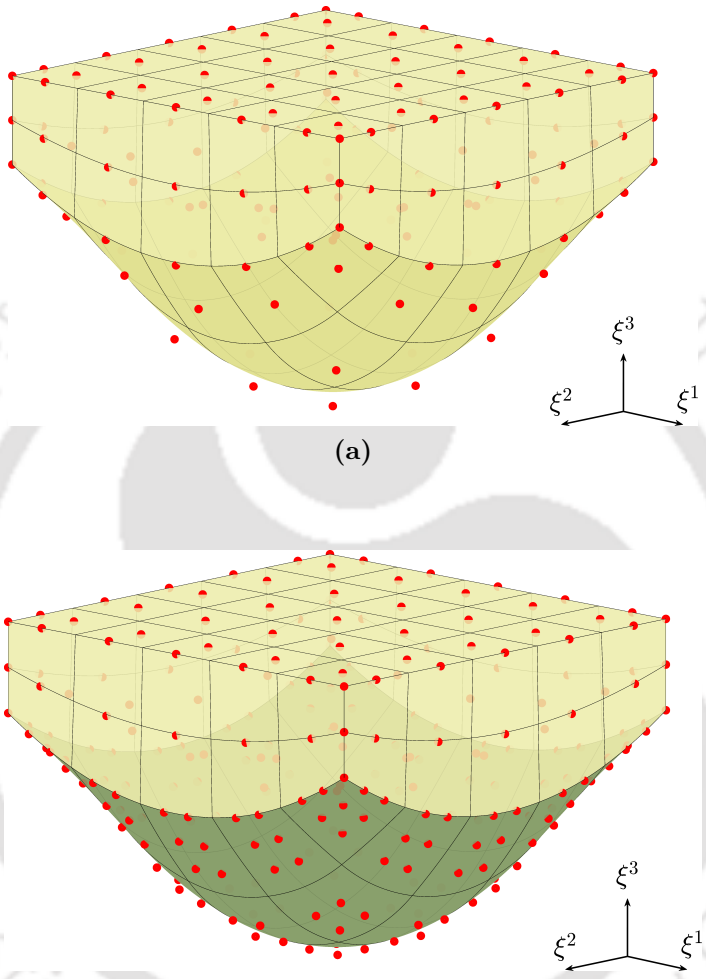

Figure 5.4: Schematic illustration of the VO based NURBS discretization of an example three-dimensional geometry. (a) Exact representation of the geometry with minimum $p_1 = p_2 = 2$ and $p_3 = 1$ order of basis functions along the ξ^1, ξ^2, and ξ^3 parametric directions with a very coarse mesh, where $\Xi^1 = \Xi^2 = [0, 0, 0, 1, 2, 3, 4, 5, 5, 5]$, and $\Xi^3 = [0, 0, 1, 2, 2]$. (b) VO based discretization of the geometry, where the higher-order functions, i.e. $\mathrm{N}_{2\cdot1}$ in each ξ^1 and ξ^2 parametric direction, are used for the description of the contact surface, and minimum N_2 order of functions are used in the remaining volume part.

a result increase the inter-element continuity or interpolation order of NURBS on the contact surface. Thus, such a discretization enables the usage of higher-continuous and higher-order NURBS as basis functions for the computation of the quantities on the contact surface, while the minimum order of NURBS are utilized for the computation of the volume region that does not come into contact.

The trivariate NURBS basis functions for a VO discretized three-dimensional contact element are defined as

$$\begin{aligned}
R_1^{p_{c1},p_{c2},p_3}(\xi^1,\xi^2,\xi^3) &:= \frac{w_{111}}{W(\xi^1,\xi^2,\xi^3)}\, N_{1,p_{c1}}(\xi^1)\, N_{1,p_{c2}}(\xi^2)\, N_{1,p_3}(\xi^3)\,, \\
&\vdots \qquad\qquad \vdots \\
R_{(p_{c1}+1)(p_{c2}+1)}^{p_{c1},p_{c2},p_3}(\xi^1,\xi^2,\xi^3) &:= \frac{w_{(p_{c1}+1)(p_{c2}+1)1}}{W(\xi^1,\xi^2,\xi^3)}\, N_{p_{c1}+1,p_{c1}}(\xi^1)\, N_{p_{c2}+1,p_{c2}}(\xi^2)\, N_{1,p_3}(\xi^3)\,, \\
R_{(p_{c1}+1)(p_{c2}+1)+1}^{p_{c1},p_{c2},p_3}(\xi^1,\xi^2,\xi^3) &:= \frac{w_{112}}{W(\xi^1,\xi^2,\xi^3)}\, N_{1,p_{c1}}(\xi^1)\, N_{1,p_{c2}}(\xi^2)\, N_{2,p_3}(\xi^3)\,, \\
&\vdots \qquad\qquad \vdots \\
R_{n_{cp}^e}^{p_{c1},p_{c2},p_3}(\xi^1,\xi^2,\xi^3) &:= \frac{w_{(p_{c1}+1)(p_{c2}+1)2}}{W(\xi^1,\xi^2,\xi^3)}\, N_{p_{c1}+1,p_{c1}}(\xi^1)\, N_{p_{c2}+1,p_{c2}}(\xi^2)\, N_{2,p_3}(\xi^3)\,,
\end{aligned} \tag{5.5}$$

where $n_{cp}^e = (p_{c1}+1)\times(p_{c2}+1)+(p_1+1)\times(p_2+1)\times p_3$ denotes the total number of basis functions having local support in a VO based NURBS discretized three-dimensional contact element and the normalizing weight function is defined as

$$\begin{aligned}
W(\xi^1,\xi^2,\xi^3) = &\sum_{i=1}^{(p_{c1}+1)}\sum_{j=1}^{(p_{c2}+1)} w_{ij1}\, N_{i,p_{c1}}(\xi^1) N_{j,p_{c2}}(\xi^2) N_{1,p_3}(\xi^3) \\
&+ \sum_{i=1}^{(p_1+1)}\sum_{j=1}^{(p_2+1)} w_{ij2}\, N_{i,p_1}(\xi^1) N_{j,p_2}(\xi^2) N_{2,p_3}(\xi^3)\,.
\end{aligned} \tag{5.6}$$

Following the same argumentation as in Eq. (5.3) and Eq. (5.4), it can be shown that these trivariate functions also exhibit the non-negativity property and form the partition of unity. Since in the present work the case $p_{1c} = p_{2c} = p_c$ is taken in the contact numerical examples (in Chapter 7), the notation used for VO based NURBS discretization of the two-dimensional contact geometry also holds for three-dimensional VO based discretization, i.e. $\mathrm{N}_p{-}\mathrm{N}_{p_c \cdot p_s}$, where N_p is interpolation order of the NURBS used for the discretization of the volume, and N_{p_c} is for the contact surface. Moreover,

the subscript p_s denote the step number of order elevation applied to the N_{p_c} discretized contact surface.

5.3 VO NURBS discretization of the weak form

Using the isoparametric concept, the NURBS functions, which are defined in Eqs. (5.1) and (5.5) for two- and three-dimensional geometries, respectively, are employed for the approximation of the unknown displacement field $\mathbf{u}^e$, its variation $\delta\mathbf{u}^e$, and to determine the current coordinates $\boldsymbol{x}^e$ within each VO based NURBS discretized contact element Ω_{c}^e as

$$\boldsymbol{u}^e = \mathbf{R}^e(\boldsymbol{\xi})\,\mathbf{u}^e\,, \quad \delta\boldsymbol{u}^e = \mathbf{R}^e(\boldsymbol{\xi})\,\delta\mathbf{u}^e\,, \quad \boldsymbol{x}^e = \mathbf{R}^e(\boldsymbol{\xi})\,\mathbf{x}^e \qquad \forall\,\boldsymbol{\xi} \in \Omega_{\mathrm{c}}^e\,. \tag{5.7}$$

Here, the new basis function array $\mathbf{R}(\boldsymbol{\xi})$ is defined in an similar fashion to Eq. $(4.4)_1$, except the modification that now it contains a total $n_{cp}^e = (p_c+1)+(p_1+1)\times p_2$ number of bivariate NURBS functions $R_a^{p_c,p_2}(\boldsymbol{\xi})$ (5.1) or $n_{cp}^e = (p_{c1}+1)\times(p_{c2}+1)+(p_1+1)\times(p_2+1)\times p_3$ number of trivariate NURBS functions $R_a^{p_{c1},p_{c2},p_3}(\boldsymbol{\xi})$ (5.5) having local support in each VO NURBS discretized two- or thee-dimensional contact element Ω_c^e. The array $\mathbf{B}^{ke}$ in Eq. (4.16) containing the derivatives of NURBS functions is also modified according to Eq. (5.7). Moreover, the array $\mathbf{R}^{ke}$ in Eq. (4.26) makes use of higher-order of univariate $R_a^{p_c}(\xi^1)$ or bivariate $R_a^{p_{c1},p_{c2}}(\xi^1,\xi^2)$ NURBS functions for the evaluation of contact integrals in two- or three-dimensional settings, respectively.

5.4 Implementation aspect

For integrating the VO NURBS discretization strategy into the standard NURBS-based isogeometric framework, only a few minor modifications are required. First of all, for a given mesh resolution, a p_c order of NURBS curve or surface representing the contact boundary layer of the initial NURBS described geometry is constructed. After that, the parametrization for an originally p order of NURBS discretized contact layer is replaced with that of the newly constructed p_c order of NURBS curve or surface. For this, a certain number of conditions are need to be fulfilled. The total number of control points defining the geometry must be updated in such a manner that it allows the incorporation of the newly constructed p_c order of the new contact layer. This means that the connectivity array for contact elements must be adapted in a way

that it contains the underlying control points of the VO based discretized geometry. The derived contact element connectivity arrays can have a different length than the bulk element connectivity arrays. The bivariate or trivariate NURBS basis functions defined in Eqs. (5.1) and (5.5) are used for the evaluation of elemental quantities for VO based NURBS described contact elements, while for the evaluation of the contact surface integrals the univariate or bivariate p_c order of NURBS functions are utilized. With the exception of these modifications, no other changes are need to be made in the standard NURBS-based isogeometric framework. The local quantities, e.g. elemental tangent matrices and force vectors, are assembled to their global part in the same way as with the standard procedure. However, new control point connectivity arrays are need to be utilized. In this work, a default $(p_c + 1)$ number of Gauss-Legendre quadrature points in each parametric directions are employed for the evaluation of the contact integrals unless stated otherwise. For the bulk, $(p + 1)$ number of quadrature points along each parametric direction are utilized. Optimal quadrature rules [124–126], which are well-suited for IGA, can also be opted for the reduced numerical evaluation.

Chapter 6

Validation of the Formulation

Based on the NURBS-based isogeometric contact formulation summarized in Chapters 3 and 4, in-house codes to perform the simulation of the contact problems using the IGA technique are developed. In this chapter, the validation of the isogeometric contact formulation and its corresponding implementation is demonstrated by comparing the numerical results obtained with the current work to those reported in the literature. This is to ascertain that there must be no implementation errors, and the developed isogeometric contact formulation is valid for the class of problems of interest. Specifically, the codes are developed to solve the small and large deformation contact problems with or without considering friction between one or two deformable bodies in two- as well as three-dimensional settings using the IGA technique.

6.1 Two-dimensional small deformation contact problem

First, the validity of the implementation is verified for a two-dimensional small deformation contact using the Hertzian contact problem. The setup of the problem, which is taken from Temizer et al. [30], is shown in Fig. 6.1. In this, the contact of an infinitely long cylinder on a rigid surface under the plane strain condition is analyzed. The geometric data, material parameters, normal penalty parameter, and the load value are given in Table 6.1, where UL and UF denote the unit of length and unit of force, respectively. The analytical solution for the current setup is given by the Hertz theory [8]. As per the analytical solution, the contact area radius is $a_c = \sqrt{4pR_o/\pi\hat{E}} = 0.048$ and

the maximum contact pressure is $p_{\max} = 2p/\pi a_c = 0.0264$, where $\hat{E} = E/(1-\nu^2)$ and $p = 2P_o \times R_o$.

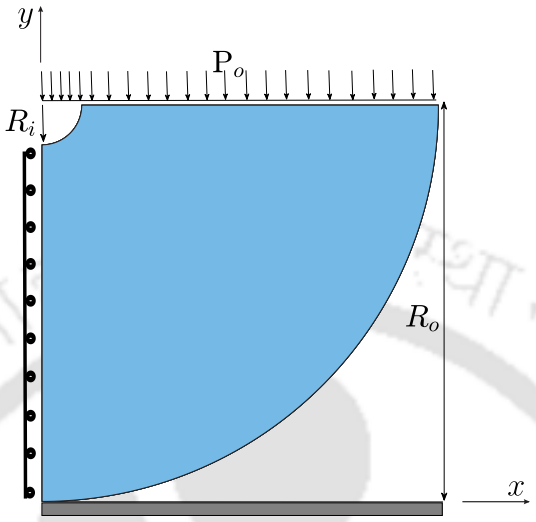

Figure 6.1: The setup of two-dimensional Hertzian contact problem.

R_o (UL)	R_i (UL)	E (UF/UL^2)	ν	ϵ_{N} (UF/UL)	P_o (UF/UL^2)
1	0.1	1	0.3	10^3	1×10^{-3}

Table 6.1: Two-dimensional Hertzian contact: Different parameters used for the analysis.

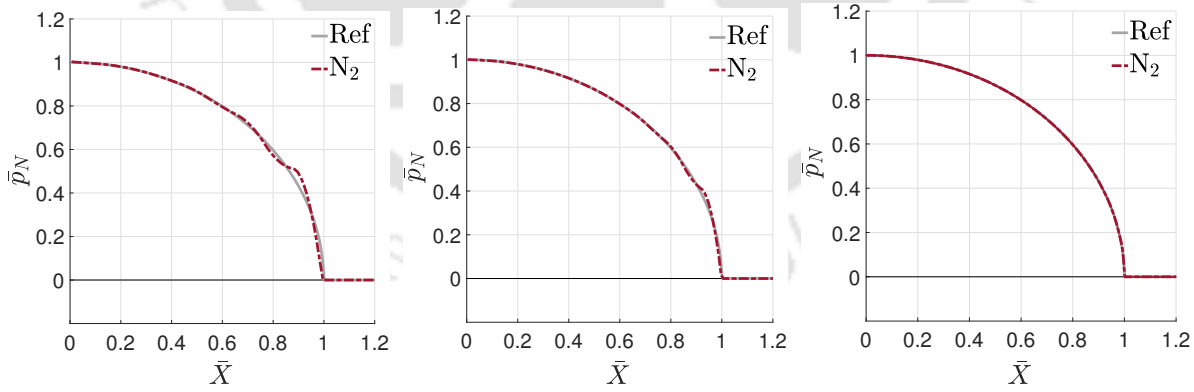

(a) Coarse mesh **(b)** Medium mesh **(c)** Fine mesh

Figure 6.2: Two-dimensional Hertzian contact: Contact pressure distributions with quadratic N_2 order of NURBS discretization at different meshes as compared to the analytical solution.

Figure 6.2 shows the results obtained with N_2 order of NURBS discretization at

different meshes as compared to the analytical solution. The dimensionless normal contact pressure $\bar{p}_N = p_N/p_{\max}$ is plotted over the dimensionless contact coordinate $\bar{X} = x/a_c$, where p_N is the normal contact pressure evaluated at active quadrature points and x is the distance of these points from the first point of contact. Based on the obtained results, it can be observed that at the fine mesh, the normal contact pressure curve nearly matches the analytical solution. Moreover, the distribution of normal stress σ_{yy} corresponding to N_2 with the fine mesh is shown in Fig. 6.3.

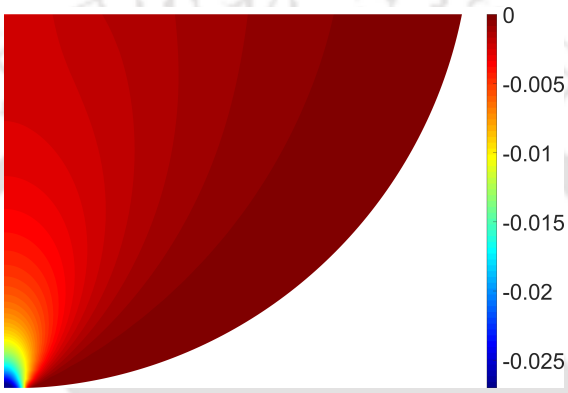

Figure 6.3: Two-dimensional Hertzian contact: Close-up view of the distribution of the normal stress σ_{yy} with the present work.

6.2 Two-dimensional large deformation frictional contact problem between deformable bodies

Next, the validity of the isogeometric contact formulation and its corresponding implementation is verified for the two-dimensional large deformation contact with friction between two deformable bodies using frictional ironing problem. The setup of the problem is taken from De Lorenzis et al. [29]. The simulation parameters that are considered to solve this problem are same as in De Lorenzis et al. [29] (numerical example 6.3). The outer and inner radius of the die are $R_o = 0.5$ UL and $R_i = 0.3$ UL, respectively, and for the slab geometric dimensions are 1.0×3.0 UL^2. The Neo-Hookean material model with material parameters $E_{\text{die}} = 1000$ UF/UL^2, $E_{\text{slab}} = 1$ UF/UL^2 and the Poisson's ratio $\nu_{\text{die}} = \nu_{\text{slab}} = 0.3$ are used. The values of the normal and tangential penalty parameters are $\epsilon_{\text{N}} = \epsilon_{\text{T}} = 10^2$ UF/UL, respectively, and the coefficient of friction is 0.3. The values of the vertical and horizontal displacement fields that applied to

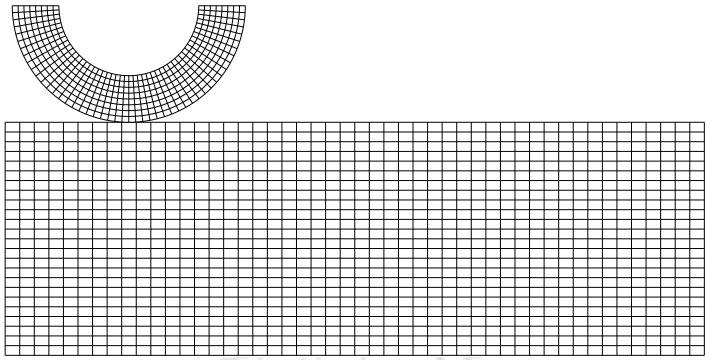

Figure 6.4: Frictional ironing problem: Meshes for the die and slab are 48×8 and 48×24 as in [29].

the top surface of the die are $U_y = -0.075$ UL and $U_x = 2.0$ UL, respectively. Further, the meshes that are taken for the die and slab from [29] are shown in Fig. 6.4.

The results (global variation of the vertical and horizontal contact forces, and their enlarged views) presented by the De Lorenzis et al. [29] are included in the left side, while the results reproduced with the present simulations with N_2 and N_4 order of NURBS discretizations are included in the right side of Fig. 6.5. It is noted that as compared to [29], wherein the mortar contact algorithm is employed, in the present work GPTS contact algorithm is utilized for the treatment of contact constraints. Thus, the marginal difference between the results obtained with the present simulations and those presented by De Lorenzis et al. [29] could be due to the use of different contact algorithms.

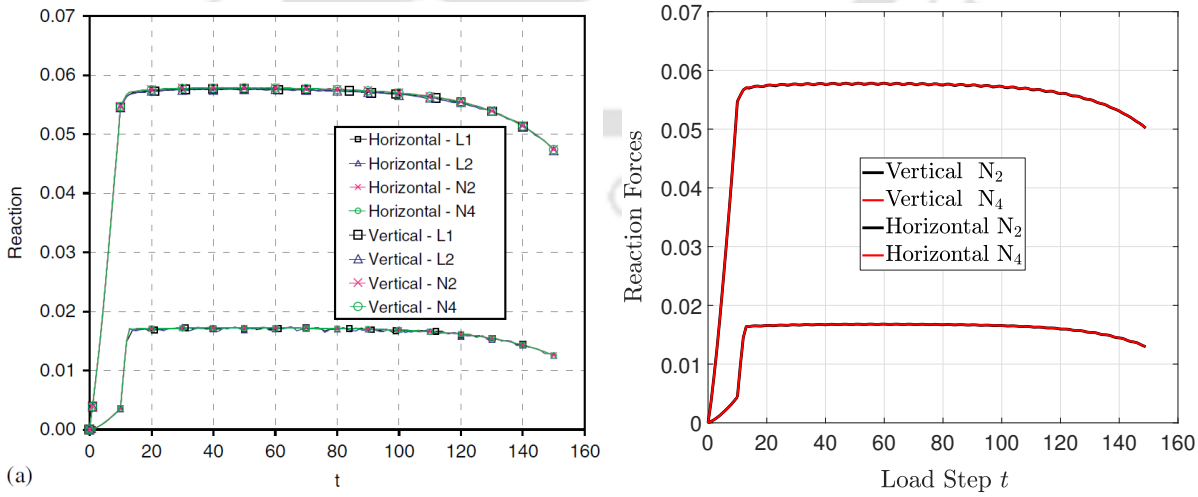

(a) **(b)**

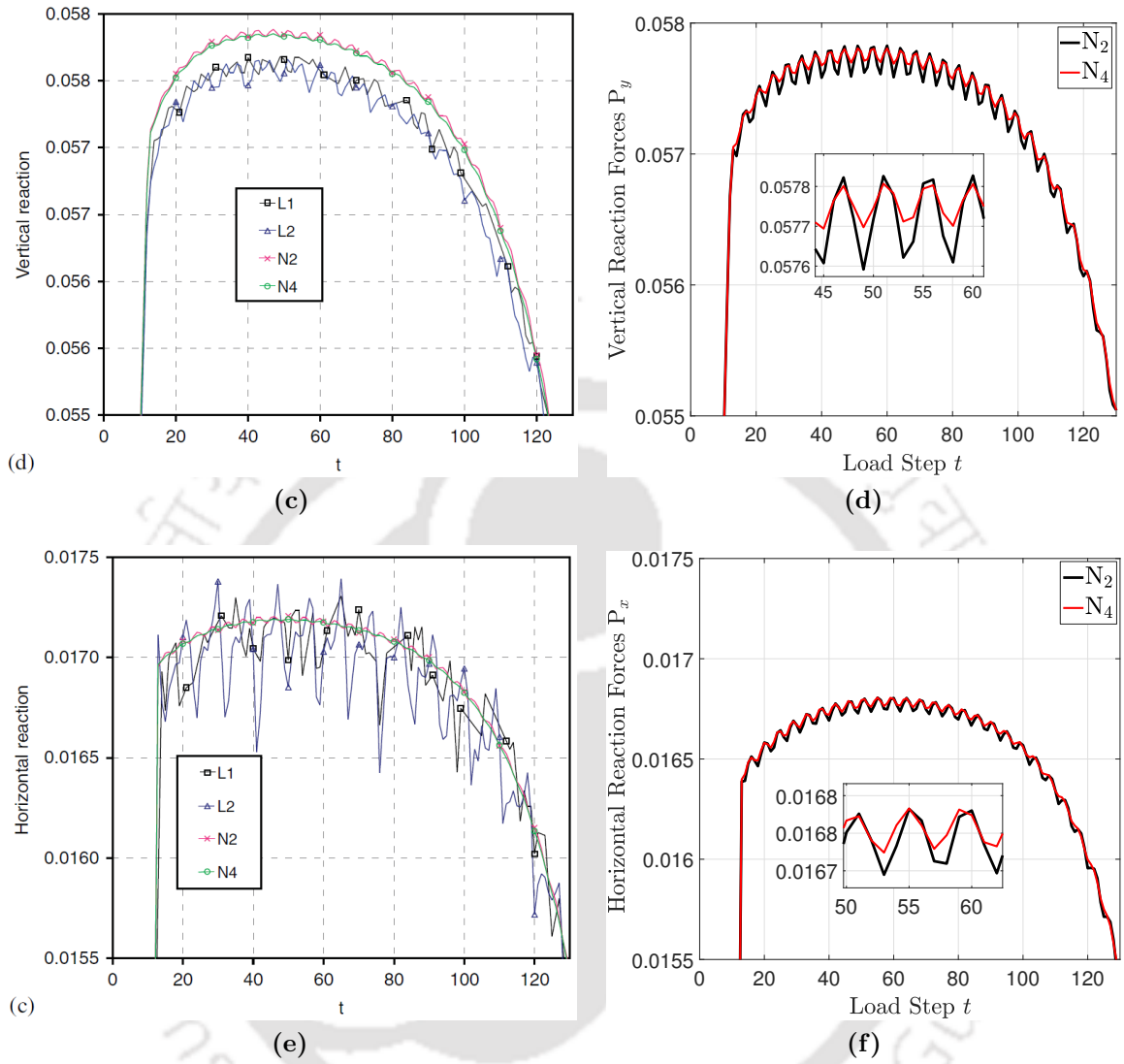

Figure 6.5: Frictional ironing problem: (a)-(b) Comparison of the global variation of the vertical and horizontal contact forces with the present work using N_2 and N_4 based discretizations (right) to the results presented by De Lorenzis et al. [29] (left). (c)-(d) The enlarged view of the vertical contact forces with the present (right) as compared to the results presented by De Lorenzis et al. [29] (left). (e)-(f) The enlarged view of the horizontal contact forces with the present work (right) as compared to the results by De Lorenzis et al. [29] (left). The results from [29] are reprinted with permission.

6.3 Three-dimensional small deformation contact problem

Next, the validity of the implementation is verified for the three-dimensional small deformation contact using the Hertzian contact problem. The setup of the problem is taken from De Lorenzis et al. [66]. In this, one-eighth of the sphere is utilized due to the symmetric boundary conditions, see Fig.6.6a. The overall mesh is redistributed in such a manner that approximately 75% number of elements are located within the 10% of the total length of knot vectors defined in the angular and radial directions as shown in Fig. 6.6b. The geometric data, material parameters, normal penalty parameter, and the load are given in Table 6.2. For the given values, the analytical solution is evaluated using the Hertz theory [8]. From the analytical solution, the radius of circular contact area is obtained as $a_c = \sqrt[3]{3pR_o/4\hat{E}} = 0.0599$ and the maximum contact pressure is obtained as $p_{\max} = 3p/(2\pi a_c^2) = 0.0418$, where $\hat{E} = E/(1-\nu^2)$ and $p = \pi R_o^2 \times \mathrm{P}_o$. It is useful to point out that although the contact pressure distribution for this problem can be obtained with the two-dimensional setting by using the axial symmetry, it is solved here to verify the validity of the three-dimensional isogeometric contact formulation and its corresponding implementation.

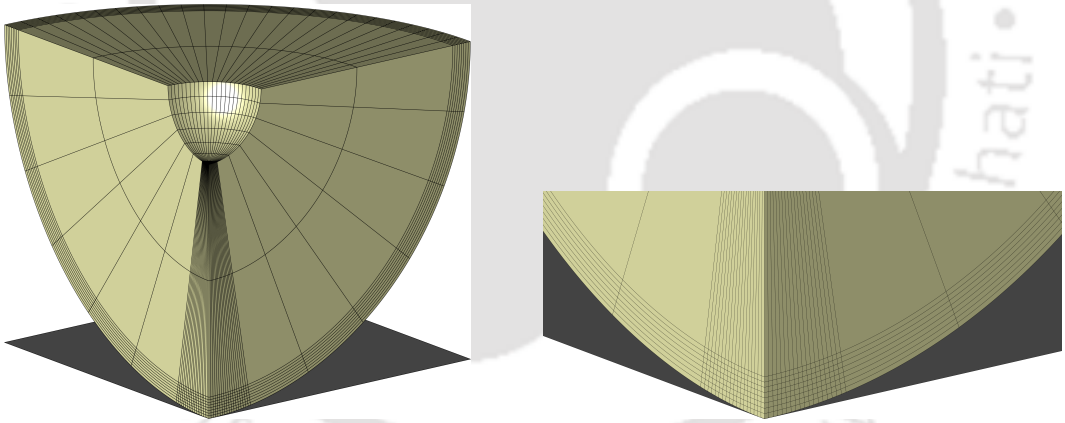

Figure 6.6: Three-dimensional Hertzian contact problem: (a) $1/8^{\text{th}}$ of the sphere along with the coarse mesh that is redistributed in the vicinity of the contact zone. (b) The enlarged view of the redistributed mesh in the contact zone.

R_o (UL)	R_i (UL)	E (UF/UL^2)	ν	ϵ_{N} (UF/UL)	P_o (UF/UL^2)
1	0.2	1	0.3	10^3	1×10^{-4}

Table 6.2: Three-dimensional Hertzian contact problem: Various parameters that are used for the analysis.

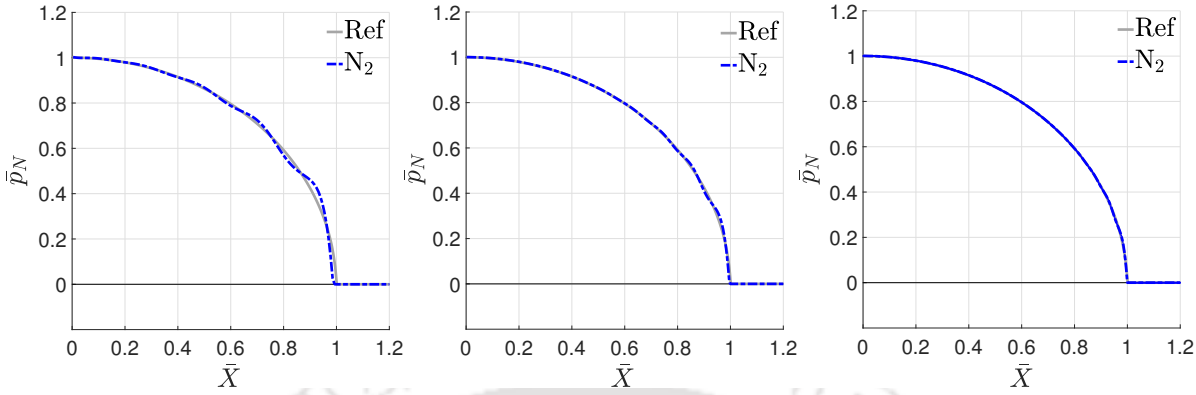

(a) Coarse mesh **(b)** Medium mesh **(c)** Fine mesh

Figure 6.7: Three-dimensional Hertzian contact: Contact pressure distributions with N_2 at different meshes as compared to the analytical solution.

The results obtained with the N_2 based NURBS discretization with three different mesh arrangements are shown in Fig. 6.7. It can be seen that at a fine mesh, the distribution of the normal contact pressure curve matches very well with the analytical solution.

6.4 Three-dimensional large deformation contact problems between deformable bodies

Next, the validity of the developed isogeometric contact formulation and its implementations is verified for three-dimensional large deformation contact between deformable bodies using two different types of ironing problems that are taken from De Lorenzis et al. [66]. In the first problem, the contact between a block and a slab is considered. In the second problem, the contact between a cylindrical die and a slab is analyzed.

6.4.1 Block ironing problem

In this, a block of dimension $4 \times 4 \times 4$ UL^3 is first pressed onto a slab of dimension $20 \times 10 \times 10$ UL^3 by applying a downward vertical displacement $U_z = -1.0$ UL on the top surface of the block. Thereafter, the block is dragged across the slab by applying the horizontal displacement $U_x = 12.5$ UL. As in [66], the Neo-Hookean hyper-elastic model with material parameters $E_{\text{block}} = 10$ UF/UL^2, $E_{\text{slab}} = 1$ UF/UL^2

and $\nu_{\text{block}} = \nu_{\text{slab}} = 0.3$ is utilized. The normal penalty parameter is taken as $\epsilon_{\text{N}} = 100$ UF/UL. The meshes used for the block and slab are shown in Fig. 6.8. Figure 6.9

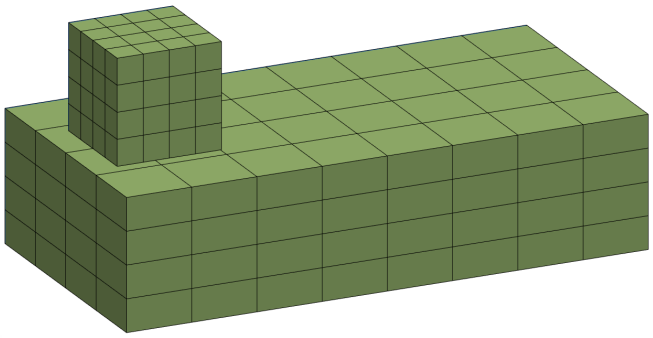

Figure 6.8: Three-dimensional block ironing problem: Meshes for the block and the slab are $4 \times 4 \times 4$ and $8 \times 4 \times 4$, respectively, that are taken from [66].

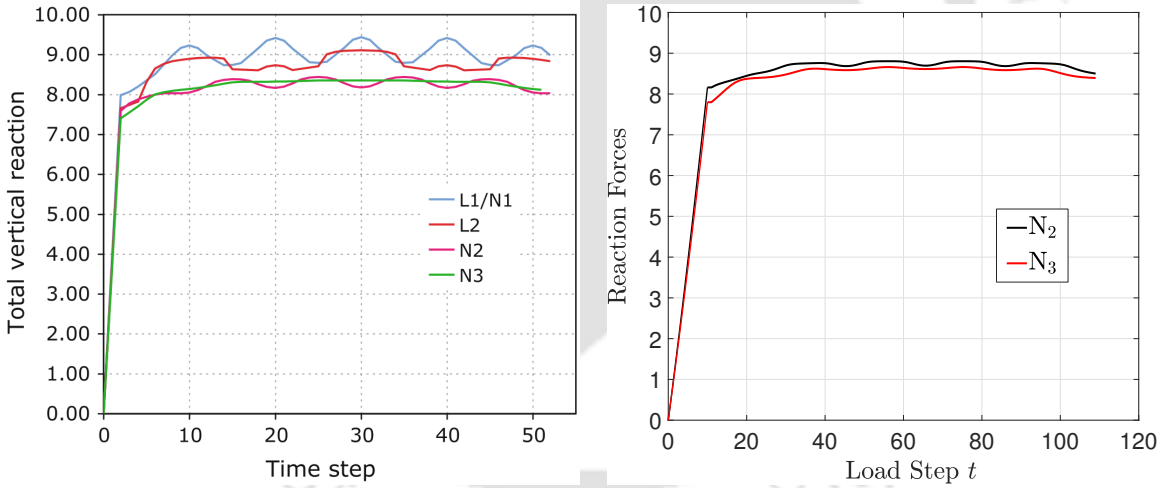

Figure 6.9: Three-dimensional block ironing problem: Comparison of the global variation of the vertical contact forces using the N_2 and N_4 based discretizations with the present work (right) to the results reported by De Lorenzis et al. [66] (left). The results from [66] are reprinted here with permission.

shows the results taken from De Lorenzis et al. [66] and ones reproduced with the current simulations for N_2 and N_3 order of NURBS discretizations. Based on the obtained results, it can be observed that the total vertical contact forces curves with current simulations are very similar to those presented by De Lorenzis et al. [66].

6.4.2 Cylinder ironing problem

In this example, the contact between the cylindrical die having dimensions: radius 0.5 UL, wall-thickness 0.1 UL and width 0.6 UL, and the slab of dimension: $2.5 \times 1.0 \times 0.6$ UL^3 is considered. The setup of the problem is taken from De Lorenzis el al. [66]. The simulation parameters are same as in [66]. The meshes used for the cylindrical die and slab are shown in Fig. 6.10. The material parameters and other details are same as for above example, except that $E_{\text{die}} = 100$ UF/UL^2. The downward vertical and horizontal displacement values are $U_z = -0.2$ UL and $U_x = 1.5$ UL, respectively.

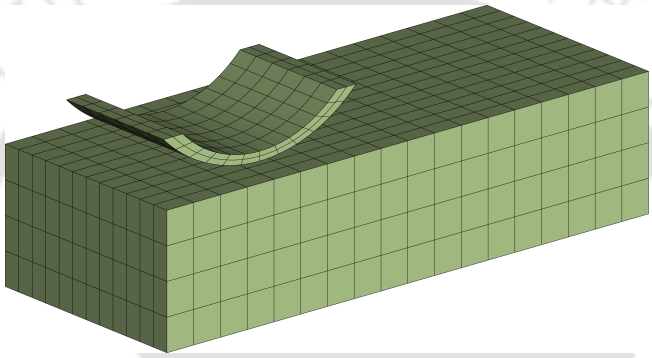

Figure 6.10: Three-dimensional cylinder ironing problem: Meshes for the die and slab are $12 \times 6 \times 2$ and $18 \times 12 \times 4$, respectively, that are taken from [66].

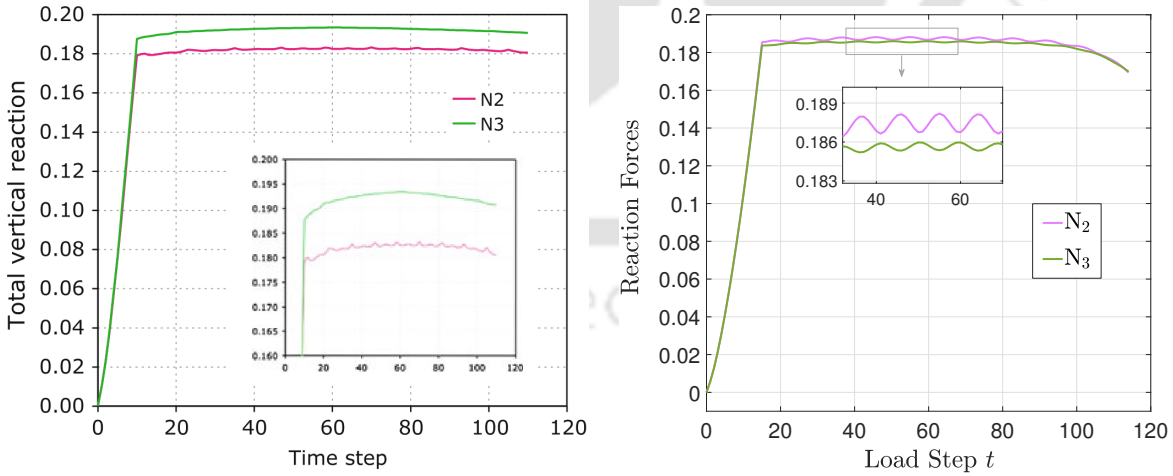

Figure 6.11: Three-dimensional cylinder ironing problem: Comparison of the global variation of vertical contact forces for N_2 and N_3 based NURBS discretizations with the present work (right) to the results presented by De Lorenzis et al. [29] (left). The results from [66] are reprinted here with permission.

The results presented by De Lorenzis et al. [66] are shown on the left side, and the results that are reproduced with the current setup with N_2 and N_3 order of NURBS discretizations are shown on the right side of Fig. 6.11. From the obtained results, it can be seen that with the present simulations, the vertical contact force curves with N_2 and N_3 discretizations are similar to those presented by De Lorenzis et al. [66]. The marginal difference between the results obtained with the current simulations and those presented by De Lorenzis et al. [66] could be due to the use of different contact algorithms, which is GPTS in this work, whereas mortar in [66].

Chapter 7

Numerical Results and Discussion

In this chapter, the capabilities and performance of the proposed varying-order based NURBS discretization method are demonstrated by means of analyzing both the two- and three-dimensional contact problems using IGA technique. The performance is shown for both the varying order based: higher-continuous $N_p{-}N_{p_c}$ and higher-order $N_p{-}N_{p_c \cdot p_s}$ types of NURBS discretizations. For each case, the results with the standard NURBS based discretizations are used for comparisons. The efficacy of the proposed methodology is assessed mainly in terms of accuracy, robustness, and computational efficiency as compared to standard NURBS discretizations.

In the first three Sections 7.1-7.3, various two-dimensional small and large deformations contact problems between one- or two-deformable bodies, with or without considering friction are analyzed. Next, in Section 7.4, a two-dimensional adhesive contact problem under the influence of van der Waals interactions is analyzed. Finally, in Section 7.5, a three-dimensional large deformation frictionless contact between two deformable bodies is simulated in order to demonstrate the performance of the proposed method over the standard NURBS discretizations.

7.1 Two-dimensional frictional ironing[1]

7.1.1 Problem setup

In the first example, the frictional sliding contact between two deformable bodies using the setup similar to the one utilized by De Lorenzis et al. [29] is considered. This

[1]The results presented in this section are taken from Agrawal and Gautam [123] with minor changes.

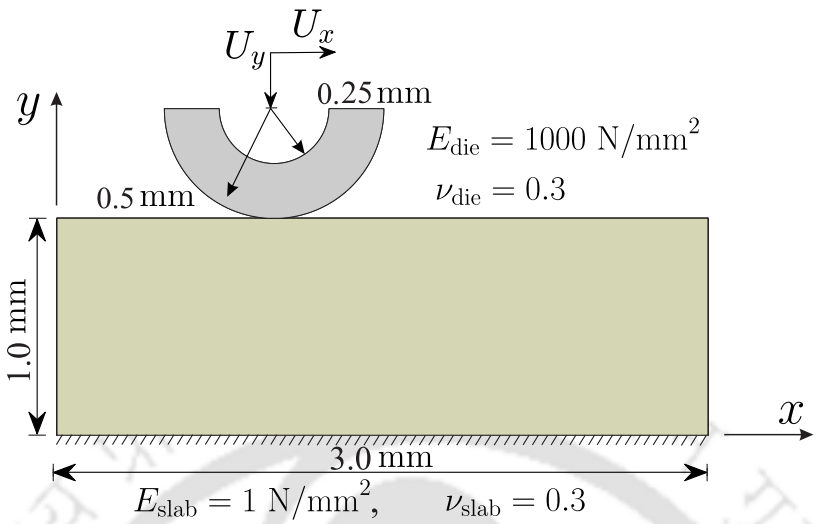

Figure 7.1: The setup of the ironing problem along with the geometric data, material details, and the boundary conditions.

example is used to carefully analyze the performance of the proposed VO NURBS discretization method for the isogeometric analysis of large deformation-large sliding frictional contact over the standard NURBS discretizations. The geometric model along with the material details and the boundary conditions are shown in Fig. 7.1.

In this, the die is first pressed onto an elastic slab and then moved relatively in the horizontal direction, as shown in Fig. 7.1. A total vertical displacement $U_y = -0.23$ mm is applied to the top surface of the die in a uniform manner in 46 load steps. Thereafter, the die is dragged across the slab by applying $U_x = 1.5$ mm in 250 load steps while keeping the vertical displacement fixed. An isotropic Neo-Hookean hyperelastic material model is considered to describe the material behaviour of the die and slab. The material parameters are shown in Fig. 7.1. The penalty parameters are taken as $\epsilon_{\text{N}} = \epsilon_{\text{T}} = 100$ N/mm. The Coulomb's friction coefficient $\mu_{\text{f}} = 0.2$ is considered.

First, a very coarse mesh is chosen to amplify the possible difference between the results with VO and standard NURBS discretizations, as discussed in the following. The coarsest mesh is denoted by m_1 and is illustrated in Fig. 7.2. Moreover, three other meshes, which are obtained through the uniform knot insertion and later used for the convergence study (in Section 7.1.3), are listed in Table 7.1. For a N_p order of NURBS contact layer, $3 \times (p+1)$ number of Gauss-quadrature points are used for the evaluation of contact integrals per contact element.

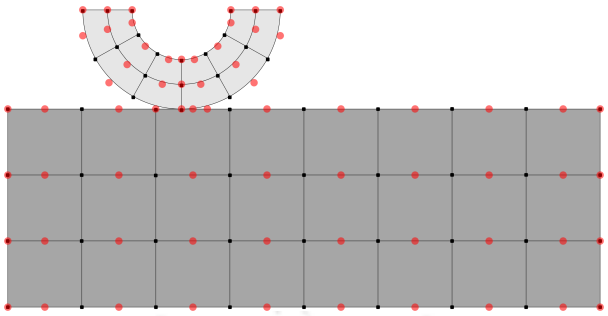

Figure 7.2: The coarsest mesh m_1 used for the ironing problem. The control points associated with N_2 discretization are indicated with the red dots and the unique knot entries on the physical mesh of each body with the black squares.

Mesh	Elements	
	Die	Slab
m_1	6×2	8×3
m_2	12×4	16×6
m_3	24×8	32×12
m_4	48×16	64×24

Table 7.1: Frictional ironing problem: Number of elements in different meshes for the die and slab.

7.1.2 Prediction of vertical and horizontal contact forces

In this section, the improvement in the accuracy of the contact responses on increasing the inter-element continuity and interpolation order of the NURBS with the proposed discretization method is analyzed. The results with standard NURBS based discretizations are used for comparison purposes.

7.1.2.1 Increasing the inter-element continuity

First, the quality of the results with different VO based discretizations: $N_2{-}N_{p_c}$ ($p_c = 4$, and 6) is compared with that of corresponding standard N_p ($p = 2, 4$, and 6) order of NURBS discretizations on increasing the inter-element continuity at the coarsest mesh m_1. In case of VO, the quadratic order of NURBS, which are sufficient to describe the geometry of the setup exactly, are kept fixed for the discretization of the bulk region, while the interpolation order of the bottom surface of the die and upper surface of the slab are elevated to 4 and 6. The results with N_3 (and N_5) are omitted from this

investigation, as they are similar to those obtained with N_4 (and N_6) cases.

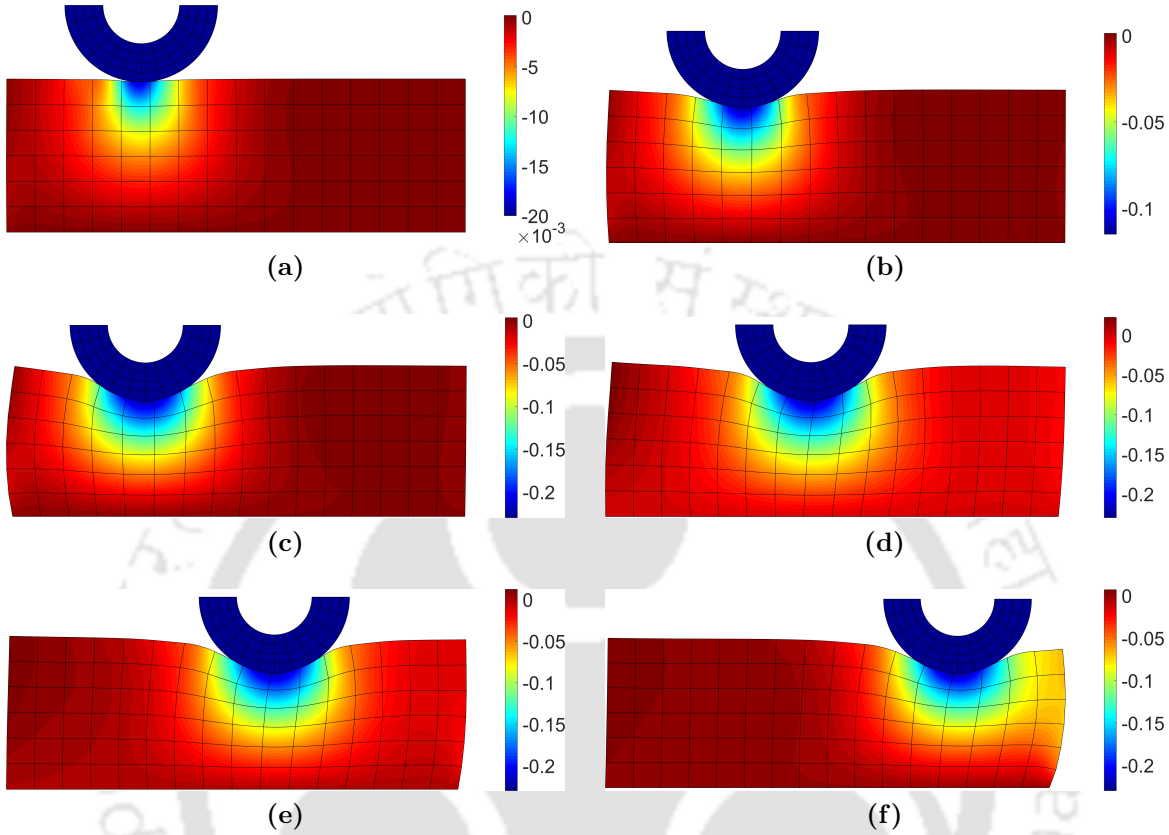

Figure 7.3: Distribution of displacement field u_y in the deformed configuration during the compression process at step $t = 4, 23,$ and 46 (first three frames) and during the sliding at step $t = 80, 160,$ and 250 (last three frames) with N_2 at mesh m_2.

The deformed configurations of the setup during downward and sliding motions are shown in Fig. 7.3 with N_2 using mesh m_2. During the indentation phase, the sum of contact forces on the top surface of the die should increase gradually, and during the sliding phase, forces should be approximately constant. Figure 7.4a shows the evolution of net vertical contact force P_y and the horizontal contact force P_x, computed at the top surface of die, as a function of load step t for both N_p and $N_2{-}N_{p_c}$ based discretizations. The enlarged views for P_y and P_x are shown in Figs. 7.4b and 7.4c, respectively. Two major observations are made. First, the results verify the validity of the proposed VO based NURBS discretization method, as the contact force curves of P_y and P_x are nearly indistinguishable for VO based $N_2{-}N_{p_c}$ ($p_c = 4,$ and 6) and standard N_p ($p = 4,$ and 6) discretizations. This is due to employing the same $C^{p-1}-$continuous NURBS for the evaluation of contact integrals and identical number of degrees of freedom

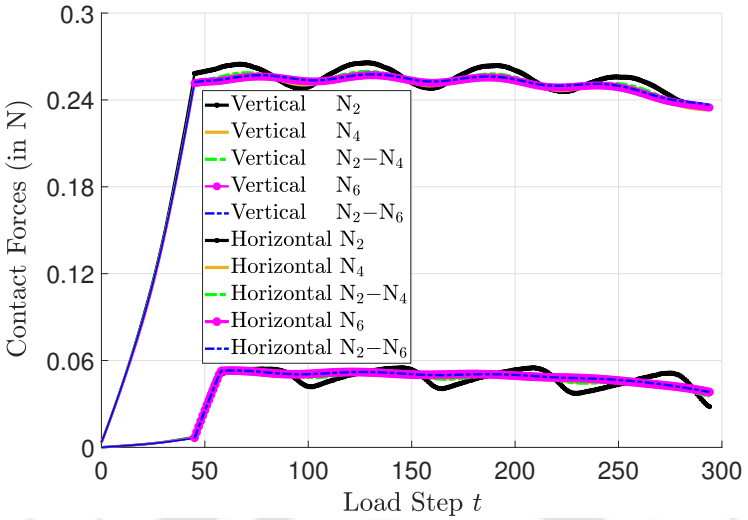

(a)

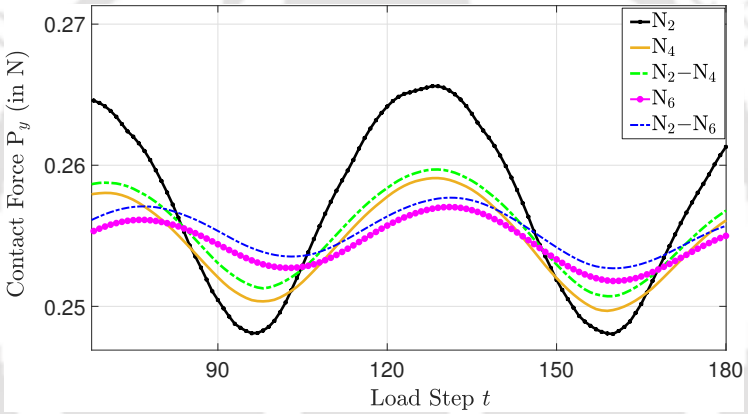

(b)

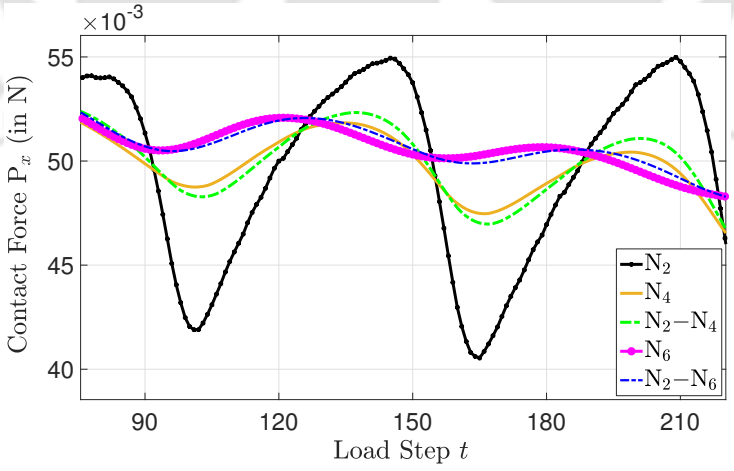

(c)

Figure 7.4: Ironing problem: (a) Computed total horizontal and vertical contact forces with load step t for different discretizations at the coarsest mesh m_1. Enlarged view: (b) vertical contact force P_y, and (c) horizontal contact reaction force P_x for $N_2-N_{p_c}$ ($p_c = 4,$ and 6) and standard N_p ($p = 2, 4,$ and 6) discretizations.

(DOFs) present across the contact boundary in both the cases of discretizations. The DOF density data for $N_2{-}N_{p_c}$ and N_p is provided in Table 7.2 for mesh m_1. Second, during sliding, large-amplitude periodic oscillations of vertical and horizontal contact forces are present, especially with standard N_2 based discretization. The source of such large-amplitude non-physical oscillations is the insufficient discretization of the NURBS contact layers with the coarse mesh m_1. This, as a result, limits the conforming ability of the master body contact layer to the finite deformations introduced by the slave body. For a fixed mesh, conforming ability of contact layers increases on increasing the inter-element continuity with NURBS discretization. Consequently, oscillation error in P_y and P_x reduces as shown in Figs. 7.4b and 7.4c, respectively. With $N_2{-}N_4$ and $N_2{-}N_6$, the oscillation amplitude of the horizontal contact force ΔP_x reduce to approximately 27% and 12%, respectively of that observed with N_2 discretization. A quantitative analysis of the reduction in the oscillation error for $N_2{-}N_{p_c}$ ($p_c = 4,$ and 6) and N_p ($p = 2,$ 3, and 4) for both the force components is provided in Table 7.3. The oscillation amplitude of the reaction forces is computed using $\Delta P_j := \max(P_j) - \min(P_j)$, where $j = x, y$. Here, the amplitude observed with N_2 is used as a reference. It is noted that the obtained results and the reduction in the oscillation amplitude on increasing the smoothness of NURBS are in the agreement to those reported in the literature [29, 47, 62, 66, 71, 95, 127]. Moreover, the convergence behaviour and the reduction in the total analysis time with $N_2{-}N_{p_c}$ as compared to N_p discretizations are reported in Section 7.1.3.

Discretization	**DOF for die**			**DOF for slab**			**Total**
Type	**Interface**	**Bulk**	**Total**	**Interface**	**Bulk**	**Total**	**DOF**
N_2	18	36	54	20	60	80	134
N_4	26	52	78	24	72	96	174
N_6	34	68	102	28	84	112	214
$N_2{-}N_4$	26	36	62	24	60	84	146
$N_2{-}N_6$	24	36	70	28	60	88	158
$N_2{-}N_{2{\cdot}1}$	30	36	66	36	60	96	162
$N_2{-}N_{2{\cdot}2}$	42	36	78	52	60	112	190
$N_2{-}N_{2{\cdot}3}$	54	36	90	68	60	128	218

Table 7.2: Degrees of freedom (DOF) density data for the die and slab with different VO and standard NURBS based discretizations at mesh m_1.

Discretization Type	ΔP_y (%)	ΔP_x (%)
N_2	100	100
N_4	49.88	23.31
N_6	24.57	11.81
$N_2{-}N_4$	48.11	27.02
$N_2{-}N_6$	23.83	12.09
$N_2{-}N_{2{\cdot}1}$	5.98	30.84
$N_2{-}N_{2{\cdot}2}$	4.31	7.51
$N_2{-}N_{2{\cdot}3}$	1.89	4.77

Table 7.3: Reduction in the oscillation amplitude of vertical and horizontal contact forces with different standard and VO based NURBS discretizations at mesh m_1. The oscillation amplitude with N_2 is used as a reference.

7.1.2.2 Elevating the interpolation order

Within the context of standard IGA, apart from increasing the inter-element continuity of NURBS discretization, the degree of conformity of the contact layer can be increased by increasing the mesh resolution. However, with the usage of a fine mesh, the computational cost increases considerably, which is not desirable. This discards one of the key advantages of IGA which is its ability to represent the geometry to high-accuracy even with a coarse mesh. Therefore, the focus of the proposed VO NURBS discretization method is to improve the solution quality while keeping the mesh m_1 fixed. For this purpose, the additional order-elevation based refinement to N_2 discretized contact layers of the die and slab at mesh m_1 is carried out. With this, although the inter-element continuity remains constant, a large number of additional DOFs are introduced across the contact layers at a fixed mesh attributed to the repetitions of knots with the order elevation process. Performing one and two steps of additional order-elevation to $N_2{-}N_2$ results in $N_2{-}N_{2{\cdot}1}$ and $N_2{-}N_{2{\cdot}2}$ discretizations, respectively. The total number of DOFs present in the contact interface and bulk domain corresponding to $N_2{-}N_{2{\cdot}p_s}$ ($p_s = 1$ and 2) are listed in Table 7.2.

Figures 7.5a, and 7.5b show the contact force curve of P_y and P_x, respectively, with VO based $N_2{-}N_{2{\cdot}p_s}$ ($p_s = 1,$ and 2) and standard N_2 based discretizations. As can be seen, the solution quality improves significantly for the new discretizations, especially with $N_2{-}N_{2{\cdot}2}$. This is due to the moderate multi knot-span of basis functions as discussed in Section 5.1.1 and a large number of DOFs present across the contact layer

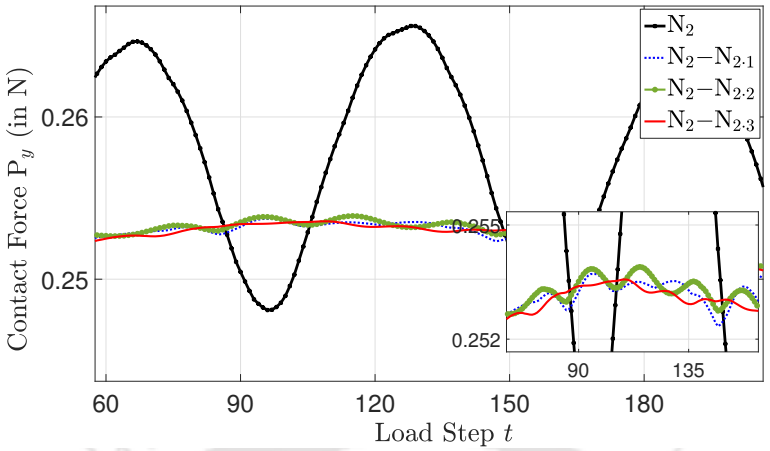

(a)

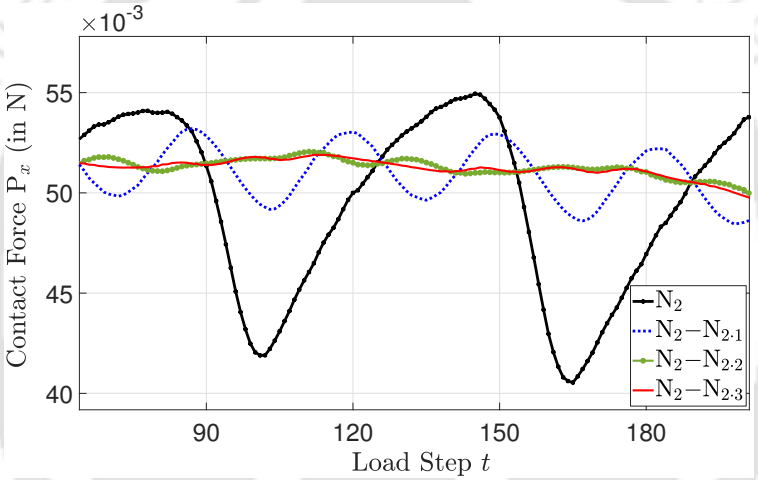

(b)

Figure 7.5: Comparison of (a) vertical contact force P_y oscillation, and (b) horizontal contact force P_x oscillation with different discretizations at mesh m_1.

with $N_2-N_{2\cdot p_s}$ ($p_s = 1$, and 2) as compared to N_2, see Table 7.2 for DOFs details. Moreover, the other higher order-elevation based discretization, i.e. $N_2-N_{2\cdot3}$, also reduces the oscillation error, as shown in Figs. 7.5a and 7.5b. However, only a slight improvement is attained as compared to $N_2-N_{2\cdot2}$, see Table 7.2. This shows that the number of DOFs more than with the $N_2-N_{2\cdot2}$ across the contact layer improves the results only slightly. The quantitative details on the reduction of oscillation amplitude for each discretizations for both the force components are shown in Table 7.3.

Finally, the influence of order-elevation based refinement to the higher continuous NURBS contact layer, i.e. N_4, again while keeping the original mesh m_1 fixed is

investigated. The contact force curve P_x corresponding to $N_2{-}N_{4\cdot p_s}$ ($p_s = 1,\ 2$ and 3) discretizations are shown in Fig. 7.6. The results with $N_2{-}N_{2\cdot p_s}$ ($p_s = 1,\ 2$ and 3) are used for the purpose of comparison. The major observation is that on increasing the inter-element continuity of the $N_{2\cdot p_s}$ discretized contact layer to $N_2{-}N_{4\cdot p_s}$, the oscillation error reduces marginally. This is expected as $N_2{-}N_{4\cdot p_s}$ has total only 12 additional DOFs across the contact interface as compared to $N_2{-}N_{2\cdot p_s}$, see Table 7.2 for DOFs. Furthermore, it can be observed that more smoother response of contact forces are obtained on increasing the continuity of NURBS discretized contact layer.

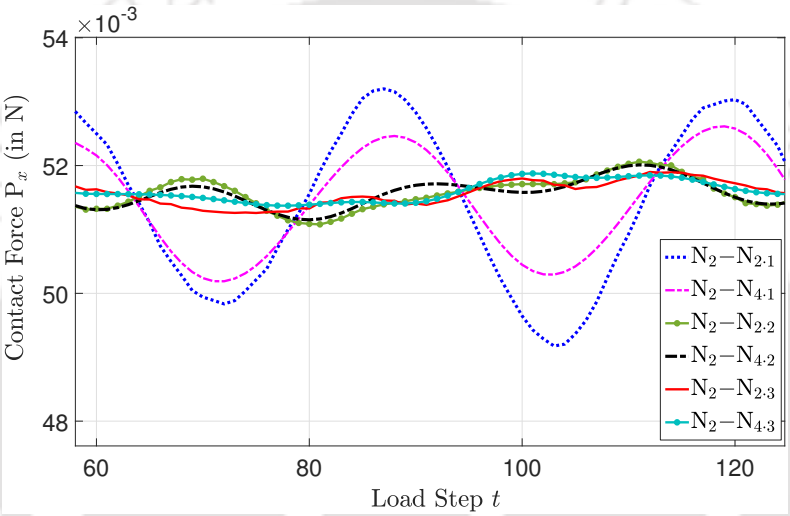

Figure 7.6: Comparison of the horizontal contact force oscillation on increasing the inter-element continuity of the NURBS with different VO based discretizations at mesh m_1.

With the obtained results, it is evident that additional order-elevation based VO NURBS discretizations, particularly $N_2{-}N_{2\cdot 2}$, is advantageous over the standard N_p ($p = 2,\ 4,$ and 6) as well as $N_2{-}N_p$ based VO NURBS discretizations, see Table 7.3. The $N_2{-}N_{2\cdot 2}$ reduces the oscillation amplitude of vertical and horizontal contact forces to 4.31% and 7.51%, respectively, as compared to N_2 at a fixed mesh m_1.

7.1.3 Convergence behaviour and analysis time

Next, the convergence of the vertical contact forces oscillation amplitude ΔP_y and horizontal contact force oscillation amplitude ΔP_x with both the discretization methods upon mesh refinement is investigated. Four nested meshes, as described in Table 7.1, are used. In case of VO, the higher-continuous and additional order-elevation based

discretizations are considered. Moreover, the total analysis time taken by VO based discretizations is compared to that with the standard NURBS discretizations for each mesh level.

Figure 7.7 shows the reduction in the oscillation amplitude of horizontal contact force curve P_x for different discretizations. The convergence plots for both ΔP_y and ΔP_x with $N_2{-}N_{p_c}$ ($p_c = 4,\ 6,\ 2\cdot 1,\ 2\cdot 2,$ and $2\cdot 3$) and standard N_p ($p = 2,\ 4,\ 6$) based discretizations for all the four meshes are shown in Fig. 7.8. The total processing time taken by different discretizations over the DOFs are shown in Fig. 7.9. For each discretization, the time in % is calculated using the following expression

$$\text{Time percentage} = \frac{\text{total analysis time}}{\text{maximum total analysis time}} \times 100\,, \tag{7.1}$$

where the maximum total analysis time is with the standard N_6 order of NURBS using the finest mesh m_4 (which is the most expensive).

From Figs 7.8a, 7.8c, and 7.9a it can be observed that to attain the accuracy equivalent to N_4, $N_2{-}N_4$ takes approximately 33.74% lower computational cost even at the coarsest mesh m_1. The reduction in the computational cost with $N_2{-}N_4$ is due to fact that it employs the lower order of NURBS, i.e. N_2, for the bulk computations as compared to N_4 based uniform discretization. The gain in the computational efficiency further improves on increasing the mesh resolution, e.g. $N_2{-}N_4$ takes approximately 52.44% lower cost as compared to N_4 at the finest mesh m_4. A similar observation is made on comparing the results with more higher-continuous NURBS discretizations, e.g. to deliver the result equivalent to N_6, $N_2{-}N_6$ takes approximately 59.58% lower analysis time at mesh m_4.

Further, from Figs. 7.8 and 7.9 it can be observed that for a fixed mesh, a significant improvement in the accuracy is achieved with additional order-elevation based VO discretizations, i.e. with $N_2{-}N_{2\cdot 1}$ and $N_2{-}N_{2\cdot 2}$, among all tested cases. The $N_2{-}N_{2\cdot 2}$ delivers the most accurate results at a cost slightly more than with the N_2. Taking a closer look at Figs. 7.8b and 7.8d reveals that the accuracy attained with $N_2{-}N_{2\cdot 2}$ at mesh m_1 and m_2 is comparable to N_2 using mesh m_3 and m_4, respectively. The corresponding total analysis time taken by $N_2{-}N_{2\cdot 2}$ is approximately 56.62% and 72.78% lower than with the N_2 for the similar accuracy level, see Fig. 7.9b. With other higher order based VO discretizations, i.e. with $N_2{-}N_{2\cdot 3}$, a slight improvement in the accuracy is achieved as compared to $N_2{-}N_{2\cdot 2}$ for the same mesh level.

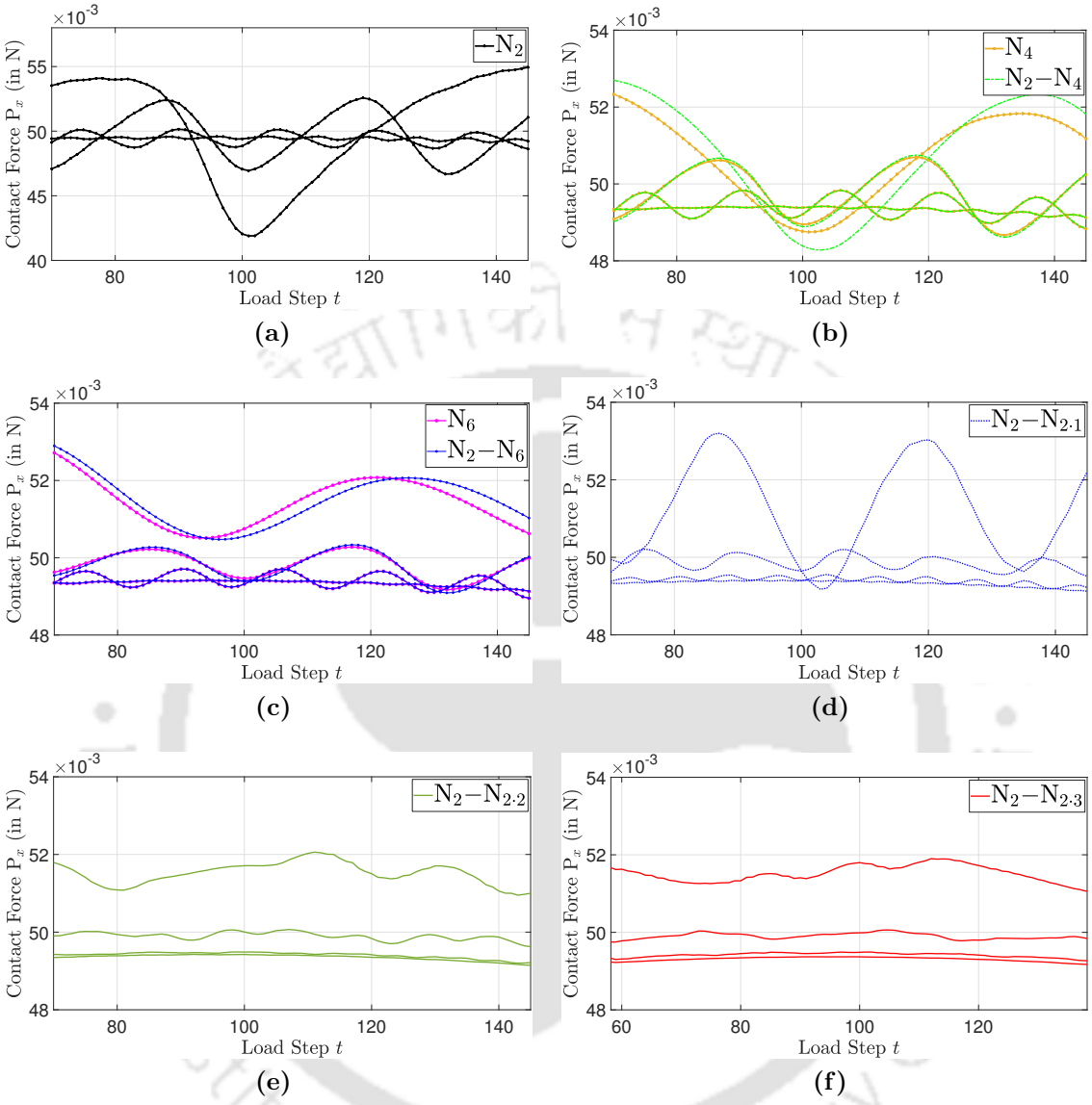

Figure 7.7: Reduction of the horizontal contact force oscillation on increasing the mesh resolution with both the standard and VO based NURBS discretizations.

In summary, this example clearly demonstrates the advantages of the proposed VO based discretizations in terms of the accuracy of results and computational efficiency over the standard fixed-order based NURBS discretizations. To attain the accuracy equivalent to N_p based discretization, $\mathrm{N}_2{-}\mathrm{N}_p$ takes much lower computational cost. Further, with the additional order-elevation based VO discretizations, a significant improvement in the accuracy is achieved even at the coarse mesh. It attains a major gain

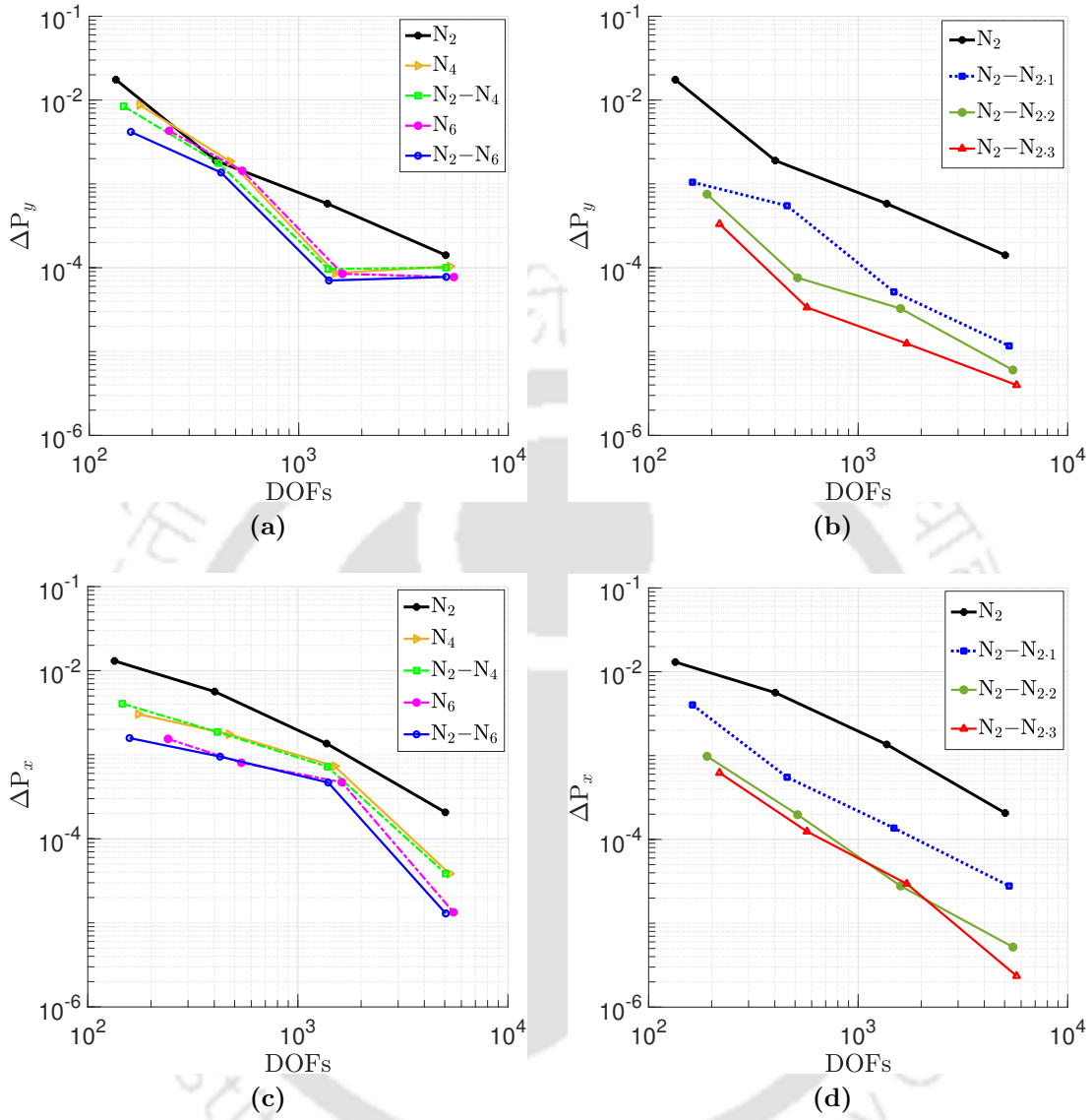

Figure 7.8: The oscillation amplitude of the vertical contact reaction force ΔP_y (top) and the horizontal contact force ΔP_x (bottom) for different VO and standard NURBS based discretizations.

in the numerical efficiency to provide the accuracy as similar to N_2 based discretization.

7.1.4 Performance at large indentation depth

Finally, in this section, the influence of the interpolation order of the underlying bulk elements on the solution quality for the ironing problem with large indentation depth

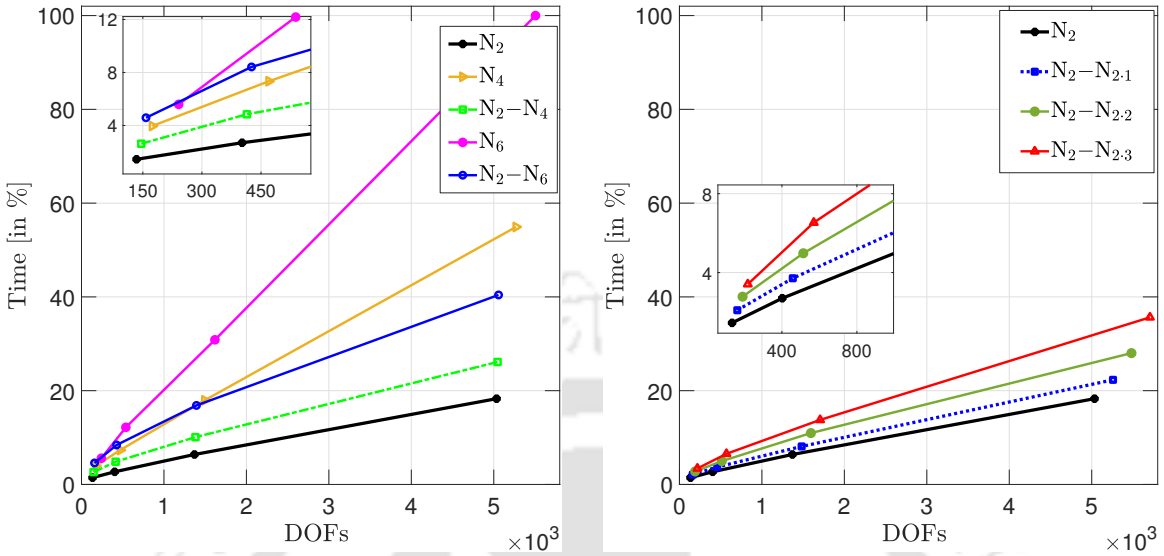

Figure 7.9: Total analysis time (in %) with different standard and VO based NURBS discretizations with meshes m_1 to m_4. The analysis time with N_6 using mesh m_4 is used for normalization.

is examined. It is known that numerical simulation of this problem can be computationally challenging if the stiffness ratio of the bodies is high and the harder body is dragged relative to the softer one after the significant indentation [32, 127]. In such a case, the strong interaction between the bulk and contact surface discretizations takes place. Therefore, it becomes important to assess the accuracy of the solution with VO discretization to that of corresponding standard NURBS discretization for large deformation contact instance. The problem setup used for this analysis is same as described in Sec 7.1.1 except the modification that higher value of the stiffness for the die $E_{\text{die}} = 10^4$ N/mm^2 and vertical displacement $U_y = -0.5$ mm are considered. The Coulomb's friction coefficient is $\mu_{\text{f}} = 0.1$. Four nested meshes that are listed in Table 7.1 are used for the analysis. The deformed configurations of the setup at the end of compression and sliding processes are shown in Fig. 7.10 with N_2 using mesh m_2.

Figure 7.11 shows the comparison of the oscillation amplitude of the vertical contact force $\Delta \mathrm{P}_y$ and horizontal contact force $\Delta \mathrm{P}_x$ with both the discretization methods for meshes m_1 to m_4. Two major observations are made. First, although N_2 based discretization is C^1-continuous across the contact layer, it fails to converge at the

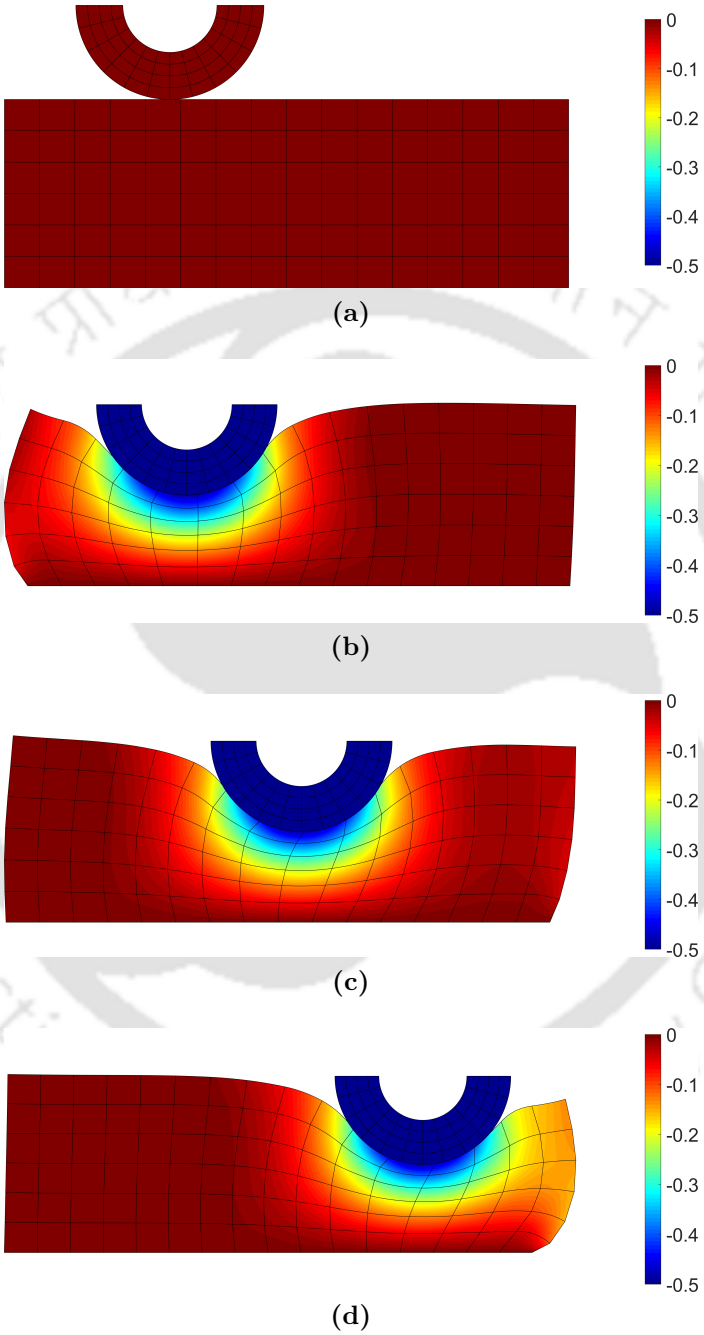

Figure 7.10: Ironing problem with large indentation depth: Deformed configuration at the (a) start and (b) end of compression process, and at the (c) mid and (d) end of sliding with N_2 at mesh m_2. The color shows the magnitude of the vertical displacement u_y. Here, $U_y = -0.5$ and $E_{\text{die}} = 10^4$.

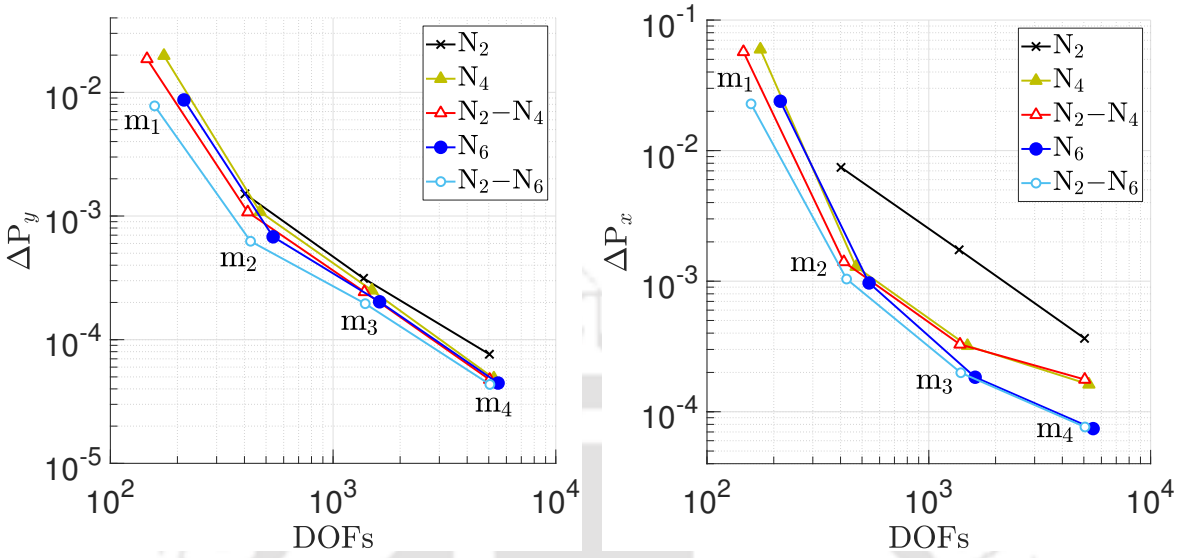

Figure 7.11: Ironing with large indentation depth: Comparison of the oscillation amplitude of contact forces with different standard and VO based discretizations for meshes m_1 to m_4.

coarsest mesh m_1. Clearly, N_2 with the mesh m_1 is not sufficient to analyze this problem. On the other hand, the higher-order based NURBS discretization is capable of providing the solution even at the coarsest mesh m_1. Second, the results obtained with the VO based discretization verify the application of the proposed methodology to large deformation contact case. The accuracy of the result achieved with VO based $N_2{-}N_{p_c}$ ($p_c = 4$ and 6) discretizations is equivalent to that of fixed-order based N_p ($p = 4$ and 6) discretizations, respectively, for the same mesh level.

7.2 Two-dimensional Hertzian contact[2]

Next, the performance of the proposed VO based NURBS discretization method is illustrated for the isogeometric analysis of classical two-dimensional Hertzian-type contact as compared to standard NURBS discretizations. In this, the contact between an infinitely long cylinder, having a outer radius $R_o = 1$, and a rigid surface is analyzed under the plane strain setting. The setup of the problem along with the boundary condition, which is taken from [30], is shown in Fig. 7.12. Due to symmetry, only a quarter of the geometry is utilized. The natural NURBS based description of geome-

[2]The results presented in this section are taken from Agrawal and Gautam [123] with minor changes.

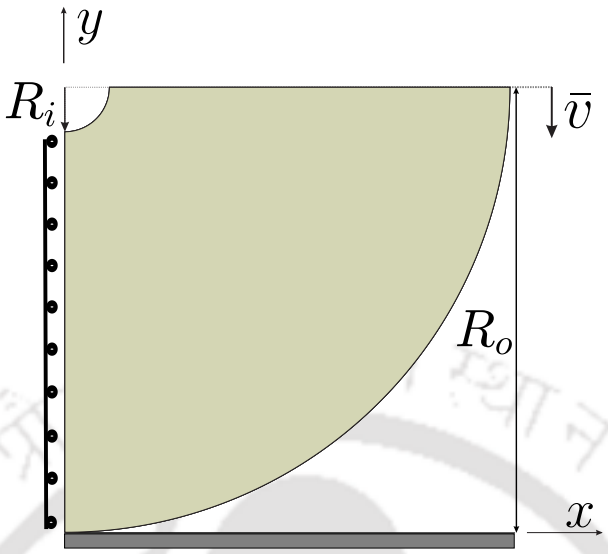

Figure 7.12: Setup of the Hertzian problem.

try consists a non-zero internal radius $R_i = 0.1$. The numerical investigation reveals that it exerts no influence on the quality of the solution. For its modeling, a linearly elastic material with Young's modulus $E = 1$ and Poisson's ration $\nu = 0.3$ is used. Here, the top surface of the cylinder is subjected to prescribed vertical displacement $\bar{v}$ and a penalty parameter $\epsilon_{\mathrm{N}} = 2 \times 10^3$ is chosen as a default value. Six uniformly refined meshes that are driven by $9n \times 48$ number of elements along each parametric directions (where $n = 1, 2, 4, 8, 16$ and 32) and are denoted by m_1 to m_6 are used for this analysis. For numerical efficiency, approximately 80% of the total elements in each parametric direction are relocated in such a manner that they lie within the 10% surface length of the geometry, as shown in Fig. 7.13. It has been tested that 48 number of redistributed elements along the radial direction is adequate for the considered example. The undeformed and deformed configurations of the setup with N_2 using mesh m_3 are shown in Figs. 7.13a and 7.13b, respectively.

Figure 7.14 shows the comparison between the local solution quality of contact pressure distribution for both the standard N_2, and VO based $\mathrm{N}_{2.1}$ and $\mathrm{N}_{2.2}$ discretizations with that of reference contact pressure distribution for meshes m_3 to m_5. Here, the dimensionless normal contact pressure $\bar{p}_N = p_N/p_{N_{ref}}$ is plotted versus the dimensionless contact coordinate $\bar{X} = x/a_{ref}$, where p_N is the normal contact pressure evaluated at an active integration point and x is the distance of this points from the

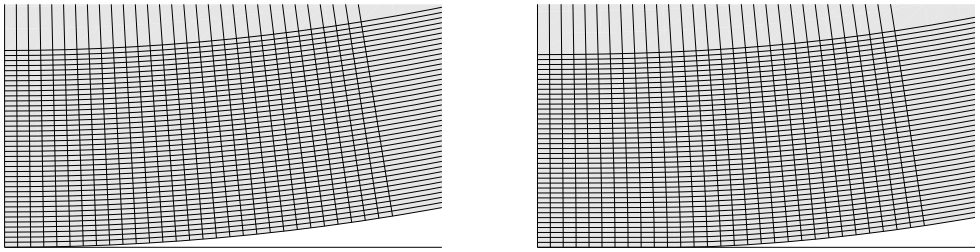

(a) (b)

Figure 7.13: (a) The undeformed and (b) deformed configuration of the setup with N_2 using mesh m_3 after performing the mesh relocation.

first point of contact. The result obtained with N_2 at the finest mesh level m_6 is used as a reference. The corresponding maximum contact pressure $p_{N_{ref}}$ and the contact area a_{ref} are used for the normalization purpose. It is noted that the results obtained with N_2 based discretization for different meshes are in agreement to those reported in literature [29–31, 47, 66, 69, 71, 79] for Hertzian-type contact problem. In case of VO based discretizations, the quadratic order of NURBS that are sufficient to represent the considered CAD geometry exactly are kept fixed for the bulk description. For contact layer, one and two steps of additional order elevation refinements that yields $N_2{-}N_{2\cdot1}$ and $N_2{-}N_{2\cdot2}$ discretizations, respectively, are performed. The total number of DOFs present in the contact interface and in the remaining bulk region with both the standard and VO based NURBS discretizations for each mesh are listed in Table 7.4.

From Fig 7.14, it can be observed that for the same mesh resolution, VO based discretizations provide more accurate results than with the standard N_2 based discretization. With N_2, the oscillation of the contact pressure near the contact interface boundary is clearly visible at the coarse mesh m_3, see Fig 7.14b. As the mesh is refined, the magnitude and extent of the oscillation reduces, as can be seen from Figs. 7.14a, 7.14d, and 7.14g. With a very fine mesh m_5, although the contact pressure curve seems to match exactly with the reference solution, a slight kink is still present near the contact interface boundary. It is noted that in case of Hertzian-type contact, the quality of the solution is often affected by the sudden change of contact status from active to non-active within an element that lies across the edge of contact region. To this date, a number of solution approaches have been introduced to fix this issue, see e.g [78, 79]. Moreover, T-splines based discretization that allows adaptive mesh refinement delivers higher accurate solution than standard NURBS for a fixed number of DOFs, see [31].

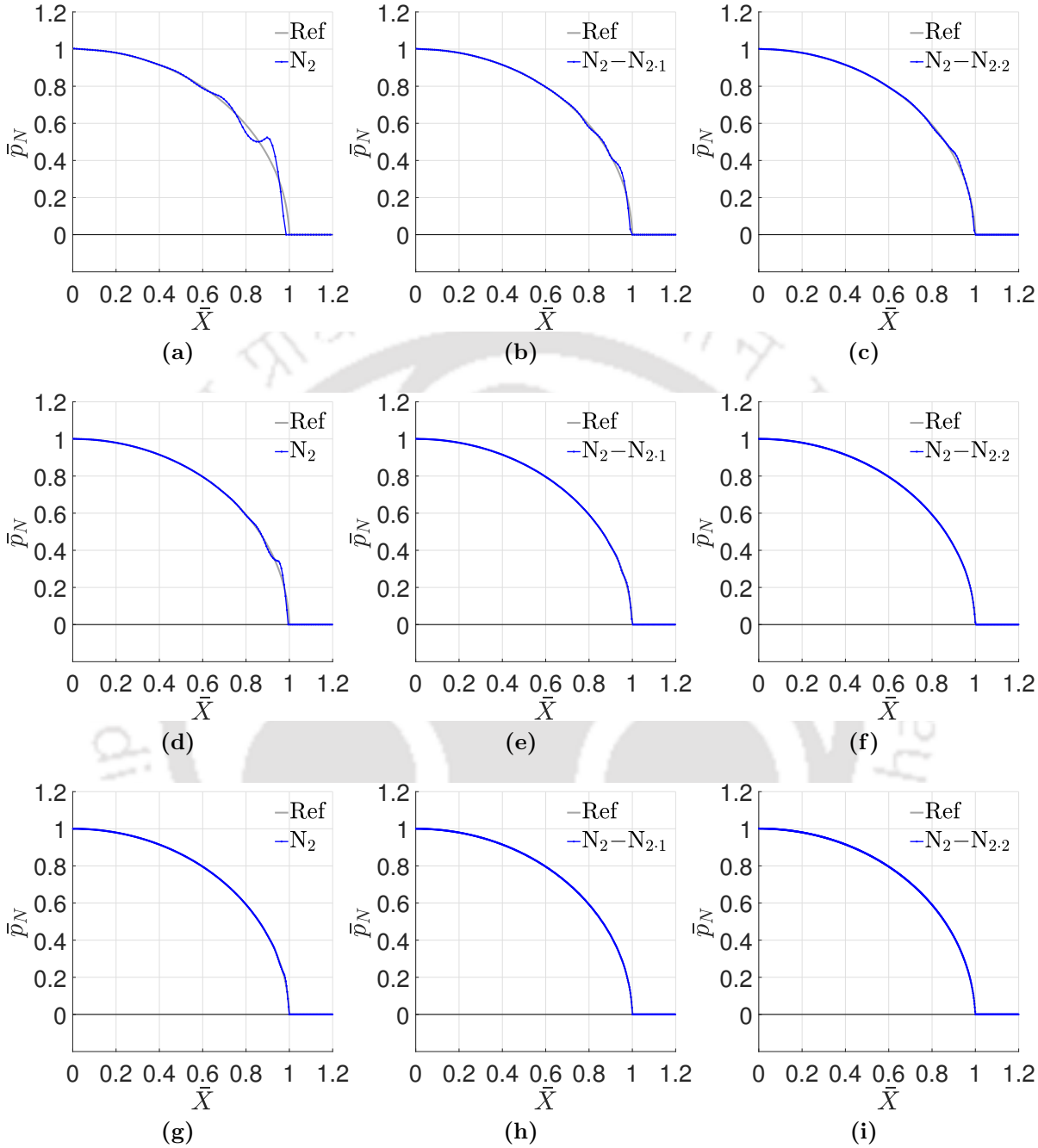

Figure 7.14: Comparison of the variation of contact pressure distribution with standard and VO based NURBS discretizations at: (a)-(c) 36×48; (d)-(f) 72×48; (g)-(i) 144×48 mesh arrangements. The result with N_2 using finest mesh m_6 is used as a reference.

However, in the present work, the focus is particularly on alleviating such an error with simpler NURBS based discretizations that exclude the remeshing strategies and

is computationally inexpensive.

Mesh	Discretization Type	DOFs		
		Interface	Bulk	Total
m_1	L_1	20	960	980
	N_2	22	1056	1078
	$N_2{-}N_{2\cdot1}$	40	1056	1096
	$N_2{-}N_{2\cdot2}$	58	1056	1114
m_2	L_1	38	1824	1862
	N_2	40	1920	1960
	$N_2{-}N_{2\cdot1}$	76	1920	1996
	$N_2{-}N_{2\cdot2}$	112	1920	2032
m_3	L_1	74	3552	3626
	N_2	76	3648	3724
	$N_2{-}N_{2\cdot1}$	148	3648	3796
	$N_2{-}N_{2\cdot2}$	220	3648	3868
m_4	L_1	146	7008	7154
	N_2	148	7104	7252
	$N_2{-}N_{2\cdot1}$	292	7104	7396
	$N_2{-}N_{2\cdot2}$	436	7104	7540
m_5	L_1	290	13920	14210
	N_2	292	14016	14308
	$N_2{-}N_{2\cdot1}$	580	14016	14596
	$N_2{-}N_{2\cdot2}$	868	14016	14884
m_6	N_2	580	27840	28420

Table 7.4: Degrees of freedom density data with different standard and VO based NURBS discretizations using different mesh arrangements.

From Figs. 7.14a-7.14c it can be observed that with VO based discretizations, especially with $N_2{-}N_{2\cdot2}$, superior quality result is obtained even at the coarse mesh m_3 as compared to N_2. It is attributed to the additional number of DOFs present across the contact interface with $N_{2\cdot2}$ over N_2. This, improves the resolution of edge region at the fixed mesh. At the intermediate mesh level m_4, the contact pressure distribution with $N_2{-}N_{2\cdot2}$ seems to match very well with the reference solution, see Fig. 7.14f. This is impressive as $N_2{-}N_{2\cdot2}$ takes only half of the elements to deliver the solution comparable to N_2 at mesh m_5, see Fig. 7.14g. Further, from Figs. 7.14e-7.14f and 7.14h-7.14i it can be seen that the quality of results remain unchanged on further increasing the mesh resolution.

Next, Fig. 7.15 shows the quantitative comparison between the error in the normalized contact pressure distribution for both the standard and VO based discretizations for each mesh level. Moreover, the error decay over these meshes with the classical linear order of Lagrange discretization, i.e. L_1, is also included for comparison purpose. The four noded element mesh describing the circular geometry in an approximate form is generated through the conversion of NURBS elements for all mesh level, i.e. m_1 to m_5. For each mesh, the error is calculated using the L_2-norm

$$L_2 = \sqrt{\int_{\Gamma_c} \left[\bar{p}_{N_{ref}} - \bar{p}_N\right]^2 \, d\Gamma} \tag{7.2}$$

where $\bar{p}_{N_{ref}}$ is the normalized reference normal contact pressure distribution that is computed with N_2 at mesh m_6. In the current work, the spatial rate of convergence is not monitored as the number of elements along the radial direction is fixed during the mesh refinement (driven by $9n \times 48$). Here, the interest is rather in the difference between the accuracy of the result with VO and standard NURBS based discretizations on increasing the mesh resolution along the contact boundary layer of the geometry. It is highlighted that for the unilateral contact problems, the spatial convergence rate is

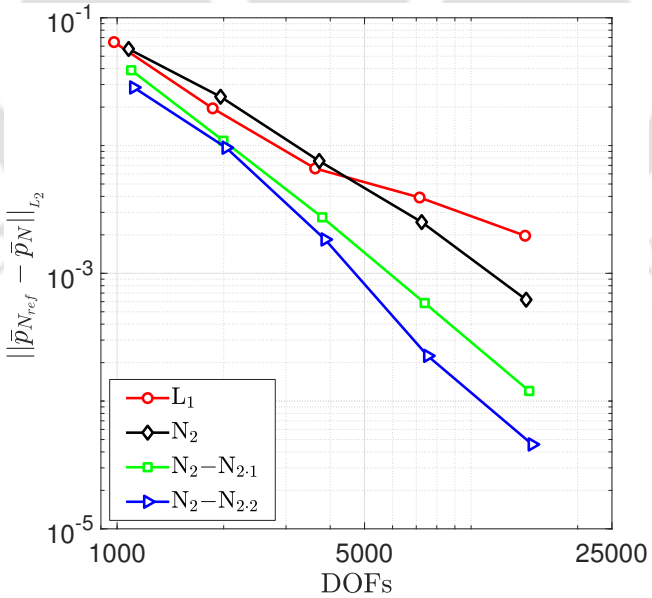

Figure 7.15: The L_2-norm based error in the normalized contact pressure distribution for both the discretization methods using meshes m_1 to m_5.

generally limited by the reduced regularity of the solution under uniform mesh refinement, see e.g. [69] for the detailed description on the convergence rate with a different order of standard NURBS discretizations using the dual mortar based contact algorithm.

Figure 7.15 clearly shows the advantage of using VO as compared to standard N_2 and L_1 based discretizations for the same mesh level. The error curve with $N_2{-}N_{2\cdot2}$ lies below the $N_2{-}N_{2\cdot1}$, N_2, and L_1 curves. This is attributed to additional number of DOFs present across contact interface with $N_2{-}N_{2\cdot2}$, see Table 7.4 for DOFs density data. A closer look reveals that accuracy in the result with $N_2{-}N_{2\cdot2}$ at mesh m_3 is comparable to N_2 using mesh m_4. Further, at mesh m_4, $N_2{-}N_{2\cdot2}$ provides a much more accurate result than with N_2 using a finer mesh m_5. As compared to L_1, a considerable gain in accuracy is obtained with $N_2{-}N_{2\cdot2}$ for the same mesh level. The result with $N_2{-}N_{2\cdot2}$ using intermediate mesh m_3 are of similar accuracy to that obtained with L_1 at a very fine mesh m_5.

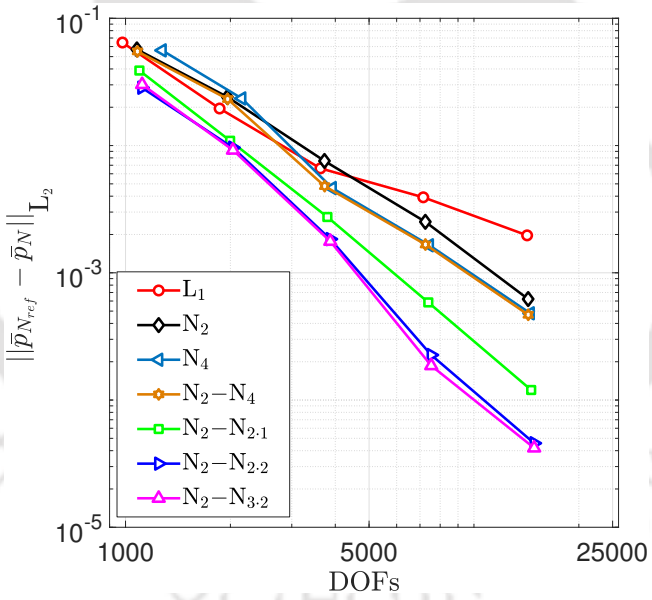

Figure 7.16: The L_2-norm based error in the normalized contact pressure distribution for the higher-continuous NURBS discretizations as compared to others using meshes m_1 to m_5.

Besides, a comparison with the higher than C^1-continuous based NURBS discretizations, i.e. with $N_2{-}N_4$, its counterpart standard N_4, and $N_2{-}N_{3\cdot2}$, is also carried out and the obtained results are shown in Fig. 7.16. It can be seen that although on increasing the continuity from C^0 (with L_1) to C^1 (with N_2), a more accurate result

can be obtained at a fixed mesh, i.e. at intermediate m_4 and fine m_5 mesh level. But, with the more than C^1-continuous NURBS discretization, i.e. with N_2-N_4 or N_4, the absolute error values are nearly equivalent to those obtained with N_2 for the same mesh. This observation also holds for the higher-continuous version, i.e. $N_2-N_{3.2}$, of the $N_2-N_{2.2}$ discretization. Consequently, it shows that NURBS functions smoother than C^1 are not advantageous to analyze the Hertzian contact problem. This behaviour is due to the inability of higher smooth NURBS functions to adequately capture the local changes in the distribution of the contact pressure result.

Finally, the associated computational efforts is compared in terms of the overall analysis time with both the discretization approaches for similar accuracy. Figure 7.17 shows the plots for L_2-norm of the error in the contact pressure with the total analysis time with meshes m_1 to m_5 for L_1, N_2, $N_2-N_{2.1}$ and $N_2-N_{2.2}$ discretizations. Here, the time in % is computed using Eq. (7.1) and the maximum analysis time, that is used for normalizing the time values, is with N_2 at mesh m_6. From Fig. 7.17 it is evident that to attain the accuracy similar to N_2, $N_2-N_{2.1}$ and $N_2-N_{2.2}$ require much lower computational efforts. With a closer look, it turns out that $N_2-N_{2.2}$ at mesh m_3 and m_4 take approximately 42.48% and 43.74% lower analysis time than that with N_2 at m_4

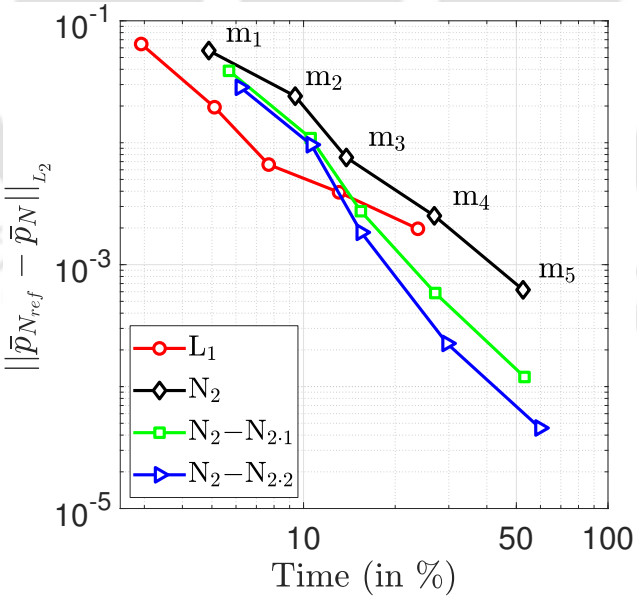

Figure 7.17: Error with total analysis time for different discretizations with meshes m_1 to m_5. The markers on each line correspond to the meshes from m_1 to m_5. For the sake of clarity, the mesh values are shown only for the N_2 line plot.

and m_5, respectively, to attain the similar accuracy. Subsequent comparison with L_1 discretization shows that to attain the comparable accuracy, $N_2{-}N_{2\cdot2}$ at mesh m_1 and m_2 takes a slightly more analysis time as compared to L_1 at m_2 and m_3, respectively. Further, $N_2{-}N_{2\cdot2}$ at mesh m_3 requires approximately 34.86% lower computational efforts as compared to L_1 at m_5 for the similar accuracy level. The additional usage of a fine mesh, e.g. m_4 or m_5, with $N_2{-}N_{2\cdot2}$ leads to a significant gain in the accuracy, which, however, comes at the expense of additional computational efforts as compared to L_1 at m_5.

In summary, this example shows the much higher accuracy and the computational efficiency of the VO based NURBS discretizations as compared to standard N_2 based discretization. For the fixed mesh, VO NURBS yields much more accurate results at a cost slightly more than with the standard NURBS based discretization. To deliver a similar accuracy, it takes much lower computational efforts as compared to N_2 discretization.

7.3 Two-dimensional frictional contact between elastic rings[3]

In the third example, the applicability of the proposed VO based NURBS discretization method is demonstrated for the isogeometric analysis of large deformation frictional contact between two elastic rings under the plane strain setting. As compared to the Hertzian-contact, this problem incorporates the large deformations combined with the friction. The setup, which is taken from [104], is shown in Fig. 7.18. The outer and inner radii of the upper and lower rings are $(10, 8)$ m and $(12, 10)$ m, respectively. The bottom surface of the lower ring is held stationary by fixing the displacement in both directions. A Neo-Hookean hyper-elastic material model, according to Eq. (3.31), is considered. The material parameters are: Young's modulus $E_{\text{upper}} = 1 \times 10^2$ N/m^2 and $E_{\text{lower}} = 3 \times 10^2$ N/m^2, and Poisson's ratio $\nu = 0.3$ for both the rings. The plane strain assumption is used. Due to the symmetry with respect to the $y-$axis, only half of the setup is utilized. The bottom surface of the upper ring is used as a slave surface, while the outer top surface of the lower one as the master surface. A vertical displacement $\bar{u}_y = 4.0$ m is applied in the downward direction to the top surface of the

[3]The results presented in this section are taken from Agrawal and Gautam [123] with minor changes.

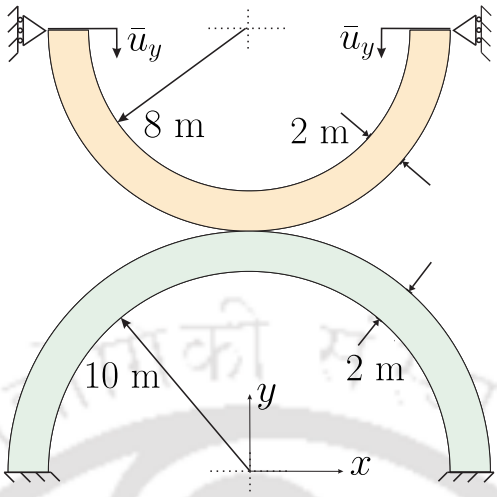

Figure 7.18: The setup of the two rings contact problem.

upper ring in 40 uniform load steps. The penalty parameters are taken as $\epsilon_{\mathrm{N}} = 100$ and $\epsilon_{\mathrm{T}} = 10$. The coefficient of friction $\mu_f = 0.1$ is used. The objective is to predict the normal and tangential reaction responses at the contact interface of the two rings using the VO based NURBS discretizations. The results obtained with standard N_2 based discretization are used for comparisons.

A coarse mesh having 12×3 number of elements in the angular and radial directions of the upper geometry, and 20×3 of the lower one is shown in Fig. 7.19a. Overall, three different meshes are used to carry out this simulation. These meshes have $(12, 20), (24, 40)$, and $(48, 80)$ number of elements across the contact boundary layer of the upper and lower geometries, and are denoted by m_1, m_2, and m_3, respectively. Numerical investigation reveals that N_2 based discretization using fine mesh m_3 delivers the converged normal and tangential contact pressure profiles for this example. Thus, the obtained result are used as the reference solutions. The deformed shapes of the setup with the vertical displacement field u_y at four different values of load steps with N_2 using mesh m_1 are shown in Figs. 7.19b-7.19e.

The normal contact pressure p_N and tangential contact pressure p_T with standard N_2 and N_4, and VO based $\mathrm{N}_2{-}\mathrm{N}_4$ and $\mathrm{N}_2{-}\mathrm{N}_{2{\cdot}1}$ discretizations using meshes m_1 and m_2 are shown in Fig. 7.20. The corresponding L_2-norm of the errors in p_N and p_T, calculated using Eq. (7.2), are summarized in Table 7.5. The overall computational time taken by different discretizations using both the meshes are provided in Table 7.6. From Fig. 7.20 two observations are made. First, the contact pressure curves of p_N

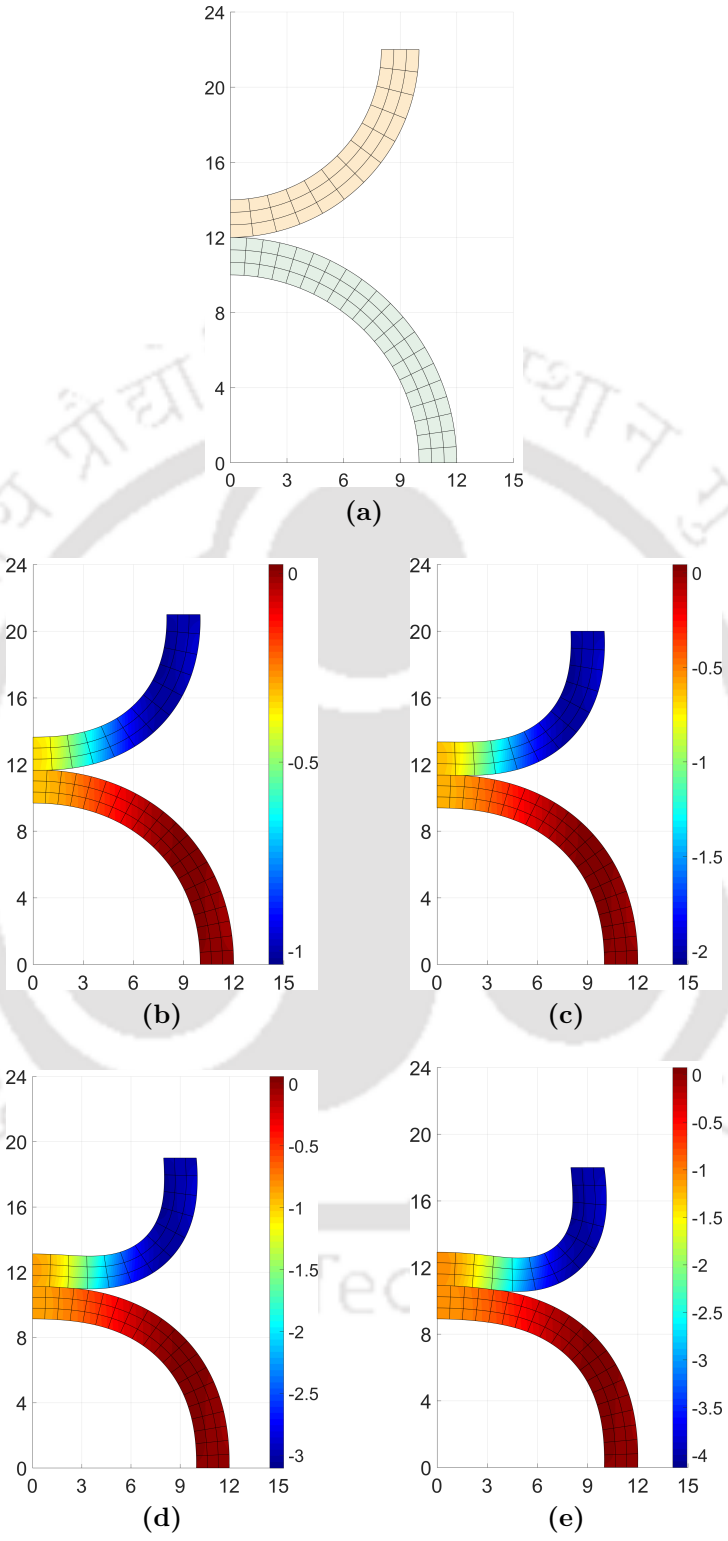

Figure 7.19: (a) The initial configuration of the setup along with the coarsest mesh m_1. The deformation configuration with the vertical displacement contours at load steps (b) $t = 10$; (c) $t = 20$; (d) $t = 30$; and (e) $t = 40$.

and p_T with higher-continuous VO based $N_2{-}N_4$ are nearly identical to those obtained with standard N_4 discretization for meshes m_1 and m_2. However, only a marginal improvement in the accuracy of results, attributed to higher smooth NURBS functions, is obtained as compared to N_2 discretization. Second, concerning the distribution of contact pressure across the contact interface at a fixed mesh, $N_2{-}N_{2\cdot1}$ is able to capture it more accurately than N_2 and $N_2{-}N_4$ (or N_4) based discretizations. As can be seen from Tables 7.5 and 7.6, it improves the accuracy of the normal contact pressure distribution by a factor of 3.4 and 9.9, and the tangential contact pressure distribution by 3.4 and 7.7 at a slightly more cost, i.e. 5.8% and 7.3%, than with the N_2 based

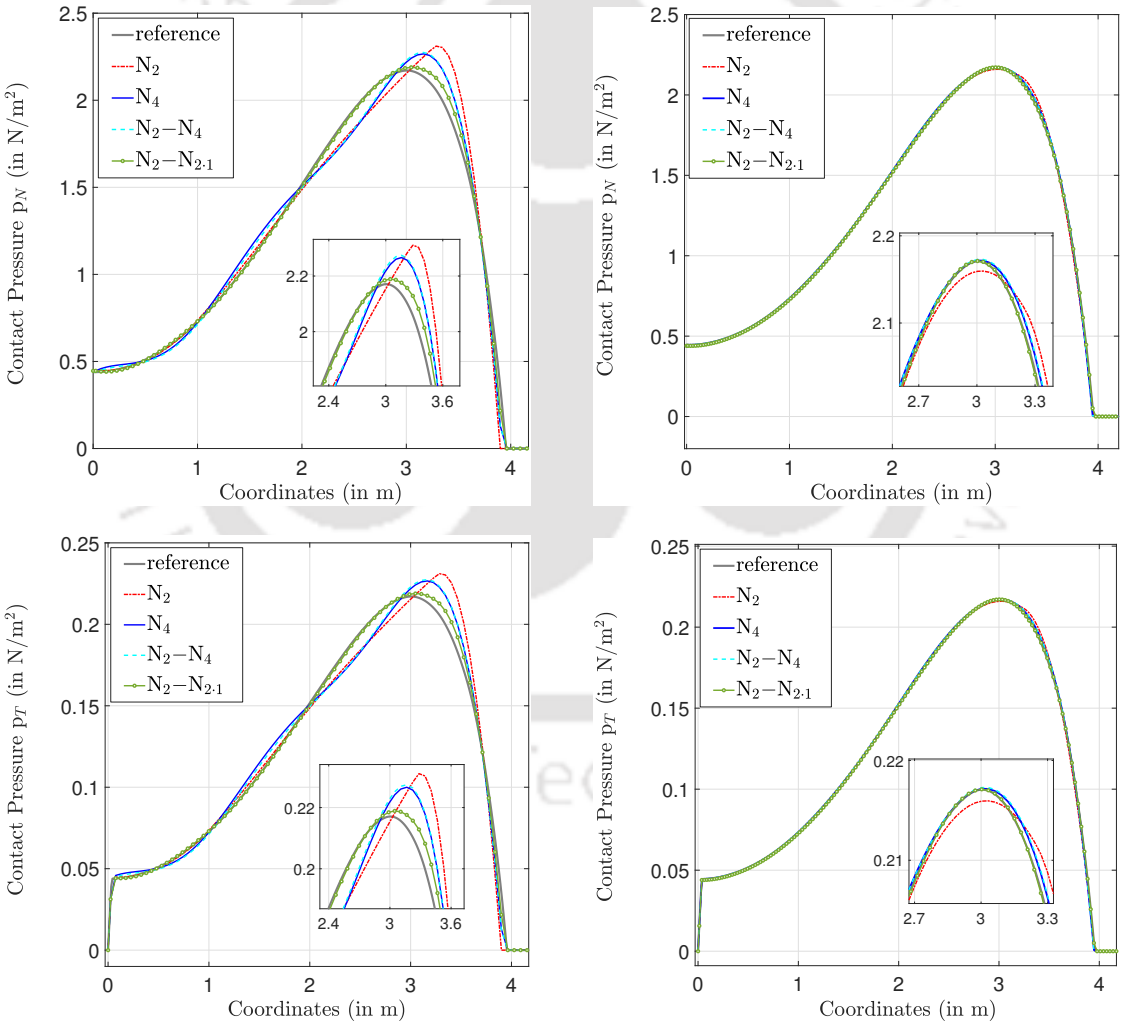

Figure 7.20: Comparison of the contact pressure p_N (top row) and p_T (bottom row) for different discretization at meshes m_1 (first column) and m_2 (last column).

discretization with meshes m_1 and m_2. In summary, this example demonstrates the benefit of using VO based NURBS discretization as compared to standard NURBS discretization. It provides a major gain in the accuracy at a cost only slightly more than with the standard NURBS discretization.

Discretization Type	$\|\|p_{N_{ref}} - p_N\|\|_2$		$\|\|p_{T_{ref}} - p_T\|\|_2$	
	m_1	m_2	m_1	m_2
N_2	24.38×10^{-2}	34.32×10^{-3}	24.38×10^{-3}	34.33×10^{-4}
N_4	17.45×10^{-2}	25.78×10^{-3}	17.45×10^{-3}	25.99×10^{-4}
N_2–N_4	17.18×10^{-2}	26.80×10^{-3}	17.18×10^{-3}	27.01×10^{-4}
N_2–$N_{2\cdot1}$	7.095×10^{-2}	3.433×10^{-3}	7.097×10^{-3}	4.429×10^{-4}

Table 7.5: L_2-norm of the error in p_N and p_T for different discretizations and meshes.

Discretization Type	**Normalized Time**	
	m_1	m_2
N_2	1.000	1.357
N_4	1.451	2.296
N_2–N_4	1.216	1.724
N_2–$N_{2\cdot1}$	1.058	1.475

Table 7.6: Overall analysis time taken by various discretizations with different meshes. The time taken by the N_2 at mesh m_1 is used for the normalization of time values.

7.4 Two-dimensional adhesive peeling problem

Next, in order to demonstrate the performance of the proposed varying-order based NURBS discretization method for other problem that is also dominated by the surface effects, a two-dimensional adhesive peeling problem is considered. The results with the standard NURBS discretizations that are taken from Agrawal and Gautam [128] are used for comparisons. But, before beginning the comparative assessment, it is useful to provide a brief overview of the different approaches that have so far been introduced for the efficient modeling of the peeling.

Numerical investigation of the peeling process has received a wide attraction due to its vast relevance in the many engineering as well as in applied science applications [50, 51, 129–135]. For example, in understanding the adhesive mechanism of various biological systems such as gecko pads [50, 51, 130–133], and elastic peeling of tape [134,

135], etc. However, the simulation of the peeling problems presents significant numerical challenges due to the localization of large peeling (or tensile) stresses within the very narrow zone ahead of the delamination front and large deformations [50, 51, 132, 136]. Unless a highly refined mesh description is chosen for the discretization of the peeling zone, the large gradient of the stresses results in a sequence of oscillation of global peeling load-deflection responses. Moreover, it strongly affects the convergence of standard Newton-Raphson (NR) iterations and can lead to the failure of the simulation [50]. As of now, a number of efficient solution approaches, namely, higher-order Lagrange FE [50], cubic-order Hermite enriched FE [50], fifth- and seventh-order Hermite enriched FE [137], NURBS-enriched FE [98], and hybrid isogeometric-FE discretizations [101] have been introduced for the accurate and stable peeling computations. Furthermore, it has also been demonstrated that the standard NURBS based discretization yields similar accurate results at a much lower number of DOFs than with the higher-order of Lagrange polynomial based discretization [137]. The results demonstrating the superior performance of the standard NURBS-based discretizations over the Lagrange polynomial based discretizations are shown in Appendix B for the reference purpose.

7.4.1 Problem setup

The setup of the problem, which is taken from Sauer [50], is shown in Fig. 7.21. In this, the peeling of an elastic strip from a flat, rigid substrate under the influence of van der Waals forces is analyzed. The geometrical details considered for the strip, i.e. $\mathrm{L} \times \mathrm{h} = 200\,\mathrm{L_o} \times 10\,\mathrm{L_o}$ ($\mathrm{L_o} = 1$ nm), resembles the dimensions of the spatula pad which is situated at the Gecko foot hairs' tip, see e.g. [132, 133, 138]. An isotropic hyperelastic Neo-Hookean model with Young's modulus $E = \mathrm{E_o}$ and Poisson's ratio $\nu = 0.2$ is taken under the plane strain condition, where $\mathrm{E_o} = 2$ GPa. The van der Waals forces are assumed to be active across the 75% length of the strip, i.e. from

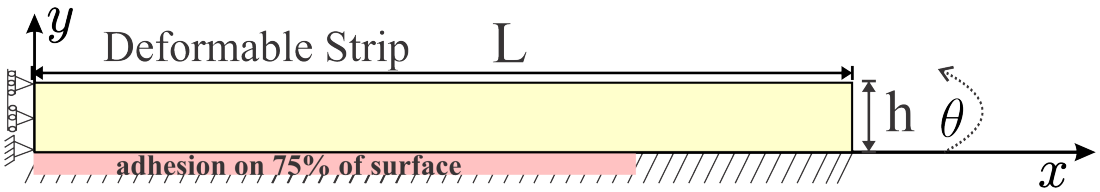

Figure 7.21: The set-up of the strip peeling example.

$x = 0$ to $x = 150$ nm as shown in Fig. 7.21 [50]. The van der Waals interaction forces are calculated using Eq. (4.29), with $r_0 = 0.4$ nm and $A_{\mathrm{H}} = 10^{-19}$ J. These parameters corresponds to the value of gecko spatula adhesion [109, 132, 133, 138]. Initially, the strip is considered to be adhering to the rigid substrate such that the setup is in the equilibrium state. Hence, no interaction forces are active. For peeling the strip from its reference configuration, an external rotation angle θ is applied to its right edge, as shown in Fig. 7.21. The rotation angle is applied in such a manner that it provides a constant bending moment M as a reaction response during the peeling process. Here, a prescribed rotation step size $\Delta\theta = 0.1^{\circ}$ is used for the overall analysis. Three different meshes that are obtained through the knot insertion strategy are used to examine the convergence performance of each discretization type, see Table 7.7 for mesh details.

The improvement in the accuracy of the peeling computations on increasing the inter-element continuity as well as the interpolation order of the NURBS with the proposed VO based discretization method is analyzed. The results with the standard higher-continuous N_p ($p = 2$, 4, 6, and 8) as well as a higher-order based $\mathrm{N}_{2\cdot1}$ NURBS discretizations are used for the comparative assessment. It is noted that in case of higher-order based NURBS discretization, i.e. denoted by $\mathrm{N}_{2\cdot1}$, one additional step of order elevation is uniformly applied to N_2 based NURBS discretization. With this, the interpolation order of the NURBS is elevated to 3, while their smoothness remains unchanged, as discussed in Section 2.3.2. Consequently, a large number of DOFs are obtained at a fixed mesh as compared to N_2, see the last column of Table 7.8. In case of VO based discretization, N_2 order of NURBS are used for the bulk computations while for the contact surface both the higher-continuous and higher order based N_{p_c} ($p_c =$ 4, 6, 8, $2 \cdot 1$, and $2 \cdot 2$) discretizations are applied.

Mesh	**Total elements** $(n_x \times n_y)$
m_1	160×8
m_2	200×10
m_3	240×12

Table 7.7: Total number of elements $(n_x \times n_y)$ along the length and height of the strip, respectively, with different meshes.

The deformed configurations of the strip at different rotation angles are shown in Fig. 7.22. Figure 7.23 shows the corresponding variation of the bending moment with the applied rotation angle θ for N_2 based NURBS discretization at mesh m_2. As the

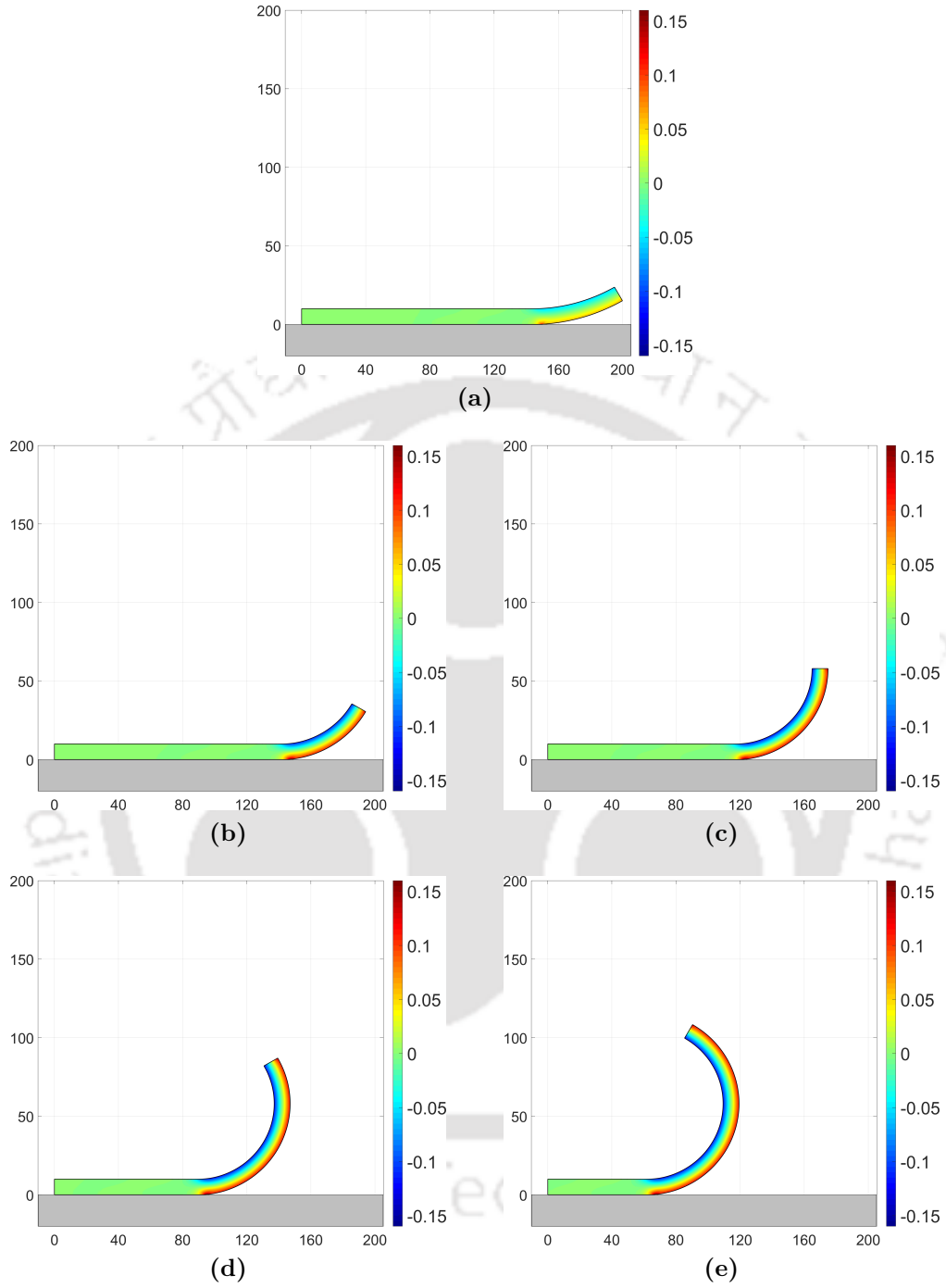

Figure 7.22: Deformed configurations of the strip with N_4 discretization at rotation angles: (a) $\theta = 30^o$, (b) 60^o, (c) 90^o, (d) 120^o, and (e) 150^o. The coloring in the deformed configurations shows the first stress invariant $I_1 = \text{tr}(\boldsymbol{\sigma})$ normalized by E.

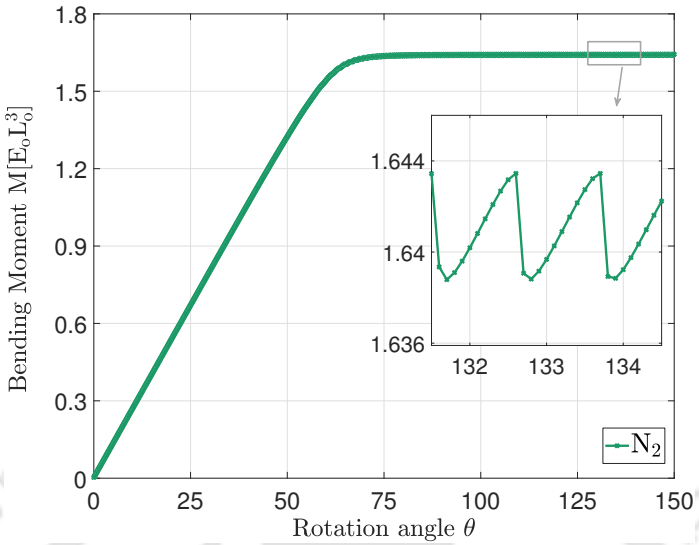

Figure 7.23: Overall bending moment responses M over a rotation angle θ with N_2 at mesh m_2. Here, $E_oL_o^3 = 2$ nN·nm.

figure illustrates, initially, the bending moment increases linearly with θ during the bending of the strip from $x = 200$ nm to $x = 150$ nm. This is due to the absence of adhesive forces within this zone, see Fig. 7.4.1. After that, during the peeling of the strip from the adhesive zone, a macroscopically constant bending curve is obtained. However, the enlarged view of the macroscopically constant part of the curve (see the inset in Fig. 7.23) shows that the bending moment oscillates around a mean value rather than being constant. The occurrence of a large gradient of peeling stress in the very narrow zone ahead of the delamination front leads to the oscillation of the peeling bending moment during the peeling process.

7.4.2 Numerical difficulty in the peeling analysis

A prerequisite for the accurate peeling computation is that the mesh size ahead of the delamination front should be sufficiently small to properly resolve the large gradient of stresses. Otherwise, insufficient or lower-order discretization causes a sequence of non-physical oscillation of the bending moment around a mean line during peeling rather than being constant, as shown by the enlarged view in Fig. 7.23. The oscillation wavelength is dictated by the element size. The steep negative slope of these bending moment oscillation strongly affects the convergence behavior of Newton-Raphson iterations utilized for the solution of a non-linear problem. It can also lead to failure

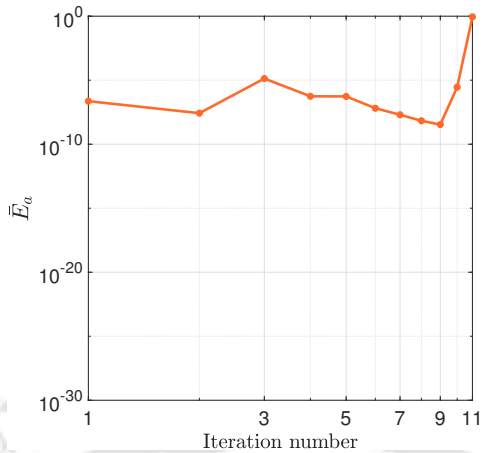

Figure 7.24: The illustration of the divergence of Newton-Raphson iterations with N_2 based discretization at the coarsest mesh m_1. The average energy residual per unconstrained DOF ($\bar{E}_a$) is plotted over the iteration number.

of the analysis if a lower order of discretization at a coarse mesh is chosen, see the plot of divergence of NR iteration with N_2 at mesh coarsest mesh m_1 in Fig. 7.24. Thus, a reduction not only in the amplitude of the oscillation of adhesive responses but also of the steep downward slope is desired for the accurate as well as stable peeling computations.

7.4.3 Computation of the peeling responses

The variation of the bending moment M over the applied rotation angle θ with different standard and VO based NURBS discretizations at mesh m_2 is shown in Fig. 7.25. Here, the influence of interpolation order as well as inter-element continuity of the NURBS discretization is investigated on the bending moment oscillation amplitude ΔM, maximum and minimum values of the bending curve slopes, i.e. max(dM/dθ) and min(dM/dθ), respectively. The quantitative details of ΔM, max(dM/dθ), min(dM/dθ) as well as total number of DOFs for each case are given in Table 7.8 with three different meshes, i.e. m_1, m_2, and m_3.

From Figs. 7.25 it can be observed that the bending moment curve with the VO based discretizations N_2–N_p ($p = 4,\ 6,\ 8,$ and $2 \cdot 1$) are nearly identical to those obtained with corresponding standard N_p cases. This is due to employing the same types of NURBS functions for the evaluation of contact integrals. While in the case of VO based discretizations, the lower order NURBS are used for the bulk computations.

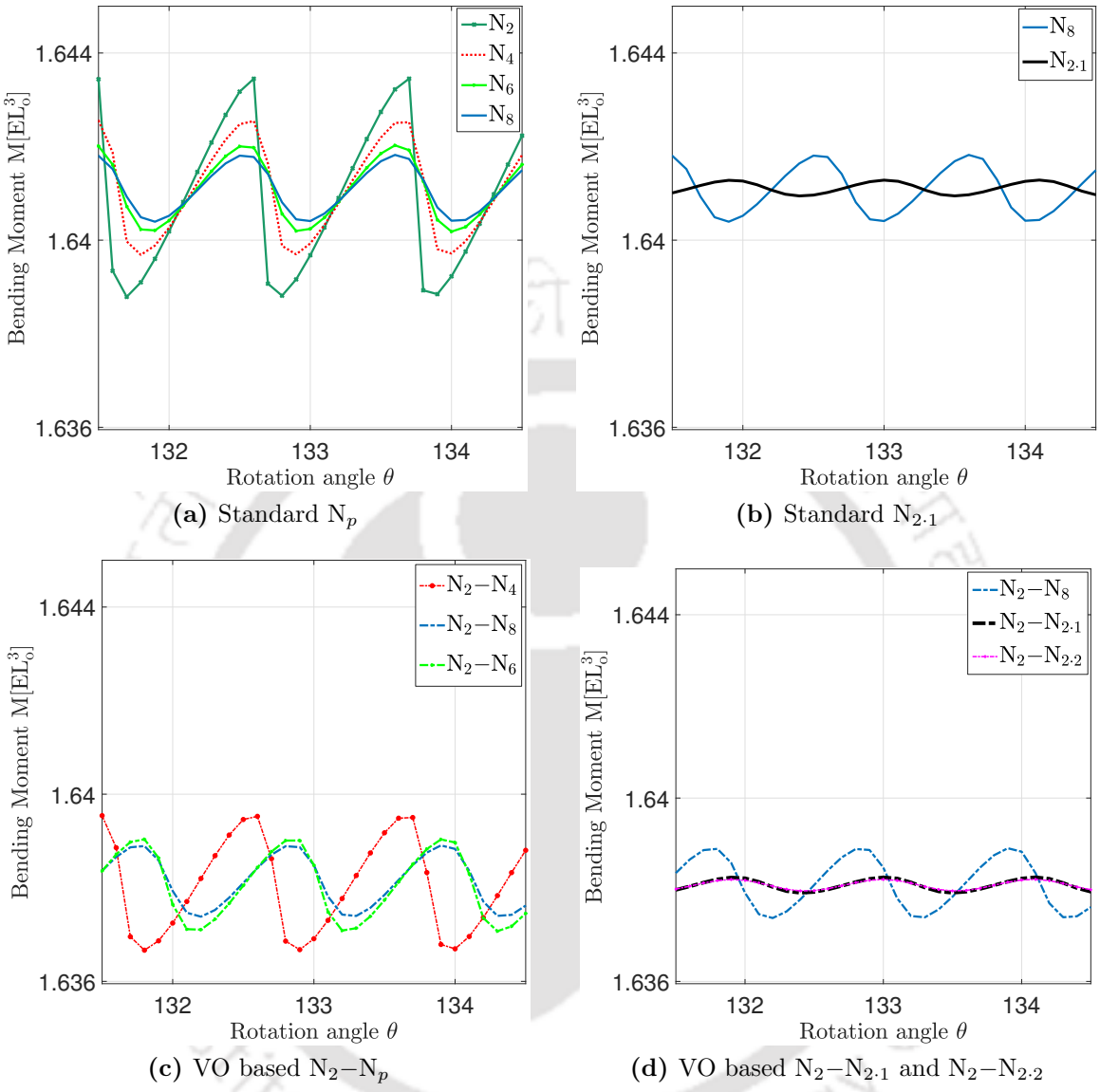

(a) Standard N_p **(b)** Standard $N_{2\cdot1}$

(c) VO based N_2-N_p **(d)** VO based $N_2-N_{2\cdot1}$ and $N_2-N_{2\cdot2}$

Figure 7.25: Variation of bending moment over the rotation angle with the standard (top), and VO (bottom) based NURBS discretizations at medium mesh m_2.

It can be seen that with increasing the continuity of the NURBS, only a monotonic improvement in the quality of the result is observed. Quantitatively, N_2-N_8 reduces the oscillation amplitude by a factor of 2.92 and negative slope by 5.25 to that attained with N_2, see Table 7.9. This is since N_2-N_8 has only 12 number of additional DOFs as compared to N_2, see Table 7.8. Thus, the improvement attained with N_2-N_8 is not very large.

On the other hand, comparing the result with higher-order based discretizations, i.e. with $N_2{-}N_{2\cdot1}$, to that of smoother N_p (p = 2, 4, 6, and 8) discretizations, it is evident that the VO based higher-order discretization is advantageous as it provides the considerable gain in the accuracy for peeling computations, see Tables 7.8 and 7.9

Discretization Type	**Mesh**	ΔM $\times10^{-3}$	max(dM/dθ) $\times10^{-3}$	min(dM/dθ) $\times10^{-3}$	**Total DOFs**
N_2	m_1	–	–	–	2916
N_4	m_1	6.9489	7.4972	-64.1522	2952
N_6	m_1	4.8673	5.9933	-35.3973	2988
N_8	m_1	3.7054	5.3543	-18.3877	3024
$N_{2\cdot1}$	m_1	0.8272	1.3965	-2.8673	5796
$N_2{-}N_4$	m_1	7.2540	6.9426	-140.119	2920
$N_2{-}N_6$	m_1	5.1649	5.9937	-44.3120	2924
$N_2{-}N_8$	m_1	3.8514	5.6709	-24.3521	2928
$N_2{-}N_{2\cdot1}$	m_1	0.8841	1.4041	-2.9066	3236
$N_2{-}N_{2\cdot2}$	m_1	0.6391	1.2819	-1.4471	3556
N_2	m_2	4.2825	6.3906	-35.1618	4444
N_4	m_2	2.8824	5.1276	-18.4271	4488
N_6	m_2	1.7963	3.8046	-7.6738	4532
N_8	m_2	1.3970	3.0044	-5.5028	4576
$N_{2\cdot1}$	m_2	0.3404	0.8285	-1.0830	8844
$N_2{-}N_4$	m_2	2.8492	4.8967	-17.6168	4448
$N_2{-}N_6$	m_2	1.9246	3.7178	-9.9547	4452
$N_2{-}N_8$	m_2	1.4904	3.1863	-6.7062	4456
$N_2{-}N_{2\cdot1}$	m_2	0.3364	0.8075	-0.9876	4844
$N_2{-}N_{2\cdot2}$	m_2	0.2498	0.6416	-0.7136	5244
N_2	m_3	1.6788	3.7233	-8.9545	6292
N_4	m_3	1.0942	2.9194	-5.0689	6344
N_6	m_3	0.6982	1.9106	-2.5468	6396
N_8	m_3	0.5464	1.4583	-1.8001	6448
$N_{2\cdot1}$	m_3	0.1309	0.4456	-0.5109	12532
$N_2{-}N_4$	m_3	1.0926	2.8125	-5.2290	6296
$N_2{-}N_6$	m_3	0.7005	2.0392	-2.5885	6300
$N_2{-}N_8$	m_3	0.5764	1.6384	-2.1005	6304
$N_2{-}N_{2\cdot1}$	m_3	0.1418	0.4584	-0.4835	6772
$N_2{-}N_{2\cdot2}$	m_3	0.0968	0.3186	-0.3282	7252

Table 7.8: Bending moment oscillation amplitude ΔM, maximum slope max(dM/dθ), minimum slope min(dM/dθ) of amplitude, and the total number of DOFs for different standard and VO based NURBS discretizations at meshes m_1, m_2, and m_3.

for the numeric values. As compared to N_2, $N_2{-}N_{2\cdot1}$ reduces the oscillation amplitude and negative slope by a factor of 12.72 and 35.58, respectively, see Table 7.9. For this, it takes only 9% number of additional DOFs than with N_2, see Table 7.8. Furthermore, for the nearly equivalent accuracy level, $N_2{-}N_{2\cdot1}$ utilizes 45% lower number of DOFs as compared to standard higher-order based $N_{2\cdot1}$ discretization. It can be further observed that with additionally elevating the interpolation order of the $N_2{-}N_{2\cdot1}$ based discretization to $N_2{-}N_{2\cdot2}$, the quality of the result improves slightly. For this, it takes only 7.62% additional number of DOFs than needed with $N_2{-}N_{2\cdot1}$. Thus, the obtained results show that VO based NURBS discretization is a much more efficient choice to obtain the similar or better accuracy for the peeling computations over the standard NURBS discretization.

Discretization Type	ΔM in (%)	max(dM/dθ) in (%)	min(dM/dθ) in (%)
N_2	100	100	100
N_4	67.31	80.23	52.41
N_6	41.95	59.54	21.82
N_8	32.62	47.01	15.65
$N_{2\cdot1}$	7.95	12.96	3.08
$N_2{-}N_4$	66.53	76.62	50.10
$N_2{-}N_6$	44.94	58.17	28.31
$N_2{-}N_8$	34.14	49.07	19.04
$N_2{-}N_{2\cdot1}$	7.86	12.64	2.81
$N_2{-}N_{2\cdot2}$	5.82	10.04	2.02

Table 7.9: Reduction in the oscillation amplitude (ΔM), maximum slope (max(dM/dθ)), and minimum slope (min(dM/dθ)) of the bending moment curve (in %) with the different standard and VO based NURBS discretizations at medium mesh m_2. The results with N_2 are used as a reference.

7.4.4 Convergence study

Next, the convergence of the bending moment oscillation amplitude and the negative slope is investigated for various discretizations for three different meshes m_1, m_2 and m_3. Figure 7.26 shows the convergences of the bending moment curves for the $N_{2\cdot1}$, $N_2{-}N_{2\cdot1}$ as well as $N_2{-}N_{2\cdot2}$ based discretizations. It can be seen that for a fixed mesh resolution, $N_2{-}N_{2\cdot1}$ (or $N_2{-}N_{2\cdot2}$) provides nearly identical (or slightly better) results

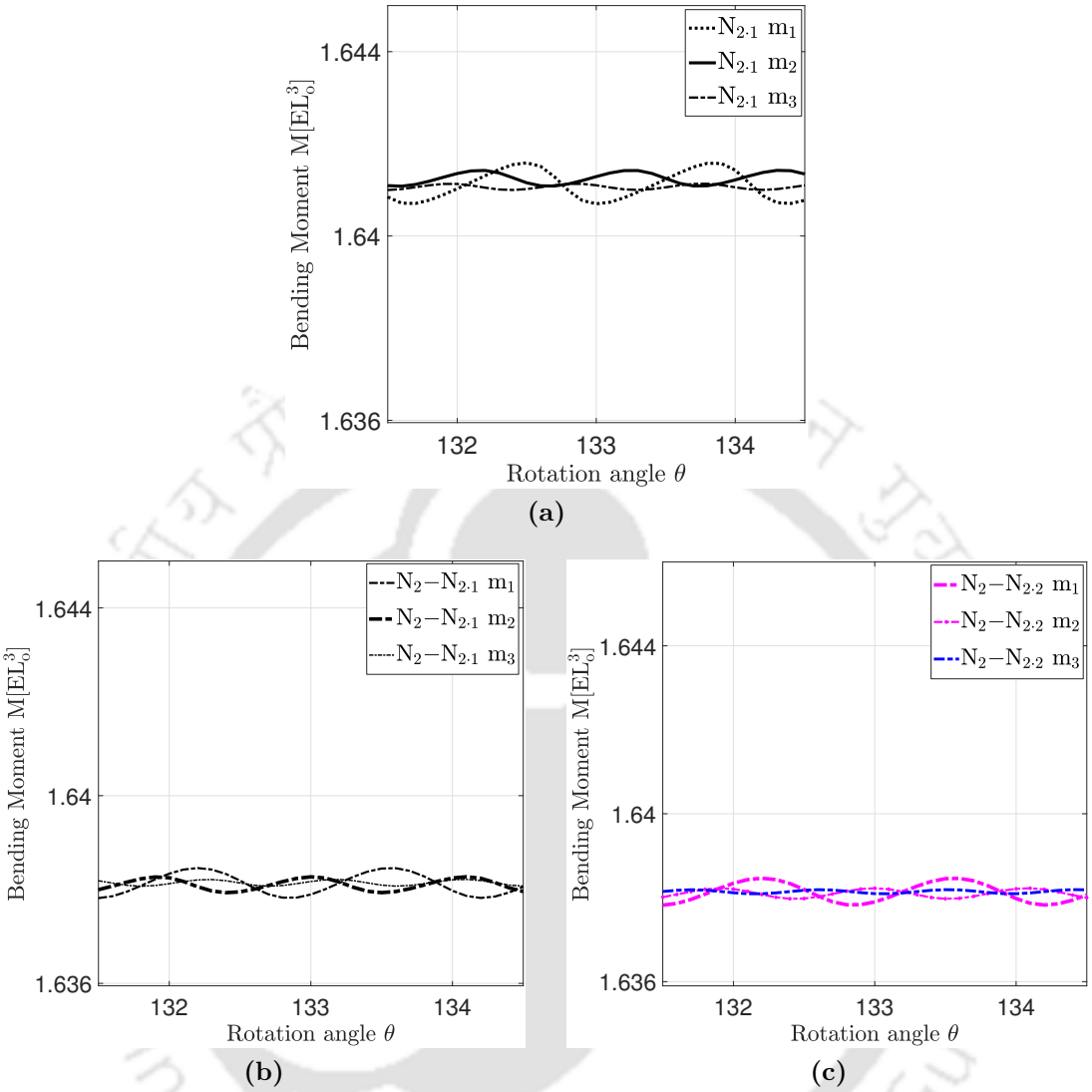

Figure 7.26: Convergence of the bending moment curves over the rotation angle with (a) standard $N_{2\cdot1}$, and VO based (b) $N_2{-}N_{2\cdot1}$ and (c) $N_2{-}N_{2\cdot2}$ NURBS based discretizations with three different meshes.

with at least 44% (or 39%) lower number of DOFs than with $N_{2\cdot1}$, see Table 7.8 for DOFs details.

The convergence of the ΔM for different VO based and standard NURBS discretizations is shown in Fig. 7.27. It can be observed that for all types of discretizations, a higher mesh resolution leads to smaller bending moment oscillation amplitude. The convergence rate of bending moment ΔM is nearly the same for all types of discretizations. However, the absolute value differs from each other. N_2 fails to converge at a

mesh m_1, being very coarse to adequately resolve the adhesion zone. Among all the tested cases, it can be observed that the proposed VO based higher-order discretizations, i.e. $N_2{-}N_{2{\cdot}1}$ and $N_2{-}N_{2{\cdot}2}$ accomplish much more accurate results than with the standard higher-continuous N_p or with higher-order $N_{2{\cdot}1}$ based discretizations for a fixed mesh resolution. However, it is again useful to note that $N_2{-}N_{2{\cdot}1}$ (or $N_2{-}N_{2{\cdot}2}$) utilizes at least 44% (or 39%) lower number of DOFs than needed with the most accurate standard $N_{2{\cdot}1}$ based discretization to obtain the nearly identical (or slightly better) result at a fixed mesh, see Table 7.8. Furthermore, a closer look at Fig. 7.27 reveals that the result with $N_{2{\cdot}2}$ at coarsest mesh m_1 nearly matches with that of obtained with N_8 at mesh fine mesh m_3, see also Table 7.8 for quantitative values. Thus, with $N_2{-}N_{2{\cdot}2}$, an accuracy similar to N_8 can be achieved at approximately 44.9% lower number of DOFs than with the N_8 based discretization, see Table 7.8.

In summary, this example shows the efficacy of the proposed method for the peeling computations over the standard NURBS based discretizations. For a fixed mesh, with the VO based NURBS discretization, a considerable gain in the accuracy can be obtained as compared to N_2 with slightly more number of DOFs. For a similar accuracy level, it uses a much lower number of DOFs than needed with the standard NURBS based discretizations.

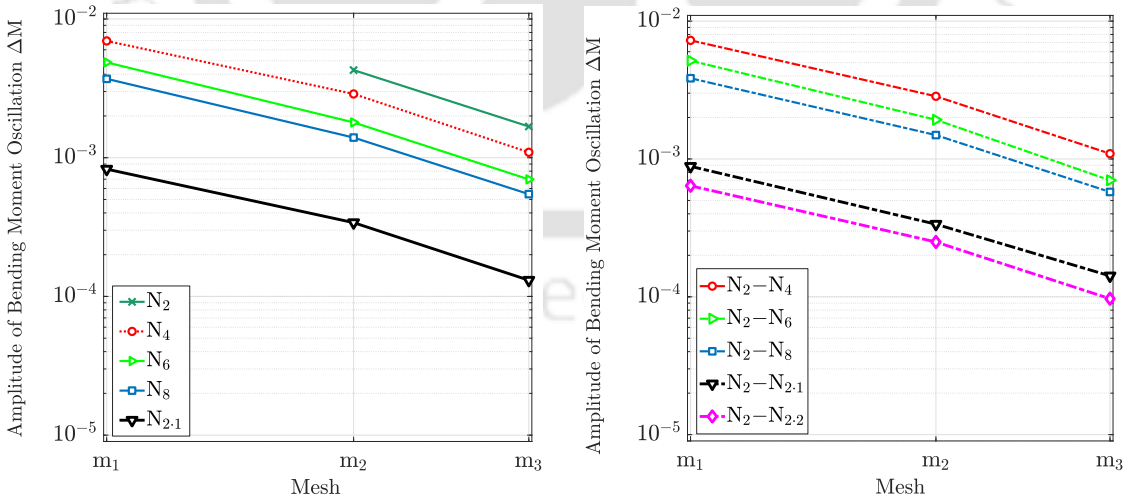

(a) Standard NURBS discretizations **(b)** VO based NURBS discretizations

Figure 7.27: Convergence of the bending moment oscillation amplitude ΔM for various NURBS discretizations with three different meshes.

7.5 Three-dimensional frictionless ironing

In this example, the three-dimensional frictionless sliding contact between two deformable bodies using the geometrical setup similar to the one utilized by Temizer et al. [47] is considered. This example is used to analyze the performance of the VO based NURBS discretization for the isogeometric analysis of three-dimensional large-deformation contact as compared to standard NURBS based discretizations. In this, a deformable indentor, which is of an approximate size $10 \times 10 \times 11$ and having spherical shaped contact surface, is first pressed onto a deformable slab of size $100 \times 30 \times 22$. After applying the vertical displacement $U_z = -10.4$ in 52 uniform load steps on its top surface, the indentor is slid across the slab by applying $U_x = 75.0$ in 250 load steps while maintaining the vertical displacement constant. The bottom surface of the slab is restrained in all the displacement directions. The mesh considered for the indentor (i.e. $5 \times 5 \times 3$) and slab (i.e. $18 \times 6 \times 4$) are shown in Fig. 7.28. The Neo-Hookean material behaviour, given by Eq. (3.31), is considered for both bodies, with the same material parameters: $E = 1$ and $\nu = 0.3$. The penalty parameter is $\epsilon_{\mathrm{N}} = 100$. The deformed configurations of the setup at different load instances are shown in Fig. 7.29 with quadratic NURBS based discretizations. Here, the half-view of the indentor and slab is shown to provide better visuals of the surface deformation and the stress within

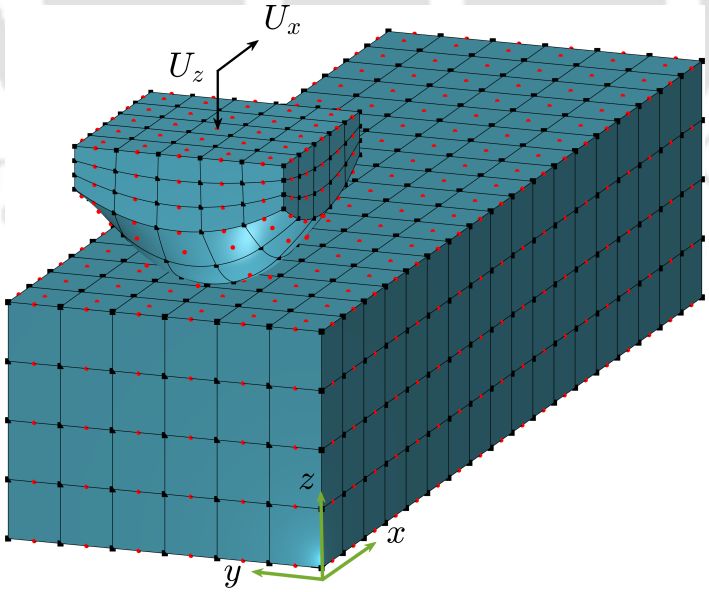

Figure 7.28: Three-dimensional frictionless ironing problem: The setup and the mesh considered for the indentor and slab.

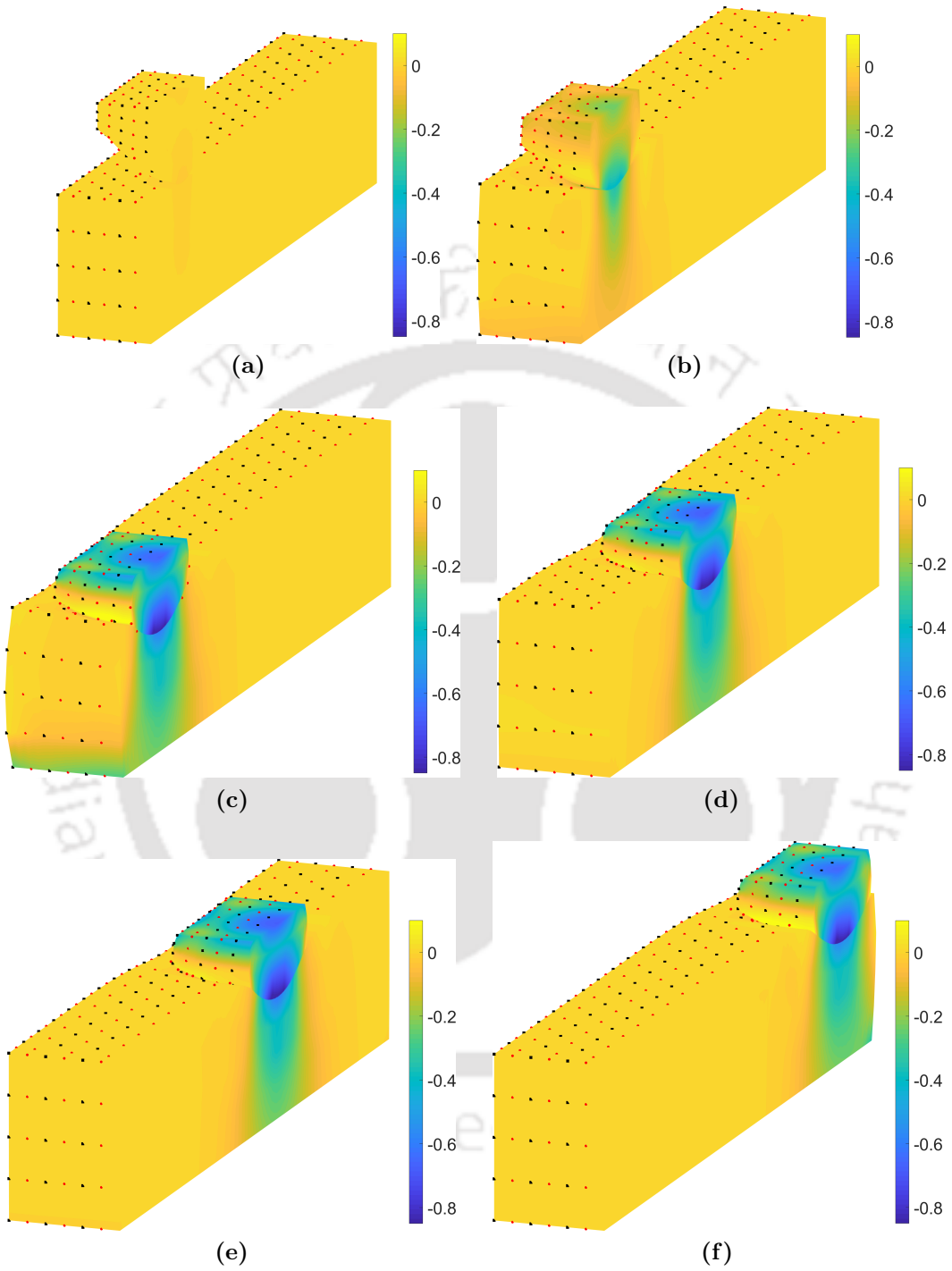

Figure 7.29: Three-dimensional frictionless ironing: Deformed configuration of the setup during the compression stage at load step (a)-(c) $t = 1,\ 26,$ and 52, and during the sliding stage at step (d)-(f) $t = 127,\ 202,$ and 302 with N_2. The color show the distribution of the vertical stress σ_{33}. The associated control points are shown with the red dots and unique knot entries with the black squares.

the interior of the bulk domain. The deformed meshes are colored by the normal stress σ_{33}. The objective is to demonstrate the coarse mesh accuracy of the proposed VO based NURBS discretization method for three-dimensional contact computations over the standard NURBS based discretizations.

Figure 7.30a shows the evolution of the total vertical and horizontal contact forces, computed at the top surface of the indentor, with different VO based $\mathrm{N}_2{-}\mathrm{N}_{p_c}$ ($p_c = 3$, and 4) and the standard N_p ($p = 2\,, 3$ and 4) based NURBS discretizations. The enlarged views of the vertical and horizontal force curves are provided in Figs. 7.30b and 7.30c, respectively. Moreover, the results with VO based higher-order NURBS discretizations, i.e. with $\mathrm{N}_2{-}\mathrm{N}_{2\cdot1}$ and $\mathrm{N}_2{-}\mathrm{N}_{2\cdot2}$, are shown in Fig. 7.31. It is noted that the small shift in the level of contact force curves is due to the increase of the number of control points with the higher-order discretizations as compared to the N_2 case. In the case of VO NURBS discretizations, since the quadratic order of NURBS are sufficient to describe the setup exactly, it is kept fixed for the bulk computations. The reduction in the oscillation error corresponding to different standard and VO based NURBS discretizations is summarized in Table 7.10 for both the vertical and horizontal contact forces. As in the first example, the oscillation amplitude of the reaction forces is computed using $\Delta P_j := \max(P_j) - \min(P_j)$, where $j = z$, and x. The total number of DOFs present on the contact surface and in the bulk domain with different discretizations are listed in Table 7.11.

With the obtained results, four major observations are drawn. First, although N_2 based discretization provides sufficient continuity across the contact surface, a large-amplitude of periodic oscillations in the vertical and horizontal contact forces is present. Clearly, N_2 at a coarse mesh is not capable of yielding sufficiently accurate contact forces for large deformation contact. This is due to the limited conforming ability of the contact surfaces with N_2. Second, the obtained results verify the validity of the proposed VO based NURBS discretization method for three-dimensional contact, as the contact force curves are nearly indistinguishable for VO based $\mathrm{N}_2{-}\mathrm{N}_{p_c}$ ($p_c = 3$, and 4) and standard N_p ($p = 3$, and 4) based discretizations. The third observation is that with employing the higher-continuous based NURBS discretizations, i.e. N_3 or $\mathrm{N}_2{-}\mathrm{N}_3$ and N_4 or $\mathrm{N}_2{-}\mathrm{N}_4$, only a small improvement in the accuracy is attained as compared to N_2, see Table 7.10 for quantitative values. This is due to the fact that the usage of higher-continuous NURBS for the evaluation of contact integrals leads to the marginal enhancement in the conforming ability of the contact interface at a fixed

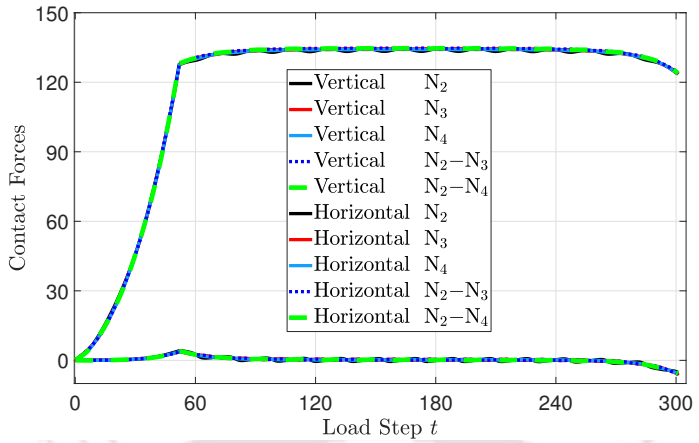

(a)

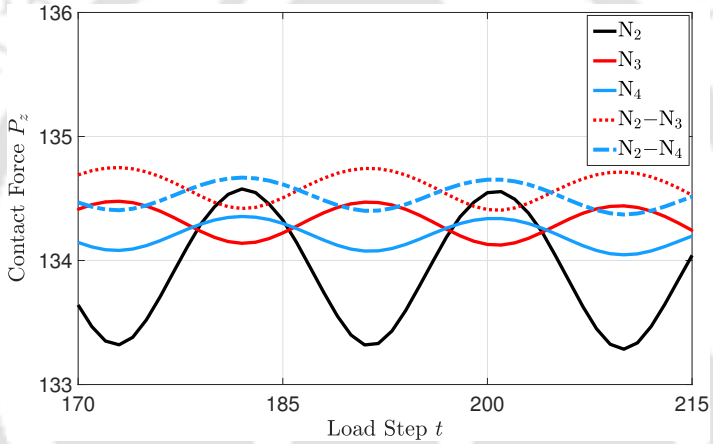

(b)

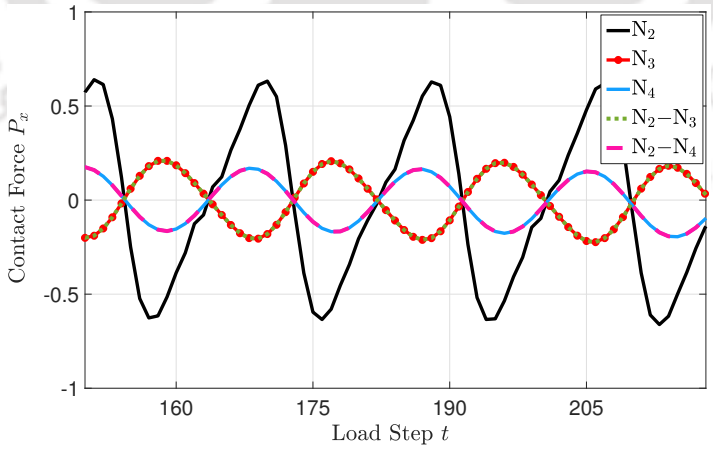

(c)

Figure 7.30: (a) Total vertical and horizontal contact forces over load step t. Enlarged view of (b) vertical contact force P_y oscillation and (c) horizontal contact force P_x oscillation with different standard and VO based NURBS discretizations.

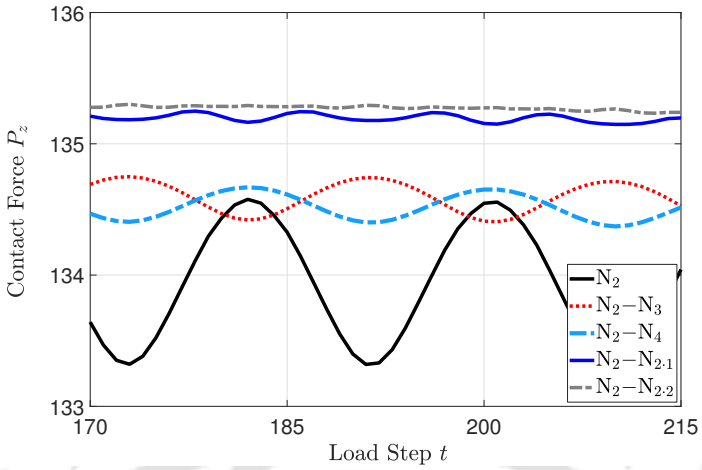

(a)

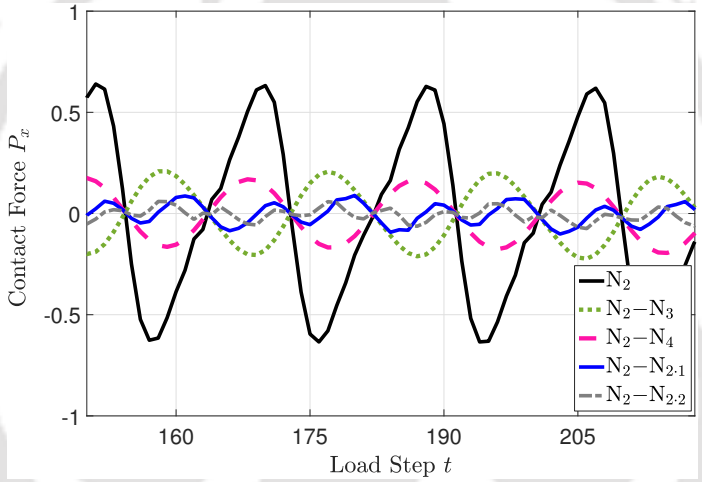

(b)

Figure 7.31: Enlarged view of the (a) vertical and (b) horizontal contact forces oscillations with VO based higher-order NURBS discretizations at mesh m_1.

mesh [47]. The fourth observation reveals that with the higher-order based VO NURBS discretization, i.e. with $N_2{-}N_{2\cdot1}$, a much more accurate result is obtained among all testes cases. Quantitatively, it reduces the oscillation error to 6.60% and 14.40% in the vertical and horizontal contact forces, respectively, as compared to that observed with N_2, see Table 7.10. This is due to moderate multi-knot span support of the higher-order basis function, as discussed in Section 5.1.1 and a large number of DOFs present on the contact surface as compared to other discretizations, see Table 7.11 for DOFs details. Furthermore, it can be observed that with the more higher-order based VO NURBS discretization, i.e. with $N_2{-}N_{2\cdot2}$, the accuracy of the results further

improves. It reduces the oscillation amplitude of the vertical and horizontal contact forces to 1.65% and 9.16%, respectively, of that observed with N_2 based discretization. However, as compared to $N_2{-}N_{2{\cdot}1}$, only a marginal improvement is achieved.

Discretization Type	ΔP_z (%)	ΔP_x (%)
N_2	100	100
N_3	27.49	33.12
N_4	22.04	26.22
$N_2{-}N_3$	26.80	33.11
$N_2{-}N_4$	21.14	26.22
$N_2{-}N_{2{\cdot}1}$	6.60	14.40
$N_2{-}N_{2{\cdot}2}$	1.65	9.16
N_2 (fine mesh)	14.06	4.54

Table 7.10: Reduction in the oscillation amplitude of the vertical and horizontal contact forces with different standard and VO based NURBS discretizations. The result with N_2 is used as a reference.

Discretization	**DOF for indentor**			**DOF for slab**			**Total**
Type	**Interface**	**Bulk**	**Total**	**Interface**	**Bulk**	**Total**	**DOF**
N_2	147	441	588	480	1920	2400	2988
N_3	192	576	768	567	2268	2835	3603
N_4	243	729	972	660	2640	3300	4272
$N_2{-}N_3$	192	441	633	567	1920	2487	3120
$N_2{-}N_4$	234	441	675	660	1920	2580	3264
$N_2{-}N_{2{\cdot}1}$	432	441	873	1596	1920	3516	4389
$N_2{-}N_{2{\cdot}2}$	867	441	1308	3360	1920	5280	6588
N_2 (fine mesh)	432	2592	3024	1596	12768	14364	17388

Table 7.11: DOFs values for the indentor and slab for different VO and standard NURBS based discretizations.

Besides, the results obtained with standard N_2 based discretization at a fine mesh, i.e. $10 \times 10 \times \times 6$ for the die and $36 \times 12 \times 8$ for the slab, are additionally shown in Fig. 7.32 to further demonstrate the comparative coarse mesh performance of the VO based $N_2{-}N_{2{\cdot}1}$ and $N_2{-}N_{2{\cdot}1}$ discretizations. The quantitative details of the reduction in the oscillation error for both the vertical and horizontal contact forces and the total number of DOFs present on the contact surface and in the bulk domain of each body with N_2 at the fine mesh are also provided in Tables 7.10 and 7.11, respectively. Based

on the obtained results, it can be observed that to attain the accuracy similar to that attained with N_2 at a fine mesh, VO based $N_2{-}N_{2\cdot1}$ and $N_2{-}N_{2\cdot2}$ discretizations at the (initial) coarse mesh take approximately 3.9 and 2.6 times lower number of total DOFs, respectively.

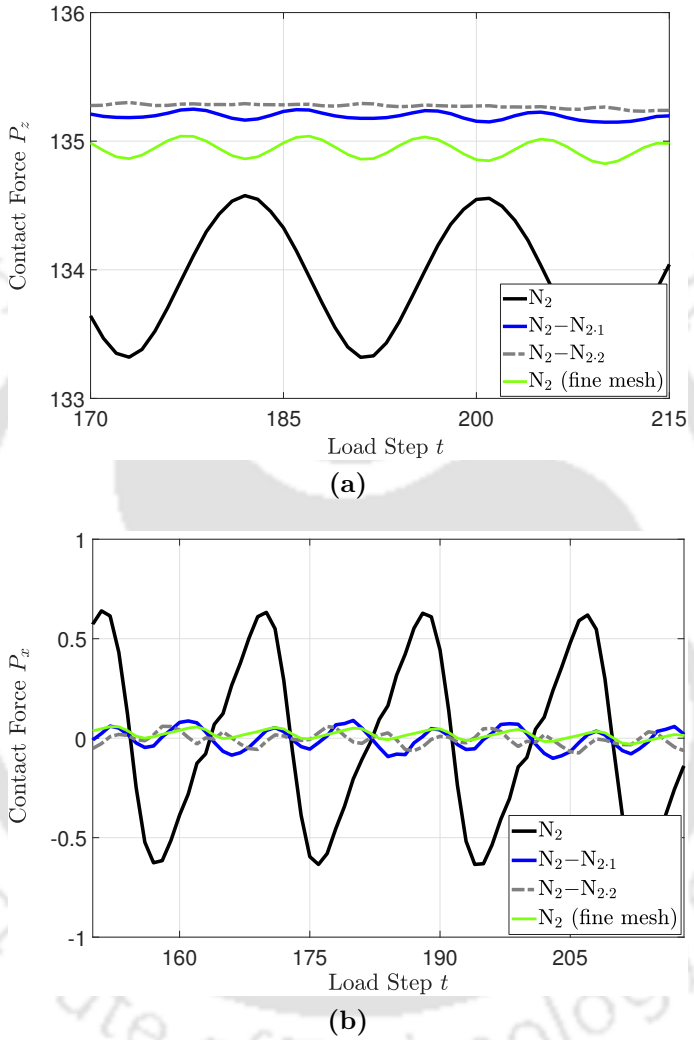

Figure 7.32: Comparison of the (a) vertical and (b) horizontal contact forces oscillations with VO based $N_2{-}N_{2\cdot1}$ and $N_2{-}N_{2\cdot2}$ at the coarse mesh and with the standard N_2 based discretization at the fine mesh.

In summary, this example demonstrates the much higher coarse mesh accuracy of the proposed VO based NURBS discretization method over the standard NURBS discretizations for three-dimensional contact computations. To yield the similar accuracy, the VO based NURBS discretization takes a much lower number of DOFs than needed with N_2.

Chapter 8

Conclusions and Scope for Future Work

This chapter first presents the summary of the work carried out in this thesis, followed by the conclusions that are drawn based on the results presented in Chapter 7. Finally, an outlook for various possible future research directions is given.

8.1 Summary

In this thesis, a novel varying order based NURBS discretization method is introduced to enhance the performance of the isogeometric analysis technique for contact problems. It enables the arbitrary order of NURBS based description of the contact boundary layer in a lower-order of NURBS discretized geometry. It allows control over the inter-element continuity as well as the interpolation order of the NURBS for the discretization of the contact surface. With this, the higher-continuous and higher-order NURBS basis functions are utilized only for the evaluation of the contact integrals, while the lower-order NURBS are used for the bulk computations.

A Gauss-point-to-surface contact formulation is combined with the introduced methodology towards developing a simple yet computationally efficient technique for the isogeometric analysis of two- and three-dimensional problems involving contact between deformable bodies. In the developed formulation, the normal and sticking contact constraints are enforced independently at each quadrature point. For the regularization of the contact constraints, the penalty method is employed. The tangential

traction during the frictional sliding is defined using Coulomb's friction law. In order to include the contributions of actual quadrature points that come into contact during the deformation of bodies, an active set strategy is utilized. The tangential traction during the advancement of frictional states from stick to slip is updated based on the predictor-corrector algorithm. An isotropic compressible Neo-Hookean hyperelastic material model is considered to describe the nonlinear stress-strain material behaviour of the contacting bodies undergoing large deformations. The system of nonlinear equations corresponding to the internal and contact force vectors is linearized and solved using the Newton-Raphson iterative method. For the evaluation of the bulk and contact integrals, the Gauss-quadrature rule is employed.

For the numerical simulation of contact problems using the NURBS-based isogeometric analysis technique, an in-house computer code is developed to simulate large deformation contact problems between two deformable bodies in two- and three-dimensional settings with or without considering friction using the standard and varying order based NURBS discretizations. The interpolation order and/or continuity of the NURBS that are to be employed for the discretization of the contact surface and the bulk domain of a given body can be set arbitrarily. The code incorporates the NURBS package by Spink et al. [139] for the evaluation of NURBS functions at a specified parametric point. The validity of the developed isogeometric contact formulation and its corresponding computer implementation is extensively verified using various two- and three-dimensional numerical examples taken from the literature. The results are found to match very well with the analytical or reference results reported in the literature.

In order to demonstrate the capabilities and efficacy of the proposed varying order based NURBS discretization method for isogeometric contact analysis, it has been applied to various two- and three-dimensional numerical examples involving small and large deformation contact between deformable bodies with or without considering friction. In addition, it has been applied to a two-dimensional adhesive contact problem, wherein an elastic strip is peeled from a flat, rigid substrate under the influence of van der Waals interactions. The efficacy of the proposed methodology is assessed mainly in terms of accuracy, robustness, and efficiency. The assessment is carried out for both the VO based: higher-continuous $\mathrm{N}_p{-}\mathrm{N}_{p_c}$ $(p_c > p)$ and higher-order $\mathrm{N}_p{-}\mathrm{N}_{p_c \cdot p_s}$ NURBS discretizations. The results with the standard N_p order of NURBS based discretizations are used for comparisons.

8.2 Conclusions

Based on the results presented in Chapter 7, the following conclusions are drawn:

8.2.1 Two-dimensional frictional ironing

- To attain the equivalent accuracy, the VO based NURBS discretization takes lower computational efforts in terms of overall analysis time, even at a very coarse mesh compared to standard NURBS based discretization. The gain in the computational efficiency further improves at a fixed mesh level for more higher-continuous NURBS based discretizations. The equivalent accuracy stems from the usage of the same continuous NURBS basis functions for the evaluation of contact integrals, while the reduction in the computational cost comes from the employment of lower-order NURBS for the bulk computations.
- With the VO based higher-order NURBS discretization, a significant improvement in the accuracy is achieved in the contact computations at a fixed mesh as compared to the standard NURBS based discretization. The improvement in the accuracy further increases at a fixed mesh on additionally elevating the interpolation order of the NURBS contact layer with the VO based NURBS discretization. The considerable improvement in the accuracy is attributed to a large number of additional DOFs introduced across the contact surface and moderate knot span support of higher-order NURBS basis functions with the additional order elevation based construction of the NURBS contact layer.
- The convergences of the oscillation amplitude of the vertical and horizontal contact forces demonstrates the consistent superior performance of the VO based NURBS discretization as compared to the standard NURBS discretization.
- For a similar accuracy level, the VO based NURBS discretization exhibits a significant gain in the computational efficiency over the standard NURBS discretizations.

8.2.2 Two-dimensional Hertzian contact

- With the VO based higher-order NURBS discretization, more accurate distribution of the normal contact pressure is obtained across the contact interface at a

fixed mesh resolution as compared to the standard NURBS discretization. The quality of the contact pressure distribution further improves at a fixed mesh on additionally elevating the interpolation order of the NURBS contact layer with the VO based discretization.

- The convergence of the norm of the error in the normal contact pressure distribution demonstrates the consistent superior performance of the VO based higher-order NURBS discretizations as compared to the standard NURBS discretization.

- The employment of higher-continuous NURBS based discretization is not advantageous as it yields the absolute error value nearly equivalent to its corresponding lower-continuous NURBS based discretization at the same mesh level.

- With the VO based higher-order NURBS discretization, a considerable improvement in the accuracy is achieved at a cost slightly more than with the standard NURBS based discretization at a fixed mesh resolution.

- To deliver the accuracy similar to the standard NURBS discretization, VO based NURBS discretization takes much lower computational efforts.

8.2.3 Two-dimensional frictional contact between elastic rings

- The VO based higher-order NURBS discretization captures the much more accurate distributions of the normal and horizontal contact pressure at a fixed mesh in comparison to the standard NURBS based discretization.

- It takes only a slightly more cost than with the standard based NURBS discretization to provide a significant improvement in the accuracy at a fixed mesh level.

8.2.4 Two-dimensional adhesive contact

- The VO based higher-order NURBS discretization attains a significant improvement in the accuracy for the peeling computation at a fixed mesh with a slightly more number of DOFs as compared to the standard same as well as higher-continuous NURBS based discretizations.

- To achieve the equivalent accuracy, the VO based higher-order NURBS discretization takes a much lower number of DOFs than needed with the standard higher-order NURBS based discretization at a fixed mesh resolution.

- The convergence of the bending moment oscillation amplitude demonstrates the consistent superior performance of the VO based NURBS discretization over the standard NURBS based discretization for the peeling computations.

- It utilizes a much lower number of DOFs than required with either the higher-continuous or higher-order NURBS based standard discretizations for the similar or nearly equivalent accuracy level.

8.2.5 Three-dimensional frictionless ironing

- To deliver the equivalent accuracy, the VO based NURBS discretization takes a lower number of DOFs than needed with the standard higher-continuous NURBS based discretization.

- With the VO based higher-order NURBS discretization, a considerable improvement in the accuracy is achieved at a fixed mesh level as compared to the standard NURBS based discretizations.

- The improvement in the accuracy further enhances at a fixed mesh on additionally elevating the interpolation order of NURBS contact layer with the VO based discretization.

- To yield the similar accuracy, the VO based higher-order NURBS discretization takes a much lower number of DOFs than needed with the standard NURBS based discretization.

8.3 Scope for future work

In this section, various possible extensions to the current thesis are discussed.

- In this work, the advantages achieved with the proposed VO based NURBS discretization method are shown for the mechanical as well as adhesive contact

problems that are dominated by the surface effects. The introduced methodology is also believed to be advantageous for other physical problems where the inaccurate capture of the driving forces at the interface adversely influence the accuracy of the result. Among others, the possible applications are: cohesive interface debonding problems, computational electromagnetics, fluid-flow problems, and fluid-structure interactions.

- In the present work, a sufficiently accurate Gauss-point-to-surface contact algorithm with the penalty method is combined with the proposed methodology as a first step towards developing a simple yet computationally efficient framework for isogeometric analysis of contact problems. Since within the GPTS approach, the contact constraints are enforced directly at an arbitrary number of quadrature points, it is over-constrained in nature and leads to numerical instability, as shown in [21, 29, 30]. Thus, incorporation of the mathematically more sophisticated isogeometric mortar algorithm, e.g. as in [29, 66, 69, 119], where the contact constraints are enforced in a weak sense at control points, is another direction to be pursued towards developing a more rigorous framework for isogeometric analysis of contact problems.

- Combining the efficient local mesh refinement techniques such as in [94–96], which enable the accurate capture of the sharp variation of the contact responses with the lower number of DOFs than with the standard NURBS discretization, with the introduced varying order based NURBS discretizations is another direction that can be pursed to develop a highly efficient framework for the isogeometric analysis of contact problems.

- Another type of advancement to consider is the local order elevation based refinement of the NURBS discretized contact surface. With such an approach, one can enable the employment of higher-order of NURBS only for the description of the part of the surface that potentially comes into contact during the analysis. As such, it can lead to a significant improvement in the computational efficiency of the isogeometric analysis technique for modelling contact problems. To develop such a method, one can possibly take inspiration from the recently devised multi-degree-splines concept introduced in [140–142].

- The incorporation of friction to the three-dimensional setting in the current

framework is the subject of future research work.

- Presently, the Gauss quadrature rule is utilized for the isogeometric analysis of contact problems using the proposed varying order based NURBS discretizations. The performance with the optimal quadrature rules [124–126], which are well-suited for IGA and employ a reduced number of quadrature points in the evaluation of the bulk and surface integrals, also needs to be investigated.

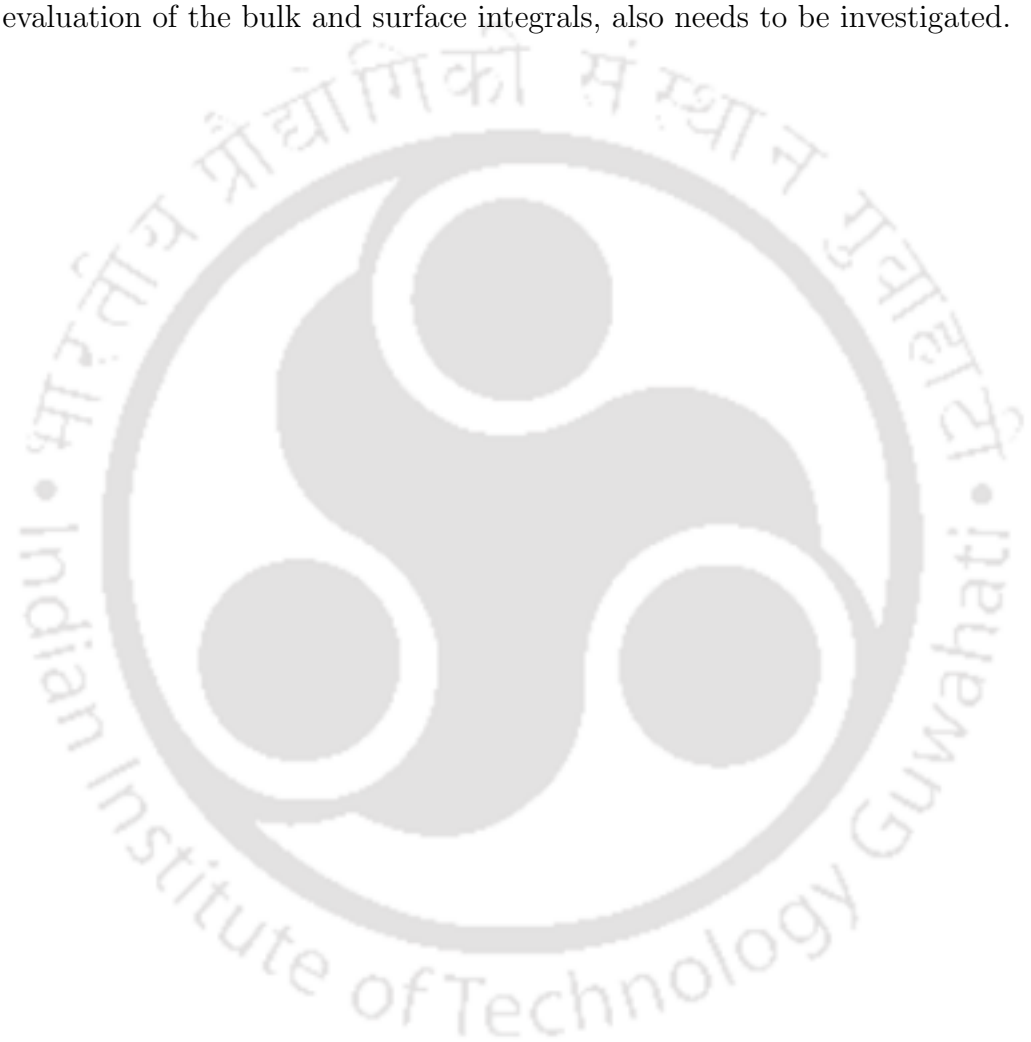

Appendix A

Linearization and Tangent Matrices for Contact Boundary Value Problem

A.1 Linearization of the internal virtual work

In this section, the linearization of the virtual internal work $\delta\mathcal{W}_{\text{int}}$ and external virtual work $\delta\mathcal{W}_{\text{ext}}$ appearing in weak form of BVP Eq. (3.38) is discussed. It is noted that the linearization of the above-mentioned terms is general in nature and holds for multi-body or two-body CBVP discussed in Section 3.2.5, except the modification that the superscript k for quantities associated with each contact body is omitted here. The details of the description on the general linearization procedure can be found in the references [6, 114].

In general, the linearization of a tensor-valued function $\boldsymbol{f}(\boldsymbol{\varphi}, \delta\boldsymbol{\varphi})$ at $\bar{\boldsymbol{\varphi}}$ in the direction of $\Delta\boldsymbol{\varphi}$ is obtained as

$$L[\boldsymbol{f}]_{\boldsymbol{\varphi}=\bar{\boldsymbol{\varphi}}} \;=\; \boldsymbol{f}(\bar{\boldsymbol{\varphi}}, \delta\boldsymbol{\varphi}) + D\boldsymbol{f}(\bar{\boldsymbol{\varphi}}, \delta\boldsymbol{\varphi})[\Delta\boldsymbol{\varphi}]\,, \tag{A.1}$$

where the higher-order terms are neglected and $D\boldsymbol{f}(\bar{\boldsymbol{\varphi}}, \delta\boldsymbol{\varphi})[\Delta\boldsymbol{\varphi}]$ is the directional derivative of $\boldsymbol{f}(\bar{\boldsymbol{\varphi}}, \delta\boldsymbol{\varphi})$ that is defined as

$$D\boldsymbol{f}(\bar{\boldsymbol{\varphi}}, \boldsymbol{\varphi})[\Delta\boldsymbol{\varphi}] = \frac{\mathrm{d}}{\mathrm{d}\eta}\left[\boldsymbol{f}(\bar{\boldsymbol{\varphi}} + \eta\Delta\boldsymbol{\varphi}, \delta\boldsymbol{\varphi})\right]\Big|_{\eta=0} \tag{A.2}$$

As such, to linearize the tensor quantities in the current configuration, they are first pulled back to the reference configuration. After computing the linearization of these tensor quantities in the reference configuration, they are pushed forward to the current configuration. Equation (3.38) can be written in the reference configuration as

$$\delta\mathcal{W}(\boldsymbol{\varphi},\delta\boldsymbol{\varphi}) = \underbrace{\int_{\mathcal{B}_0} \boldsymbol{F}\boldsymbol{S} : \mathrm{Grad}(\delta\boldsymbol{\varphi})\,\mathrm{d}V}_{\delta\mathcal{W}_{\mathrm{int}}(\boldsymbol{\varphi},\delta\boldsymbol{\varphi})} \underbrace{- \int_{\mathcal{B}_0} \rho\,\bar{\boldsymbol{B}}\cdot\delta\boldsymbol{\varphi}\,\mathrm{d}V - \int_{\Gamma_t} \bar{\boldsymbol{T}}\cdot\delta\boldsymbol{\varphi}\,\mathrm{d}A}_{-\delta\mathcal{W}_{\mathrm{ext}}(\boldsymbol{\varphi},\delta\boldsymbol{\varphi})} = 0\,, \quad \text{(A.3)}$$

where the gradient of $\delta\boldsymbol{\varphi}$ can be defined as

$$\mathrm{Grad}(\delta\boldsymbol{\varphi}) = \frac{\partial(\delta\boldsymbol{\varphi})}{\partial\boldsymbol{X}} = \delta\boldsymbol{F}\,. \quad \text{(A.4)}$$

It is noted that for dead loading, which is considered in this work, the term $\delta\mathcal{W}_{\mathrm{ext}}(\boldsymbol{\varphi},\delta\boldsymbol{\varphi})$ remains independent of the deformation, which implies that $D\delta\mathcal{W}_{\mathrm{ext}}(\bar{\boldsymbol{\varphi}},\delta\boldsymbol{\varphi})[\Delta\boldsymbol{\varphi}] = 0$. The directional derivative of the virtual internal work $\delta\mathcal{W}_{\mathrm{int}}(\boldsymbol{\varphi},\delta\boldsymbol{\varphi})$ at $\bar{\boldsymbol{\varphi}}$ in the direction of $\Delta\boldsymbol{\varphi}$ is given by

$$\begin{aligned} D\delta\mathcal{W}_{\mathrm{int}}(\bar{\boldsymbol{\varphi}},\delta\boldsymbol{\varphi})[\Delta\boldsymbol{\varphi}] = &\int_{\mathcal{B}_0} \delta\boldsymbol{F} : D\boldsymbol{F}(\bar{\boldsymbol{\varphi}},\delta\boldsymbol{\varphi})[\Delta\boldsymbol{\varphi}]\bar{\boldsymbol{S}}\,\mathrm{d}V \\ &+ \int_{\mathcal{B}_0} \delta\boldsymbol{F} : \bar{\boldsymbol{F}}D\boldsymbol{S}(\bar{\boldsymbol{\varphi}},\delta\boldsymbol{\varphi})[\Delta\boldsymbol{\varphi}]\,\mathrm{d}V\,, \end{aligned} \quad \text{(A.5)}$$

where $(\bar{\bullet})$ denotes the quantity is evaluated at $\bar{\boldsymbol{\varphi}}$. The above equations after a few manipulations can be reformulated in the following form (see [114] for the detailed discussion)

$$D\delta\mathcal{W}_{\mathrm{int}}(\bar{\boldsymbol{\varphi}},\delta\boldsymbol{\varphi})[\Delta\boldsymbol{\varphi}] = \int_{\mathcal{B}_0} \delta\boldsymbol{\varphi}^{\mathrm{T}}_{,I}\,\bar{\boldsymbol{S}}_{IJ}\,\Delta\boldsymbol{\varphi}_{,J}\,\mathrm{d}V + \int_{\mathcal{B}_0} \delta\bar{\boldsymbol{E}} : \bar{\mathbb{C}} : \Delta\bar{\boldsymbol{E}}\,\mathrm{d}V\,. \quad \text{(A.6)}$$

where the material derivative of the virtual deformation function defined is given as $\delta\boldsymbol{\varphi}_{,I} = \partial(\delta\boldsymbol{\varphi})/\partial\boldsymbol{X}_I$ and $\Delta\boldsymbol{\varphi}_{,I} = \partial(\Delta\boldsymbol{\varphi})/\partial\boldsymbol{X}_I$. After performing the push forward transformation, the above equation in the current configuration can be expressed as

$$D\delta\mathcal{W}_{\mathrm{int}}(\bar{\boldsymbol{\varphi}},\delta\boldsymbol{\varphi})[\Delta\boldsymbol{\varphi}] = \int_{\mathcal{B}} \delta\boldsymbol{\varphi}^{\mathrm{T}}_{,i}\,\bar{\boldsymbol{\sigma}}_{ij}\,\Delta\boldsymbol{\varphi}_{,j}\,\mathrm{d}v + \int_{\mathcal{B}} (\mathrm{grad}\,\delta\boldsymbol{\varphi})^{\mathrm{s}} : \bar{\mathbb{c}} : (\mathrm{grad}\,\Delta\boldsymbol{\varphi})^{\mathrm{s}}\,\mathrm{d}v\,. \quad \text{(A.7)}$$

where $(\bullet)^{\mathrm{s}}$ represents the symmetric part of $(\bullet)$. The spatial derivative of the virtual

deformation function defined is given as $\delta\boldsymbol{\varphi}_{,i} = \partial(\delta\boldsymbol{\varphi})/\partial\boldsymbol{x}_i$ and $\Delta\boldsymbol{\varphi}_{,i} = \partial(\Delta\boldsymbol{\varphi})/\partial\boldsymbol{x}_i$. Moreover, $\bar{\mathbb{c}}$ is the fourth-order spatial elasticity tensor defined in Eq. (3.34) for Neo-Hooken material model. The Cauchy stress tensor $\bar{\boldsymbol{\sigma}}$ is defined in Eq. (3.31).

In Eq. (A.7), the first term, which arises from the geometric deformation, i.e.

$$D\delta\mathcal{W}_{\text{geo}}(\bar{\boldsymbol{\varphi}}, \delta\boldsymbol{\varphi})[\Delta\boldsymbol{\varphi}] = \int_{\mathcal{B}} \delta\boldsymbol{\varphi}_{,i}^{\mathrm{T}}\, \bar{\boldsymbol{\sigma}}_{ij}\, \Delta\boldsymbol{\varphi}_{,j}\, \mathrm{d}v\,, \tag{A.8}$$

is generally referred as the *geometric part* of $D\delta\mathcal{W}_{\text{int}}$, see e.g. [6, 114]. Since the second term, i.e.

$$D\delta\mathcal{W}_{\text{mat}}(\bar{\boldsymbol{\varphi}}, \delta\boldsymbol{\varphi})[\Delta\boldsymbol{\varphi}] = \int_{\mathcal{B}} (\operatorname{grad}\delta\boldsymbol{\varphi})^{\mathrm{s}} : \bar{\mathbb{c}} : (\operatorname{grad}\Delta\boldsymbol{\varphi})^{\mathrm{s}}\, \mathrm{d}v\,, \tag{A.9}$$

consists the material responses due to the constitutive tensor $\bar{\ }$, it is usually referred as the *material part* of $D\delta\mathcal{W}_{\text{int}}$.

A.2 Internal tangent matrix

Since the linearization of the internal virtual work is defined in terms of its geometric and material contributions (A.7), the internal tangent matrix is obtained from its geometric and material contributions.

Recall the discretization of the domain $\mathcal{B}^k$ into n_{el}^k number of NURBS described elements, the linearization of the geometric part of the internal virtual work can be written in terms of its element contributions. The substitution of $\delta\boldsymbol{\varphi}$ and $\Delta\boldsymbol{\varphi}$ from Eq. (4.6) into Eq. (A.8) leads to

$$D\delta\mathcal{W}_{\text{geo}}^k = \bigcup_{e=1}^{n_{\text{el}}^k} D\delta\mathcal{W}_{\text{geo}}^{ke} = \bigcup_{e=1}^{n_{\text{el}}^k} (\delta\mathbf{u}^{ke})^{\mathrm{T}}\, \mathbf{k}_{\text{geo}}^{ke}\, \Delta\mathbf{u}^k \tag{A.10}$$

where the elemental geometric tangent matrix is obtained as

$$\mathbf{k}_{\text{geo}}^{ke} = \int_{\Omega^{ke}} (\mathbf{R}_{,x_i}^k)^{\mathrm{T}}\, \sigma_{ij}\, \mathbf{R}_{,x_j}^k\, \mathrm{d}\Omega\,. \tag{A.11}$$

By inserting approximations for $(\operatorname{grad}\delta\boldsymbol{\varphi})^{\mathrm{s}}$ and $(\operatorname{grad}\Delta\boldsymbol{\varphi})^{\mathrm{s}}$ given in Eq. (4.14) into

Eq. (A.9), the linearization of the material part of the internal virtual work yields

$$D\delta\mathcal{W}^{k}_{\text{mat}} = \bigcup_{e=1}^{n^{k}_{\text{el}}} D\delta\mathcal{W}^{ke}_{\text{mat}} = (\delta\mathbf{u}^{ke})^{\text{T}}\,\mathbf{k}^{ke}_{\text{mat}}\,\Delta\mathbf{u}^{k}\,. \tag{A.12}$$

In the above equation, the elemental material tangent matrix is given as

$$\mathbf{k}^{ke}_{\text{mat}} = \int_{\Omega^{ke}} (\mathbf{B}^{ke})^{\text{T}}\,\mathbb{c}\,\mathbf{B}^{ke}\,\text{d}\Omega\,, \tag{A.13}$$

where $\mathbb{c}$ is the spatial elasticity or the constitutive tensor specified in Eq. (3.34).

A.3 Contact tangent matrices

In this section, the contact tangent matrices corresponding to the contact force vectors given in Eq. (4.26) are provided. The derivation of the contact tangent matrices for the classical full-pass contact formulation, which is employed in the present work, is based on the two half-pass contact formulation of Sauer and De Lorenzis [76, 77]. In the following, the contact quantities, e.g. normal and tangential vectors, computed at the projection point $\bar{\boldsymbol{\xi}}_{\text{m}} \in \Gamma^{\text{m}}_{c}$ are denoted with bar as in Section 3.2.1.

As discussed in Sections 3.2.5 and 4.4.3, the contact force vector $\mathbf{f}^{ke}_{\text{c}}$ depends on the displacement of the contact surface elements Γ^{ke}_{c} of both bodies. This implies that $\mathbf{f}^{\text{s}e}_{\text{c}} = \mathbf{f}^{\text{s}e}_{\text{c}}(\mathbf{u}^{\text{s}e}, \mathbf{u}^{\text{m}e})$, and $\mathbf{f}^{\text{m}e}_{\text{c}} = \mathbf{f}^{\text{m}e}_{\text{c}}(\mathbf{u}^{\text{s}e}, \mathbf{u}^{\text{m}e})$, where $\mathbf{u}^{\text{s}e}$ and $\mathbf{u}^{\text{m}e}$ denote the displacement vectors of $\Gamma^{\text{s}e}_{c}$ and $\Gamma^{\text{m}e}_{c}$, respectively. Thus, the linearization of $\mathbf{f}^{ke}_{\text{c}}$ at $(\mathbf{u}^{\text{s}e}, \mathbf{u}^{\text{m}e})$ in the direction of $(\Delta\mathbf{u}^{\text{s}e}, \Delta\mathbf{u}^{\text{m}e})$ leads to

$$\begin{aligned}
\mathbf{f}^{\text{s}e}_{\text{c}}(\mathbf{u}^{\text{s}e} + \Delta\mathbf{u}^{\text{s}e}, \mathbf{u}^{\text{m}e} + \Delta\mathbf{u}^{\text{m}e}) &= \mathbf{f}^{\text{s}e}_{\text{c}}(\mathbf{u}^{\text{s}e}, \mathbf{u}^{\text{m}e}) \;+\; \mathbf{k}^{\text{ss}e}_{\text{c}}\Delta\mathbf{u}^{\text{s}e} \;+\; \mathbf{k}^{\text{sm}e}_{\text{c}}\Delta\mathbf{u}^{\text{m}e} \\
\mathbf{f}^{\text{m}e}_{\text{c}}(\mathbf{u}^{\text{s}e} + \Delta\mathbf{u}^{\text{s}e}, \mathbf{u}^{\text{m}e} + \Delta\mathbf{u}^{\text{m}e}) &= \mathbf{f}^{\text{m}e}_{\text{c}}(\mathbf{u}^{\text{s}e}, \mathbf{u}^{\text{m}e}) \;+\; \mathbf{k}^{\text{ms}e}_{\text{c}}\Delta\mathbf{u}^{\text{s}e} \;+\; \mathbf{k}^{\text{mm}e}_{\text{c}}\Delta\mathbf{u}^{\text{m}e}\,,
\end{aligned} \tag{A.14}$$

where the contact tangent matrices in the current configuration are given by (see Appendix B of [77]):

$$\begin{aligned}
\mathbf{k}^{\text{ss}e}_{\text{c}} &:= \frac{\partial \mathbf{f}^{\text{s}e}_{\text{c}}}{\partial \mathbf{u}^{\text{s}e}} = -\int_{\Gamma^{\text{s}e}_{c}} (\mathbf{R}^{\text{s}e})^{\text{T}}\,\frac{\partial \boldsymbol{t}_{c}}{\partial \mathbf{u}^{\text{s}e}}\,\text{d}\Gamma - \int_{\Gamma^{\text{s}}_{c}} (\mathbf{R}^{\text{s}e})^{\text{T}}\,\boldsymbol{t}_{c}\otimes\boldsymbol{\tau}^{\alpha}_{\text{s}}\,\mathbf{R}^{\text{s}e}_{,\alpha}\,\text{d}\Gamma,\quad \alpha=\{1,2\} \\
\mathbf{k}^{\text{sm}e}_{\text{c}} &:= \frac{\partial \mathbf{f}^{\text{s}e}_{\text{c}}}{\partial \mathbf{u}^{\text{m}e}} = \int_{\Gamma^{\text{s}e}_{c}} (\mathbf{R}^{\text{s}e})^{\text{T}}\,\frac{\partial \boldsymbol{t}_{c}}{\partial \mathbf{u}^{\text{m}e}}\,\text{d}\Gamma
\end{aligned} \tag{A.15}$$

$$\mathbf{k}_{\mathrm{c}}^{\mathrm{mse}} := \frac{\partial \mathbf{f}_{\mathrm{c}}^{\mathrm{me}}}{\partial \mathbf{u}^{se}} = \int_{\Gamma_c^{se}} (\mathbf{R}_{,\alpha}^{me})^{\mathrm{T}}\, \boldsymbol{t}^{\mathrm{s}} \otimes \frac{\partial \bar{\xi}_{\mathrm{m}}^{\alpha}}{\partial \mathbf{u}^{se}}\, \mathrm{d}\Gamma + \int_{\Gamma_c^{se}} (\mathbf{R}^{me})^{\mathrm{T}} \frac{\partial \boldsymbol{t}_c}{\partial \mathbf{u}^{se}}\, \mathrm{d}\Gamma + \int_{\Gamma_c^{\mathrm{s}}} (\mathbf{R}^{me})^{\mathrm{T}}\, \boldsymbol{t}_c \otimes \boldsymbol{\tau}_{\mathrm{s}}^{\alpha}\, \mathbf{R}_{,\alpha}^{se}\, \mathrm{d}\Gamma$$

$$\mathbf{k}_{\mathrm{c}}^{\mathrm{mme}} := \frac{\partial \mathbf{f}_{\mathrm{c}}^{\mathrm{me}}}{\partial \mathbf{u}^{\mathrm{me}}} = \int_{\Gamma_c^{\mathrm{s}}} (\mathbf{R}_{,\alpha}^{me})^{\mathrm{T}}\, \boldsymbol{t}_c \otimes \frac{\partial \bar{\xi}_{\mathrm{m}}^{\alpha}}{\partial \mathbf{u}^{\mathrm{me}}}\, \mathrm{d}\Gamma + \int_{\Gamma_c^{\mathrm{s}}} (\mathbf{R}^{me})^{\mathrm{T}} \frac{\partial \boldsymbol{t}_c}{\partial \mathbf{u}^{\mathrm{me}}}\, \mathrm{d}\Gamma\,.$$

Here, $\mathbf{R}^{se} = \mathbf{R}^{se}(\boldsymbol{\xi}^{\mathrm{s}})$ and $\mathbf{R}^{me} = \mathbf{R}^{me}(\bar{\boldsymbol{\xi}}_{\mathrm{m}})$. The partial derivative of the closest projection point $\bar{\xi}_{\mathrm{m}}^{\alpha}$ with respect to displacement $\mathbf{u}^{se}$ is obtained from Eq. (3.45). With $\dfrac{d}{d\xi_{\mathrm{m}}^{\alpha}}\, \hat{d} = 0$ and taking differentiation with respect to $\mathbf{u}^{se}$, one obtains after rearranging the terms (see Appendix B of [76])

$$\frac{\partial \bar{\xi}_{\mathrm{m}}^{\alpha}}{\partial \mathbf{u}^{se}} = \frac{\partial \bar{\xi}_{\mathrm{m}}^{\alpha}}{\partial \boldsymbol{x}^{se}} \frac{\partial \boldsymbol{x}^{se}}{\partial \mathbf{u}^{se}} = \bar{c}^{\alpha\beta}\, \bar{\boldsymbol{\tau}}_{\beta}\, \mathbf{R}^{se}\,, \tag{A.16}$$

where the contravariant components $\bar{c}_{\mathrm{m}}^{\alpha\beta}$ of a tensor $\boldsymbol{c}_{\mathrm{m}}$ are computed using

$$[\bar{c}^{\alpha\beta}] = \left[\bar{m}_{\alpha\beta} - \mathrm{g_N}\, \bar{k}_{\alpha\beta}\right]^{-1}\,. \tag{A.17}$$

Similarly, the derivative $\partial \bar{\xi}_{\mathrm{m}}^{\alpha} / \partial \mathbf{u}^{\mathrm{me}}$ is obtained by taking the differentiation of Eq. (3.45) with respect to $\mathbf{u}^{\mathrm{me}}$, and is given as [76]

$$\frac{\partial \bar{\xi}_{\mathrm{m}}^{\alpha}}{\partial \mathbf{u}^{\mathrm{me}}} = -\bar{c}^{\alpha\beta} \left(\bar{\boldsymbol{\tau}}_{\beta}\, \mathbf{R}^{me} - \mathbf{g}_{\mathrm{N}}\, \bar{\boldsymbol{n}}\, \mathbf{R}_{,\beta}^{me}\right)\,, \tag{A.18}$$

Since the contact traction contains the normal and tangential contributions, i.e. $\boldsymbol{t}_c := \boldsymbol{t}_{\mathrm{N}} - \boldsymbol{t}_{\mathrm{T}}$ as shown in Eq. (3.52), the partial derivatives of the contact traction is given as

$$\frac{\partial \boldsymbol{t}_c}{\partial \mathbf{u}^{ke}} = \frac{\partial \boldsymbol{t}_{\mathrm{N}}}{\partial \mathbf{u}^{ke}} - \frac{\partial \boldsymbol{t}_{\mathrm{T}}}{\partial \mathbf{u}^{ke}}, \qquad \text{where } k = \{\mathrm{s}, \mathrm{m}\}\,, \tag{A.19}$$

where the derivative of the normal component of the contact traction, and tangential component of the contact traction for the sticking and slipping steps with respect to $\mathbf{u}^{ke}$ are given in the following.

A.3.1 Normal contact

The normal traction is given by (see Eq. (3.73)):

$$\boldsymbol{t}_{\mathrm{N}} = -\epsilon_{\mathrm{N}}\, \mathrm{g_N}\, \bar{\boldsymbol{n}}, \quad \text{if } \mathrm{g_N} < 0\,. \tag{A.20}$$

The normal gap function at $\boldsymbol{x}^{\mathrm{s}}$ is given by (see Eq. (3.46))

$$\mathrm{g_N} = (\boldsymbol{x}^{\mathrm{s}} - \bar{\boldsymbol{x}}^{\mathrm{m}}) \cdot \bar{\boldsymbol{n}} \,. \tag{A.21}$$

The partial derivatives of normal contact traction with respect to $\boldsymbol{u}^{se}$ and $\boldsymbol{u}^{\mathrm{m}e}$ is obtained as

$$\begin{aligned} \frac{\partial \boldsymbol{t}_{\mathrm{N}}}{\partial \mathbf{u}^{se}} &= -\epsilon_{\mathrm{N}} \bar{\boldsymbol{n}} \frac{\partial \mathrm{g_N}}{\partial \mathbf{u}^{se}} - \epsilon_{\mathrm{N}}\, \mathrm{g_N} \frac{\partial \bar{\boldsymbol{n}}}{\partial \mathbf{u}^{se}} \,, \\ \frac{\partial \boldsymbol{t}_{\mathrm{N}}}{\partial \mathbf{u}^{\mathrm{m}e}} &= -\epsilon_{\mathrm{N}} \bar{\boldsymbol{n}} \frac{\partial \mathrm{g_N}}{\partial \mathbf{u}^{\mathrm{m}e}} - \epsilon_{\mathrm{N}}\, \mathrm{g_N} \frac{\partial \bar{\boldsymbol{n}}}{\partial \mathbf{u}^{\mathrm{m}e}} \,. \end{aligned} \tag{A.22}$$

Differentiating Eq. (A.21) with respect to $\mathbf{u}^{ke}$, followed by the substitution of $\boldsymbol{x}^{ke}$ from Eq. (4.3) yields

$$\begin{aligned} \frac{\partial \mathrm{g_N}}{\partial \mathbf{u}^{se}} &= \frac{\partial \mathrm{g_N}}{\partial \boldsymbol{x}^{se}} \frac{\partial \boldsymbol{x}^{se}}{\partial \mathbf{u}^{se}} = \bar{\boldsymbol{n}}^{\mathrm{T}}\, \mathbf{R}^{se} \\ \frac{\partial \mathrm{g_N}}{\partial \mathbf{u}^{\mathrm{m}e}} &= \frac{\partial \mathrm{g_N}}{\partial \boldsymbol{x}^{\mathrm{m}e}} \frac{\partial \boldsymbol{x}^{\mathrm{s}e}}{\partial \mathbf{u}^{se}} = -\bar{\boldsymbol{n}}^{\mathrm{T}}\, \mathbf{R}^{\mathrm{m}e} \end{aligned} \tag{A.23}$$

The partial derivative of unit normal vectors with respect to $\boldsymbol{u}^{se}$ and $\boldsymbol{u}^{\mathrm{m}e}$ is given by (see Appendix C of [76])

$$\begin{aligned} \frac{\partial \bar{\boldsymbol{n}}}{\partial \mathbf{u}^{se}} &= \frac{1}{\mathrm{g_N}} \left[\boldsymbol{I} - \bar{\boldsymbol{n}} \otimes \bar{\boldsymbol{n}} - \bar{c}^{\alpha\beta} \bar{\boldsymbol{\tau}}_\alpha \otimes \bar{\boldsymbol{\tau}}_\beta \right] \mathbf{R}^{se} \,, \\ \frac{\partial \bar{\boldsymbol{n}}}{\partial \mathbf{u}^{\mathrm{m}e}} &= -\frac{1}{\mathrm{g_N}} \left[\boldsymbol{I} - \bar{\boldsymbol{n}} \otimes \bar{\boldsymbol{n}} - \bar{c}^{\alpha\beta} \bar{\boldsymbol{\tau}}_\alpha \otimes \bar{\boldsymbol{\tau}}_\beta \right] \mathbf{R}^{\mathrm{m}e} - \bar{c}^{\alpha\beta} \bar{\boldsymbol{\tau}}_\alpha \otimes \bar{\boldsymbol{n}}\, \mathbf{R}^{\mathrm{m}e}_{,\beta} \end{aligned} \tag{A.24}$$

By substituting Eqs. (A.23) and (A.24) into Eq. (A.22) and after rearranging the terms, the derivatives of the normal contact traction are given as

$$\begin{aligned} \frac{\partial \boldsymbol{t}_{\mathrm{N}}}{\partial \mathbf{u}^{se}} &= -\epsilon_{\mathrm{N}} \left[\boldsymbol{I} - \bar{c}^{\alpha\beta}\, \bar{\boldsymbol{\tau}}_\alpha \otimes \bar{\boldsymbol{\tau}}_\beta \right] \mathbf{R}^{se} \,, \quad \text{and} \\ \frac{\partial \boldsymbol{t}_{\mathrm{N}}}{\partial \mathbf{u}^{me}} &= \epsilon_{\mathrm{N}} \left[\boldsymbol{I} - \bar{c}^{\alpha\beta} \bar{\boldsymbol{\tau}}_\alpha \otimes \bar{\boldsymbol{\tau}}_\beta \right] \mathbf{R}^{\mathrm{m}e} + \epsilon_{\mathrm{N}}\, \mathrm{g_N}\, \bar{c}^{\alpha\beta} \bar{\boldsymbol{\tau}}_\alpha \otimes \bar{\boldsymbol{n}}\, \mathbf{R}^{\mathrm{m}e}_{,\beta} \end{aligned} \tag{A.25}$$

A.3.2 Tangential sticking step

For sticking state, the tangential contact traction is given by (see Eq. (3.74))

$$\boldsymbol{t}_{\mathrm{T}} = \epsilon_{\mathrm{T}} \left(\boldsymbol{x}^{\mathrm{m}}(\bar{\boldsymbol{\xi}}_{\mathrm{m}}) \,-\, \boldsymbol{x}^{\mathrm{m}}(\boldsymbol{\xi}_{\mathrm{m}\,sl\,n}) \right) \,. \tag{A.26}$$

It is noted that in the above equation and in the following, the subscript $n+1$, denoting the contact quantities in the current configuration at load step t_{n+1}, is dropped for

convenience.

The partial derivative of $\boldsymbol{t}_{\mathrm{T}}$ with respect to $\mathbf{u}^{ke}$ is given by

$$\begin{aligned}\frac{\partial \boldsymbol{t}_{\mathrm{T}}}{\partial \mathbf{u}^{\mathrm{s}e}} &= \epsilon_{\mathrm{T}} \frac{\partial \bar{\boldsymbol{x}}^{\mathrm{m}}}{\partial \mathbf{u}^{\mathrm{s}e}}\,, \\ \frac{\partial \boldsymbol{t}_{\mathrm{T}}}{\partial \mathbf{u}^{\mathrm{m}e}} &= \epsilon_{\mathrm{T}} \left(\frac{\partial \bar{\boldsymbol{x}}^{\mathrm{m}}}{\partial \mathbf{u}^{\mathrm{m}e}} - \frac{\partial \boldsymbol{x}^{\mathrm{m}}(\boldsymbol{\xi}_{\mathrm{m}\,sl\,n})}{\partial \mathbf{u}^{\mathrm{m}e}} \right)\,,\end{aligned} \tag{A.27}$$

where the derivatives of the physical projection point $\bar{\boldsymbol{x}}^{\mathrm{m}}$ with respect to $\mathbf{u}^{ke}$ are given as (see Appendix B in [76] and B.2 in [77])

$$\begin{aligned}\frac{\partial \bar{\boldsymbol{x}}^{\mathrm{m}}}{\partial \mathbf{u}^{\mathrm{s}e}} &= \bar{c}^{\alpha\beta} \bar{\boldsymbol{\tau}}_{\alpha} \otimes \bar{\boldsymbol{\tau}}_{\beta}\,, \\ \frac{\partial \bar{\boldsymbol{x}}^{\mathrm{m}}}{\partial \mathbf{u}^{\mathrm{m}e}} &= \mathbf{R}^{\mathrm{m}e} - \bar{c}^{\alpha\beta} \bar{\boldsymbol{\tau}}_{\alpha} \otimes \left(\bar{\boldsymbol{\tau}}_{\beta} \mathbf{R}^{\mathrm{m}e} - \mathrm{g}_{\mathrm{N}}\, \bar{\boldsymbol{n}}\, \mathbf{R}^{\mathrm{m}e}_{,\beta} \right)\,, \\ \frac{\partial \boldsymbol{x}^{\mathrm{m}}(\boldsymbol{\xi}_{\mathrm{m}\,sl\,n})}{\partial \mathbf{u}^{\mathrm{m}e}} &= \mathbf{R}^{\mathrm{m}e}(\boldsymbol{\xi}_{\mathrm{m}\,sl\,n})\,.\end{aligned} \tag{A.28}$$

By inserting Eqs. (A.27) and (A.28) into Eq. (A.26), and after rearranging the terms, the partial derivatives of tangential contact traction for the stick step are given as

$$\begin{aligned}&\frac{\partial \boldsymbol{t}_{\mathrm{T}}}{\partial \mathbf{u}^{se}} = \epsilon_{\mathrm{T}}\, \bar{c}^{\alpha\beta} \bar{\boldsymbol{\tau}}_{\alpha} \otimes \bar{\boldsymbol{\tau}}_{\beta}\, \mathbf{R}^{se}\,, \quad \text{and} \\ &\frac{\partial \boldsymbol{t}_{\mathrm{T}}}{\partial \mathbf{u}^{me}} = -\epsilon_{\mathrm{T}}\, \bar{c}^{\alpha\beta} \bar{\boldsymbol{\tau}}_{\alpha} \otimes \bar{\boldsymbol{\tau}}_{\beta}\, \mathbf{R}^{me} + \epsilon_{\mathrm{T}} \left(\mathbf{R}^{me} - \mathbf{R}^{me}(\boldsymbol{\xi}_{\mathrm{m}\,sl\,n}) \right) + \epsilon_{\mathrm{T}}\, \mathrm{g}_{\mathrm{N}}\, \bar{c}^{\alpha\beta} \bar{\boldsymbol{\tau}}_{\alpha} \otimes \bar{\boldsymbol{n}}\, \mathbf{R}^{\mathrm{m}e}_{,\beta}\,,\end{aligned} \tag{A.29}$$

A.3.3 Tangential sliding step

For sliding step, the tangential contact traction is given by (see Eq. $(3.76)_2$)

$$\boldsymbol{t}_{\mathrm{T}} = \mu_f\, t_{\mathrm{N}}\, \boldsymbol{n}_{\mathrm{T}}\,, \tag{A.30}$$

with $t_{\mathrm{N}} = -\epsilon_{\mathrm{N}}\, \mathrm{g}_{\mathrm{N}}$ and $\boldsymbol{n}_{\mathrm{T}} = \boldsymbol{t}_{\mathrm{T}}^{\mathrm{trial}} / ||\boldsymbol{t}_{\mathrm{T}}^{\mathrm{trial}}||$, where the trial traction $\boldsymbol{t}_{\mathrm{T}}^{\mathrm{trial}}$ is given by Eq. (3.74). For a slip step, the partial derivatives of the tangential contact traction are given as

$$\begin{aligned}\frac{\partial \boldsymbol{t}_{\mathrm{T}}}{\partial \mathbf{u}^{\mathrm{s}e}} &= -\mu_f\, \epsilon_{\mathrm{N}}\, \frac{\partial \mathrm{g}_{\mathrm{N}}}{\partial \mathbf{u}^{\mathrm{s}e}}\, \boldsymbol{n}_{\mathrm{T}} - \mu_f\, \epsilon_{\mathrm{N}}\, \mathrm{g}_{\mathrm{N}}\, \frac{\partial \boldsymbol{n}_{\mathrm{T}}}{\partial \mathbf{u}^{\mathrm{s}e}}\,, \\ \frac{\partial \boldsymbol{t}_{\mathrm{T}}}{\partial \mathbf{u}^{\mathrm{m}e}} &= -\mu_f\, \epsilon_{\mathrm{N}}\, \frac{\partial \mathrm{g}_{\mathrm{N}}}{\partial \mathbf{u}^{\mathrm{m}e}}\, \boldsymbol{n}_{\mathrm{T}} - \mu_f\, \epsilon_{\mathrm{N}}\, \mathrm{g}_{\mathrm{N}}\, \frac{\partial \boldsymbol{n}_{\mathrm{T}}}{\partial \mathbf{u}^{\mathrm{m}e}}\,,\end{aligned} \tag{A.31}$$

where the derivatives of $\boldsymbol{n}_{\mathrm{T}}$ with respect to $\mathbf{u}^{ke}$ are given as (see Appendix B.2 of [77])

$$\begin{aligned}\frac{\partial \boldsymbol{n}_{\mathrm{T}}}{\partial \mathbf{u}^{\mathrm{se}}} &= \frac{1}{||\boldsymbol{t}_{\mathrm{T}}^{\mathrm{trial}}||}\left(\boldsymbol{I}-\boldsymbol{n}_{\mathrm{T}}\otimes\boldsymbol{n}_{\mathrm{T}}\right)\frac{\partial \boldsymbol{t}^{\mathrm{trial}}}{\partial \mathbf{u}^{\mathrm{se}}}\,,\\ \frac{\partial \boldsymbol{n}_{\mathrm{T}}}{\partial \mathbf{u}^{\mathrm{me}}} &= \frac{1}{||\boldsymbol{t}_{\mathrm{T}}^{\mathrm{trial}}||}\left(\boldsymbol{I}-\boldsymbol{n}_{\mathrm{T}}\otimes\boldsymbol{n}_{\mathrm{T}}\right)\frac{\partial \boldsymbol{t}^{\mathrm{trial}}}{\partial \mathbf{u}^{\mathrm{me}}}\,.\end{aligned} \tag{A.32}$$

In the above equations, the derivatives of $\boldsymbol{t}_{\mathrm{T}}$ with respect to $\mathbf{u}^{ke}$ are defined by Eq. (A.29). By substituting Eqs. (A.23), (A.32), and (A.29) into Eq. (A.31), and after rearranging terms, the partial derivatives of the tangential traction for sliding step are given as

$$\begin{aligned}\frac{\partial \boldsymbol{t}_{\mathrm{T}}}{\partial \mathbf{u}^{se}} &= \left(-\mu_f\,\epsilon_{\mathrm{N}}\,\boldsymbol{n}_{\mathrm{T}}\otimes\bar{\boldsymbol{n}}-\epsilon_{\mathrm{T}}\,\frac{\mu_f\,\epsilon_{\mathrm{N}}\,\mathrm{g}_{\mathrm{N}}}{||\boldsymbol{t}_{\mathrm{T}}^{\mathrm{trial}}||}[\boldsymbol{I}-\boldsymbol{n}_{\mathrm{T}}\otimes\boldsymbol{n}_{\mathrm{T}}]\,\bar{c}^{\alpha\beta}\,\bar{\boldsymbol{\tau}}_{\alpha}\otimes\bar{\boldsymbol{\tau}}_{\beta}\right)\mathbf{R}^{se}\,,\\ \frac{\partial \boldsymbol{t}_{\mathrm{T}}}{\partial \mathbf{u}^{me}} &= \left(\mu_f\,\epsilon_{\mathrm{N}}\,\boldsymbol{n}_{\mathrm{T}}\otimes\bar{\boldsymbol{n}}+\epsilon_{\mathrm{T}}\,\frac{\mu_f\,\epsilon_{\mathrm{N}}\,\mathrm{g}_{\mathrm{N}}}{||\boldsymbol{t}_{\mathrm{T}}^{\mathrm{trial}}||}[\boldsymbol{I}-\boldsymbol{n}_{\mathrm{T}}\otimes\boldsymbol{n}_{\mathrm{T}}]\,\bar{c}^{\alpha\beta}\,\bar{\boldsymbol{\tau}}_{\alpha}\otimes\bar{\boldsymbol{\tau}}_{\beta}\right)\mathbf{R}^{me}\\ &\quad-\epsilon_{\mathrm{T}}\frac{\mu_f\,\epsilon_{\mathrm{N}}\,\mathrm{g}_{\mathrm{N}}}{||\boldsymbol{t}_{\mathrm{T}}^{\mathrm{trial}}||}(\boldsymbol{I}-\boldsymbol{n}_{\mathrm{T}}\otimes\boldsymbol{n}_{\mathrm{T}})\,(\mathbf{R}^{me}-\mathbf{R}^{me}(\xi_{sl\,n}^{\mathrm{m}}))\\ &\quad-\epsilon_{\mathrm{T}}\,\frac{\mu_f\,\epsilon_{\mathrm{T}}\,\mathrm{g}_{\mathrm{N}}}{||\boldsymbol{t}_{\mathrm{T}}^{\mathrm{trial}}||}(\boldsymbol{I}-\boldsymbol{n}_{\mathrm{T}}\otimes\boldsymbol{n}_{\mathrm{T}})\,\bar{c}^{\alpha\beta}\,\bar{\boldsymbol{\tau}}_{\alpha}\otimes\bar{\boldsymbol{n}}\,\mathbf{R}^{me}_{,\beta}\,.\end{aligned} \tag{A.33}$$

A.4 Tangent matrix for adhesive contact

Since in the present work the master body for the adhesive contact problem is considered as a rigid substrate, the tangent matrix is derived only for the slave body. With this, the elemental tangent matrix, which is obtained through the linearization of the adhesive force vector defined in Eq. (4.29), is given as (see Appendix A in [117] for the derivation of the tangent matrix for finite element formulation)

$$\mathbf{k}_{\mathrm{c}}^{se}=-\int_{\Gamma^{\mathrm{se}}}(\mathbf{R}^{\mathrm{se}})^{\mathrm{T}}\left(\frac{\partial T_{\mathrm{c}}(r)}{\partial r}\,\bar{\boldsymbol{n}}\otimes\bar{\boldsymbol{n}}\right)\mathbf{R}^{se}\,\mathrm{d}\Gamma\,, \tag{A.34}$$

where the derivative of $T_{\mathrm{c}}(r)$ with respect to surface distance r is defined in Eq. (3.88).

Appendix B

Supplementary Results for Adhesive Peeling Problem

In this appendix, the performance of the standard NURBS discretizations is demonstrated as compared to the higher-order Lagrange discretizations for the peeling analysis. The setup of the problem and the considered simulation parameters are the same as considered in Section 7.4. Moreover, the three different meshes that are used for the convergence study are given by Table 7.7. The results presented in the following are taken from Agrawal and Gautam [128].

In the first section, the performance of the standard N_p order of NURBS discretizations is demonstrated as compared to L_p order of Lagrange discretization for the computation of the peeling responses. After that, in the second section, the convergence of the results for the different interpolation order of NURBS and Lagrange based discretizations are shown with the mesh refinement.

B.1 Computation of peeling responses

From Fig. B.1(a) it can be observed that on increasing the interpolation order of the Lagrange discretization from L_1 to L_4, the quality of the result improves substantially as both the oscillation amplitude and negative downward slope, which is critical for convergence, reduce. In particular, L_4 reduces the oscillation amplitude by a factor of 10.11 and the negative downward slope by 30.96 as compared to L_1, see Table B.1. Such an improvement is attributed to a large number of additional degrees of freedom

(DOFs), i.e. 13200, present with L_4 than with L_1 based discretization. On the

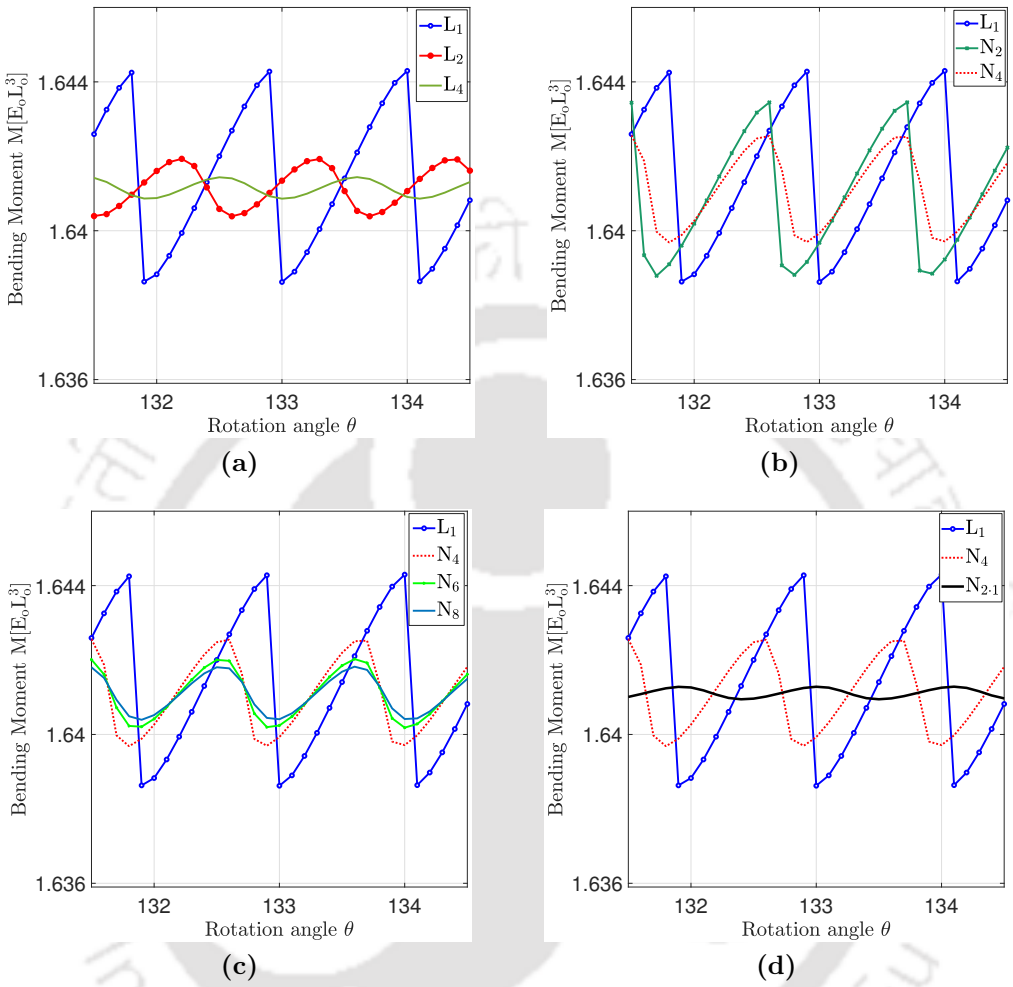

Figure B.1: Variation of bending moment with rotation angle for (a) L_1, L_2 and L_4 order of Lagrange discretization, (b) N_1/L_1, N_2 and N_4, (c) N_4, N_6 and N_8, and (d) N_4 and $N_{2\cdot1}$ based NURBS discretizations with mesh m_2.

other hand, from Fig. B.1(b), it can be observed that with N_2 and N_4, although the inter-element continuity C^{p-1} increases, only a marginal improvement can be achieved. Quantitatively, they reduce the oscillation amplitude by a factor of 1.3 and 1.93 and negative slope by 1.56 and 2.97, respectively, see Table B.1. This is since N_2 and N_4 have only 44 and 88 number of additional DOFs as compared to N_1 or L_1 based discretization, respectively. Thus, the improvement attained with N_4 is not very large. The quality of the result improves monotonically on further increasing the continuity of the NURBS with N_6 and N_8 discretizations, see Fig. B.1(c). Such a monotonic

Function Type	Discretization Type	ΔM in (%)	max(dM/dθ) in (%)	min(dM/dθ) in (%)
Lagrange	L_1	100	100	100
	L_2	26.74	42.83	11.13
	L_4	9.89	19.94	3.23
NURBS	N_2	76.79	84.98	64.18
	N_4	51.69	68.19	33.64
	N_6	32.21	50.59	14.01
	N_8	25.05	39.95	10.05
	$N_{2\cdot1}$	6.10	11.02	1.97

Table B.1: Reduction in the oscillation amplitude, and maximum and minimum slope of the peeling moment curve (in %) with the different Lagrange and NURBS based discretizations at mesh m_2. The result with L_1 is used as a reference.

improvement is due to an increase of only 44 number of total DOFs with each step of N_p, see Table B.2. With N_8, a result slightly better than L_2 and close to L_4 in terms of ΔM and min(dM/dθ) is obtained with an approximately 32% and 74% lower number of DOFs than with L_2 and L_4, respectively, see Table B.2.

Furthermore, the bending moment curve corresponding to $N_{2\cdot1}$ is shown in Fig. B.1(d). The figure shows that as compared to N_1, $N_{2\cdot1}$ significantly reduces the oscillation amplitude and negative slope by a factor of 16.39 and 50.76, respectively, see Table B.1. Comparing the result with $N_{2\cdot1}$ to that of smoother N_p ($p = 4, 6,$ and 8), it is evident that the higher-order NURBS based discretization is advantageous, see Table B.2 for the numeric values. Moreover, a careful observation between $N_{2\cdot1}$ and L_4 reveals that $N_{2\cdot1}$ delivers approximately 1.62 times better result in terms of ΔM and min(dM/dθ) at an approximately 49% lower number of DOFs than with L_4. Thus, the obtained results clearly show that higher-order NURBS based discretization is a much more accurate and efficient choice for the peeling computations over its counterparts higher-order Lagrange discretizations, and higher-continuous NURBS discretizations.

B.2 Convergence study

Figure B.2 shows the convergences of the bending moment curves for the L_4 and $N_{2\cdot1}$ based discretizations. As earlier, for a fixed mesh resolution, $N_{2\cdot1}$ provides a more accurate result at an approximately 49% of a lower number of total DOFs than with L_4, see also Table B.2 for DOFs details. The convergence of the ΔM for the different

Function Type	**Discretization Type**	**Mesh**	ΔM $\times 10^{-3}$	max(dM/dθ) $\times 10^{-3}$	min(dM/dθ) $\times 10^{-3}$	Total DOFs
Lagrange	L_1	m_1	–	–	–	2898
	L_2	m_1	4.0237	5.5705	-15.7641	5778
	L_4	m_1	1.6427	2.9272	-4.8585	11538
NURBS	N_2	m_1	–	–	–	2900
	N_4	m_1	6.9489	7.4972	-64.1522	2952
	N_6	m_1	4.8673	5.9933	-35.3973	2988
	N_8	m_1	3.7054	5.3543	-18.3877	3024
	$N_{2\cdot1}$	m_1	0.8272	1.3965	-2.8673	5796
Lagrange	L_1	m_2	5.5763	7.5197	-54.7829	4422
	L_2	m_2	1.4916	3.2205	-6.0977	6722
	L_4	m_2	0.5517	1.4996	-1.7733	17622
NURBS	N_2	m_2	4.2825	6.3906	-35.1618	4444
	N_4	m_2	2.8824	5.1276	-18.4271	4488
	N_6	m_2	1.7963	3.8046	-7.6738	4532
	N_8	m_2	1.3970	3.0044	-5.5028	4576
	$N_{2\cdot1}$	m_2	0.3404	0.8285	-1.0830	8844
Lagrange	L_1	m_3	2.0576	4.6868	-11.9711	6266
	L_2	m_3	0.5589	1.7117	-2.2874	12506
	L_4	m_3	0.2069	0.6591	-0.5951	24986
NURBS	N_2	m_3	1.6788	3.7233	-8.9545	6292
	N_4	m_3	1.0942	2.9194	-5.0689	6344
	N_6	m_3	0.6982	1.9106	-2.5468	6396
	N_8	m_3	0.5464	1.4583	-1.8001	6448
	$N_{2\cdot1}$	m_3	0.1309	0.4456	-0.5109	12532

Table B.2: Peeling moment oscillation amplitude ΔM, maximum slope max(dM/dθ), minimum slope min(dM/dθ) of peeling moment curve, and the total number of DOFs with the different order of Lagrange and NURBS based discretization with three meshes.

L_p and N_p order of discretizations is shown in Fig. 7.27. Clearly, higher-order based $N_{2\cdot1}$ discretization accomplishes more accurate results than higher-continuous N_p or its counterpart L_p based discretizations for a fixed mesh resolution.

Thus, based on the obtained results, it can be summarized that with higher-continuous NURBS, a similar accuracy can be achieved as compared to higher-order Lagrange discretizations at a much lower computational cost in terms of DOFs. Moreover, the comparative analysis shows that higher-order NURBS based discretization is a much better choice for peeling computations. It considerably improves the quality of the results with much lower computational cost as compared to higher-order Lagrange

based discretizations.

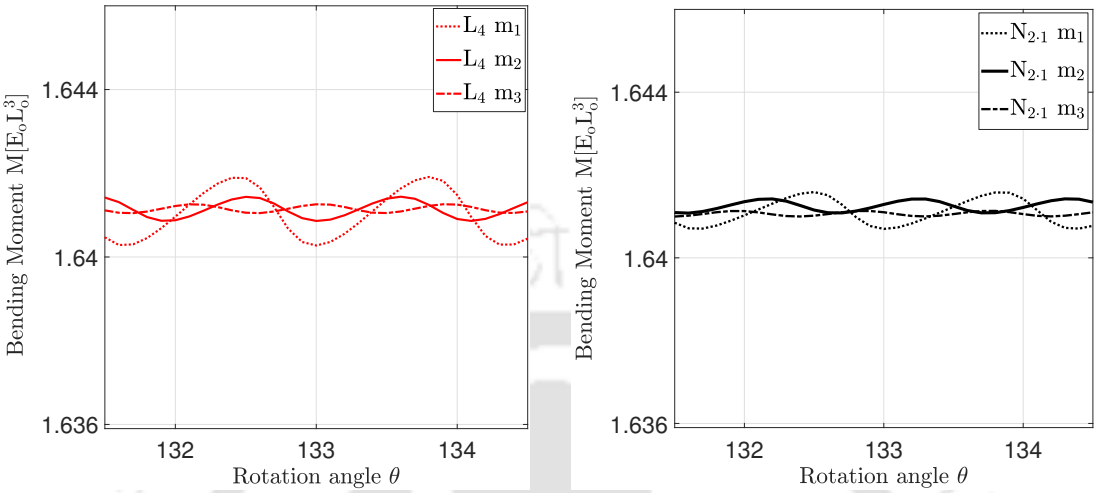

(a) **(b)**

Figure B.2: Variation of bending moment with rotation angle for (a) L_4 order of Lagrange, and (b) $N_{2\cdot1}$ order of NURBS based discretization with different meshes.

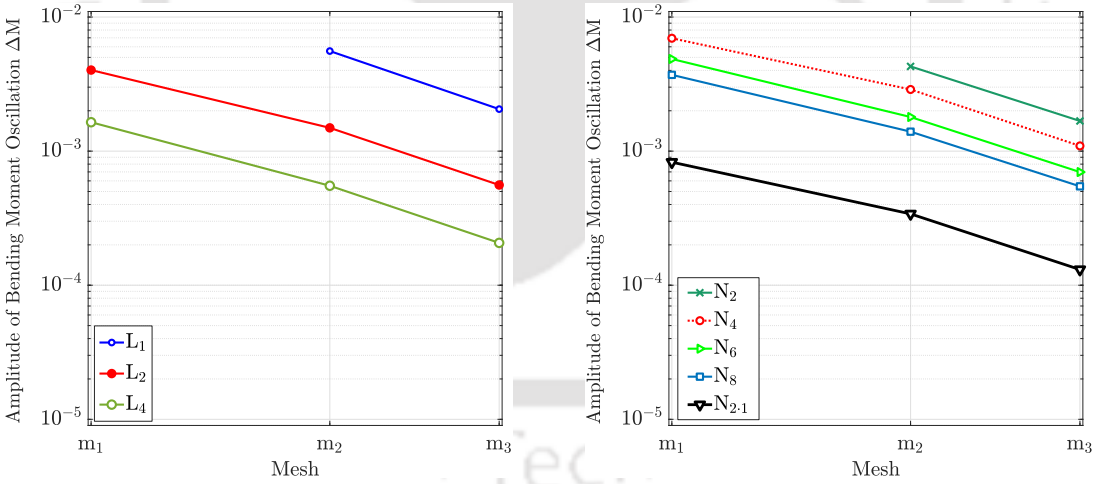

(a) Lagrange based discretizations **(b)** NURBS based discretizations

Figure B.3: Bending moment oscillation amplitude ΔM with three different meshes for various type of discretizations.

References

[1] Neto, D. M., Oliveira, M. C., and Menezes, L. F. "Surface smoothing procedures in computational contact mechanics". *Archives of Computational Methods in Engineering*, Vol. 24, 37–87, **2017**. DOI: 10.1007/s11831-015-9159-7.

[2] Carlsson, P. "Surface engineering in sheet metal forming". PhD thesis. Uppsala Universitet, Uppsala, Sweden, **2005**.

[3] Khoshgoftar, M., Vrancken, A. C. T., van Tienen, T. G., Buma, P., Janssen, D., and Verdonschot, N. "The sensitivity of cartilage contact pressures in the knee joint to the size and shape of an anatomically shaped meniscal implant". *Journal of Biomechanics*, Vol. 48, No. 8, 1427–1435, **2015**. DOI: 10.1016/j.jbiomech.2015.02.034.

[4] Viegas, C. and Tavakoli, M. "Bio-inspired climbing robots". In: *Biomimetic Technologies*. Ed. by Ngo, T. D. Woodhead Publishing, **2015**, 301–320. DOI: 10.1016/B978-0-08-100249-0.00014-8.

[5] Zhong, Z. H. *Finite element procedures for contact-impact problems*. Oxford: Oxford University Press, **1993**.

[6] Wriggers, P. *Computational contact mechanics*. Berlin, Heidelberg: Springer, **2006**.

[7] Hertz, H. R. "Über die Berüehrung fester elastischer Körper (On the contact of solid elastic bodies)". *Journal für die reine und angewandte Mathematik (Journal for the pure and applied mathematics)*, Vol. 92, 156–171, **1881**.

[8] Johnson, K. L. *Contact mechanics*. Cambridge: Cambridge University Press, **1987**.

[9] Kikuchi, N. and Oden, J. T. *Contact problems in elasticity: a study of variational inequalities and finite element methods*. Philadelphia: SIAM, **1998**.

[10] Hughes, T. J. R. *The finite element method: linear static and dynamic finite element analysis*. Dover Publications, **2000**.

[11] Turner, M. J., Clough, R. W., Martin, H. C., and Topp, L. J. "Stiffness and deflection analysis of complex structures". *Journal of the Aeronautical Sciences*, Vol. 23, No. 9, 805–823, **1956**. DOI: 10.2514/8.3664.

[12] Wilson, E. A. and Parsons, B. "Finite element analysis of elastic contact problems using differential displacements". *International Journal for Numerical Methods in Engineering*, Vol. 2, No. 3, 387–395, **1970**. DOI: 10.1002/nme.1620020307.

[13] Chan, S. K. and Tuba, I. S. "A finite element method for contact problems of solid bodies-Part I. Theory and validation". *International Journal of Mechanical Sciences*, Vol. 13, No. 7, 615–625, **1971**. DOI: 10.1016/0020-7403(71)90032-4.

[14] Hughes, T. J. R., Taylor, R. L., Sackman, J. L., Curnier, A., and Kanoknukulchai, W. "A finite element method for a class of contact-impact problems". *Computer Methods in Applied Mechanics and Engineering*, Vol. 8, No. 3, 249–276, **1976**. DOI: 10.1016/0045-7825(76)90018-9.

[15] Campos, L. T., Oden, J. T., and Kikuchi, N. "A numerical analysis of a class of contact problems with friction in elastostatics". *Computer Methods in Applied Mechanics and Engineering*, Vol. 34, No. 1, 821–845, **1982**. DOI: 10.1016/0045-7825(82)90090-1.

[16] Wriggers, P., Vu Van, T., and Stein, E. "Finite element formulation of large deformation impact-contact problems with friction". *Computers & Structures*, Vol. 37, No. 3, 319–331, **1990**. DOI: 10.1016/0045-7949(90)90324-U.

[17] Laursen, T. A. and Simo, J. C. "A continuum-based finite element formulation for the implicit solution of multibody, large deformation-frictional contact problems". *International Journal for Numerical Methods in Engineering*, Vol. 36, No. 20, 3451–3485, **1993**. DOI: 10.1002/nme.1620362005.

[18] Laursen, T. A. *Computational contact and impact mechanics: fundamentals of modeling interfacial phenomena in nonlinear finite element analysis*. Springer, Berlin, **2002**.

[19] Wriggers, P. "Finite element algorithms for contact problems". *Archives of Computational Methods in Engineering volume*, Vol. 2, 1–49, **1995**. DOI: 10.1007/BF02736195.

[20] De Lorenzis, L., Wriggers, P., and Weißenfels, C. "Computational contact mechanics with the finite element method". In: *Encyclopedia of Computational Mechanics Second Edition*. American Cancer Society, **2017**, 1–45. DOI: 10.1002/9781119176817.ecm2033.

[21] De Lorenzis, L., Wriggers, P., and Hughes, T. J. R. "Isogeometric contact: a review". *GAMM Mitteilungen*, Vol. 37, No. 1, 85–123, **2014**. DOI: 10.1002/gamm.201410005.

[22] Hallquist, J. O., Goudreau, G. L., and Benson, D. J. "Sliding interfaces with contact-impact in large-scale Lagrangian computations". *Computer Methods in Applied Mechanics and Engineering*, Vol. 51, No. 1, 107–137, **1985**. DOI: 10.1016/0045-7825(85)90030-1.

[23] Bathe, K. J. and Chaudhary, A. "A solution method for planar and axisymmetric contact problems". *International Journal for Numerical Methods in Engineering*, Vol. 21, No. 1, 65–88, **1985**. DOI: 10.1002/nme.1620210107.

[24] Alart, P. and Curnier, A. "A mixed formulation for frictional contact problems prone to Newton like solution methods". *Computer Methods in Applied Mechanics and Engineering*, Vol. 92, No. 3, 353–375, **1991**. DOI: 10.1016/0045-7825(91)90022-X.

[25] Simo, J. C. and Laursen, T. A. "An augmented lagrangian treatment of contact problems involving friction". *Computers & Structures*, Vol. 42, No. 1, 97–116, **1992**. DOI: 10.1016/0045-7949(92)90540-G.

[26] Pietrzak, G. and Curnier, A. "Large deformation frictional contact mechanics: continuum formulation and augmented Lagrangian treatment". *Computer Methods in Applied Mechanics and Engineering*, Vol. 177, No. 3, 351–381, **1999**. DOI: 10.1016/S0045-7825(98)00388-0.

[27] Papadopoulos, P. and Taylor, R. L. "A mixed formulation for the finite element solution of contact problems". *Computer Methods in Applied Mechanics and Engineering*, Vol. 94, No. 3, 373–389, **1992**. DOI: 10.1016/0045-7825(92)90061-N.

[28] Fischer, K. A. and Wriggers, P. "Frictionless 2D contact formulations for finite deformations based on the mortar method". *Computational Mechanics*, Vol. 36, No. 3, 226–244, **2005**. DOI: 10.1007/s00466-005-0660-y.

[29] De Lorenzis, L., Temizer, I., Wriggers, P., and Zavarise, G. "A large deformation frictional contact formulation using NURBS-based isogeometric analysis". *International Journal for Numerical Methods in Engineering*, Vol. 87, No. 13, 1278–1300, **2011**. DOI: 10.1002/nme.3159.

[30] Temizer, I., Wriggers, P., and Hughes, T. J. R. "Contact treatment in isogeometric analysis with NURBS". *Computer Methods in Applied Mechanics and Engineering*, Vol. 200, No. 9–12, 1100–1112, **2011**. DOI: 10.1016/j.cma.2010.11.020.

[31] Dimitri, R., De Lorenzis, L., Scott, M. A., Wriggers, P., Taylor, R. L., and Zavarise, G. "Isogeometric large deformation frictionless contact using T-splines". *Computer Methods in Applied Mechanics and Engineering*, Vol. 269, 394–414, **2014**. DOI: 10.1016/j.cma.2013.11.002.

[32] Puso, M. A. and Laursen, T. A. "A mortar segment-to-segment contact method for large deformation solid mechanics". *Computer Methods in Applied Mechanics and Engineering*, Vol. 193, No. 6, 601–629, **2004**. DOI: 10.1016/j.cma.2003.10.010.

[33] Yang, B., Laursen, T. A., and Meng, X. "Two dimensional mortar contact methods for large deformation frictional sliding". *International Journal for Numerical Methods in Engineering*, Vol. 62, No. 9, 1183–1225, **2005**. DOI: 10.1002/nme.1222.

[34] Yang, B. and Laursen, T. A. "A large deformation mortar formulation of self contact with finite sliding". *Computer Methods in Applied Mechanics and Engineering*, Vol. 197, No. 6, 756–772, **2008**. DOI: 10.1016/j.cma.2007.09.004.

[35] Tur, M., Fuenmayor, F. J., and Wriggers, P. "A mortar-based frictional contact formulation for large deformations using Lagrange multipliers". *Computer Methods in Applied Mechanics and Engineering*, Vol. 198, No. 37, 2860–2873, **2009**. DOI: 10.1016/j.cma.2009.04.007.

[36] Popp, A., Gitterle, M., Gee, M. W., and Wall, W. A. "A dual mortar approach for 3D finite deformation contact with consistent linearization". *International Journal for Numerical Methods in Engineering*, Vol. 83, No. 11, 1428–1465, **2010**. DOI: 10.1002/nme.2866.

[37] Popp, A., Seitz, A., Gee, M. W., and Wall, W. A. "Improved robustness and consistency of 3D contact algorithms based on a dual mortar approach". *Computer Methods in Applied Mechanics and Engineering*, Vol. 264, 67–80, **2013**. DOI: 10.1016/j.cma.2013.05.008.

[38] Padmanabhan, V. and Laursen, T. A. "A framework for development of surface smoothing procedures in large deformation frictional contact analysis". *Finite Elements in Analysis and Design*, Vol. 37, No. 3, 173–198, **2001**. DOI: 10.1016/S0168-874X(00)00029-9.

[39] Wriggers, P., Krstulovic-Opara, L., and Korelc, J. "Smooth C^1-interpolations for two-dimensional frictional contact problems". *International Journal for Numerical Methods in Engineering*, Vol. 51, No. 12, 1469–1495, **2001**. DOI: 10.1002/nme.227.

[40] Elabbasi, N., Meguid, S. A., and Czekanski, A. "On the modelling of smooth contact surfaces using cubic splines". *International Journal for Numerical Methods in Engineering*, Vol. 50, No. 4, 953–967, **2001**. DOI: 10.1002/1097-0207(20010210)50:4<953::AID-NME64>3.0.CO;2-P.

[41] Al-Dojayli, M. and Meguid, S. A. "Accurate modeling of contact using cubic splines". *Finite Elements in Analysis and Design*, Vol. 38, No. 4, 337–352, **2002**. DOI: 10.1016/S0168-874X(01)00088-9.

[42] Stadler, M., Holzapfel, G. A., and Korelc, J. "C^n-continuous modelling of smooth contact surfaces using NURBS and application to 2D problems". *International Journal for Numerical Methods in Engineering*, Vol. 57, No. 15, 2177–2203, **2003**. DOI: 10.1002/nme.776.

[43] Lengiewicz, J., Korelc, J., and Stupkiewicz, S. "Automation of finite element formulations for large deformation contact problems". *International Journal for Numerical Methods in Engineering*, Vol. 85, No. 10, 1252–1279, **2011**. DOI: 10.1002/nme.3009.

[44] Puso, M. and Laursen, T. A. "A 3D contact smoothing method using Gregory patches". *International Journal for Numerical Methods in Engineering*, Vol. 54, No. 8, 1161–1194, **2002**. DOI: 10.1002/nme.466.

[45] Krstulović-Opara, L., Wriggers, P., and Korelc, J. "A C^1-continuous formulation for 3D finite deformation frictional contact". *Computational Mechanics*, Vol. 29, No. 1, 27–42, **2002**. DOI: 10.1007/s00466-002-0317-z.

[46] Stadler, M. and Holzapfel, G. A. "Subdivision schemes for smooth contact surfaces of arbitrary mesh topology in 3D". *International Journal for Numerical Methods in Engineering*, Vol. 60, No. 7, 1161–1195, **2004**. DOI: 10.1002/nme.1001.

[47] Temizer, I., Wriggers, P., and Hughes, T. J. R. "Three-dimensional mortar-based frictional contact treatment in isogeometric analysis with NURBS". *Computer Methods in Applied Mechanics and Engineering*, Vol. 209–212, 115–128, **2012**. DOI: 10.1016/j.cma.2011.10.014.

[48] Konyukhov, A. and Schweizerhof, K. "Incorporation of contact for high–order finite elements in covariant form". *Computer Methods in Applied Mechanics and Engineering*, Vol. 198, No. 13, 1213–1223, **2009**. DOI: 10.1016/j.cma.2008.04.023.

[49] Konyukhov, A. and Schweizerhof, K. *Computational contact mechanics-geometrically exact theory for arbitrary shaped bodies*. Vol. 67. Springer, Heildelberg, **2013**. DOI: 10.1007/978-3-642-31531-2.

[50] Sauer, R. A. "Enriched contact finite elements for stable peeling computations". *International Journal for Numerical Methods in Engineering*, Vol. 87, No. 6 **2011**. DOI: 10.1002/nme.3126.

[51] Sauer, R. A. "Local finite element enrichment strategies for 2D contact computations and a corresponding post-processing scheme". *Computational Mechanics*, Vol. 52, No. 2, 301–319, **2013**. DOI: 10.1007/s00466-012-0813-8.

[52] Hughes, T. J. R., Cottrell, J. A., and Bazilevs, Y. "Isogeometric analysis: CAD, finite elements, NURBS, exact geometry and mesh refinement". *Computer Methods in Applied Mechanics and Engineering*, Vol. 194, No. 39–41, 4135–4195, **2005**. DOI: 10.1016/j.cma.2004.10.008.

[53] Cottrell, J. A., Hughes, T. J. R., and Bazilevs, Y. *Isogeometric analysis: toward integration of CAD and FEA*. Wiley, **2009**.

[54] Kiendl, J., Bletzinger, K.-U., Linhard, J., and Wüchner, R. "Isogeometric shell analysis with Kirchhoff-Love elements". *Computer Methods in Applied Mechanics and Engineering*, Vol. 198, No. 49, 3902–3914, **2009**. DOI: 10.1016/j.cma.2009.08.013.

[55] Kiendl, J., Bazilevs, Y., Hsu, M. C., Wüchner, R., and Bletzinger, K. U. "The bending strip method for isogeometric analysis of Kirchhoff-Love shell structures comprised of multiple patches". *Computer Methods in Applied Mechanics and Engineering*, Vol. 199, No. 37, 2403–2416, **2010**. DOI: 10.1016/j.cma.2010.03.029.

[56] Wall, W. A., Frenzel, M. A., and Cyron, C. "Isogeometric structural shape optimization". *Computer Methods in Applied Mechanics and Engineering*, Vol. 197, No. 33, 2976–2988, **2008**. DOI: 10.1016/j.cma.2008.01.025.

[57] Qian, X. "Full analytical sensitivities in NURBS based isogeometric shape optimization". *Computer Methods in Applied Mechanics and Engineering*, Vol. 199, No. 29, 2059–2071, **2010**. DOI: 10.1016/j.cma.2010.03.005.

[58] Cottrell, J. A., Hughes, T. J. R., and Reali, A. "Studies of refinement and continuity in isogeometric structural analysis". *Computer Methods in Applied Mechanics and Engineering*, Vol. 196, No. 41–44, 4160–4183, **2007**. DOI: 10.1016/j.cma.2007.04.007.

[59] Hughes, T. J. R., Reali, A., and Sangalli, G. "Duality and unified analysis of discrete approximations in structural dynamics and wave propagation: comparison of p-method finite elements with k-method NURBS". *Computer Methods in Applied Mechanics and Engineering*, Vol. 197, No. 49, 4104–4124, **2008**. DOI: 10.1016/j.cma.2008.04.006.

[60] Verhoosel, C. V., Scott, M. A., Borst, R. de, and Hughes, T. J. R. "An isogeometric approach to cohesive zone modeling". *International Journal for Numerical Methods in Engineering*, Vol. 87, No. 1–5, 336–360, **2011**. DOI: 10.1002/nme.3061.

[61] Dimitri, R., De Lorenzis, L., Wriggers, P., and Zavarise, G. "NURBS- and T-spline-based isogeometric cohesive zone modeling of interface debonding". *Computational Mechanics*, Vol. 54, No. 2, 369–388, **2014**. DOI: 10.1007/s00466-014-0991-7.

[62] Dimitri, R. and Zavarise, G. "Isogeometric treatment of frictional contact and mixed mode debonding problems". *Computational Mechanics*, Vol. 60, No. 2, 315–332, **2017**. DOI: 10.1007/s00466-017-1410-7.

[63] Bhardwaj, G., Singh, I. V., and Mishra, B. K. "Stochastic fatigue crack growth simulation of interfacial crack in bi-layered FGMs using XIGA". *Computer Methods in Applied Mechanics and Engineering*, Vol. 284, 186–229, **2015**. DOI: 10.1016/j.cma.2014.08.015.

[64] Bhardwaj, G., Singh, S. K., Singh, I. V., Mishra, B. K., and Rabczuk, T. "Fatigue crack growth analysis of an interfacial crack in heterogeneous materials using homogenized XIGA". *Theoretical and Applied Fracture Mechanics*, Vol. 85, 294–319, **2016**. DOI: 10.1016/j.tafmec.2016.04.004.

[65] Singh, S. K., Singh, I. V., Mishra, B. K., and Bhardwaj, G. "Analysis of cracked functionally graded material plates using XIGA based on generalized higher-order shear deformation theory". *Composite Structures*, Vol. 225, 111038, **2019**. DOI: 10.1016/j.compstruct.2019.111038.

[66] De Lorenzis, L., Wriggers, P., and Zavarise, G. "A mortar formulation for 3D large deformation contact using NURBS-based isogeometric analysis and the augmented Lagrangian method". *Computational Mechanics*, Vol. 49, No. 1, 1–20, **2012**. DOI: 10.1007/s00466-011-0623-4.

[67] Lu, J. "Isogeometric contact analysis: geometric basis and formulation for frictionless contact". *Computer Methods in Applied Mechanics and Engineering*, Vol. 200, No. 5–8, 726–741, **2011**. DOI: 10.1016/j.cma.2010.10.001.

[68] Dittmann, M., Franke, M., Temizer, I., and Hesch, C. "Isogeometric analysis and thermomechanical mortar contact problems". *Computer Methods in Applied Mechanics and Engineering*, Vol. 274, 192–212, **2014**. DOI: 10.1016/j.cma.2014.02.012.

[69] Seitz, A., Farah, P., Kremheller, J., Wohlmuth, B. I., Wall, W. A., and Popp, A. "Isogeometric dual mortar methods for computational contact mechanics". *Computer Methods in Applied Mechanics and Engineering*, Vol. 301, 259–280, **2016**. DOI: 10.1016/j.cma.2015.12.018.

[70] Matzen, M. E., Cichosz, T., and Bischoff, M. "A point to segment contact formulation for isogeometric, NURBS based finite elements". *Computer Methods in Applied Mechanics and Engineering*, Vol. 255, 27–39, **2013**. DOI: 10.1016/j.cma.2012.11.011.

[71] Matzen, M. E. and Bischoff, M. "A weighted point-based formulation for isogeometric contact". *Computer Methods in Applied Mechanics and Engineering*, Vol. 308, 73–95, **2016**. DOI: 10.1016/j.cma.2016.04.010.

[72] De Lorenzis, L., Evans, J. A., Hughes, T. J. R., and Reali, A. "Isogeometric collocation: Neumann boundary conditions and contact". *Computer Methods in Applied Mechanics and Engineering*, Vol. 284, 21–54, **2015**. DOI: 10.1016/j.cma.2014.06.037.

[73] Kruse, R., Nguyen-Thanh, N., De Lorenzis, L., and Hughes, T. J. R. "Isogeometric collocation for large deformation elasticity and frictional contact problems". *Computer Methods in Applied Mechanics and Engineering*, Vol. 296, 73–112, **2015**. DOI: 10.1016/j.cma.2015.07.022.

[74] Weeger, O., Narayanan, B., and Dunn, M. L. "Isogeometric collocation for nonlinear dynamic analysis of Cosserat rods with frictional contact". *Nonlinear Dynamics*, Vol. 91, No. 2, 1213–1227, **2018**. DOI: 10.1007/s11071-017-3940-0.

[75] Nguyen-Thanh, N., Li, W., Huang, J., Srikanth, N., and Zhou, K. "An adaptive isogeometric analysis meshfree collocation method for elasticity and frictional contact problems". *International Journal for Numerical Methods in Engineering*, Vol. 120, No. 2, 209–230, **2019**. DOI: 10.1002/nme.6132.

[76] Sauer, R. A. and De Lorenzis, L. "A computational contact formulation based on surface potentials". *Computer Methods in Applied Mechanics and Engineering*, Vol. 253, 369–395, **2013**. DOI: 10.1016/j.cma.2012.09.002.

[77] Sauer, R. A. and De Lorenzis, L. "An unbiased computational contact formulation for 3D friction". *International Journal for Numerical Methods in Engineering*, Vol. 101, No. 4, 251–280, **2015**. DOI: 10.1002/nme.4794.

[78] Franke, D., Düster, A., Nübel, V., and Rank, E. "A comparison of the $h-$, $p-$, $hp-$, and $rp-$ version of the FEM for the solution of the 2D Hertzian contact problem". *Computational Mechanics*, Vol. 45, No. 5, 513–522, **2010**. DOI: 10.1007/s00466-009-0464-6.

[79] Kim, J. Y. and Youn, S. K. "Isogeometric contact analysis using mortar method". *International Journal for Numerical Methods in Engineering*, Vol. 89, No. 12, 1559–1581, **2012**. DOI: 10.1002/nme.3300.

[80] Bidkhori, E. and Hassani, B. "A parametric knot adaptation approach to isogeometric analysis of contact problems". *Engineering with Computers* **2020**. DOI: 10.1007/s00366-020-01073-0.

[81] De Lorenzis, L. and Wriggers, P. "Computational homogenization of rubber friction on rough rigid surfaces". *Computational Materials Science*, Vol. 77, 264–280, **2013**. DOI: 10.1016/j.commatsci.2013.04.049.

[82] Temizer, I. "Multiscale thermomechanical contactCo: computational homogenization with isogeometric analysis". *International Journal for Numerical Methods in Engineering*, Vol. 97, No. 8, 582–607, **2013**. DOI: 10.1002/nme.4604.

[83] Sauer, R. A., Duong, T. X., and Corbett, C. J. "A computational formulation for constrained solid and liquid membranes considering isogeometric finite elements". *Computer Methods in Applied Mechanics and Engineering*, Vol. 271, 48–68, **2014**. DOI: 10.1016/j.cma.2013.11.025.

[84] Lu, J. and Zheng, C. "Dynamic cloth simulation by isogeometric analysis". *Computer Methods in Applied Mechanics and Engineering*, Vol. 268, 475–493, **2014**. DOI: 10.1016/j.cma.2013.09.016.

[85] Seong-Geun, S. and Chang-Ock, L. "Splitting basis techniques in cloth simulation by isogeometric analysis". *Computer Methods in Applied Mechanics and Engineering*, Vol. 362, 112871, **2020**. DOI: 10.1016/j.cma.2020.112871.

[86] Cardoso, R. P. R., Adetoro, O. B., and Adan, D. "Contact modelling in isogeometric analysis: application to sheet metal forming processes". *Journal of Physics: Conference Series*, Vol. 734, 032123, **2016**. DOI: 10.1088/1742-6596/734/3/032123.

[87] Cardoso, R. P. R. and Adetoro, O. B. "On contact modelling in isogeometric analysis". *European Journal of Computational Mechanics*, Vol. 26, 1–30, **2017**. DOI: 10.1080/17797179.2017.1354575.

[88] Morganti, S., Auricchio, F., Benson, D. J., Gambarin, F. I., Hartmann, S., Hughes, T. J. R., and Reali, A. "Patient-specific isogeometric structural analysis of aortic valve closure". *Computer Methods in Applied Mechanics and Engineering*, Vol. 284, 508–520, **2015**. DOI: 10.1016/j.cma.2014.10.010.

[89] Nishi, S., Terada, K., and Temizer, I. "Isogeometric analysis for numerical plate testing of dry woven fabrics involving frictional contact at meso-scale". *Computational Mechanics*, Vol. 64, 211–229, **2019**. DOI: 10.1007/s00466-018-1666-6.

[90] Pi, T. and Zhang, Y. "Modeling and simulation of revolute clearance joint with friction using the NURBS-based isogeometric analysis". *Nonlinear Dynamics*, Vol. 95, 195–215, **2019**. DOI: 10.1007/s11071-018-4559-5.

[91] Piegl, L. and Tiller, W. *The NURBS book (monographs in visual communication)*. Springer, Berlin Heidelberg, **2012**.

[92] Bazilevs, Y., Calo, V. M., Cottrell, J. A., Evans, J. A., Hughes, T. J. R., Lipton, S., Scott, M. A., and Sederberg, T. W. "Isogeometric analysis using T-splines". *Computer Methods in Applied Mechanics and Engineering*, Vol. 199, No. 5, 229–263, **2010**. DOI: 10.1016/j.cma.2009.02.036.

[93] Scott, M. A., Borden, M. J., Verhoosel, C. V., Sederberg, T. W., and Hughes, T. J. R. "Isogeometric finite element data structures based on Bézier extraction of T-splines". *International Journal for Numerical Methods in Engineering*, Vol. 88, No. 2, 126–156, **2011**. DOI: 10.1002/nme.3167.

[94] Temizer, I. and Hesch, C. "Hierarchical NURBS in frictionless contact". *Computer Methods in Applied Mechanics and Engineering*, Vol. 299, 161–186, **2016**. DOI: 10.1016/j.cma.2015.11.006.

[95] Hesch, C., Franke, M., Dittmann, M., and Temizer, I. "Hierarchical NURBS and a higher-order phase-field approach to fracture for finite-deformation contact problems". *Computer Methods in Applied Mechanics and Engineering*, Vol. 301, 242–258, **2016**. DOI: 10.1016/j.cma.2015.12.011.

[96] Zimmermann, C. and Sauer, R. A. "Adaptive local surface refinement based on LR NURBS and its application to contact". *Computational Mechanics*, Vol. 60, No. 6, 1011–1031, **2017**. DOI: 10.1007/s00466-017-1455-7.

[97] Dimitri, R. "Isogeometric treatment of large deformation contact and debonding problems with T-splines: a review". *Curved and Layered Structures*, Vol. 2, 59–90, **2015**. DOI: 10.1515/cls-2015-0005.

[98] Corbett, C. J. and Sauer, R. A. "NURBS-enriched contact finite elements". *Computer Methods in Applied Mechanics and Engineering*, Vol. 275, 55–75, **2014**. DOI: 10.1016/j.cma.2014.02.019.

[99] Borden, M. J., Scott, M. A., Evans, J. A., and Hughes, T. J. R. "Isogeometric finite element data structures based on Bézier extraction of NURBS". *International Journal for Numerical Methods in Engineering*, Vol. 87, No. 1–5, 15–47, **2011**. DOI: 10.1002/nme.2968.

[100] Corbett, C. J. and Sauer, R. A. "Three-dimensional isogeometrically enriched finite elements for frictional contact and mixed-mode debonding". *Computer Methods in Applied Mechanics and Engineering*, Vol. 284, 781–806, **2015**. DOI: 10.1016/j.cma.2014.10.025.

[101] Maleki-Jebeli, S., Mosavi-Mashhadi, M., and Baghani, M. "A large deformation hybrid isogeometric-finite element method applied to cohesive interface contact/debonding". *Computer Methods in Applied Mechanics and Engineering*, Vol. 330, 395–414, **2018**. DOI: 10.1016/j.cma.2017.10.017.

[102] Otto, P., De Lorenzis, L., and Unger, J. F. "Coupling a NURBS contact interface with a higher order finite element discretization for contact problems using the mortar method". *Computational Mechanics*, Vol. 63, No. 6, 1203–1222, **2019**. DOI: 10.1007/s00466-018-1645-y.

[103] Otto, P., De Lorenzis, L., and Unger, J. F. "Explicit dynamics in impact simulation using a NURBS contact interface". *International Journal for Numerical Methods in Engineering*, Vol. 121, No. 6, 1248–1267, **2019**. DOI: 10.1002/nme.6264.

[104] Dias, A. P. C., Proenca, S. P. B., and Bittencourt, M. L. "High-order mortar-based contact element using NURBS for the mapping of contact curved surfaces". *Computational Mechanics*, Vol. 64, No. 1, 85–112, **2019**. DOI: 10.1007/s00466-018-1658-6.

[105] Dias, A. P. C., Serpa, A. L., and Bittencourt, M. L. "High-order mortar-based element applied to nonlinear analysis of structural contact mechanics". *Computer Methods in Applied Mechanics and Engineering*, Vol. 294, 19–55, **2015**. DOI: 10.1016/j.cma.2015.05.013.

[106] Dias, A. P. C., Proenca, S. P. B., and Bittencourt, M. L. "Standard and generalized high-order mortar-based finite elements in computational contact mechanics". In: *Advances in computational coupling and contact mechanics*. **2018**, 55–107. DOI: 10.1142/9781786344786_0002.

[107] Tadmor, E. B., Ortiz, M., and Phillips, R. "Quasicontinuum analysis of defects in solids". *Philosophical Magazine A*, Vol. 73, No. 6, 1529–1563, **1996**. DOI: 10.1080/01418619608243000.

[108] Miller, R. E. and Tadmor, E. "The quasicontinuum method: overview, applications and current directions". *Journal of Computer-Aided Materials Design*, Vol. 9, 203–239, **2002**. DOI: https://doi.org/10.1023/A:1026098010127.

[109] Sauer, R. A. and Li, S. A. "An atomic interaction-based continuum model for adhesive contact mechanics". *Finite Elements in Analysis and Design*, Vol. 43, No. 5, 384–396, **2007**. DOI: 10.1016/j.finel.2006.11.009.

[110] Malvern, L. E. *Introduction to the mechanics of a continuous medium*. Prentice-Hall, **1969**.

[111] Bonet, J. and Wood, R. D. *Nonlinear continuum mechanics for finite element analysis*. Cambridge University Press, **1997**.

[112] Holzapfel, G. A. *Nonlinear solid mechanics: a continuum approach for engineering*. Wiley, **2000**.

[113] Reddy, J. N. *An Introduction to continuum mechanics*. Cambridge University Press, **2007**.

[114] Wriggers, P. *Nonlinear finite element methods*. Springer Berlin Heidelberg, **2008**.

[115] Belytschko, T., Liu, W., Moran, B., and Elkhodary, K. *Nonlinear finite elements for continua and structures*. Wiley, **2013**.

[116] Kreyszig, E. *Advanced engineering mathematics*. John Wiley & Sons, **2010**.

[117] Sauer, R. A. and Wriggers, P. "Formulation and analysis of a three-dimensional finite element implementation for adhesive contact at the nanoscale". *Computer Methods in Applied Mechanics and Engineering*, Vol. 198, No. 49–52, 3871–3883, **2009**. DOI: 10.1016/j.cma.2009.08.019.

[118] Zavarise, G. and De Lorenzis, L. "A modified node-to-segment algorithm passing the contact patch test". *International Journal for Numerical Methods in Engineering*, Vol. 79, No. 4, 379–416, **2009**. DOI: 10.1002/nme.2559.

[119] Duong, T. X., De Lorenzis, L., and Sauer, R. A. "A segmentation-free isogeometric extended mortar contact method". *Computational Mechanics*, Vol. 63, No. 2, 383–407, **2019**. DOI: 10.1007/s00466-018-1599-0.

[120] Popp, A. and Wall, W. A. "Dual mortar methods for computational contact mechanics-overview and recent developments". *GAMM-Mitteilungen*, Vol. 37, No. 1, 66–84, **2014**. DOI: 10.1002/gamm.201410004.

[121] Popp, A. *State-of-the-Art computational methods for finite deformation contact modeling of solids and structures*. Ed. by Popp, A. and Wriggers, P. Springer International Publishing, **2018**, 1–86. DOI: 10.1007/978-3-319-90155-8_1.

[122] Duong, T. X. and Sauer, R. A. "An accurate quadrature technique for the contact boundary in 3D finite element computations". *Computational Mechanics*, Vol. 55, No. 1, 145–166, **2015**. DOI: 10.1007/s00466-014-1087-0.

[123] Agrawal, V. and Gautam, S. S. "Varying-order NURBS discretization: an accurate and efficient method for isogeometric analysis of large deformation contact problems". *Computer Methods in Applied Mechanics and Engineering*, Vol. 367, 113125, **2020**. DOI: 10.1016/j.cma.2020.113125.

[124] Hughes, T. J. R., Reali, A., and Sangalli, G. "Efficient quadrature for NURBS-based isogeometric analysis". *Computer Methods in Applied Mechanics and Engineering*, Vol. 199, No. 5–8, 301–313, **2010**. DOI: 10.1016/j.cma.2008.12.004.

[125] Auricchio, F., Calabrò, F., Hughes, T. J. R., Reali, A., and Sangalli, G. "A simple algorithm for obtaining nearly optimal quadrature rules for NURBS-based isogeometric analysis". *Computer Methods in Applied Mechanics and Engineering*, Vol. 249–252, 15–27, **2012**. DOI: 10.1016/j.cma.2012.04.014.

[126] Fahrendorf, F., De Lorenzis, L., and Gomez, H. "Reduced integration at superconvergent points in isogeometric analysis". *Computer Methods in Applied Mechanics and Engineering*, Vol. 328, 390–410, **2018**. DOI: 10.1016/j.cma.2017.08.028.

[127] Temizer, I., Abdalla, M. M., and Gurdal, Z. "An interior point method for isogeometric contact". *Computer Methods in Applied Mechanics and Engineering*, Vol. 276, 589–611, **2014**. DOI: 10.1016/j.cma.2014.03.018.

[128] Agrawal, V. and Gautam, S. S. "NURBS based isogeometric analysis for stable and accurate peeling computations". *Sadhana*, Vol. 43, No. 3 **2021**. DOI: 10.1007/s12046-020-01513-z.

[129] Wei, Y. and Hutchinson, J. W. "Interface strength, work of adhesion and plasticity in the peel test". In: *Recent Advances in Fracture Mechanics*. Springer, **1998**, 315–333.

[130] Autumn, K., Liang, Y. A., Hsieh, S. T., Zesch, W., Chan, W. P., Kenny, T. W., Fearing, R., and Full, R. J. "Adhesive force of a single gecko foot-hair". *Nature*, Vol. 405, 681–684, **2000**. DOI: 10.1038/35015073.

[131] Autumn, K., Sitti, M, Liang, Y. A., Peattie, A. M., Hansen, W. R., Sponberg, S., Kenny, T. W., Fearing, R., Israelachvili, J. N., and Full, R. J. "Evidence for van der Waals adhesion in gecko setae". *Proceedings of the National Academy of Sciences of the United States of America*, Vol. 99, No. 19, 12252–12256, **2002**. DOI: 10.1073/pnas.192252799.

[132] Gautam, S. S. and Sauer, R. A. "A composite time integration scheme for dynamic adhesion and its application to gecko spatula peeling". *International Journal of Computational Methods*, Vol. 11, No. 05, 1350104, **2014**. DOI: 10.1142/S0219876213501041.

[133] Gouravaraju, S., Sauer, R. A., and Gautam, S. S. "Investigating the normal and tangential peeling behaviour of gecko spatulae using a coupled adhesion-friction model". *Journal of Adhesion* **2020**. DOI: 10.1080/00218464.2020.1719838.

[134] Begley, M. R., Collino, R. R., Israelachvili., J. N., and McMeeking, R. M. "Peeling of a tape with large deformations and frictional sliding". *Journal of the Mechanics and Physics of Solids*, Vol. 61, No. 5, 1265–1279, **2013**. ISSN: 0022 - 5096. DOI: 10.1016/j.jmps.2012.09.014.

[135] De Zotti, V., Rapina, K., Cortet, P. P., Vanel, L., and Santucci, S. "Bending to kinetic energy transfer in adhesive peel front microinstability". *Physical Review Letters*, Vol. 122, No. 5, 068005, **2019**. DOI: 10.1103/PhysRevLett.122.068005.

[136] Noda, N., Li, R., Miyazaki, T., Takaki, R., and Sano, Y. "Convenient adhesive strength evaluation method in terms of the intensity of singular stress field". *International Journal of Computational Methods*, Vol. 16, No. 01, 1850085, **2019**. DOI: 10.1142/S0219876218500858.

[137] Agrawal, V. and Gautam, S. S. "Higher-order Hermite enriched contact finite elements for adhesive contact problems". *International Journal of Materials and Structural Integrity*, Vol. 13, No. 1/2/3, 16–31, **2019**. DOI: 10.1504/IJMSI.2019.100380.

[138] Sauer, R. A. "Multiscale modelling and simulation of the deformation and adhesion of a single gecko seta". *Computer Methods in Biomechanics and Biomedical Engineering*, Vol. 12, No. 6, 627–640, **2009**. DOI: 10.1080/10255840902802917.

[139] Spink, M., Claxton, D., Falco, C. de, and Vázquez, R. *The NURBS toolbox*. http://octave.sourceforge.net/nurbs/index.html.

[140] Speleers, H. "Algorithm 999: computation of multi-degree B-Splines". *ACM Transactions on Mathematical Software*, Vol. 45, No. 4 **2019**. DOI: 10.1145/3321514.

[141] Toshniwal, D., Speleers, H., Hiemstra, R. R., Manni, C., and Hughes, T. J. R. "Multi-degree B-splines: algorithmic computation and properties". *Computer Aided Geometric Design*, Vol. 76, 101792, **2020**. DOI: 10.1016/j.cagd.2019.101792.

[142] Beccari, C. V. and Casciola, G. "Matrix representations for multi-degree B-splines". *Journal of Computational and Applied Mathematics*, Vol. 381, 113007, **2021**. DOI: 10.1016/j.cam.2020.113007.

List of Publications

Journals:

1. V. Agrawal, and S. S. Gautam. NURBS-based isogeometric analysis for stable and accurate peeling computations. *Sadhana*, 46(3), **2021**. (DOI:10.1007/s12046-020-01513-z)

2. V. Agrawal, and S. S. Gautam. Varying-order NURBS discretization: An accurate and efficient method for isogeometric analysis of large deformation contact problems. *Computer Methods in Applied Mechanics and Engineering*, 367, 113125, **2020**. (DOI:10.1016/j.cma.2020.113125)

3. V. Agrawal, and S. S. Gautam. Higher-order Hermite enriched contact finite elements for adhesive contact problems. *International Journal of Materials and Structural Integrity*, 13(1-3), pp. 16–31, **2019**. (DOI:10.1504/IJMSI.2019.100380)

4. V. Agrawal, and S. S. Gautam. IGA: A simplified introduction and implementation details for finite element users. *Journal of The Institution of Engineers (India): Series C*, 100, pp. 561–585, **2018**. (DOI:10.1007/s40032-018-0462-6)

Conferences (National/International):

1. V. Agrawal, and S. S. Gautam. Investigating the influence of higher-order NURBS discretization on contact force oscillation for large deformation contact using isogeometric analysis. *International Conference on Applied Mechanical Engineering Research (IC-AMER 2019)*, 2nd–5th May, NIT Warangal, Warangal, India, **2019**.

2. V. Agrawal, S. Gouravaraju, and S. S. Gautam. Application of varying order B-splines discretization for accurate peeling computations, *10th International Conference on Computational Methods (ICCM 2019)*, 9th–13th July, NTU Singapore, Singapore, **2019**.

3. V. Agrawal, and S. S. Gautam. An Isogeometric based study of mortar contact algorithm for frictionless sliding, *1st International Conference on Future Learning Aspects of Mechanical Engineering (FLAME 2018)*, 3rd–5th October, Amity University, Noida, India, **2018** (Best paper award).

4. V. Agrawal, and S. S. Gautam. Investigation of contact pressure oscillations with different segment-to-segment based isogeometric contact formulations. *1st International Conference on Numerical Modelling in Engineering (NME 2018)*, 28th–29th August, Ghent University, Belgium, **2018**.

5. V. Agrawal, and S. S. Gautam. NURBS–enriched contact isogeometric element for adhesive contact problems. *International Conference on Theoretical, Applied, Computational and Experimental Mechanics (ICTACEM 2017*, 28th–30th December, IIT Kharagpur, India, **2017**.

6. V. Agrawal, and S. S. Gautam. Enrichment of finite elements with Higher-order Hermite polynomials for adhesive peeling problem. *Indian Conference on Applied Mechanics (INCAM 2017)*, 5th–7th July, MNNIT Allahabad, India, **2017**.

Conferences (Abstract Published Online):

1. V. Agrawal, and S. S. Gautam. An accurate and efficient varying-order NURBS discretization method for there-dimensional isogeometric contact analysis *World Congress in Computational Mechanics (WCCM 2020)*, Paris, France, **2021**.

2. V. Agrawal, T. X. Duong, R. A. Sauer, and S. S. Gautam. An accurate and efficient varying-order NURBS discretization method for isogeometric contact analysis, *VII International Conference on Isogeometric Analysis (IGA 2019)*, 18th - 20th September, Munich, Germany, **2019**.

3. V. Agrawal, S. Gouravaraju, R. A. Sauer, and S. S. Gautam. A varying-order B-splines discretization method for peeling computations. *VI. International Conference on Computational Contact Mechanics (ICCCM 2019) - An ECCOMAS Thematic Conference*, 3rd–5th July, Leibnizhaus Hannover, Germany, **2019**.

4. V. Agrawal, and S. S. Gautam. A comparative study of contact problem solution based on different isogeometric contact formulations. *World Congress in Computational Mechanics (WCCM 2018)*, 22nd–27th July, New York, USA, **2018**.

Poster Presentation:

1. V. Agrawal, and S. S. Gautam. An efficient varying-order NURBS discretization technique for isogeometric analysis of contact problems, *Research Conclave*, 14th–17th March, Indian Institute of Technology Guwahati, Guwahati, India, **2019**.